REPORT DOCUMENTATION PAGE

Form Approved OMB NO. 0704-0188

The public reporting burden for this collection of information is estimated to average 1 hour per response, including the time for reviewing instructions, searching existing data sources, gathering and maintaining the data needed, and completing and reviewing the collection of information. Send comments regarding this burden estimate or any other aspect of this collection of information, including suggesstions for reducing this burden, to Washington Headquarters Services, Directorate for Information Operations and Reports, 1215 Jefferson Davis Highway, Suite 1204, Arlington VA, 22202-4302. Respondents should be aware that notwithstanding any other provision of law, no person shall be subject to any oenalty for failing to comply with a collection of information if it does not display a currently valid OMB control number.
PLEASE DO NOT RETURN YOUR FORM TO THE ABOVE ADDRESS.

1. REPORT DATE (DD-MM-YYYY)	2. REPORT TYPE	3. DATES COVERED (From - To)
12-01-2018	Final Report	1-Oct-2010 - 30-Jun-2017

4. TITLE AND SUBTITLE
Final Report: MURI: An Integrated Multi-Scale Approach for Understanding Ion Transport in Complex Heterogeneous Organic Materials

5a. CONTRACT NUMBER
W911NF-10-1-0520

5b. GRANT NUMBER

5c. PROGRAM ELEMENT NUMBER
611103

6. AUTHORS

5d. PROJECT NUMBER

5e. TASK NUMBER

5f. WORK UNIT NUMBER

7. PERFORMING ORGANIZATION NAMES AND ADDRESSES
Colorado School of Mines
1500 Illinois Street, Guggenheim Hall, Room 130

Golden, CO 80401 -1887

8. PERFORMING ORGANIZATION REPORT NUMBER

9. SPONSORING/MONITORING AGENCY NAME(S) AND ADDRESS (ES)
U.S. Army Research Office
P.O. Box 12211
Research Triangle Park, NC 27709-2211

10. SPONSOR/MONITOR'S ACRONYM(S)
ARO

11. SPONSOR/MONITOR'S REPORT NUMBER(S)
58161-CH-MUR.101

12. DISTRIBUTION AVAILIBILITY STATEMENT
Approved for public release; distribution is unlimited.

13. SUPPLEMENTARY NOTES
The views, opinions and/or findings contained in this report are those of the author(s) and should not contrued as an official Department of the Army position, policy or decision, unless so designated by other documentation.

14. ABSTRACT

15. SUBJECT TERMS

16. SECURITY CLASSIFICATION OF:			17. LIMITATION OF ABSTRACT	15. NUMBER OF PAGES	19a. NAME OF RESPONSIBLE PERSON
a. REPORT	b. ABSTRACT	c. THIS PAGE			Andrew Herring
UU	UU	UU	UU		19b. TELEPHONE NUMBER 303-384-2082

RPPR Final Report
as of 23-Jan-2018

Agency Code:

Proposal Number: 58161CHMUR **Agreement Number: W911NF-10-1-0520**
INVESTIGATOR(S):

Name: Andrew M. Herring
Email: aherring@mines.edu
Phone Number: 3033842082
Principal: Y

Organization: **Colorado School of Mines**
Address: 1500 Illinois Street, Guggenheim Hall, Room 130, Golden, CO 804011887
Country: USA

DUNS Number: 010628170 EIN: 846000551
Report Date: 30-Sep-2017 Date Received: 12-Jan-2018
Final Report for Period Beginning 01-Oct-2010 and Ending 30-Jun-2017
Title: MURI: An Integrated Multi-Scale Approach for Understanding Ion Transport in Complex Heterogeneous Organic Materials
Begin Performance Period: 01-Oct-2010 **End Performance Period:** 30-Jun-2017
Report Term: 0-Other

Submitted By: Andrew Herring Email: aherring@mines.edu
Phone: (303) 384-2082

Distribution Statement: 1-Approved for public release; distribution is unlimited.

STEM Degrees: 20 **STEM Participants:** 5

Major Goals: (1) To produce revolutionary, robust, durable, thin anion exchange membranes with sufficiently high ionic conductivities for practical devices.
(2) To fundamentally understand, with combined experimental and computational approaches, the interplay of chemistry, processing, and morphology on the performance and durability of anion exchange membranes.

Accomplishments: 1. Theoretical Model of Hydroxide Anion.
The first Multiscale reactive molecular dynamics (MS-RMD) simulation for hydroxide was developed. By carefully studying the simulations, we discovered that the solvation structure of the hydroxide ion in bulk water is significantly different from that in an anion exchange membrane (AEM). In bulk water, the water coordination of hydroxide is typically 4-fold with a transient fifth water that promotes proton transfer. However, in an AEM, because of the much lower water content and the physical blockages of the cationic groups, the water coordination number drops by about one water. This change in water coordination, along with the geometric constraints imposed by the polymer, fundamentally alters the proton transfer mechanism of the hydroxide for the case of an AEM, and a reasonable hydroxide model for AEM must take this into account. With the successful hydroxide model at hand, we were able to compute the self-diffusion constant of the hydroxide in AEM as a function of (inverse) temperature. The calculated activation barrier, 5 kcal/mol, is larger than that of the hydrated excess proton in Nafion. This implies that hydroxide transport is more temperature-dependent that proton transport in proton exchange membranes.

The recently developed MS-RMD hydroxide model was utilized to investigate the effect of varying block mole ratio (PPO:PVBTMA) on the solvation and diffusion behavior of hydroxide and water in an AEM system made with PPO-b-PVBTMA block copolymer. Under the same hydration level, the increase of hydrophobic PPO block causes water channels to become narrower, resulting in a decrease of diffusion coefficient for both water and hydroxide. However, above certain block mole ratio, the hydrophilic/hydrophobic phase separation becomes more effective in enhancing or “recovering” the hydroxide transport. The simulation results not only confirm the enhancement of transport properties observed in AEMs made with block copolymers, but also provides a detailed explanation of these effects as well as their limitations.

2. A Deeper Understanding of Cation Clustering.
The organic cations introduced into these materials are strong dipoles. We showed that simply increasing the IEC of an AEM only increases the ionic conductivity at low IEC, at high IEC conductivity does not increase as the additional cations cluster and do not contribute. This can be overcome to a certain extent by using block co-polymers to enhance phase separation in the materials. Clustering was shown to be temperature dependent.

When AEMs are heated under wet conditions the initially disordered cations order and cluster at a temperature between 0 and 100°C. Not only does this limit the conductivity of the material but the resultant mechanical transition has implications for the materials properties in a working device. On the microscopic scale the clustering of the cations leads to a heterogeneous distribution of water in the hydrophilic ion conducting channels of the polymers. At low IEC this was shown to produce a water stripe in the channel center. Water was shown to be heterogeneously distributed at larger length scales implying that some water solvated the cation/anion pair while other water was more dissociated with the polat groups. This phenomenon could be advantageous to fuel cells where water produced at the cathode must be back-diffused o the anode where it is a reactant.

3. High Hydroxide and Anion Conductivity Achieved
Considerable effort was put into robust methods for the determination of the pure hydroxide conductivity of AEMs. Many of the early model polymers developed for this project did not survive the ion-exchange procedure and so it was only with well phase-separated materials and those with advanced cations that data could be obtained. We showed that several AEMs, notably the PPO-b-PVBTMA and an ABA triblock polymer developed by the team, could easily exceed 0.1 S/cm under high RH at temperatures <60°C. Recently a high IEC version of the ABA triblock polymer has shown chloride conductivities of 0.1 S/cm. These ionic conductivities would allow films of 20 microns to enable practical devices.

4.Chemicaly Stable AEMS with Lifetimes Suitable for Applications
Our initial attempts to make chemically stable AEMs were based on bulky and sterically hindered cations. While some modest improvements in chemically stability were observed, it was not possible to achieve high IECs with bulky cations and these same large cations disrupted the AEMs morphology on multiple length scales. Recently small molecule studies have suggested that ammonium cations based on saturated 6 carbon rings had significant stability when compared to almost all other small molecules. We synthesized several polymers with these unique cations and all demonstrated significantly improved stability over first generation trimethylbenzyl ammonium cations in similar polymers. The ABA tribock polymer when functionalized with these cations only lost 20% of its IEC when exposed to 1M KOH at 80°C for one month. This stability is suitable for a number of applications.

5. Mechanically Robust Thin Films Through Cross-Linking and Processing
A extensional rheometer was modified with an environmental chamber such that it could measure mechanical properties as a function of both RH and temperature. Many of the polymers that we synthesized could be cast as thin film from common solvents in the halide form and then quaternized. When the IEC was above 2 meq/g these polymers often swelled or became too soft to work with. We developed two distinct methods of cross-linking the materials to obtain polymers that did not swell excessively. In one method polymers in the halide form after solvent casting were hot pressed to eliminate halogen and cross-link the polymer, this resulted in a loss of IEC but could be optimized to still produce materials with high IEC conductivity and controlled swelling. In a second more powerful method we showed that we could make very tough materials by taking advantage of excess double bonds in the hydrophilic parts of the polymers by photo-crosslinking with a dithiol and UV light. In this way we were able to synthesize high IEC AEMs that did not swell excessively, and had suitable mechanical properties for device integration.

Training Opportunities: 5 undergraduate students took part in the URAP program and 2 High School students in the HSAP program.

Results Dissemination: The Major findings of the research were published in 70+ peer reviewed journal articles, 15 PhD thesis, and 20+ conference proceedings articles. Almost all project personal participated in annual meetings of the relevant scientific societies, The American Chemical Society, The American Physical Society, The Materials Research Society, The Electrochemical Society, The International Society of Electrochemistry and The American Institute of Chemical Engineers to give oral and poster presentations. In addition a number of specialist conferences were attended including the International Society of Polymer Electrolytes, and Fuel Cell and Polymer Gordon Research Conferences.
Annula meetings were held at which DoD scientists were invited so that the project findings could be widely disseminated to DoD laboratory personnel.

RPPR Final Report
as of 23-Jan-2018

Honors and Awards: Gregory A. Voth, Award in Theoretical Chemistry, American Chemical Society Division of Physical Chemistry, 2013.
Gregory A. Voth, Elected Fellow, the International Academy of Quantum Molecular Science, 2013.
Gregory A. Voth, Elected Fellow, the Biophysical Society, 2012.
Gerrick Lindberg, Best Poster Award, 2013 Midwest Theoretical Chemistry Conference
Daniel Knauss, Colorado School of Mines Alumni Teaching Award, Colorado School of Mines 2013.
Andrew M. Herring, Elected Fellow, The American Chemical Society, 2016.
Melissa Vandiver, 2nd place ECS Fall Student poster competition, 2011, 2nd place ECS Fuel Cell symposium student poster competition, 2012

Protocol Activity Status:

Technology Transfer: Patent applications:
Bingzi Zhang, Shuang Gu, Yushan Yan, A Series of Novel Phosphonium Cations and Those Cations-Based Polymers for Hydroxide Exchange Membranes/Ionomers, US Provisional Patent Application 62/026,755, 7/21/2014.

Andrew M. Herring, Mei-Chen Kuo, E. Bryan Coughlin, Tara P. Pandey and Ye Liu
"High Performance Cross-linked Triblock Cationic Functionalized Polymer for Electrochemical Applications, Methods of Making and Methods of Using." US Provisional Patent Application 62/567,038, 10/2/2017

Interactions with DOD Laboratories:
Samples of anion exchange membranes were sent to Dr Xiaomen Ren and Dr. Joshua McClure, ARL, for evaluation in fuel cells. Samples were sent to Dr. Frederick Beyer, ARL, for investigation by HR TEM. Samples were sent to Dr. Walter Zukas, NSSC, for evaluation as solider barrier layers. Discussion with Dr. Michele Anderson, NRL, on sample transfer and development are on-going.

PARTICIPANTS:

Participant Type: PD/PI
Participant: Andrew M. Herring
Person Months Worked: 12.00 **Funding Support:**
Project Contribution:
International Collaboration:
International Travel:
National Academy Member: N
Other Collaborators:

Participant Type: Graduate Student (research assistant)
Participant: Daniel Herbst
Person Months Worked: 12.00 **Funding Support:**
Project Contribution:
International Collaboration:
International Travel:
National Academy Member: N
Other Collaborators:

Participant Type: Co PD/PI
Participant: Yushan Yan
Person Months Worked: 4.00 **Funding Support:**
Project Contribution:
International Collaboration:
International Travel:
National Academy Member: N
Other Collaborators:

RPPR Final Report
as of 23-Jan-2018

Participant Type: Co PD/PI
Participant: Gregory A. Voth
Person Months Worked: 6.00 **Funding Support:**
Project Contribution:
International Collaboration:
International Travel:
National Academy Member: N
Other Collaborators:

Participant Type: Co PD/PI
Participant: Daniel Knauss
Person Months Worked: 6.00 **Funding Support:**
Project Contribution:
International Collaboration:
International Travel:
National Academy Member: N
Other Collaborators:

Participant Type: Co PD/PI
Participant: Matthew W. Liberatore
Person Months Worked: 6.00 **Funding Support:**
Project Contribution:
International Collaboration:
International Travel:
National Academy Member: N
Other Collaborators:

Participant Type: Co PD/PI
Participant: Thomas T. Witten
Person Months Worked: 6.00 **Funding Support:**
Project Contribution:
International Collaboration:
International Travel:
National Academy Member: N
Other Collaborators:

Participant Type: Staff Scientist (doctoral level)
Participant: James L. Horan
Person Months Worked: 12.00 **Funding Support:**
Project Contribution:
International Collaboration:
International Travel:
National Academy Member: N
Other Collaborators:

Participant Type: Technician
Participant: Mei-Chen Kuo
Person Months Worked: 12.00 **Funding Support:**
Project Contribution:
International Collaboration:
International Travel:
National Academy Member: N
Other Collaborators:

RPPR Final Report
as of 23-Jan-2018

Participant Type: Graduate Student (research assistant)
Participant: Ashley M. Maes
Person Months Worked: 12.00 **Funding Support:**
Project Contribution:
International Collaboration:
International Travel:
National Academy Member: N
Other Collaborators:

Participant Type: Graduate Student (research assistant)
Participant: Melissa Vandiver
Person Months Worked: 12.00 **Funding Support:**
Project Contribution:
International Collaboration:
International Travel:
National Academy Member: N
Other Collaborators:

Participant Type: Graduate Student (research assistant)
Participant: Ye Liu
Person Months Worked: 12.00 **Funding Support:**
Project Contribution:
International Collaboration:
International Travel:
National Academy Member: N
Other Collaborators:

Participant Type: Graduate Student (research assistant)
Participant: Tara Pandey
Person Months Worked: 12.00 **Funding Support:**
Project Contribution:
International Collaboration:
International Travel:
National Academy Member: N
Other Collaborators:

Participant Type: Graduate Student (research assistant)
Participant: Himanshu Sarode
Person Months Worked: 12.00 **Funding Support:**
Project Contribution:
International Collaboration:
International Travel:
National Academy Member: N
Other Collaborators:

Participant Type: Graduate Student (research assistant)
Participant: Benjamin Care
Person Months Worked: 12.00 **Funding Support:**
Project Contribution:
International Collaboration:
International Travel:
National Academy Member: N
Other Collaborators:

Participant Type: Graduate Student (research assistant)
Participant: Yating Yan
Person Months Worked: 12.00 **Funding Support:**
Project Contribution:
International Collaboration:
International Travel:
National Academy Member: N
Other Collaborators:

Participant Type: Graduate Student (research assistant)
Participant: Derek Strasser
Person Months Worked: 12.00 **Funding Support:**
Project Contribution:
International Collaboration:
International Travel:
National Academy Member: N
Other Collaborators:

Participant Type: Graduate Student (research assistant)
Participant: Feilong Liu
Person Months Worked: 12.00 **Funding Support:**
Project Contribution:
International Collaboration:
International Travel:
National Academy Member: N
Other Collaborators:

Participant Type: Graduate Student (research assistant)
Participant: Yifan Li
Person Months Worked: 12.00 **Funding Support:**
Project Contribution:
International Collaboration:
International Travel:
National Academy Member: N
Other Collaborators:

Participant Type: Postdoctoral (scholar, fellow or other postdoctoral position)
Participant: Gerrick Lindberg
Person Months Worked: 12.00 **Funding Support:**
Project Contribution:
International Collaboration:
International Travel:
National Academy Member: N
Other Collaborators:

Participant Type: Postdoctoral (scholar, fellow or other postdoctoral position)
Participant: James Damma
Person Months Worked: 3.00 **Funding Support:**
Project Contribution:
International Collaboration:
International Travel:
National Academy Member: N

Other Collaborators:

Participant Type: Postdoctoral (scholar, fellow or other postdoctoral position)
Participant: Christopher Knight
Person Months Worked: 3.00 **Funding Support:**
Project Contribution:
International Collaboration:
International Travel:
National Academy Member: N
Other Collaborators:

Participant Type: Co PD/PI
Participant: E. Bryan Coughlin
Person Months Worked: 6.00 **Funding Support:**
Project Contribution:
International Collaboration:
International Travel:
National Academy Member: N
Other Collaborators:

Participant Type: Postdoctoral (scholar, fellow or other postdoctoral position)
Participant: Ying-Lung Tse
Person Months Worked: 12.00 **Funding Support:**
Project Contribution:
International Collaboration:
International Travel:
National Academy Member: N
Other Collaborators:

Participant Type: Postdoctoral (scholar, fellow or other postdoctoral position)
Participant: Chen Chen
Person Months Worked: 12.00 **Funding Support:**
Project Contribution:
International Collaboration:
International Travel:
National Academy Member: N
Other Collaborators:

Participant Type: Graduate Student (research assistant)
Participant: Feilong Liu
Person Months Worked: 12.00 **Funding Support:**
Project Contribution:
International Collaboration:
International Travel:
National Academy Member: N
Other Collaborators:

Participant Type: Graduate Student (research assistant)
Participant: Yifan Li
Person Months Worked: 12.00 **Funding Support:**
Project Contribution:
International Collaboration:
International Travel:

National Academy Member: N
Other Collaborators:

Participant Type: Graduate Student (research assistant)
Participant: Yating Yang
Person Months Worked: 12.00 **Funding Support:**
Project Contribution:
International Collaboration:
International Travel:
National Academy Member: N
Other Collaborators:

Participant Type: Graduate Student (research assistant)
Participant: Derek Strasser
Person Months Worked: 12.00 **Funding Support:**
Project Contribution:
International Collaboration:
International Travel:
National Academy Member: N
Other Collaborators:

Participant Type: Graduate Student (research assistant)
Participant: WenXu Zhang
Person Months Worked: 12.00 **Funding Support:**
Project Contribution:
International Collaboration:
International Travel:
National Academy Member: N
Other Collaborators:

Participant Type: Graduate Student (research assistant)
Participant: S. Piril Ertem
Person Months Worked: 12.00 **Funding Support:**
Project Contribution:
International Collaboration:
International Travel:
National Academy Member: N
Other Collaborators:

Participant Type: Graduate Student (research assistant)
Participant: Haomiao Yuan
Person Months Worked: 12.00 **Funding Support:**
Project Contribution:
International Collaboration:
International Travel:
National Academy Member: N
Other Collaborators:

Participant Type: Graduate Student (research assistant)
Participant: Chinomoso Nwosu
Person Months Worked: 12.00 **Funding Support:**
Project Contribution:
International Collaboration:

International Travel:
National Academy Member: N
Other Collaborators:

Participant Type: Postdoctoral (scholar, fellow or other postdoctoral position)
Participant: Ying Jin
Person Months Worked: 12.00 **Funding Support:**
Project Contribution:
International Collaboration:
International Travel:
National Academy Member: N
Other Collaborators:

Participant Type: Graduate Student (research assistant)
Participant: Bingzi Zhang
Person Months Worked: 12.00 **Funding Support:**
Project Contribution:
International Collaboration:
International Travel:
National Academy Member: N
Other Collaborators:

Participant Type: Postdoctoral (scholar, fellow or other postdoctoral position)
Participant: Shuang Gu
Person Months Worked: 12.00 **Funding Support:**
Project Contribution:
International Collaboration:
International Travel:
National Academy Member: N
Other Collaborators:

Participant Type: Graduate Student (research assistant)
Participant: Robert Kasper
Person Months Worked: 12.00 **Funding Support:**
Project Contribution:
International Collaboration:
International Travel:
National Academy Member: N
Other Collaborators:

Participant Type: High School Student
Participant: Beau Baker
Person Months Worked: 3.00 **Funding Support:**
Project Contribution:
International Collaboration:
International Travel:
National Academy Member: N
Other Collaborators:

Participant Type: High School Student
Participant: Paul Love
Person Months Worked: 3.00 **Funding Support:**
Project Contribution:

International Collaboration:
International Travel:
National Academy Member: N
Other Collaborators:

Participant Type: Research Experience for Undergraduates (REU) Participant
Participant: Jarupa Jitsanguan
Person Months Worked: 3.00 **Funding Support:**
Project Contribution:
International Collaboration:
International Travel:
National Academy Member: N
Other Collaborators:

Participant Type: Research Experience for Undergraduates (REU) Participant
Participant: Bethanne Peters
Person Months Worked: 3.00 **Funding Support:**
Project Contribution:
International Collaboration:
International Travel:
National Academy Member: N
Other Collaborators:

Participant Type: Research Experience for Undergraduates (REU) Participant
Participant: Samuel Galito
Person Months Worked: 3.00 **Funding Support:**
Project Contribution:
International Collaboration:
International Travel:
National Academy Member: N
Other Collaborators:

Participant Type: Research Experience for Undergraduates (REU) Participant
Participant: Jacob Miraldi
Person Months Worked: 3.00 **Funding Support:**
Project Contribution:
International Collaboration:
International Travel:
National Academy Member: N
Other Collaborators:

Participant Type: Research Experience for Undergraduates (REU) Participant
Participant: Jason Ziolo
Person Months Worked: 3.00 **Funding Support:**
Project Contribution:
International Collaboration:
International Travel:
National Academy Member: N
Other Collaborators:

ARTICLES:

RPPR Final Report
as of 23-Jan-2018

Publication Type: Journal Article Peer Reviewed: Y **Publication Status:** 1-Published
Journal: RSC Advances
Publication Identifier Type: DOI Publication Identifier: 10.1039/c1ra00286d
Volume: 2 Issue: 3 First Page #: 849
Date Submitted: Date Published:
Publication Location:
Article Title: Physicochemical properties of 1,2,3-triazolium ionic liquids
Authors:
Keywords: Ionic liquids, Cation stability
Abstract: Ionic liquids composed of four different 1,2,3-triazolium cations with tosylate or triflate counter anions have been synthesized and characterized. Physicochemical properties of these ionic liquids including ion cluster behavior, thermal properties, electrochemical stability and ionic conductivity were determined and compared to corresponding imidazolium based ionic liquids. The impact of structure variations, in terms of substituents on the ring of the 1,2,3-triazolium cation and identity of the anion (i.e. tosylate versus triflate) is discussed. Stability of the 1,2,3-triazolium salts towards hydroxide ion at 80 °C was studied. Key features of 1,2,3-triazolium salts are their high electrochemical stability and ionic conductivity, comparable to imidazolium ionic liquids, but better chemical stability under alkaline conditions.
Distribution Statement: 1-Approved for public release; distribution is unlimited.
Acknowledged Federal Support:

Publication Type: Journal Article Peer Reviewed: Y **Publication Status:** 1-Published
Journal: The Journal of Chemical Physics
Publication Identifier Type: DOI Publication Identifier: 10.1063/1.4743958
Volume: 137 Issue: 22 First Page #: 0
Date Submitted: Date Published:
Publication Location:
Article Title: Multiscale reactive molecular dynamics
Authors:
Keywords: Proton, hydroxide, multi-scale modelling
Abstract: Many processes important to chemistry, materials science, and biology cannot be described without considering electronic and nuclear-level dynamics and their coupling to slower, cooperative motions of the system. These inherently multiscale problems require computationally efficient and accurate methods to converge statistical properties. In this paper, a method is presented that uses data directly from condensed phase ab initio simulations to develop reactive molecular dynamics models that do not require predefined empirical functions. Instead, the interactions used in the reactive model are expressed as linear combinations of interpolating functions that are optimized by using a linear least-squares algorithm. One notable benefit of the procedure outlined here is the capability to minimize the number of parameters requiring nonlinear optimization. The method presented can be generally applied to multiscale problems and is demonstrated by generating reactive models for the hydrated ex
Distribution Statement: 1-Approved for public release; distribution is unlimited.
Acknowledged Federal Support:

RPPR Final Report
as of 23-Jan-2018

Publication Type: Journal Article Peer Reviewed: Y **Publication Status:** 1-Published
Journal: Journal of Polymer Science Part B: Polymer Physics
Publication Identifier Type: DOI Publication Identifier: 10.1002/polb.23164
Volume: 0 Issue: 0 First Page #: 0
Date Submitted: Date Published:
Publication Location:
Article Title: Understanding anion transport in an aminated trimethyl polyphenylene with high anionic conductivity
Authors:
Keywords: ionomer;polyaromatics;diffusion;SAXS;alkaline exchange membrane;fuel cell;anion conductivity; anion diffusion
Abstract: An alkaline exchange membrane (AEM) based on an aminated trimethyl poly(phenylene) is studied in detail. This article reports hydroxide ion conductivity through an in situ method that allows for a more accurate measurement. The ionic conductivities of the membrane in bromide and carbonate forms at 90 °C and 95% RH are found to be 13 and 17 mS cm?1 respectively. When exchanged with hydroxide, conductivity improved to 86 mS cm?1 under the same experimental conditions. The effect of relative humidity on water uptake and the SAXS patterns of the AEM membranes were investigated. SAXS analysis revealed a rigid aromatic structure of the AEM membrane with no microphase separation. The synthesized AEM is shown to be mechanically stable as seen from the water uptake and SAXS studies. Diffusion NMR studies demonstrated a steady state long-range diffusion constant, D? of 9.8 × 10?6 cm2 s?1 after 50–100 ms.
Distribution Statement: 1-Approved for public release; distribution is unlimited.
Acknowledged Federal Support:

Publication Type: Journal Article Peer Reviewed: Y **Publication Status:** 1-Published
Journal: Journal of Polymer Science Part B: Polymer Physics
Publication Identifier Type: DOI Publication Identifier: 10.1002/polb.23170
Volume: 0 Issue: 0 First Page #: 0
Date Submitted: Date Published:
Publication Location:
Article Title: Synthesis and structure-conductivity relationship of polystyrene-
Authors:
Keywords: amphiphilic block copolymers; anion exchangemembrane fuel cell; atom transfer radical polymerization(ATRP); phase separation; polymeric electrolyte membranes;polystyrene; poly(vinyl benzyl trimethylammonium); structure;conductivity relationship
Abstract: Block copolymers of polystyrene-b-poly(vinyl benzyl trimethylammonium tetrafluoroborate) (PS-b-[PVBTMA][BF4]) were synthesized by sequential monomer addition using atom transfer radical polymerization. Membranes of the block copolymers were prepared by drop casting from dimethylformamide. Initial evaluation of the microphase separation in these PS-b-[PVBTMA][BF4] materials via SAXS revealed the formation of spherical, cylindrical, and lamellar morphologies. Block copolymers of polystyrene-b-poly(vinyl benzyl trimethylammonium hydroxide) (PS-b-[PVBTMA][OH]) were prepared as polymeric alkaline anion exchange membranes materials by ion exchange from PS-b-[PVBTMA][BF4] with hydroxide in order to investigate the relationship between morphology and ionic conductivity. Studies of humidity [relative humidity (RH)]-dependent conductivity at 80 ┐C showed that the conductivity increases with increasing humidity. Moreover, the investigation of the temperature-dependent conductivity at RH ¼ 50, 70,
Distribution Statement: 1-Approved for public release; distribution is unlimited.
Acknowledged Federal Support:

RPPR Final Report
as of 23-Jan-2018

Publication Type: Journal Article Peer Reviewed: Y **Publication Status:** 1-Published
Journal: Journal of Polymer Science Part B: Polymer Physics
Publication Identifier Type: DOI Publication Identifier: 10.1002/polb.23171
Volume: 0 Issue: 0 First Page #: 0
Date Submitted: Date Published:
Publication Location:
Article Title: Synthesis and characterization of perfluoro quaternary ammonium anion exchange membranes
Authors:
Keywords: ionomers; fluoropolymers; NMR; SAXS
Abstract: In this study, new alkaline exchange membranes were prepared from the perfluorinated 3M ionomer with various quaternary ammonium cations attached with sulfonamide linkage. The degree of functionalization varied depending on the cation species, resulting in different ion exchange capacities (IECs), 0.33–0.72 meq g┌1. There was evidence of polymer degradation when the films were exposed to hydroxide, and hence all membrane characterization was performed in the chloride form. Conductivity was dependent on cation species and IEC, Ea ¼ 36–59 kJ mol┌1. Diffusion of water through the membrane was relatively high 1.6 ┐ 10┌5 cm2 s┌1 and indicated restriction over a range of diffusion times, 6–700 ms. Water uptake (WU) in the membranes was generally low and the hydration level varied based on cation species, k ¼ 6–11. Small-angle scattering experiments suggested ionic aggregation, 37–42 A°, independent of cation species but slight differences in long-range order with cation species.
Distribution Statement: 1-Approved for public release; distribution is unlimited.
Acknowledged Federal Support:

Publication Type: Journal Article Peer Reviewed: Y **Publication Status:** 1-Published
Journal: RSC Advances
Publication Identifier Type: DOI Publication Identifier: 10.1039/c2ra21402d
Volume: 0 Issue: 0 First Page #: 0
Date Submitted: Date Published:
Publication Location:
Article Title: Tertiary Sulfonium as Cationic Functional Group for Hydroxide Exchange Membranes
Authors:
Keywords: Anion Exchange Membrane, Sulfonium cation
Abstract: Tertiary sulfonium is introduced as the cationic functional group for hydroxide exchange membranes (HEMs). The methoxyl-substituted triarylsulfonium functionalized HEM (i.e., PSf-MeOTASOH) exhibits excellent thermal stability (TOD: 242 oC), acceptable hydroxide conductivity (15.4 mS cm?1 at 20 oC), and good chemical stability. Our work shows that, similar to nitrogen and phosphorus, sulfur element with designed side groups can also be used to construct HEM cationic functional groups.
Distribution Statement: 1-Approved for public release; distribution is unlimited.
Acknowledged Federal Support:

Publication Type: Journal Article Peer Reviewed: Y **Publication Status:** 1-Published
Journal: ChemSusChem
Publication Identifier Type: DOI Publication Identifier: 10.1002/cssc.201300285
Volume: 0 Issue: 0 First Page #: 0
Date Submitted: Date Published:
Publication Location:
Article Title: Stabilizing the Imidazolium Cation in Hydroxide-Exchange Membranes for Fuel Cells
Authors:
Keywords: cations;fuel cells;imidazolium;membranes;synergy
Abstract: The hydroxide-conducting cationic functional group used in the hydroxide-exchange membranes of fuel cells is key to controlling chemical stability and solubility. A new imidazolium cation, 1,4,5-trimethyl-2-(2,4,6-trimethoxyphenyl)imidazolium, is designed to take advantage of both strong electron-donation properties and steric hindrance. Synergy between these two effects leads to an efficient hydroxide-exchange membrane, with increased alkaline stability and improved OH? conductivity.
Distribution Statement: 1-Approved for public release; distribution is unlimited.
Acknowledged Federal Support:

RPPR Final Report
as of 23-Jan-2018

Publication Type: Journal Article Peer Reviewed: Y **Publication Status:** 1-Published
Journal: Electrochimica Acta
Publication Identifier Type: DOI Publication Identifier: 10.1016/j.electacta.2013.04.033
Volume: 0 Issue: 0 First Page #: 0
Date Submitted: Date Published:
Publication Location:
Article Title: Preparation and characterization of an alkaline anion exchange membrane from chlorinated poly (propylene) aminated with branched poly(ethyleneimine)
Authors:
Keywords: Anion exchange membrane, Fuel Cell, Poly(ethyleneimine), Quaternary ammonium caton, Hydroxide
Abstract: A new randomly crosslinked polymer is investigated for use as an ion-exchange membrane. The polymer was produced through amination of chlorinated poly(propylene) (PP) with poly(ethyleneimine) (PEI) and quaternized with iodoethane. The synthesis of the new polymer is confirmed by FTIR 1 H and 13 C NMR. The microstructure of the polymer consists of aggregates on the order of 1 micometer. Environmentally controlled small and wide angle X-ray analysis showed a relatively featureless amorphous morphology over length scales less than 105 nm through a full range of humidity environments. Little physical swelling of the films were observed, but very high internal water uptake was observed with lambda = 50. The highest in-plane ionic conductivity with chloride as the counter ion observed was 0.29 mS cm?1 at 90 ? C and 95% relative humidity. Infrared spectroscopy was used to monitor the relatively rapid rate of counter-ion reaction of hydroxide with ambient CO2 to form a mixture of carbonate and
Distribution Statement: 1-Approved for public release; distribution is unlimited.
Acknowledged Federal Support:

Publication Type: Journal Article Peer Reviewed: Y **Publication Status:** 1-Published
Journal: Journal of Polymer Science Part B: Polymer Physics
Publication Identifier Type: DOI Publication Identifier: 10.1002/polb.23245
Volume: 0 Issue: 0 First Page #: 0
Date Submitted: Date Published:
Publication Location:
Article Title: Poly(phenylene oxide) copolymer anion exchange membranes
Authors:
Keywords: alkaline exchange membrane, block copolymer, ionomers, poly(phenylene oxide)
Abstract: Poly(phenylene oxide) block and random copolymers are synthesized by oxidative polymerization of 2,6-dimethylphenol and 2,6-diphenylphenol for potential alkaline exchange membrane application. The copolymers are functionalized on the methyl substituted repeat units through a two-step process to produce pendent quaternary ammonium cationic groups. The amount of quaternary ammonium cations and the ion exchange capacity are quantified through titration measurements. Ionic conductivity of the copolymer membranes is measured by electrochemical impedance spectroscopy. Block copolymers show increased bromide conductivity at higher ion exchange capacities compared with the random copolymer analogs. The bromide conductivity for a block copolymer film with an ion exchange capacity of 1.27 mequiv/g reaches 26 mS/cm at 90 °C and 95% relative humidity. The hydroxide conductivity for the same film was measured to be 84 mS/cm at 80 °C and 95% relative humidity.
Distribution Statement: 1-Approved for public release; distribution is unlimited.
Acknowledged Federal Support:

RPPR Final Report
as of 23-Jan-2018

Publication Type: Journal Article Peer Reviewed: Y **Publication Status:** 1-Published
Journal: Journal of Polymer Science Part B: Polymer Physics
Publication Identifier Type: DOI Publication Identifier: 10.1002/polb.23395
Volume: 51 Issue: 24 First Page #: 1727
Date Submitted: Date Published:
Publication Location:
Article Title: Anion exchange membranes: Current status and moving forward
Authors:
Keywords: anion exchange membrane, cationic polymer, con- ductivity, fuel cell, hydrophilic polymers, membranes, phase separation, stability
Abstract: This short review is meant to provide the reader with highlights in anion exchange membrane research, describe current needs in the field, and point out promising directions for future work. Anion exchange membranes (AEMs) provide one possible route to low platinum or platinum-free fuel cells with the potential for facile oxidation of complex fuels beyond hydrogen and methanol. AEMs and related stable cationic polymers also have applications in energy storage and other electrochemical technologies such as water electrolyzers and redox flow batteries. While anion exchange membranes have been known for a long time in water treatment applica- tions, materials for electrochemical technology with robust mechanical properties in thin film format have only recently become more widely available. High hydroxide and bicarbon- ate anion conductivity have been demonstrated in a range of AEM formats, but intrinsic stability of the polymers and dem- onstration of long device lifetime remain major ro
Distribution Statement: 1-Approved for public release; distribution is unlimited.
Acknowledged Federal Support:

Publication Type: Journal Article Peer Reviewed: Y **Publication Status:** 1-Published
Journal: ECS Transactions
Publication Identifier Type: DOI Publication Identifier: 10.1149/05801.0393ecst
Volume: 58 Issue: 1 First Page #: 393
Date Submitted: Date Published:
Publication Location:
Article Title: Progress towards Robust Anion Exchange Membranes for Fuel Cell Applications
Authors:
Keywords: Anion Exchange Membranes, Ionomers, Anion Transport
Abstract: Extensive transport and modeling studies have been performed on a series of polymers based on vinylbenzyltrimethylamonium cations. Flouride is used as a non-reactive surrogate for hydroxide to increase the computational efficiency of transport calculations that can be performed. Interesting effects of water and residual chloride in the film have been explained. In ordered di-block polymers we have strong theoretical evidence for narrow water domains that facilitate rapid transport of anions. With this model we will be able to predict diblock polymer structures that require less water for efficient anion transport. In addition to these studies we are discovering new base stable polymer backbones and cations. A large part of this effort is dedicated to discovering new methods for the production of robust thin anion exchange membranes.
Distribution Statement: 1-Approved for public release; distribution is unlimited.
Acknowledged Federal Support:

RPPR Final Report
as of 23-Jan-2018

Publication Type: Journal Article Peer Reviewed: Y **Publication Status:** 1-Published
Journal: ECS Transactions
Publication Identifier Type: DOI Publication Identifier: 10.1149/05801.1361ecst
Volume: 58 Issue: 1 First Page #: 1361
Date Submitted: Date Published:
Publication Location:
Article Title: FTIR Analysis of the State of Water in Radiation Grafted ETFE Anion Exchange Membrane for Fuel Cell Applications
Authors:
Keywords: Fourier Transform Infrared Spectroscopy, Anion Exchange Membrane, Ionomer, Carbonate, Bicarbonate
Abstract: Infrared study of water in a poly(ethylene-co-tetrafuloroethylene) anion exchange membrane at different level of hydration (%RH 0, 25, 50, 75 and 100) was performed using a Fourier transform infrared (FTIR) microscope. FTIR spectra showed at least two different states of water present in the membrane. The presence of both the non-hydrogen bonded water molecules at the lower hydration level and the hydrogen bonded water molecules at the higher hydration level, unambiguously, are altered with changing humidity.
Distribution Statement: 1-Approved for public release; distribution is unlimited.
Acknowledged Federal Support:

Publication Type: Journal Article Peer Reviewed: Y **Publication Status:** 1-Published
Journal: ECS Transactions
Publication Identifier Type: DOI Publication Identifier: 10.1149/05801.1367ecst
Volume: 58 Issue: 1 First Page #: 1367
Date Submitted: Date Published:
Publication Location:
Article Title: 19F and 13C PGSTE-NMR Diffusion Study to Understand Ion Transport in Alkaline Anion Exchange Membranes
Authors:
Keywords: Anion Exchange Membrane, Ionomer, Pulse Field Gradient NMR, Anion Transport
Abstract: Understanding ion transport in Anion Exchange Membranes (AEMs) has been a widely researched area. In this work we have utilized the method of 19F diffusion NMR to our advantage for this purpose. Fluoride ion and hydroxide ion have similar ionic sizes which makes it as an ideal replacement for the caustic anion. In particular we have studied the effect of temperature and increasing diffusion times (?) on self diffusion of fluoride ions. We have also made a unique effort at measuring bicarbonate and carbonate diffusion through AEMs in this article.
Distribution Statement: 1-Approved for public release; distribution is unlimited.
Acknowledged Federal Support:

RPPR Final Report
as of 23-Jan-2018

Publication Type: Journal Article Peer Reviewed: Y **Publication Status:** 1-Published
Journal: ECS Transactions
Publication Identifier Type: DOI Publication Identifier: 10.1149/05801.1543ecst
Volume: 58 Issue: 1 First Page #: 1543
Date Submitted: Date Published:
Publication Location:
Article Title: Mechanical Characterization of Anion Exchange Membranes
Authors:
Keywords: Anion Exchange Membranes, Polymer Rheology, Ionomers
Abstract: Alkali anion exchange membrane (AEM) fuel cells have the potential for electrochemical energy conversion using inexpensive catalyst and a variety of fuel types. Stability and transport must be improved in AEMs before these devices can be fully realized. Mechanical failure of the membrane can contribute to failure of the fuel cell, thus membrane durability is critical to overall system design. Compared to well researched proton exchange membranes, there is no standard baseline AEM to compare mechanical properties. This work attempts a fundamental study of the mechanical properties of three well-established AEMs using a modified extensional rheometer platform that simulates tensile testing using small membrane samples. The limitations of using this instrument for tensile tests with brittle polymers are also discussed.
Distribution Statement: 1-Approved for public release; distribution is unlimited.
Acknowledged Federal Support:

Publication Type: Journal Article Peer Reviewed: Y **Publication Status:** 1-Published
Journal: The Journal of Physical Chemistry C
Publication Identifier Type: DOI Publication Identifier: 10.1021/jp409728a
Volume: 118 Issue: 1 First Page #: 845
Date Submitted: Date Published:
Publication Location:
Article Title: Chloride Enhances Fluoride Mobility in Anion Exchange Membrane/Polycationic Systems
Authors:
Keywords: Anion exchange membrane, Chloride transport, flouride transport, ionic diffusion
Abstract: We have studied anion exchange membrane/polycationic systems with different percentages of fluoride and chloride as counterions by molecular dynamics simulations. We also experimentally measured the self-diffusion constant of fluoride in a diblock copolymer that has the same hydrophilic block and found satisfactory agreement with simulations within a factor of 2. At 300 K, our simulations showed that the self-diffusion constant of fluoride increases by about 70% when fluoride content decreases from 100% to 40% (and 60% Cl), and it increases by about 140% when fluoride content decreases from 100% to 10%. Increasing % Cl also slightly decreases the attraction between fluoride and the cations. We hypothesize that the root cause of the enhancement in fluoride mobility is due to the larger size of the chloride ion, which more readily loses its water solvation shells because of a lower charge/radius squared (surface electric field). This in turn frees up more water for ion transport. We beli
Distribution Statement: 1-Approved for public release; distribution is unlimited.
Acknowledged Federal Support:

RPPR Final Report
as of 23-Jan-2018

Publication Type: Journal Article Peer Reviewed: Y **Publication Status:** 1-Published
Journal: The Journal of Physical Chemistry B
Publication Identifier Type: DOI Publication Identifier: 10.1021/jp4085662
Volume: 0 Issue: 0 First Page #: 0
Date Submitted: Date Published:
Publication Location:
Article Title: Insights into the Transport of Aqueous Quaternary Ammonium Cations: A Combined Experimental and Computational Study
Authors:
Keywords: Anion Transport; Molecular Dynamics
Abstract: This study focuses on understanding the relative effects of ammonium substituent groups (we primarily consider tetramethylammonium, benzyltrimethylammonium, and tetraethy- lammonium cations) and anion species (OH?, HCO3?, CO32?, Cl?, and F?) on ion transport by combining experimental and computational approaches. We characterize transport experimen- tally using ionic conductivity and self-diffusion coefficients measured from NMR. These experimental results are interpreted using simulation methods to describe the transport of these cations and anions considering the effects of the counterion. It is particularly noteworthy that we directly probe cation and anion diffusion with pulsed gradient stimulated echo NMR and molecular dynamics simulations, corroborating these methods and providing a direct link between atomic-resolution simulations and macroscale experiments. By pairing diffusion measurements and simulations with residence times, we were able to understand the interplay between s
Distribution Statement: 1-Approved for public release; distribution is unlimited.
Acknowledged Federal Support:

Publication Type: Journal Article Peer Reviewed: Y **Publication Status:** 1-Published
Journal: The Journal of Physical Chemistry C
Publication Identifier Type: DOI Publication Identifier: 10.1021/jp5027674
Volume: 118 Issue: 28 First Page #: 15136
Date Submitted: Date Published:
Publication Location:
Article Title: Anion Transport in a Chemically Stable, Sterically Bulky ?-C Modified Imidazolium Functionalized Anion Exchange Membrane
Authors:
Keywords: Anion Exchange Membrane, stable cation, anion transport, morphology
Abstract: The morphology and anion transport of an ?-C modified imidazolium functionalized anion exchange membrane, 1,4,5-trimethyl-2-(2,4,6-trimethoxyphenyl)imidazolium functionalized polyphenylene oxide (with ion exchange capacity {IEC} = 1.53 or 1.82 mequiv/g), were studied in detail. The novel cation is less susceptible to OH– attack (0% degradation) compared to unsubstituted imidazolium functionalized polyphenylene oxide (25% degradation) after 24 h at 80 °C in 1 M KOH. The two different IEC materials (with the same protected cation) show interesting differences in membrane performance. From AFM and SAXS under humid conditions, the domain sizes of the membrane change, which impact the transport properties. The lower IEC sample showed a smaller tortuosity and, thus, needs a longer diffusion time for the water molecules to be fully hindered inside the hydrophobic clusters, which is confirmed by water self-diffusion measurements from pulsed field gradient NMR. From conductivity and diffusion m
Distribution Statement: 1-Approved for public release; distribution is unlimited.
Acknowledged Federal Support:

RPPR Final Report
as of 23-Jan-2018

Publication Type: Journal Article Peer Reviewed: Y **Publication Status:** 1-Published
Journal: Journal of the Electrochemical Society
Publication Identifier Type: DOI Publication Identifier: 10.1149/2.0971410jes
Volume: 161 Issue: 10 First Page #: 677
Date Submitted: Date Published:
Publication Location:
Article Title: Mechanical Characterization of Anion Exchange Membranes by Extensional Rheology under Controlled Hydration
Authors:
Keywords: Polymer rheology, anion exchange membrane, mechanical properties
Abstract: Alkali anion exchange membrane (AEM) based devices have the potential for electrochemical energy conversion using inexpensive catalysts and a variety of fuel types. Membrane stability and anion transport must be improved in AEMs before these devices can be fully realized. Mechanical failure of the membrane can contribute to failure of the device, thus membrane durability is critical to overall system design. Here, a study of the mechanical properties of three well-established AEMs uses a modified extensional rheometer platform to simulate tensile testing using small membrane samples. Mechanical properties were tested at 30 and 60°C under dry or water saturated gas conditions. Water in the membrane has a plasticizing effect, softening the membrane and reducing strength. PEEK membrane reinforcement limits swelling producing negligible softening and only a 9% decrease in strength from dry to hydrated conditions at 30°C. Higher cation concentration increases water uptake resulting in signi
Distribution Statement: 1-Approved for public release; distribution is unlimited.
Acknowledged Federal Support:

Publication Type: Journal Article Peer Reviewed: Y **Publication Status:** 1-Published
Journal: Energy Environ. Sci.
Publication Identifier Type: DOI Publication Identifier: 10.1039/C4EE01303D
Volume: 0 Issue: 0 First Page #: 0
Date Submitted: Date Published:
Publication Location:
Article Title: Anion-exchange membranes in electrochemical energy systems
Authors:
Keywords: Anion Exchange Membranes, Fuel Cells, Anion Transport
Abstract: This article provides an up-to-date perspective on the use of anion-exchange membranes in fuel cells, electrolysers, redox flow batteries, reverse electrodialysis cells, and bioelectrochemical systems (e.g. microbial fuel cells). The aim is to highlight key concepts, misconceptions, the current state-of-the-art, technological and scientific limitations, and the future challenges (research priorities) related to the use of anion-exchange membranes in these energy technologies. All the references that the authors deemed relevant, and were available on the web by the manuscript submission date (30th April 2014), are included.
Distribution Statement: 1-Approved for public release; distribution is unlimited.
Acknowledged Federal Support:

RPPR Final Report
as of 23-Jan-2018

Publication Type: Journal Article Peer Reviewed: Y **Publication Status:** 1-Published
Journal: Macromolecules
Publication Identifier Type: DOI Publication Identifier: 10.1021/ma500993s
Volume: 0 Issue: 0 First Page #: 0
Date Submitted: Date Published:
Publication Location:
Article Title: Poly(2,6-dimethyl-1,4-phenylene oxide) Blended with Poly(vinylbenzyl chloride)-
Authors:
Keywords: Anion Exchange Membrane, Polymer synthesis, SAXS, Polymer tensile testing
Abstract: A block copolymer of poly(vinylbenzyl chloride)-b-polystyrene (PVBC-b-PS) was synthesized through nitroxide-mediated polymerization, then blended with poly(2,6-dimethyl-1,4-phenylene oxide) (PPO) at different compositions, and solution cast to prepare a series of blend films. Differential scanning calorimetry analysis of the PVBC-b-PS and PVBC-b-PS blended with the PPO showed a single glass transition temperature for each of the compositions examined, suggesting that all components in the blend membranes are compatible. The benzyl chloride groups in the blend films were converted to quaternary ammonium groups by reaction with trimethylamine, and the functionalization reached high conversion as characterized by ion exchange capacity (IEC) measurements. The PPO blend anion exchange membranes (AEMs) show improved mechanical properties compared to the styrenic copolymer, particularly in a hydrated condition. The membranes were subjected to thermal and THF/water annealing procedures to stud
Distribution Statement: 1-Approved for public release; distribution is unlimited.
Acknowledged Federal Support:

CONFERENCE PAPERS:

Publication Type: Conference Paper or Presentation **Publication Status:** 1-Published
Conference Name: 220th ECS Meeting
Date Received: 25-May-2017 Conference Date: 10-Oct-2011 Date Published:
Conference Location: Boston, MA
Paper Title: Designing Alkaline Exchange Membranes from Scratch
Authors: Himanshu Sarode, Melissa A. Vandiver, Ashley M. Maes, Benjamin Caire, James L. Horan, Yating Yang
Acknowledged Federal Support: **Y**

Publication Type: Conference Paper or Presentation **Publication Status:** 1-Published
Conference Name: 222nd Meeting of ECS — The Electrochemical Society
Date Received: 13-Sep-2016 Conference Date: 09-Oct-2012 Date Published:
Conference Location: Honolulu, HI
Paper Title: Synthesis and Characterization of Perfluoro Quaternary Ammonium Ion ExchangeMembranes for Fuel Cell Applications
Authors: Melissa A. Vandiver, Soenke Seifert, Matthew W. Liberatore, Andrew M. Herring
Acknowledged Federal Support: **Y**

DISSERTATIONS:

Publication Type: Thesis or Dissertation
Institution:
Date Received: 12-Nov-2013 Completion Date:
Title: Ionic Copolymers for Alkaline Anion Exchange Membrane Fuel Cells (AAEMFCs)
Authors:
Acknowledged Federal Support:

RPPR Final Report
as of 23-Jan-2018

Publication Type: Thesis or Dissertation
Institution:
Date Received: 30-Jul-2014 Completion Date:
Title: Block Copolymers for Alkaline Fuel Cell Membrane Materials
Authors:
Acknowledged Federal Support:

Publication Type: Thesis or Dissertation
Institution:
Date Received: 15-Dec-2014 Completion Date:
Title: Water Uptake Profile In a Model Ion-Exchange Membrane: Conditions For Water-Rich Channels
Authors:
Acknowledged Federal Support:

Publication Type: Thesis or Dissertation
Institution:
Date Received: 19-Jan-2015 Completion Date:
Title: Effect of Hydration on the Mechanical Properties of Anion Exchange Memebranes
Authors:
Acknowledged Federal Support:

Publication Type: Thesis or Dissertation
Institution:
Date Received: 20-Jan-2015 Completion Date:
Title: Cationic Polymers Developed for Alkaline Fuel Cell Applications
Authors:
Acknowledged Federal Support:

Publication Type: Thesis or Dissertation
Institution:
Date Received: 29-Apr-2015 Completion Date:
Title: Exploring Alkaline Stable Organic Cations for Polymer Hydroxide Exchange Membranes
Authors:
Acknowledged Federal Support:

Publication Type: Thesis or Dissertation
Institution:
Date Received: 15-May-2015 Completion Date:
Title: Mechanical Characterization Of Anion Exchange Membranes Under Controlled Environmental Conditions
Authors:
Acknowledged Federal Support:

Publication Type: Thesis or Dissertation
Institution:
Date Received: 16-Sep-2015 Completion Date:
Title: Understanding ion and solvent transport in anion exchange membranes under humidified conditions
Authors:
Acknowledged Federal Support:

RPPR Final Report
as of 23-Jan-2018

Publication Type: Thesis or Dissertation
Institution: Colorado School of Mines
Date Received: 01-Sep-2016 Completion Date: 8/22/16 6:00AM
Title: Effect of bulky cations on the function and stability of anion Exchange membranes
Authors: Ye Liu
Acknowledged Federal Support: **Y**

Publication Type: Thesis or Dissertation
Institution: Colorado School of Mines
Date Received: 02-Sep-2016 Completion Date: 9/1/16 6:00AM
Title: Transport properties of anion exchange membranes for fuel cell Applications
Authors: Tara P. Pandey
Acknowledged Federal Support: **Y**

Publication Type: Thesis or Dissertation
Institution: University of Massachusetts, Amherst
Date Received: 04-Sep-2016 Completion Date: 5/31/16 8:32PM
Title: Synthesis and characterization of polymeric anion exchange membranes
Authors: Wenxu Zhang
Acknowledged Federal Support: **Y**

Publication Type: Thesis or Dissertation
Institution: Universit
Date Received: 04-Sep-2016 Completion Date: 7/31/16 8:41PM
Title: Polymer and small molecule designs for anion conducting Membranes: connected ion-channel morphologies and highly Alkaline stable ammonium cations
Authors: Seder Piril Ertem
Acknowledged Federal Support: **Y**

Publication Type: Thesis or Dissertation
Institution: Colorado
Date Received: 24-May-2017 Completion Date: 5/16/17 10:04AM
Title: Development of functional polymers for ion exchange membranes
Authors: Feilong Liu
Acknowledged Federal Support: **Y**

Publication Type: Thesis or Dissertation
Institution: Colorado School of Mines
Date Received: 14-Nov-2017 Completion Date: 7/15/17 3:31AM
Title: Multiblock Copolymers Containing Hydrophobic and Hydrophilic Segments for Anion Exchange Membranes
Authors: Derek J. Strasser
Acknowledged Federal Support: **Y**

MURI: An integrated multi-scale approach for understanding ion transport in complex heterogeneous organic materials

Vito Di Noto,[h] E. Bryan Coughlin,[c] Daniel M. Knauss,[b] Yushan Yan,[d] Gregory A. Voth,[e] Thomas A. Witten,[f] Matthew W. Liberatore,[a] and Andrew M. Herring,[a,*]

[a] Department of Chemical and Biological Engineering and
[b]Department of Chemistry and Geochemistry, Colorado School of Mines, Golden, CO 80401, USA
[c]Department of Polymer Science and Engineering, Conte Research Center, University of Massachusetts, Amherst, MA 01003, USA
[d]Department of Chemical and Biomolecular Engineering, University of Delaware, Newark, DE 19716, USA
[e]Department of Chemistry and [f]Department of Physics, James Franck Institute and Computation Institute, University of Chicago, Chicago, IL 60637, USA
[g]Advanced Photon Source, Argonne National Laboratory, Argonne, IL, 60439, USA
[h]Department of Chemical Sciences, University of Padova, Via Marzolo 1, I-35151, Padova (PD), Italy

Final Report, submitted January 12th 2018.

Prepared for ARO under contract W911NF-10-1-0520

*Email: aherring@mines.edu

Table of Contents

Project Goals 4
Major Achievements 4
1. Simulations of ion transport 7
1.1 Hydroxide model development 7
1.2Assessing the effects of various unbound ammonium cations on hydroxide properties 10
1.3 Building and simulating anion exchange membranes 14
1.4 Fluoride Transport in Anion Exchange Membranes 16
1.5 Advanced Methodology for Preparation of Anion Exchange Membrane Configurations 18
2. Model Polymer Systems. 19
2.1 Tailoring water partitioning in PVBTMA 22
Methylbutylene co-polymers 28
3. Optimized Polymer systems 33
3.1 Polystyrene-block-poly(vinylbenzylammonium salt) (chloride, bicarbonate, and hydroxide). 33
3.2 Film Casting and characterization of PS-*b*-PVBC block copolymer and corresponding blends 46
3.3 Poly(ethylene glycol) (mPEG) Grafted AEMs (Graft copolymer) 47
3.4 Poly(phenylene oxide)-b-PVBTMA Copolymers 49
3.5 Polyformal block copolymers 54
3.6 Polyisoprene Block Polymers 58
3.7 Random Co-polymers with isoprene 60
Characterization of the UV cross-linked membranes 63
Water Uptake 64
Ion Conductivity 65
Morphology 67
Correlation of Morphology with Ion Conductivity 69
Comparison of UV cross-linked membranes with their thermally cross-linked equivalents 70
3.8 Polysulfone Block Polymers 71
3.9 Functionalization of 3M Ionomer with quaternary ammonium cations 80
4. Incorporation of Novel Cations. 81
4.1 Sulfonium 81
4.2 Phosphonium cations 86
Long-term alkaline stability test on model molecules 86
Identification of the degradation mechanism of three molecules analogous to the QP model 90
Identification of the major degradation mechanism of the QP model. 91
Verification of the degradation mechanism of the QP model compound. 92
Design of a superior quaternary phosphonium-based cation. 94
Synthesis of the 9Me-QP model. 95
Degradation of the the 9Me-QP model ($9MeTPP_{Me}$). 97
Synthesis of $9MeTPP_{Me}$ functionalized polymer. 99
4.3 Cobaltocenium 101

4.4 Stabilized and sterically hindered imidazolium cations 104
4.5 Strung cation architecture 107
4.6 Spiro C6 cations 110
4.7 C6 cations from hydrogenation of pyridine 115
4.8 C6 cations via quaternization 119
5. Physical Chemistry Studies 124
5.1 Influence of AEMS on Carbon based anions 124
5.2 1,4,5-trimethyl-3-benzyl-2-(2,4,6-trimethoxyphenyl)imidazolium Functionalized AEM 126
5.3 Fluoride Transport 136
5.4 Hydroxide ion conductivity and IR water study on the ETFE-g-PVBTMA anion exchange membrane 141
5.5 Polyphenylene Oxide co-Polymers 150
5.6 Polyethylene Co-Polymers 151
5.7 Quaternary Phosphonium 153
6. Mechanical Studies and Film Forming 155
6.1 Simultaneous extensional rheology and SAXS of AEMs 155
6.2 Film Casting and characterization of PS-*b*-PVBC block copolymer and corresponding blends 157
6.3 Effect of crosslinking method on mechanical properties of poly(isoprene)-ran-poly(vinylbenzyl trimethylammonium) films. 160
6.4 Build out of humidity controlled rheometry tool 162
Modification of SER2 fixture 163
SER Tool as Tensile Tester 164
Baseline Data 165
6.5 Mechanical properties of Anion Exchange Membranes 166
6.6 Mechanical performance of crosslinked polyiosoprene copolymers 184
Membrane Swelling 186
Extensional Tests 188
Polyethylene-b-poly(vinylbenzyl trimethylammonium) anion exchange membrane. 194
References 201

Project Goals

(1) To produce **revolutionary, robust, durable, thin anion exchange membranes** with sufficiently high ionic conductivities for practical devices.

(2) To fundamentally understand, with combined experimental and computational approaches, the interplay of **chemistry, processing, and morphology** on the performance and durability of anion exchange membranes.

Major Achievements

1. Theoretical Model of Hydroxide Anion.

The first Multiscale reactive molecular dynamics (MS-RMD) simulation for hydroxide was developed. By carefully studying the simulations, we discovered that the solvation structure of the hydroxide ion in bulk water is significantly different from that in an anion exchange membrane (AEM). In bulk water, the water coordination of hydroxide is typically 4-fold with a transient fifth water that promotes proton transfer. However, in an AEM, because of the much lower water content and the physical blockages of the cationic groups, the water coordination number drops by about one water. This change in water coordination, along with the geometric constraints imposed by the polymer, fundamentally alters the proton transfer mechanism of the hydroxide for the case of an AEM, and a reasonable hydroxide model for AEM must take this into account. With the successful hydroxide model at hand, we were able to compute the self-diffusion constant of the hydroxide in AEM as a function of (inverse) temperature. The calculated activation barrier, 5 kcal/mol, is larger than that of the hydrated excess proton in Nafion. This implies that hydroxide transport is more temperature-dependent that proton transport in proton exchange membranes.

The recently developed MS-RMD hydroxide model was utilized to investigate the effect of varying block mole ratio (PPO:PVBTMA) on the solvation and diffusion behavior of hydroxide and water in an AEM system made with PPO-b-PVBTMA block copolymer. Under the same hydration level, the increase of hydrophobic PPO block causes water channels to become narrower, resulting in a decrease of diffusion coefficient for both water and hydroxide. However, above certain block mole ratio, the hydrophilic/hydrophobic phase separation becomes more effective in enhancing or "recovering" the hydroxide transport. The simulation results not only confirm the enhancement of transport properties observed in AEMs made with block copolymers, but also provides a detailed explanation of these effects as well as their limitations.

2. A Deeper Understanding of Cation Clustering.

The organic cations introduced into these materials are strong dipoles. We showed that simply increasing the IEC of an AEM only increases the ionic conductivity at low IEC, at high IEC conductivity does not increase as the additional cations cluster and do not contribute. This can be overcome to a certain extent by using block co-polymers to enhance phase separation in the materials. Clustering was shown to be temperature dependent. When AEMs are heated under wet conditions the initially disordered cations order and cluster at a temperature between 0 and 100°C. Not only does this limit the

conductivity of the material but the resultant mechanical transition has implications for the materials properties in a working device. On the microscopic scale the clustering of the cations leads to a heterogeneous distribution of water in the hydrophilic ion conducting channels of the polymers. At low IEC this was shown to produce a water stripe in the channel center. Water was shown to be heterogeneously distributed at larger length scales implying that some water solvated the cation/anion pair while other water was more dissociated with the polat groups. This phenomenon could be advantageous to fuel cells where water produced at the cathode must be back-diffused o the anode where it is a reactant.

3. High Hydroxide and Anion Conductivity Achieved

Considerable effort was put into robust methods for the determination of the pure hydroxide conductivity of AEMs. Many of the early model polymers developed for this project did not survive the ion-exchange procedure and so it was only with well phase-separated materials and those with advanced cations that data could be obtained. We showed that several AEMs, notably the PPO-b-PVBTMA and an ABA triblock polymer developed by the team, could easily exceed 0.1 S/cm under high RH at temperatures <60°C. Recently a high IEC version of the ABA triblock polymer has shown chloride conductivities of 0.1 S/cm. These ionic conductivities would allow films of 20 microns to enable practical devices.

4.Chemicaly Stable AEMS with Lifetimes Suitable for Applications

Our initial attempts to make chemically stable AEMs were based on bulky and sterically hindered cations. While some modest improvements in chemically stability were observed, it was not possible to achieve high IECs with bulky cations and these same large cations disrupted the AEMs morphology on multiple length scales. Recently small molecule studies have suggested that ammonium cations based on saturated 6 carbon rings had significant stability when compared to almost all other small molecules. We synthesized several polymers with these unique cations and all demonstrated significantly improved stability over first generation trimethylbenzyl ammonium cations in similar polymers. The ABA tribock polymer when functionalized with these cations only lost 20% of its IEC when exposed to 1M KOH at 80°C for one month. This stability is suitable for a number of applications.

5. Mechanically Robust Thin Films Through Cross-Linking and Processing

A extensional rheometer was modified with an environmental chamber such that it could measure mechanical properties as a function of both RH and temperature. Many of the polymers that we synthesized could be cast as thin film from common solvents in the halide form and then quaternized. When the IEC was above 2 meq/g these polymers often swelled or became too soft to work with. We developed two distinct methods of cross-linking the materials to obtain polymers that did not swell excessively. In one method polymers in the halide form after solvent casting were hot pressed to eliminate halogen and cross-link the polymer, this resulted in a loss of IEC but could be optimized to still produce materials with high IEC conductivity and controlled swelling. In a second more powerful method we showed that we could make very tough materials by taking advantage of excess double bonds in the hydrophilic parts of the polymers by

photo-crosslinking with a dithiol and UV light. In this way we were able to synthesize high IEC AEMs that did not swell excessively, and had suitable mechanical properties for device integration.

1. Simulations of ion transport

1.1 Hydroxide model development

The solvation structure of hydroxide and the process by which a proton is transferred from a water molecule in the first solvation shell to the hydroxide ion have been characterized by *ab initio* molecular dynamics.[i] *Ab initio* molecular dynamics is effective for understanding short timescale and small length-scale phenomena, but it is not feasible for studying the coupling of hydroxide dynamics to large-scale morphological features and the slower cooperative motions of some systems, like anion exchange membranes. Traditional nonreactive molecular dynamics simulations, while significantly more economical and capable of probing many orders of magnitude greater time- and length-scales than *ab initio* molecular dynamics, are unable to capture the bond breaking and forming processes of the proton transfer process. Consequently traditional nonreactive models provide only a partial glimpse of the physics responsible for the behavior of hydroxide. Therefore, more sophisticated models have been developed.

A few models have been introduced in the last few years for the simulation of hydroxide, but we believe these models are ill suited for expanded use. Ufimtsev and coworkers[ii] developed a model for hydroxide where the charge distribution around oxygen is represented by a charged ring,[iii, iv] mimicking the charge distribution determined by *ab initio* calculations.[i] Charged ring hydroxide models, like the Ufimtsev and coworkers model[ii] and the Knight and Voth model,[v] effectively reproduce the properties of hydroxide, but suffer from a large, as of yet undiagnosed, energy drift (on the order of ~100 kcal/mol/ns).[iv] Wick and Dang have parameterized MS-EVB models for hydroxide[vi] and hydronium,[vii] using experimental properties and cluster *ab initio* calculations. These models[vi,vii] incorporate molecular polarization via configuration dependent electrostatics (e.g., bond distance-dependent atomic charges and induced point polarizabilities), in addition to the delocalization of the proton defect across multiple molecules in MS-EVB. The hydronium model[vii] results in a more localized excess proton (c_1^2 = 0.896 +/- 0.002) when compared to the previously reported occupation of MS-EVB states ($c_1^2 \approx 0.6$).[viii] The increased localization of the excess proton will result in a reduced effective radius, which is expected to affect defect transport and affinity for the interface. To our knowledge there have been no extensive studies of the charge distribution of molecular models containing both configuration dependent electrostatics in multi-state reactive models, but AIMD simulations and nonreactive polarizable simulations have been shown to result in distinctly different induced dipole distributions.[ix]

While the models discussed have had some limited success simulating hydroxide, they either suffer from large energy drifts or over-polarization. Both of these effects are unphysical and expected to result in limited representability of the true system physics. Therefore, the Voth group has developed a hydroxide model that avoids these issues.[x] We found that introducing a Stillinger-Weber potential[xi] to the angle formed by water oxygen, hydroxide oxygen, and water oxygen to a two site point charge hydroxide model can

reproduce the correct hydroxide solvation structure while maintaining an energy drift comparable to typical empirical force fields.[x] In addition to reproducing the known local solvation structure of hydroxide and improved energy conservation, the Stillinger-Weber hydroxide model we constructed is found to have properties that compare favorably with *ab initio* simulations.

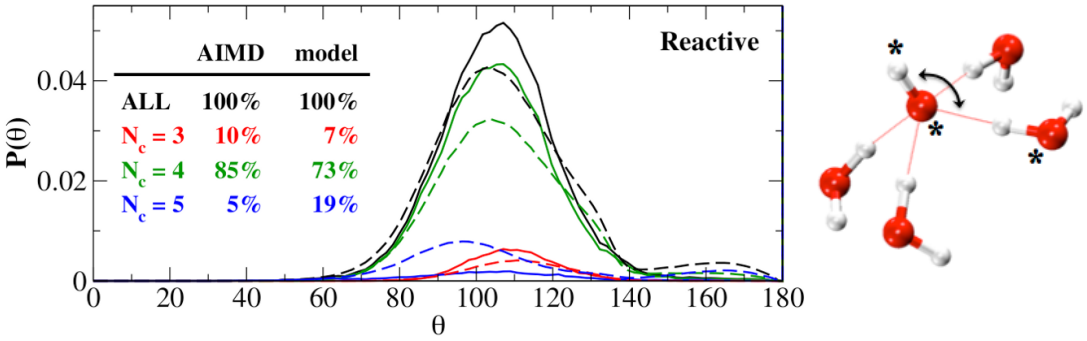

Figure 1 The average solvation of hydroxide with the first solvation shell is shown on the right, where the identified angle formed by the hydroxide hydrogen, hydroxide oxygen and a neighboring water oxygen is a descriptive metric to quantify hydroxide solvation structure. The plot shows the distribution of this angle for situations where there is three-fold coordination (red), four-fold coordination (green) and five-fold coordination. The black line is the sum of all coordination states. The solid lines show results obtained from reference *ab initio* simulations and the dashed lines are for the Stillinger-Weber based hydroxide model.

The proton transfer mechanism in hydroxide is closely linked to a dynamically changing local solvation structure. There are significant populations of three-, four- and five-fold coordination of water molecules around hydroxide, but while the four-fold coordination state dominates, proton transfer events are most likely to occur in the three-fold coordination state.[i] Therefore, to correctly model the transport of hydroxide it is important to capture the correct solvation structure and the interconversion between these local solvation states. **Figure 1** shows the distribution of the angles formed by the hydroxide hydrogen, hydroxide oxygen, and a neighboring water oxygen for the different coordination states and the average four-fold coordination state of hydroxide. The Stillinger-Weber based hydroxide model is found to perform similarly to the far more expensive *ab initio* molecular dynamics simulations.[x]

Figure 2 shows the potential of mean force for proton transport, quantifying the energetics of proton transfer from water to hydroxide. The barrier for proton transfer in the reactive model is 1.9 kcal/mol is very similar to the barrier calculated from the *ab initio* simulations is 1.6 kcal/mol (about 0.5 k_BT). It can also be clearly seen that the nonreactive model results in a distinctly different free energy surface, which will distort the local solvation structure of hydroxide. The self-diffusion of the hydroxide ion was calculated from the mean squared displacement. The MS-EVB model yields a diffusion constant of 0.28 +/- 0.20 $Å^2$/ps, which is much larger than the diffusion constant of the nonreactive model, 0.08 +/- 0.05 $Å^2$/ps. The diffusion constant calculated from the reference *ab initio* simulation was 0.05 +/- 0.02 $Å^2$/ps. The ordering of water and hydroxide diffusion constants is the same as experiment and *ab initio*.

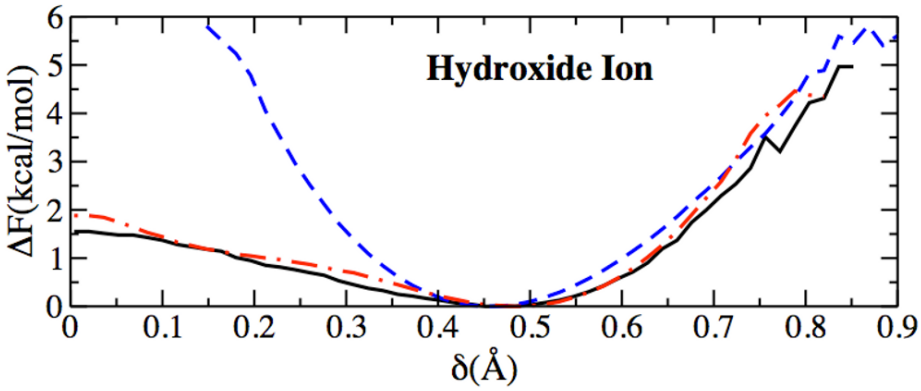

Figure 2 The potential of mean force along a proton transfer coordinate for hydroxide ion. Results are shown for the *ab initio* (solid black), nonreactive (dashed blue), and reactive (dot-dashed red) models.

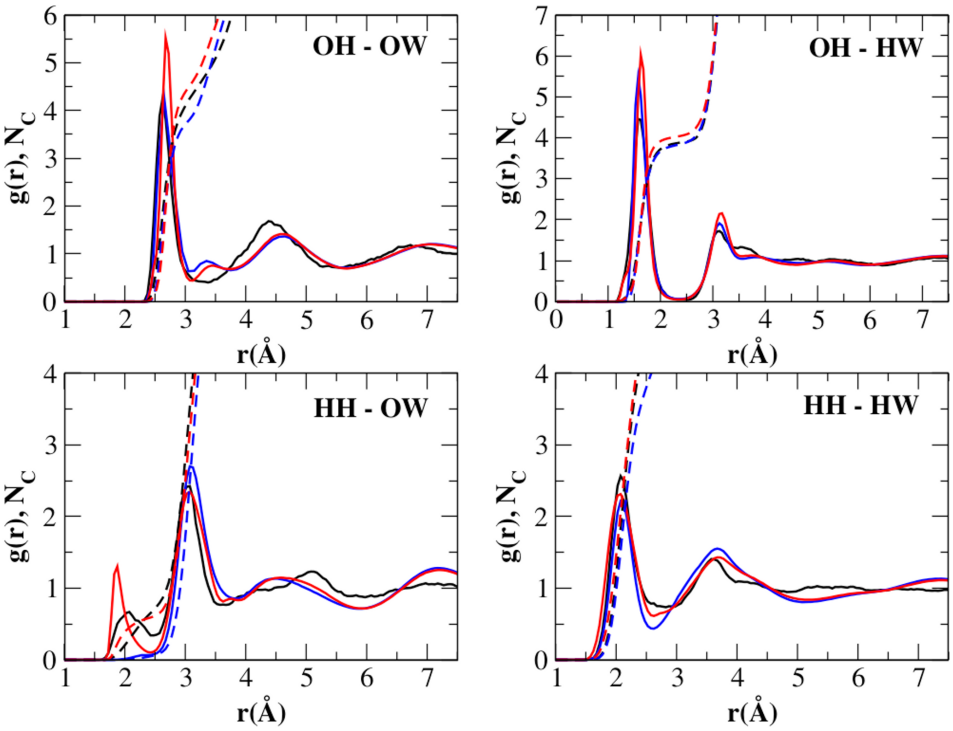

Figure 3 Radial distribution functions (solid lines) and integrated coordination numbers (dashed lines) between atoms of the hydroxide ion and water molecules. For each plot, results from the AIMD (black), nonreactive (blue), and reactive MS-EVB (red) models are shown.

Last the intermolecular hydroxide ion and water molecule radial distribution functions were calculated (Figure 3). The *ab initio* simulations and nonreactive and reactive models generally agree. In the OH-OW radial distribution function the first peak is very similar for the different methods, but the models have a peak at about 3.5 Å that does not occur in the *ab initio* simulations. This peak is due to the donation of a hydrogen-bond from hydroxide to a neighboring water. The first peak in the HH-OW radial distribution function is also due to the donation of a hydrogen-bond from hydroxide to a neighboring water. The nonreactive model and a previous charged ring

reactive model[iv] were unable to capture this hydrogen-bond, but our model and ab initio simulations do show a hydrogen-bond donated to water. While the peak is over-structured in the MS-EVB model, this water is believed to be important in the proton transfer process.[i]

1.2Assessing the effects of various unbound ammonium cations on hydroxide properties

While there are numerous possible backbone and cation options for anion exchange membranes, there is not currently a dominant material in terms of performance. Judging the relative merits of these varied materials can be challenging because of the wide range of relevant operating conditions, the large number of permutations of backbone, cation and side group moieties, and the unclear dependence of membrane properties on membrane preparation and morphology. The goal of these simulations is to understand the effects of ammonium cations on hydroxide solvation and transport, without the complications of backbone, membrane morphology and system preparation. We have simulated tetramethyl ammonium, benzyltrimethyl ammonium and tetraethyl ammonium in aqueous solution as representative analogues of cations suitable to tether in anion exchange membranes. In **Figure 4**, the density is shown as a function of temperature and density for tetramethyl ammonium, benzyltrimethyl ammonium and tetraethyl ammonium. The three membranes display similar temperature dependence for the density. The concentration-dependence shows different behavior depending on the cation. The tetramethyl- and tetraethyl- ammoniums increase in density as the concentration increases, but have much weaker concentration dependence than benzyltrimethyl ammonium. It is unclear if this result is related to the membrane swelling behavior.

The limited stability of these materials under realistic operating conditions is a challenge when testing materials. While chemically unstable materials are not viable for large-scale use in fuel cells, those materials may have other properties that are desirable for anion exchange fuel cell operation (for example fast hydroxide transport, high morphological control or high chemical selectivity). It may be possible to design materials that capture these desired traits with the additional requirement of chemical stability in the presence of hydroxide. Therefore it is useful and often easier to measure properties of membranes under conditions similar to operational conditions, but avoiding possible complications that may arise from true fuel cell operation. For example, many membranes are susceptible to hydroxide attack,[xii,xiii] which has lead to the testing of membranes with less reactive anions, like halides. To understand the possible representability of chloride for hydroxide in an environment relevant for anion exchange membranes, simulations of benzyltrimethyl ammonium have been completed using both hydroxide and chloride separately as counter ions. Figure 5 shows the coordination number for benzyltrimethyl ammonium with hydroxide and chloride. The coordination number for the temperatures considered for chloride at this concentration are essentially indistinguishable, but for hydroxide there is a noticeable spread. There are noticeable differences between the anions though. The onset of population is at ~3.5 Å and ~4.5 Å, in the hydroxide and the chloride systems, respectively, so the hydroxide is on average able to approach closer to the cation. The population grows more slowly for hydroxide than chloride, so that at intermediate separations there are fewer hydroxide ions on

average around the ammonium ion. The effects of these subtle differences on anion transport remain unclear.

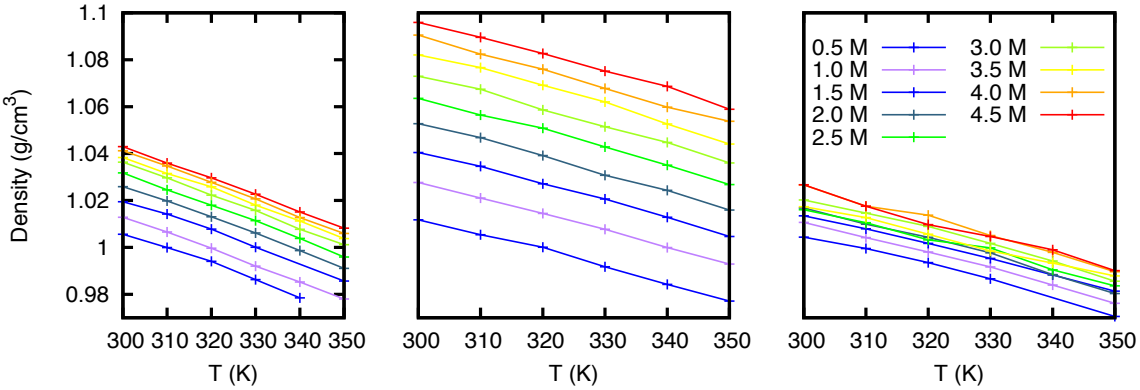

Figure 4 The plots show the concentration and temperature dependence of the density for aqueous hydroxide solutions of tetramethyl ammonium (left), benzyltrimethyl ammonium (center) and tetraethyl ammonium (right). The concentration ranges from 0.5 to 4.5 M in increments of 0.5 M, where the bottom curve is the lowest concentration and the top curve is the highest concentration in each plot.

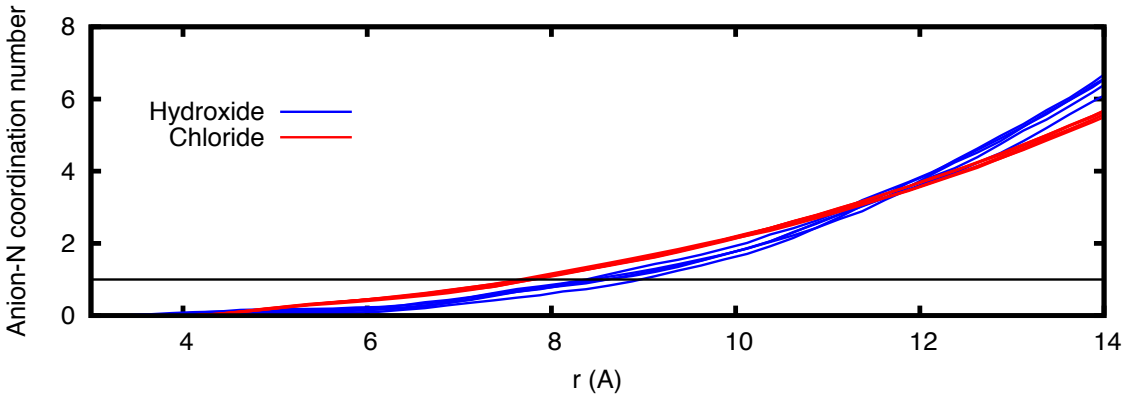

Figure 5 The plot shows the anion-nitrogen coordination number for benzyltrimethyl ammonium with either hydroxide (blue) or chloride (red). These simulations were performed at 1 M and 300, 310, 320, 330, 340 and 350 K. The expected behavior is observed as the temperature is increased so, to simplify the plot, different temperatures are shown in the same color to show that temperature has little effect on the chloride system while the hydroxide system shows a larger response. The horizontal black line indicates a coordination number of one, which, when it intersects with the coordination number, is the distance by which on average one pair is found.

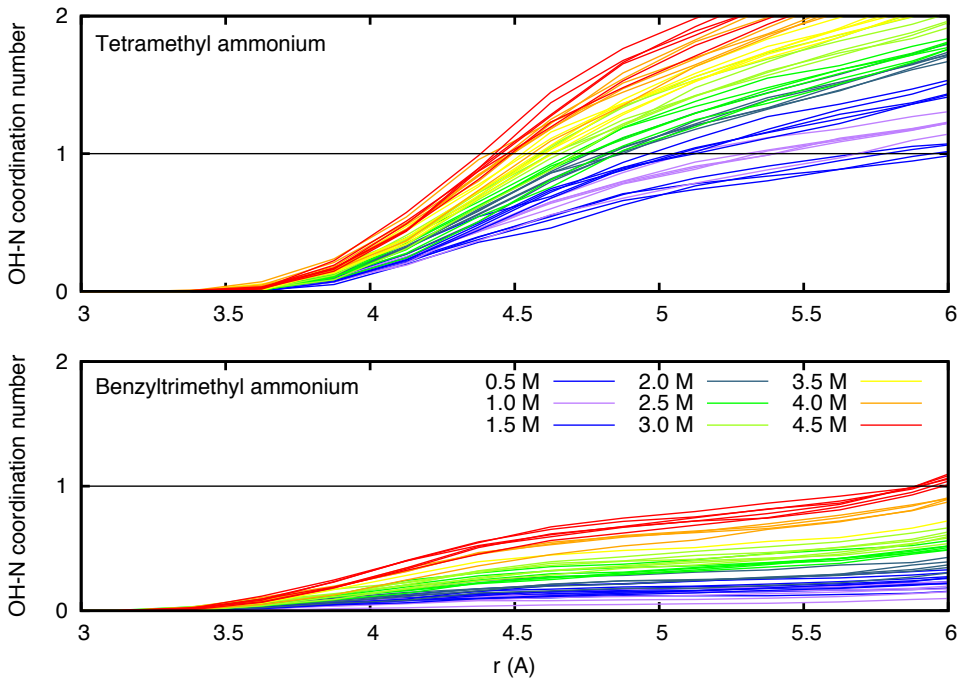

Figure 6 The plots show the coordination number for the hydroxide oxygen and ammonium nitrogen pair for tetramethyl ammonium and benzyltrimethyl ammonium. The different molarities considered are labeled with color and all temperatures at the same concentration are shown in the same color to show the temperature-induced spread.

Additionally we have considered the relative solvation around different ammonium cations, tetramethyl ammonium and benzyltrimethyl ammonium. The ammonium nitrogen and hydroxide oxygen coordination number is shown in Figure 6 for tetramethyl ammonium and benzyltrimethyl ammonium for each concentration and temperature simulated. The concentration dependence of the coordination number shows that as the concentration increases, the ions are packed closer together. The different temperatures are included in the plots as multiple curves shown with the same color revealing that, while the expected temperature dependence is observed, the overall effect is minimal. It is more interesting though to compare the coordination number observed for the two cations. The onset of population begins at ~3.4 Å for both cations, but the increase in population and the shape of the curves are distinctly different. The tetramethyl ammonium coordination number increases such that for all of the concentrations considered they reach the value of one hydroxide oxygen atom coordinating nitrogen by 6 Å. In the benzyltrimethyl ammonium solutions however, the coordination number increases more gradually and only in the highest concentration solutions is a hydroxide oxygen atom found to be on average coordinating nitrogen at 6 Å. The ability of the anion-cation pair to achieve similar separations in both cations, but with reduced probability in benzyltrimethyl ammonium may reveal an important feature of ammonium solvation that leads to important anion transport pathways while protecting the cation from degradation. More investigation into the structural features and their correlation with anion transport, as well as the effects of the backbone material and morphology is needed. We are working with the Herring's group to align our simulation results with

experiments on the same system, corroborating each other's work and more importantly providing micro- and macroscopic information about the effects of these cations on anion properties.

Diffusion of small molecules through water plays an important role from fundamental point of view. Water has a very complicated solution dynamics by virtue of its intricate hydrogen bonding. Water is known to have ordering at smaller length and time scales which vanishes on longer length scales. Diffusion of various species through water is a governed by thermal motion of that species and this is the most fundamental form of transport. For various species, diffusion through water is governed by thermal motion of the species, which is the most fundamental form of transport. Self Diffusion Coefficient measurements were carried out using a ^{13}C PGSTE-NMR probe at CSM. The diffusion measurements carried out here are leading to validation of the water model used in the simulations. For the diffusion study the 5 cations shown in Figure 7 were synthesized with a ^{13}C methyl label on each of them.

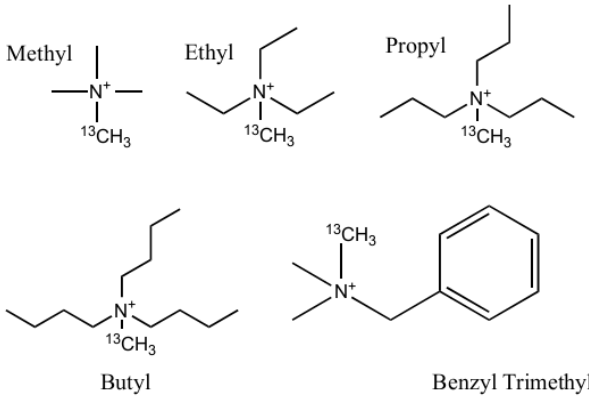

Figure 7: Structures of the synthesized quaternary ammonium cations with ^{13}C labeled methyl groups.

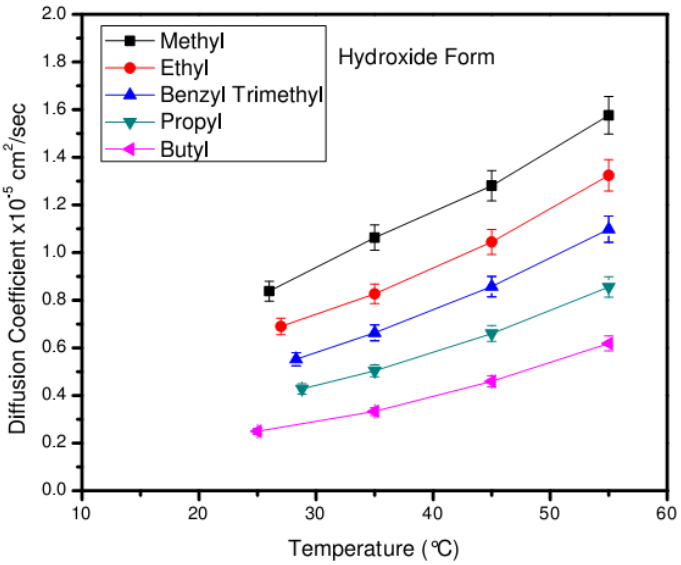

Figure 8: Self-Diffusion Coefficients of 5 different cations measured using ^{13}C Pulse Gradient Stimulated Echo (PGSTE)-NMR Technique **Methyl, Ethyl, Benzyl Trimethyl, Propyl, Butyl**

As shown in **Figure 8** the diffusion coefficient increases as expected with increasing temperature. Self diffusion coefficients were found to be strongly affected by the size and shape of the moving species here the quaternary ammonium cations. The sterically hindered benzyl trimethyl ammonium cation shows an intermediate diffusion among the 5 cations. As the size of the cation increases there is a decrease in the value of D. The room temperature self diffusion coefficient value of each cation was compared with the published values at infinite dilution from the CRC Handbook. All the values are less than the reported values, which can be attributed to the finite dilution of 0.92M as compared to the infinite dilution. A comparison between these experiment and the simulations for three of the cations is shown in **Figure 9**. The agreement between the two for the ethyl case is very encouraging, however, the theory over predicts the experiment for the other two. We are still working on interpreting these results.

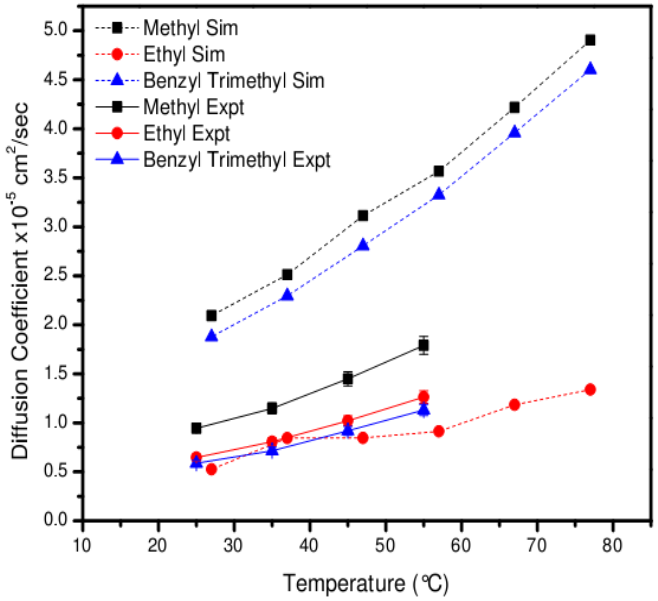

Figure 9: Comparison of experimental and Simulated Self -Diffusion coefficients for three cations Methyl, Ethyl, and Benzyl trimethyl ammonium Chloride.

1.3 Building and simulating anion exchange membranes

To understand the properties of hydroxide in anion exchange membranes we have begun looking at six cations and four backbones for anion exchange membranes. Ammonium cations are the most common choice for anion exchange membrane cations and we have chosen two common cations: tetramethyl ammonium and benzyltrimethyl ammonium. Ammonium cations promote reasonably high hydroxide conductivity, but they are hindered by low chemical stability in the presence of hydroxide. A similar nitrogen containing cation we are also considering is DABCO, which also contains a quaternary ammonium moiety. The Yan group has developed a number of phosphorous and sulfur-based cations that may retain the favorable conductivity of ammonium cations with increased stability. We have selected benzyltriphenyl phosphonium, tris(2,4,6-trimethoxyphenyl) quaternary phosphonium and benzyldiphenyl sulfonium. The backbones being considered are an alkane, polyether sulfone, polyarylether sulfone and

polyethylene glycol. By contrasting these materials and looking at the observed properties with each permutation of cation and backbone we are working to understand the relative effects of these materials.

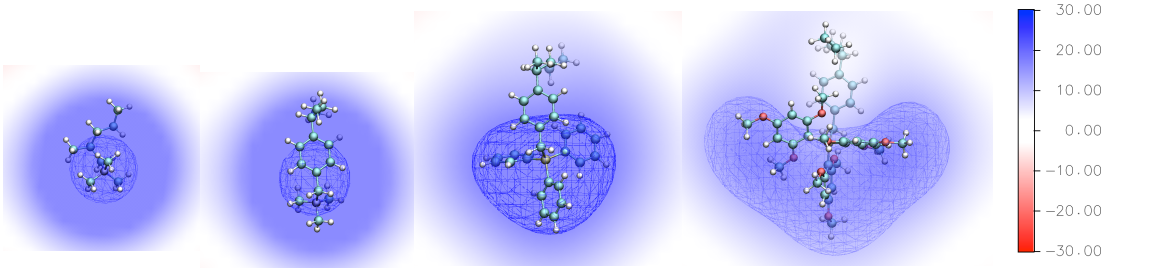

Figure 10 A snapshot of the electrostatic potential generated by the cations in the minimized geometry is shown for four anion exchange membrane monomers. The monomers are depicted with an alkane backbone with, from left to right, tetramethyl ammonium, benzyltrimethyl ammonium, benzyltriphenyl phosphonium and tris(2,4,6-trimethoxyphenyl) quaternary phosphonium cations. The electrostatic potential is in units of k_BT/e, where k_B is Boltzmann's constant, T is temperature and e is the magnitude of the elementary charge. The cloud depicted around each cation shows the dramatically different shapes, which are shown with a wire frame at +30 k_BT/e, and electrostatic field intensities, which are demonstrated by the cloud intensity around the cation.

We are developing force fields suitable for simulating these systems and analyzing the differences in size, shape, and charge distribution for the monomers. Figure 10 shows the minimum potential energy structures for four of the monomers being considered and the electrostatic potential generated by those monomers. For each monomer the alkane backbone is oriented toward the top of the image. Tetramethyl ammonium is the simplest cation considered and one of the most common cations for anion exchange membranes. The charge distribution is distributed over the four methyl moieties and results in a spherical shape. The positive charge in the benzyltrimethyl ammonium cation is focused around the benzyl group. This results also in a spherical charge distribution, but with a slightly more diffuse field intensity than tetramethyl ammonium. The charge in benzyltriphenyl phosphonium is distributed over the three terminal benzyl groups on the cation. The linking benzyl group that attaches the phosphoium moiety to the polymer backbone has little positive charge localization and leads to a distorted spherical shape with a larger, more diffuse electric field. Tris(2,4,6-trimethoxyphenyl) quaternary phosphonium is the largest cation considered. Again the linking benzyl group has little positive charge localization. The bulky trimethoxyphenyl groups result in a large bowl-like shape and the most diffuse charge distribution. The size and shape of these cations will lead to different cation-cation packing in the membrane and also very different paths for anion transport.

Additionally we are performing molecular dynamics simulations with these membranes. The various systems are at different stages of completion. Figure 11 shows the radial distribution function between cation center and hydroxide for the six cations all on an alkane backbone. Figure 11 shows that the six cations interact very differently with hydroxide. The ammonium-based cations, BMA and TMA, are similar with a very sharp peak near 4 Å. The third nitrogen-containing cation, DABCO, has a peak slightly shifted and broadened when compared to the ammonium cations, but similar in intensity. The

phosphorous-based cations are much larger than the nitrogen-based cations and this increased size results in density shifted to larger separations. The benzyltriphenyl phosphonium and tris(2,4,6-trimethoxyphenyl) quaternary phosphonium cations show first peak maxima at ~5 and ~7.5 Å, respectively. Interestingly, the large benzyldiphenyl sulfonium cation shows the onset of density at the shortest separations for the cations studied. Generally it is also important to note that shifting the first peak to larger values, results in reduced intensity. It is clear that basic attributes of the cation (e.g. size and charge distribution) have a significant effect on the distribution of hydroxide ions around the cation-hydroxide. We are now working to complete these simulations and add information about the transport of hydroxide and to correlate transport with these basic structural attributes.

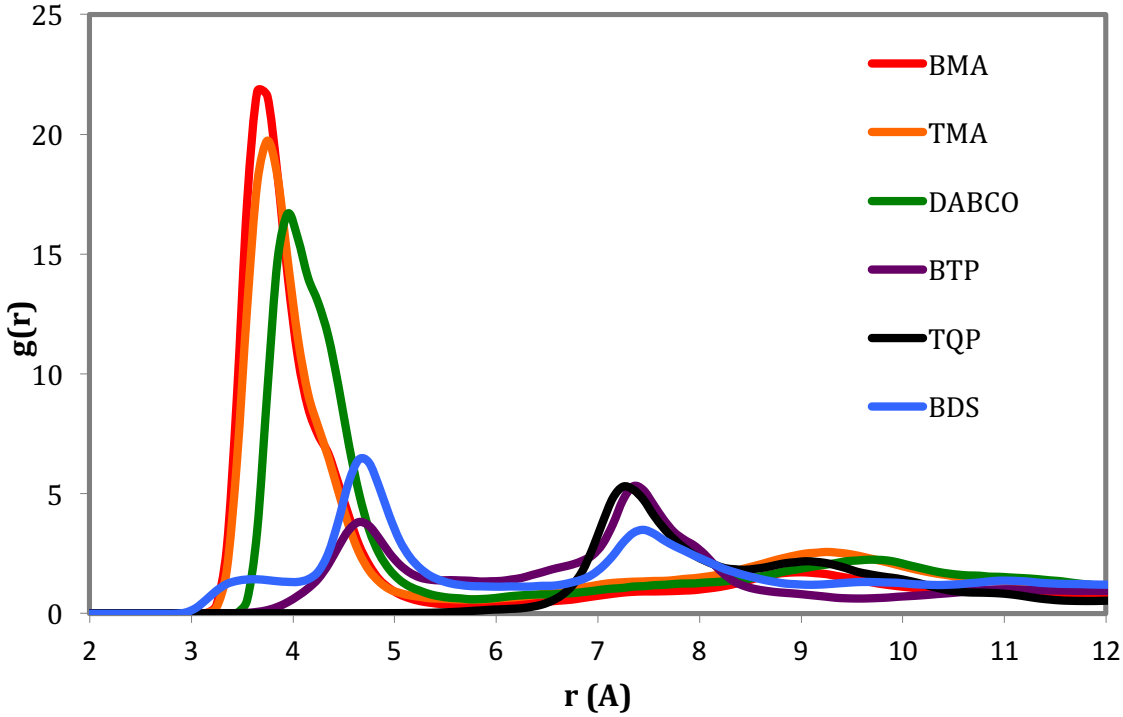

Figure 11 The radial distribution function between each cation and hydroxide. The cations names are abbreviated as benzyltrimethyl ammonium (BMA, red); tetramethyl ammonium (TMA, orange); DABCO (green); benzyltriphenyl phosphonium (BTP, purple); tris(2,4,6-trimethoxyphenyl) quaternary phosphonium (TQP, black); and benzyldiphenyl sulfonium (BDS, blue).

1.4 Fluoride Transport in Anion Exchange Membranes

An important goal in this project is to better understand the ion transport mechanisms in AEMs by studying the dynamics of moving anions and the molecular environment in which the ion transport happens. With molecular dynamics (MD) simulations, our attention has focused on the homopolymer PVBTMA with fluoride as the counterions. Even though the fluoride ion would not be utilized in the actual fuel cell operation because of its relatively slow self-diffusion constant, the ^{19}F nucleus being NMR active provides an opportunity for direct comparison between the estimates of the self-diffusion constant by PFGSE experiments and MD simulations, and these fluoride simulations

provide us with ideas on how to proceed with the more difficult simulations of hydroxide transport in PVBTMA.

The self-diffusion constants of fluoride in PVBTMA is remarkably sensitive to the hydration levels. At the lowest hydration level (λ = 5), the estimated self-diffusion constant of fluoride is of the order of 10^{-9} cm^2/s, but it increases to about $7.7x10^{-7}$ cm^2/s at hydration level λ = 14. This large increase in the mobility of fluoride ion is caused by the large difference in the connectedness of the water domains in PVBTMA. In Figure 12, the volume in space visited by each fluoride ion in 250 picoseconds is shown. At the low hydration level (Figure 12, left), the water domains become more disconnected and the fluoride ions have a hard time to overcome the Columbic attraction with the ammonium cation centers. As the hydration is increased (Figure 12, right), the fluoride ions become more mobile and are able to move through the connected water domains.

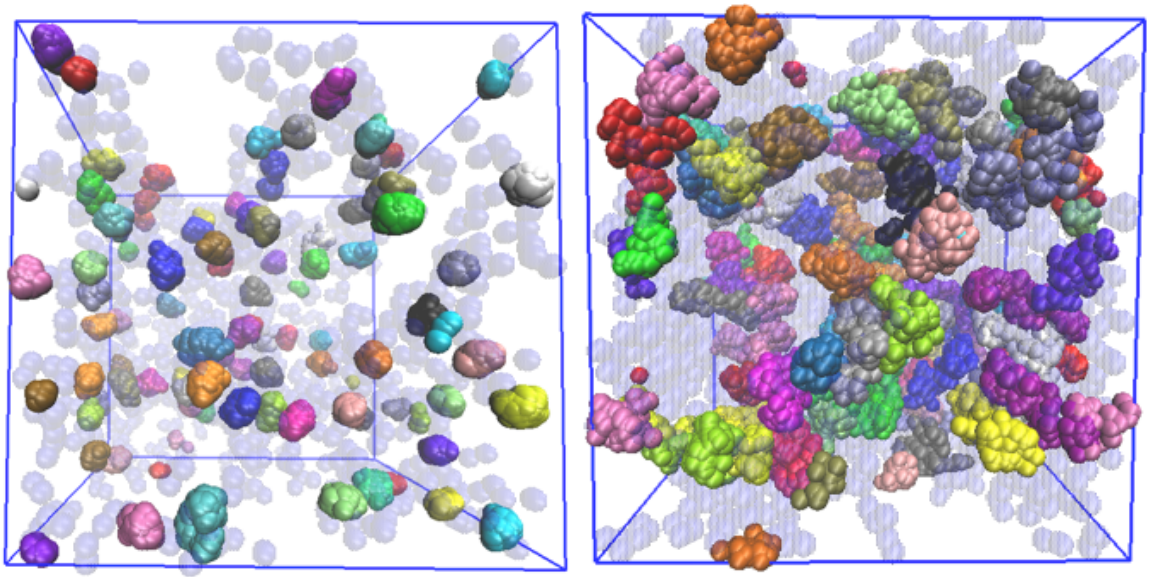

Figure 12. Each different blob represents the volume visited by each fluoride ion by diffusion in 250 ps. The initial positions of water atoms are shown as transparent blue. The hydration level is λ = 5 and 14 respectively, left to right.

One complication arises when experimental data are compared with simulations. It turns out that the binding between the ammonium cation and the chloride ions, the natural counterions left in the syntheses, is strong enough that 100% exchange with fluoride cannot be easily accomplished. As we learned from the early results of our simulations, the presence of the remaining chloride ions in this system has a surprising effect on the self-diffusion constant of fluoride. At 300 K and lambda = 14, our simulations showed the self-diffusion constant of fluoride increases by about 60% when fluoride content decreases from 100% to 40% (and 60% Cl), and it increases by about 130% when fluoride content decreases from 100% to 10%. We studied this unexpected effect by investigating the interplay between the ammonium cation centers, the halide ions, and water. We hypothesize that the chloride ions, which more easily lose their water solvation shells because of their lower surface electric field, free up more water for ion transport.

We believe this effect should be general to other systems in which there is more than one kind of mobile ions.

Studying hydroxide transport in PVBTMA is our next goal. Even though such simulations with hydroxide are more challenging and expensive because of the Grotthuss proton shuttling mechanism, experience gained from these fluoride simulations along with the recently developed MS-RMD hydroxide model(3) has put us in a good position to obtain a better understanding of hydroxide transport in AEMs.

1.5 Advanced Methodology for Preparation of Anion Exchange Membrane Configurations

The hydroxide transport in a hydrated environment is influenced by the Grotthuss proton hopping mechanism. In this mechanism, excess negative charge is shuttled through a chain of water molecules through a series of O-H bond breaking and formation processes. Conventional classical molecular dynamics (MD) approaches based on empirical force fields are not capable of describing the Grotthuss mechanism, because they allow for only constant bonding topologies. *Ab initio* molecular dynamics (AIMD), on the other hand, is a natural choice for this purpose, which explicitly treats the electronic degrees of freedom, but the significant computational cost strongly restricts the application to only small systems and short time scales. One promising solution to such problems is the multiscale reactive molecular dynamics (MS-RMD) algorithm.[3] In the MS-RMD framework, various resonance structures are defined as basis states, which are coupled to each other and form the overall Hamiltonian matrix. Each diagonal element in the matrix contains information about the bonded and non-bonded interaction energies for the basis state of the system, while each off-diagonal element contains a coupling term between two basis states that share a proton. The states in an MS-RMD algorithm are able to dynamically adopt different bonding configurations in response to the changes in the environment, with significantly less computational expense than AIMD. The higher efficiency makes it suitable for the study of more complicated systems in condensed phase such as proton transport in anion exchange membranes (AEMs).

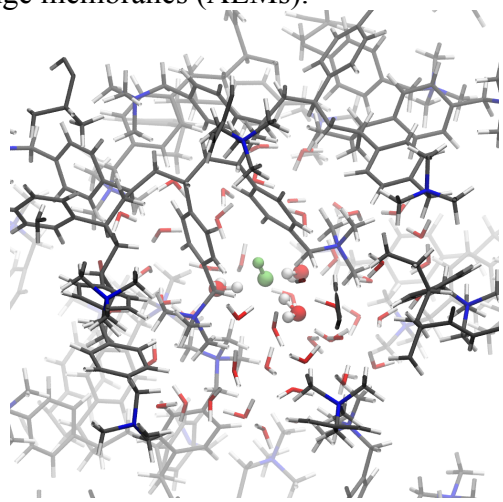

Figure 13: Typical configuration of hydroxide solvation in an anion-exchange membrane. The hydroxide ion (green) is 3-fold coordinated, which is significantly different from the case in bulk water solution.

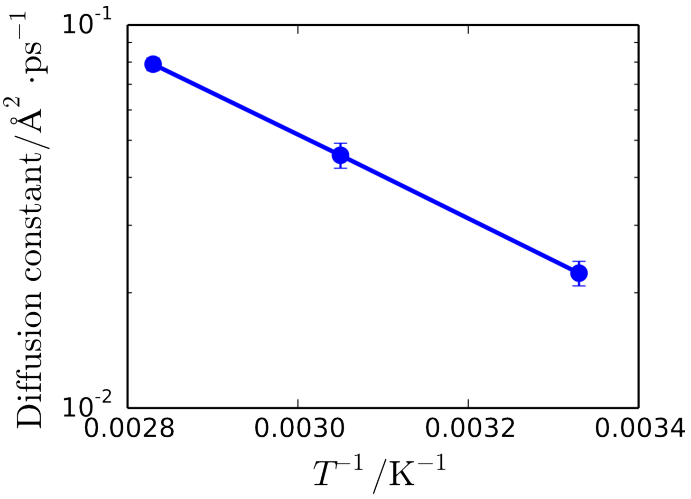

Figure 14: The self-diffusion constant of hydroxide as a function of inverse temperature. The hydration level is 14. The calculated activation barrier, calculated from the slope, is 5 kcal/mol.

By carefully studying the AIMD simulations, we discovered that the solvation structure of the hydroxide ion in bulk water is significantly different from that in an AEM. In bulk water, the water coordination of hydroxide is typically 4-fold with a transient fifth water that promotes proton transfer. However, in an AEM, because of the much lower water content and the physical blockages of the cationic groups, the water coordination number drops by about one water (3-fold, Fig. 1). This change in water coordination, along with the geometric constraints imposed by the polymer, fundamentally alters the proton transfer mechanism of the hydroxide for the case of an AEM, and a reasonable hydroxide model for AEM should must this into account. Indeed, our hydroxide model described in this document does satisfy this requirement. With the successful hydroxide model at hand, we were able to compute the self-diffusion constant of the hydroxide in AEM as a function of (inverse) temperature, shown in Fig. 2. The calculated activation barrier, 5 kcal/mol, is larger than that of hydrated excess proton in Nafion®. This implies that hydroxide transport is more temperature-dependent that proton transport in proton exchange membranes.

2. Model Polymer Systems.

The requirements for an AAEM polymeric electrolyte are a robust polymer backbone as well as an alkaline stable cationic charge to facilitate anion transport, both the backbone of the polymer and the cationic charge must be stable to highly alkaline conditions for longer periods of time. An all carbon polymer backbone will be hydrolytically stable. Benzyl trimethyl ammonium cations have proven to be stable under alkaline conditions because of the presence of steric hindrance, and the absence of β-hydrogens preventing Hofmann elimination.[xiv] The combined efforts of Coughlin (polymer synthesis), Witten (polymer theory), Voth (theory of ion transport), along with Herring and Liberatore (polymer and ion transport characterization studies) are directed towards developing well-defined novel block copolymers for use in alkaline anion exchange membranes with

a full understanding of the corresponding structure property relationship in these material. The synthetic efforts are guided by theory and the results of characterization studies are used in an information feedback loop to motivate further preparative efforts.

Recently, Varcoe and co-workers demonstrated radiation-grafted polyvinylidene fluoride (PVDF), poly(ethylene-co-tetrafluoroethylene) (ETFE) and fluorinated ethylene propylene (FEP) containing polymeric benzyl trimethylammonium hydroxide ions for AAEMFCs.[xv] Additionally, chloromethylated polysulfones quaternized by treatment with trimethylamine, are another class of AAEMFCs because of their good mechanical, thermal and chemical stability.[xvi] Brominated benzylmethyl-containing polysulfones for AAEMFC, as investigated by Hickner's group,[xvii] avoid the chloromethylation step which is known to be a toxic and carcinogenic process. Cross-linked tetraalkylammonium-functionalized polyethylenes have been synthesized by ring-opening metathesis copolymerization of tetraalkylammonium-functionalized cyclooctenes with unfunctionalized cyclooctenes.[xviii] These cross-linked structures provide good mechanical properties and allow incorporation of higher proportion of ion conductive groups. Other cross-linked copolymers based on imidazolium and bis-imidazolium groups exhibited high hydroxide ion conductivity and good mechanical properties.[xix] Incorporation of novel phosphonium cations with methoxyphenyl group into polysulfones was studied.[xx] The electron donating nature of oxygen in the phosphonium moieties stabilizes the cations, leading to good chemical durability under basic conditions. Guanidinium functionalized poly(arylene ether sulfone) shows higher ion conductivity than trimethylammonium functionalized polysulfone because of the higher basicity of guanidinium cation.[xxi] There is some question about the long term stability of quanidinium cation under highly caustic conditions. Base stable benzimidazolium polymer designed with steric protection around the C2 position have recently been developed.[xxii] Solvent processable polyfluorene ionomers containing pendant imidazolium moieties were investigated. These polyfluorene ionomer membranes show long-term stability under basic condition at elevated temperature and hydroxide conductivity is above 10^{-2} S cm^{-1} at room temperature.[xxiii] A random copolymer of poly(methyl methacrylate-*co*-butyl acrylate-*co*-vinylbenzyl chloride) was prepared and revealed the feasible preparation for the AAEM.[xxiv] Another kinds of random copolymer with methyl methacrylate, vinylbenzyl chloride and ethyl acrylate was fabricated as potential AAEM for direct methanol alkaline fuel cell.[xxv] Until now, most of the studies on AAEM have been based on random copolymers containing cation conductive moieties.

Using well-defined block copolymers with polycations as ionic conductive pathways our MURI team efforts, augmented by now well established collaborations with DiNoto (Univ. of Padova ITALY) and Beyer (Army Research Labs, Aberdeen MD) have greatly furthered the fundamental understanding of the relationship between polymeric structure and ionic conductivity of ordered membranes. To date microphase separation in block

copolymers has provided a versatile platform for the fabrication of nanostructured materials with a wide range of morphologies depending on the segregation strength (χ) and degree of polymerization (N) accessible structures include cylinders, lamellas and gyroids.[xxvi] Polymeric conductive membranes made from block copolymers can provide well-oriented and continuous conductive hydrophilic channels to enhance ion conductivity. Because of the presence of the hydrophobic domain in the membranes, the mechanical property of the membranes can also be enhanced. Therefore, more ion conductive groups can be incorporated into the polyelectrolyte leading to higher conductivity (higher ion exchange capacity (IEC) > 1.5 meq/g). In contrast with random copolymers it is difficult to achieve higher IEC because of the swelling encountered at high states of hydration leading to disintegration of the membranes. Several studies about structure-morphology-property relationships of block copolymers for PEM have shown that the morphology of the conductive membranes strongly influences their proton conductivity on the aspect of type and orientation of structure.[xxvii] Until now, fundamental investigations about the relationship between morphology and conductivity in AAEM made from well-defined block copolymers are sparse. The blocky copolymers poly(arylene ether)s containing ammonium-functionalized fluorene groups explored by Watanabe *et al.*[xxviii] show high IEC up to 1.93meq/g and high conductivity (144ms/cm) at 80^{o}C. Although these blocky copolymer are segmentally segregated they are not well ordered enough to show full microphase separation. These membranes are mechanically and chemically stable, similar to the membranes from random copolymers. Blocky copolymers with hydrophilic blocks can improve the ionic conductivity of AEM by incorporating more conductive group without losing mechanical properties. However, there is no corresponding structural information present in these materials to allow for detailed structure-property correlation studies that could ultimately lead to the design of superior membranes once a more detailed fundamental understanding of ionic conduction in complex heterogeneous organic media has been established.

An illustration of the combined team efforts of our MURI collaboration is presented here. Synthetic efforts have been focused toward the development of a series of well-defined block copolymers with benzyl trimethyl ammonium ion blocks for ion conduction and a low glass transition temperature chemical inert hydrophobic block. For this later component of the block copolymer we chose hydrogenated poly-isoprene, also referred to as poly methyl butylene (PMB). This rubbery hydrophobic portion of the block copolymer allow for good mechanical properties of solvent cast membranes. The overall synthetic scheme is illustrated below. Due to the controlled polymerization conditions employed we have excellent control in both overall molecular weight of the copolymer along with the respective volume fractions of both components, and thus the resultant morphology. Furthermore, additional fine tuning of the ion exchange capacity of the final composition can be directly controlled by the extent of bromination performed in the next to last synthetic step. The nomenclature developed for these materials is to

follow the convention of x-y-z, where x represent the molecular weight in g/mol of the polyvinyl benzyl ammonium block, y represent the molecular weight in g/mol of the PMB block and z represents the ion exchange capacity in meq/g of the block copolymer. A full range of block copolymers have been prepared and are actively being investigate by a number of spectroscopic techniques and theoretical investigations.

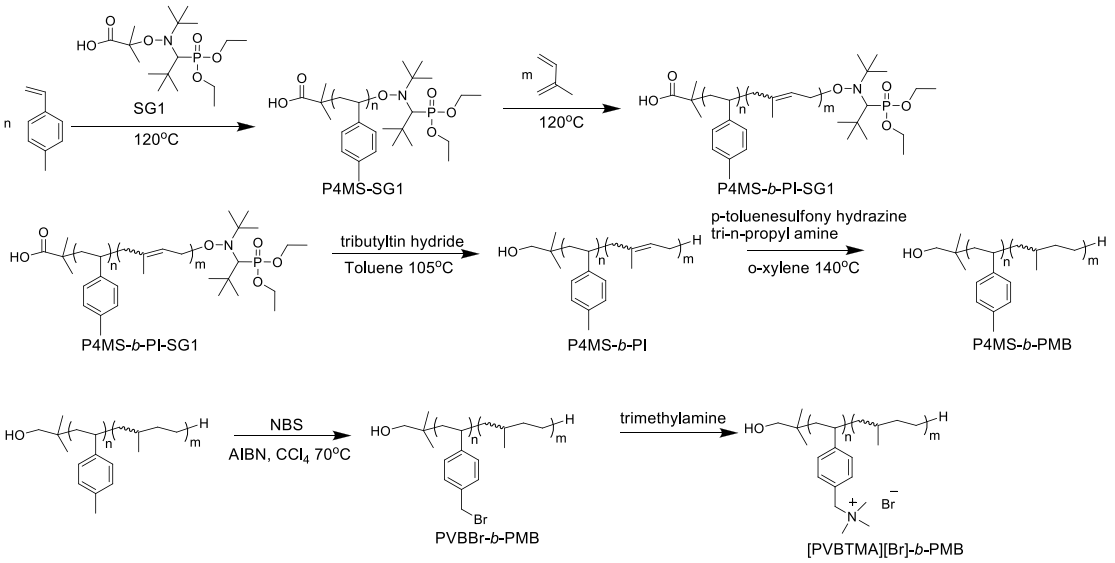

Figure 15 Synthetic route to poly (vinyl benzyl bromide)-*b*-poly (methylbutylene)

(PVBBr-*b*-PMB)

The well-ordered [PVBTMA][Br]-*b*-PMB copolymer are responsive to environmental conditions as evident from the humidity dependent small angles X-ray scattering patterns. Water uptake measurements by dynamic vapor sorption studies indicate that the responsive swelling/deswelling that occurs in the ion block copolymer segments alters the lamellar symmetry as water is gained or lost and the polymer brushes expand or collapse to accommodate volume expansion or contraction.

An advantage of our well-characterized diblock model polymers is that they permit us to confirm our understanding of the structural response to humidity in light of the statistics of the constituent polymers. The block molecular weights and characteristic ratios, together with the observed lamellar spacing (Figure 17 and Figure 19) imply that the blocks are mildly extended, to about 1.3 times their ideal dimensions, in the dry state. Established theory of diblock microphases[xxix] indicates the structural and thermodynamic consequences of this extension can be well captured by representing the chains as random walks on a lattice modified by the varying osmotic pressure within the block domains.[xxx] At the high ionic fractions of interest, we expect long-range Coulomb effects to be negligible.

2.1 Tailoring water partitioning in PVBTMA

We studied water partitioning in PVBTMA diblock copolymers with alternating hydrophobic lamellae (for structural support) and hydrophilic lamellae (to conduct ions). In order to be conductive, the hydrophilic block must absorb water. The water is often thought of as uniformly permeating the hydrophilic lamella, but that need not be so. Since the hydrophilic block is effectively tethered to the hydrophilic-hydrophobic interface, the polymers must stretch on average to accommodate the water. For typical well-solvated grafted layers (5) the optimal stretching profile leads to strongly non-uniform swelling with solvent. In a simple example the polymer concentration decreases quadratically with the distance z from the tethering surface and reaches zero at a specific height h set by the solvent quality and the elastic properties of the polymer coils (6). Likewise for weaker solvation, there will be more polymer near the hydrophilic-hydrophobic interface, and more water at the midplane. This nonuniformity takes a special form for marginal solvation, where two concentrations exist in equilibrium. Here the tethering constraint favors the polymer-rich phase to reside near the tethering surface, while the dilute phase occupies a “water channel" near the midplane. The water configuration has potential implications for the ion conductivity of the membrane. The polymer-rich region is packed with ions (good for conductivity), but the small amount of water there inhibits ion mobility (bad for conductivity). In the water channel, this tradeoff is reversed. Potential benefits of the water channel for overall conductivity are sketched below.

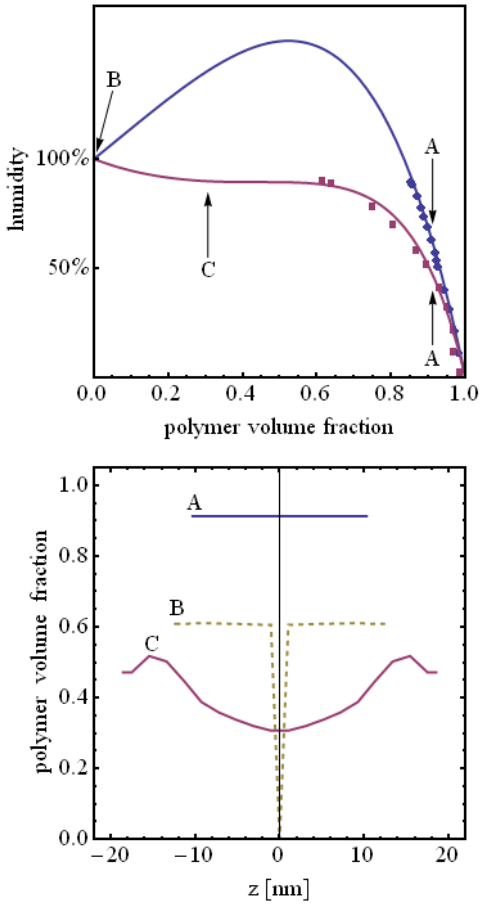

Figure 16. (Top) Dynamic Vapor Sorption experiment gives equilibrium humidity vs. polymer concentration for 2 samples of isolated hydrophilic block. Flory-Huggins curves

with fitted linear and quadratic interaction terms fit the points well. The top set is random copolymer PVBTMA (45%) and 4-methyl styrene (55%). Due to having less N^+, this sample has limited solubility, max ~20% water by volume. The bottom set (84% PVBTMA) is nearly at the critical point of coexisting phases, indicated by the flattening of the curve between ~30% and ~50% polymer concentration. (Bottom) Three sample profiles of a hydrophilic lamella. The vertical line represents the midplane of the lamella and the left-to-right range of the curves represents the swelled width of each lamella. (A) is a typical profile, showing uniform 91% polymer, 9% water by volume throughout. This corresponds to 62% humidity for the first sample and 47% humidity for the second sample. (B) The first sample swells gradually until 100% humidity, at which point a plane of pure water may abruptly form at the middle. (C) The second sample at ~89% humidity, where it exhibits phase coexistence, forms a water channel in the middle.

We have studied the structure of the lamellae using existing polymer-brush theory (7), Figure 2. All the necessary parameters were found from experiment or literature. In the conditions of our study the PVBTMA polymer absorbs little water. In the lamellar copolymer of our study the tethering constraint is a weak perturbation, adding less than kT of free energy per polymer. Under these conditions (8) the solvent is distributed nearly uniformly throughout the layer, as it would be without the tethering constraint. Any deviation from the preferred concentration will have to pay a large penalty in free energy because of the large number of degrees of freedom in the water molecules. Therefore, the profiles we find are locally uniform in concentration.

Something interesting happens, though, when the hydrophilic polymer material is partially insoluble. In that case, there are generally three coexisting phases, each with chemical potential equal to the other two phases. In that case, the solvation penalty for being non-uniform is removed, as long as the profile jumps rapidly from one of the preferred concentrations to another. The result is a well-defined water channel. The system chooses the proportions of each critical concentration that minimizes the total free energy, including the random walk of the polymer paths.

The specifics of whether a water channel forms, and how wide and wet it is, depend on the exact details of the hydrophilic polymer solubility. Some of the effects happen only near the critical point, in which case the temperature and humidity can be tuned to generate the desired water channel. We consider three possibilities: uniform solubility (mixes at any concentration), binodal solubility (2+ concentrations coexist within a certain humidity range), and limited solubility (mixes up to a cut-off concentration). For uniform solubility, the model (using PVBTMA under our experimental conditions) predicts that the water is always distributed uniformly across the lamella. For binodal solubility, it predicts that in the humidity range where two concentrations coexist, the system chooses a proportion of each of two concentrations. It does this in such a way as to minimize the overall free energy of the system. Usually, that means that a water-rich channel forms in the middle of each lamella. In systems with limited solubility, the model predicts that water cannot be absorbed beyond the cut-off concentration, except at 100% humidity (i.e., soaked in water). At that point, a thin plane of pure water may exist at the centerline, but the system has no thermodynamic incentive to make the water region any

thicker. In fact, surface tension (ignored in our model) may be enough to prevent the water region from forming at all.

To summarize, the model robustly predicts uniform absorption of water throughout the entire region, except when the hydrophilic block is binodal. In that case, water is preferentially absorbed in the middle of the hydrophilic block. Although such a configuration awaits experimental confirmation, it is worthwhile to investigate. In principle water channels can improve conductivity by creating a conductive double-layer between the two phases. However, our Boltzmann-Poisson estimates suggest that this effect is small for the high ionic strength of our membranes.

These profiles suggest ways to account for the behavior of the peaks in **Figure 17**. Though a lamellar structure ordinarily produces peaks at all integer multiples of the basic wavevector q*, the 3 q* peak is suppressed for the dry sample. This suggests strongly that the volume fractions of the A and B subdomains are near 1/3 and 2/3. This differs from the 42 percent volume fraction of the hydrophilic A domain inferred from molecular weights and densities. The suppression is less apparent for higher-molecular weight diblocks. We are exploring the possible role of nonuniform bromination in producing this effect. Upon maximal swelling, the 3 q* peak re-emerges and the even multiples of q* have suppressed peaks. This is consistent with symmetric 50-50 diblocks of uniform scattering density. This uniform composition is consistent with our predicted composition profiles.

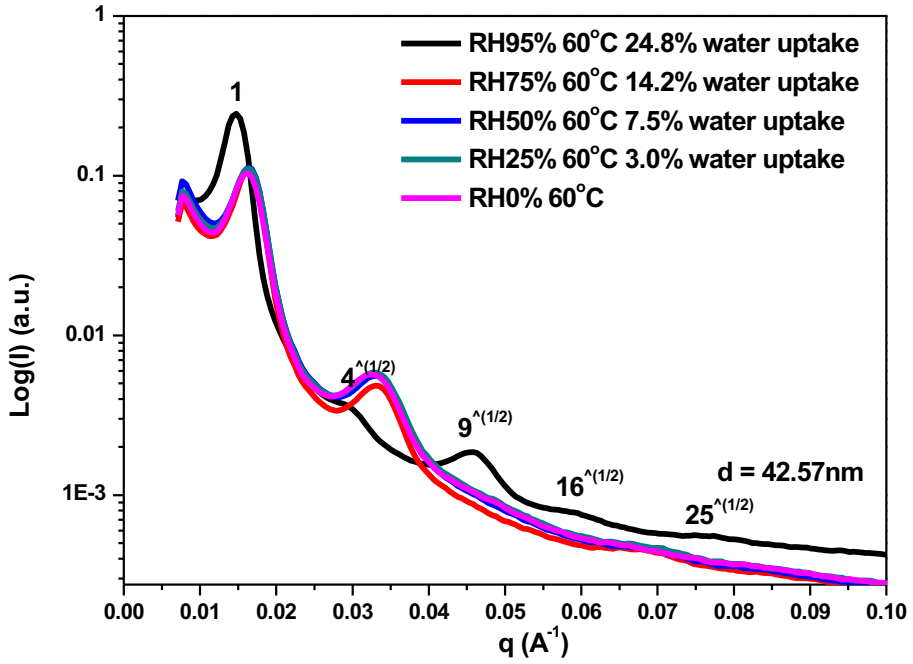

Figure 17 SAXS data of [PVBTMA][Br]-*b*-PMB 40.9-43.5-84 casted from $CHCl_3$ at 60°C with decreasing relative humidity from 95% to 25%.

We first assumed that the hydrophobic PMB lamellae remain at a fixed width, independent of water absorption. It turns out that this is not the case, and the hydrophobic lamellae indirectly react to changing water levels, as pointed out by Karen I. Winey.[xxxi] When the membrane absorbs water, the water molecules penetrate the PVBTMA, tending to spread apart the chains. This can happen in one of two ways. The PVBTMA can fan out away from the block interface, tending to form a polymer brush and causing the PVBTMA lamellae to widen. This is the behavior that we can predict from the mean-field model. Alternatively, the interface can expand in area, spacing the polymers out laterally. By itself, the latter effect causes the combined lamellar spacing to narrow. In reality, both effects happen concurrently and compete in a complex manner.

We have recently been able to quantify these effects and have used the results to improve the mean-field calculation. To measure how the thickness of both blocks varies with water uptake, we combined SAXS and DVS data taken under identical conditions for our MURI project. From the SAXS, we collected the primary *q* peak which determines the *d*-spacing, the sum of the hydrophilic and hydrophobic lamellar widths. The *d*-spacing actually decreases slightly with increasing water absorption up to 74% relative humidity before increasing (see Figure 2). This is indicative of lateral chain swelling, where the PMB lamellae narrow. The DVS experiment determines how much water the membrane absorbs. Assuming ideal mixture, this gives the increase in volume of the hydrophilic block. Therefore, taken together the two experiments give the width of each lamella as a function of humidity (see Figure 2). This can be used to calculate the grafting density, σ, of the hydrophilic polymers, a quantity that feeds into the mean-field calculation.

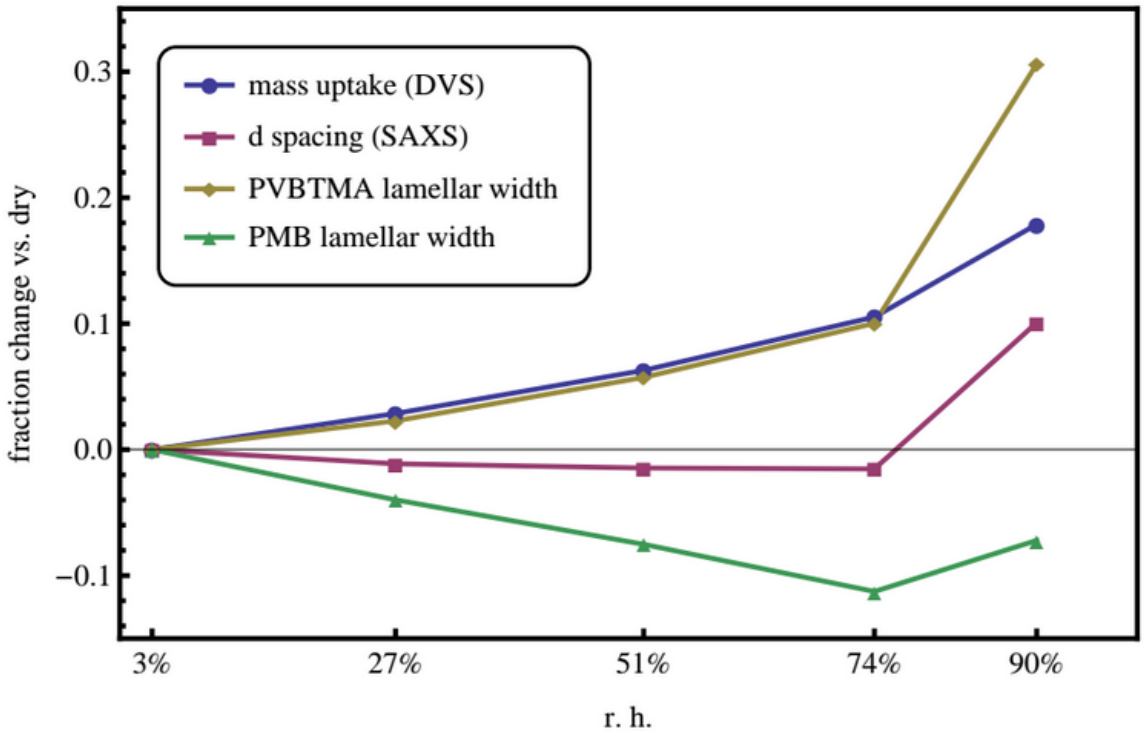

Figure 18: A comparison of fractional change vs. relative humidity of: mass change of the total membrane measured in DVS (blue circles); d-spacing from SAXS (purple squares); the inferred width of the PVBTMA lamellae (gold diamonds); and the inferred

width of the PMB lamellae (green triangles). The thickening vs thinning of the two blocks is due to competition between brush swelling and lateral swelling.

The Scheutjens-Fleer mean-field model is used to calculate the spatial water distribution within a hydrophilic lamella. Similar methods have been used to calculate the water distribution within a polymer brush, where polymers are attached to a rigid surface.[xxxii] With slight modifications, the calculation handles the variable grafting density, σ (humidity), calculated from the experiments. As we have shown previously,[xxxiii] the water distribution strongly favors a near-uniform osmotic pressure throughout. This permits two types of water distributions: either a uniform water distribution, or one where the polymer concentration jumps between two co-existing phases. In the latter case, the dilute phase usually arranges into a slab centered around the lamellar midplane, which we have termed a "water channel". With the new σ (humidity) input, as well as improvements to other inputs, the predicted swelling is now within 10% of the experimental measurements. This adds confidence to the ability of mean-field theory to describe solvent uptake in di-block lamellar membranes in general, and to the possibility of water channels.

Collaborative efforts with Dr. Aaron C. Jackson and Dr. Frederick L. Beyer at the Army Research Labs (Aberdeen Proving Ground) were initiated during this funding period. Transmission Electron Microscopy experiments are being performed to determine the morphology of various copolymer compositions being prepared in this MURI. Real spacing imaging of microtomed block copolymer samples under both dry and hydrated conditions are shown below. Correlation of lamellar spacing matches well with the d-spacing between layering seen in SAXS.

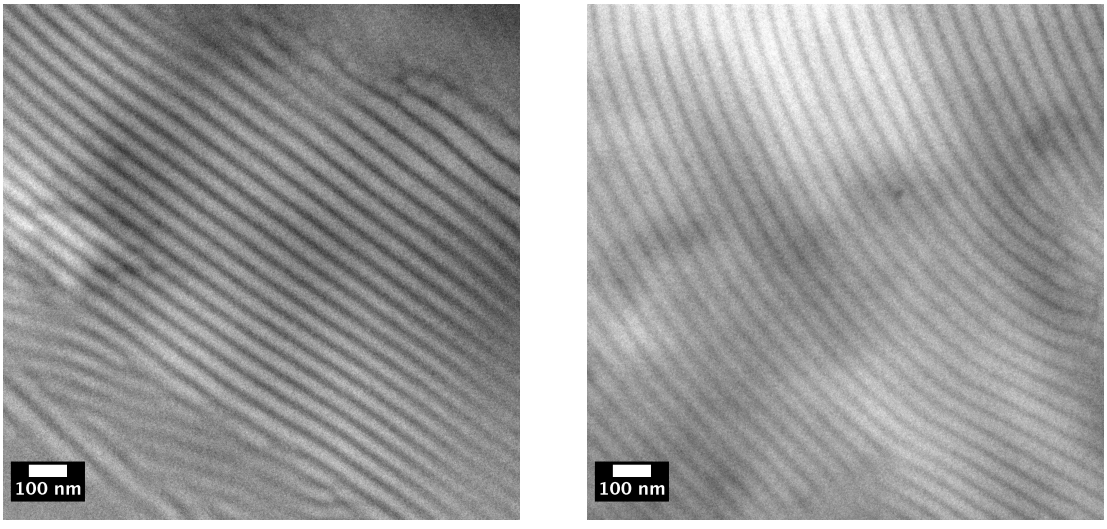

A B

Figure 19 TEM images of the [PVBTMA][Br]-*b*-PMB 64.2-71.5-89.4 in (a) dry and (b) hydrated states.

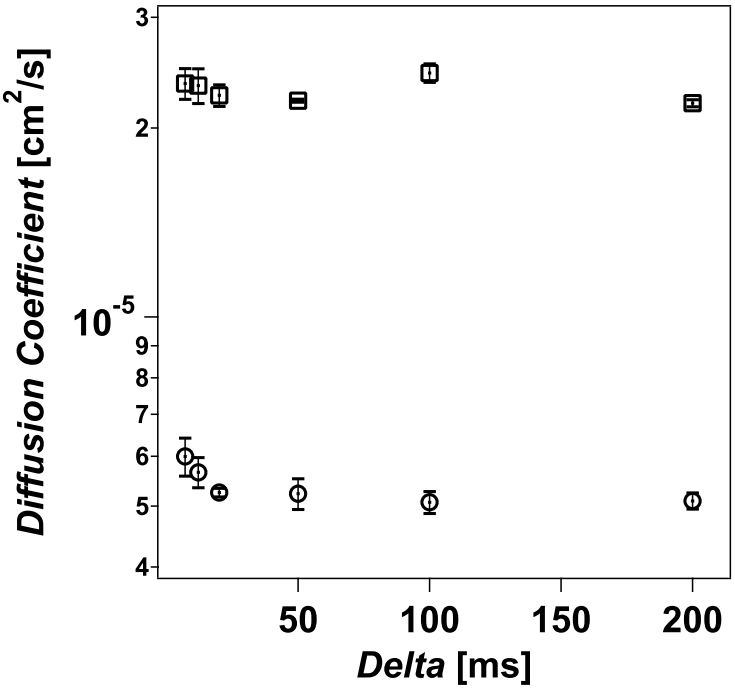

Figure 20 Self-diffusion coefficients of free water open squares and water in the [PVBTMA][Br]-*b*-PMB membrane open circles at different time intervals Δt at 30°C.

Ion and water diffusion experiments are currently in progress using pulse field gradient NMR spectroscopy. Preliminary data are shown below for water diffusion in the polymer with bromide anions under 100% RH. The material shows some restriction in the water diffusion under these wet conditions and we are working o these observations under drier conditions.

Methylbutylene co-polymers

A series of poly (vinyl benzyl trimethy ammonium bromide)-*b*-poly (methylbutylene) ([PVBTMA][Br]-*b*-PMB) were synthesized by nitroxide mediated radical polymerization (NMP) followed by hydrogenation, brominzation and quaternization. The degree of functionality (DF) (from 24.4% to 89.4%) of [PVBTMA][Br] can be well controlled by bromination using optimized concentration of N-bromosuccinimide (NBS) as brominating agent and azobisisobutyronitrile (AIBN) as initiator without polymer degradation compared to chloromethylation synthetic methodologies. Ion conductivities of the [PVBTMA][Br]-*b*-PMB membranes cast from tetrahydrofuran as a function of IEC at various temperature are shown in Figure 30.

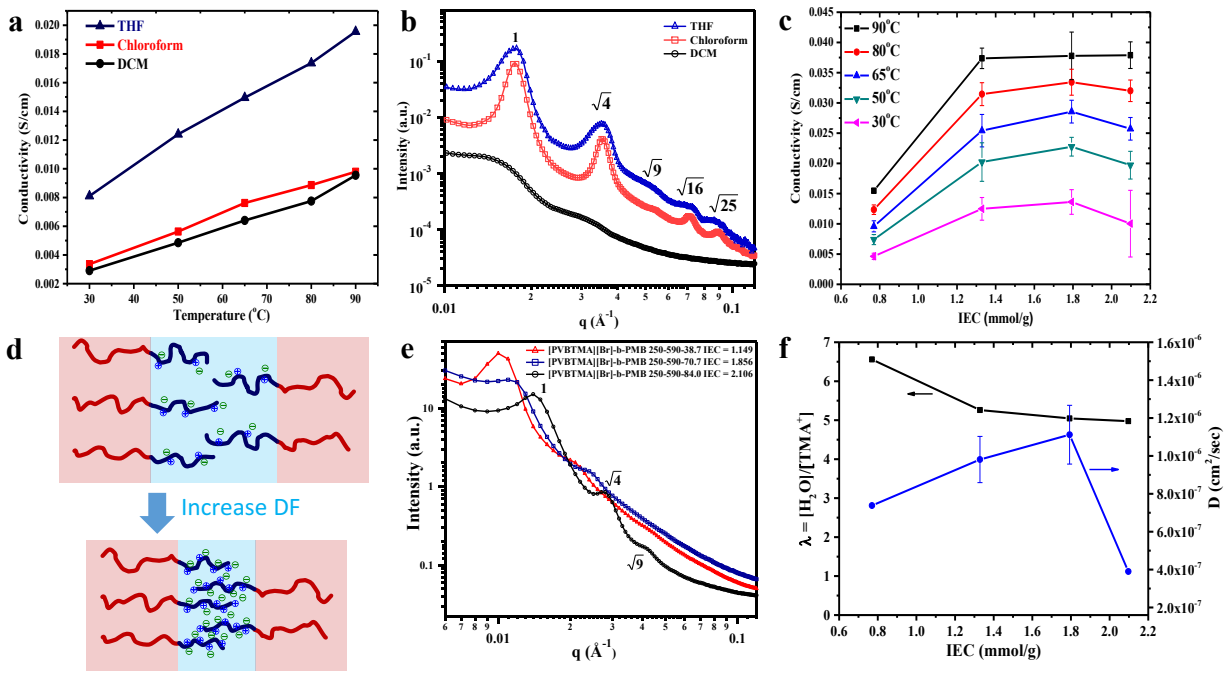

Figure 21. (a) Temperature dependent ion conductivity of [PVBTMA][Br]-*b*-PMB 160-390-81.8 cast from different solvents at RH 95%. (b) SAXS profiles of [PVBTMA][Br]-*b*-PMB 160-390-81.8 cast from different solvents. (c) IEC dependent ion conductivity of [PVBTMA][Br]-*b*-PMB 250-590 membranes with different DF cast from THF at RH 95% and different temperature. (d) Structure evolution of the [PVBTMA][Br]-*b*-PMB membranes as DF increase. (e) SAXS profile of [PVBTMA]-*b*-PMB with different IEC cast from $CHCl_3$ at 60°C and RH 95%. (f) water level (λ) at 60°C, RH 95% and diffusivity of water (D_{water}) within [PVBTMA][Br]-*b*-PMB 250-590 membranes cast from THF with different IEC.

The bromide conductivity of the [PVBTMA][Br]-*b*-PMB 250-590 with IEC 2.097 increase from 0.01 S/cm to 0.038 S/cm as the temperature increase from 30°C to 90°C at RH 95%. The bromide conductivity of this membrane is the highest among values reported in the literature. The reason for the highest bromide conductivity could be a result of the well-defined and inter-connected lamellar structure within the membrane leading to more efficient ionic transport pathway. The ion conductivity increases as increasing IEC when the IEC is below 1.4 mmol/g. The conductivity reaches a maximum (38 mS/cm at 90°C and RH 95%) as IEC above 1.4 mmol/g which indicates that higher IEC is not necessary for high conductivity. Well-connected conducting channel can be fully developed at moderate IEC which can be attributed to the well-ordered and aligned structures so that the percolation point of these ionic block polymer materials is low (below IEC = 0.8 mmol/g).

Ionic clusters of polymer electrolyte are formed by the nanoscale ionic aggregation resulting from randomly distributed charged and uncharged domain. They can be characterized by small angle X-ray scattering (SAXS) and small angle neutron scattering (SANS) to determine the average distance between clusters, dcluster, which is typically between 1.8 and 6.0 nm.40-45 Recently, Balsara *et al.* proposed these ionic clusters can impede ion transport because ions must hop across a distance of ion-free regions between

two ionic clusters (dion-free) and the enhanced counterion condensation due to the contiguity of fixed ion group in the clusters ($d_{fixed\text{-}ion}$). This argument was also recognized in the initial discussion of clusters by Hsu and Gierke. For ionic block copolymer, decreasing the d_{block} of ionic block copolymers by reduction of molecular weight is one avenue to eliminate ion clusters for achieving homogeneous ion conducting domain and further improving conductivity. However, the low molecular weight of the membrane will result in poor mechanical properties. The formation of ion cluster can be attributed to the low level of sulfonation in the ionic domain because of the limitation of sulfonation chemistry as well. Here, we propose that by increasing the level of functionality in the ionic domain can also eliminate ion clusters for improving the conductivity without sacrificing the mechanical properties of the membranes. Three [PVBTMA][Br]-b-PMB 250-590-z containing different degree of functionality (DF, 38.7%, 70.7% and 84.0% respectively) were investigated by humidity controlled SANS using D2O at 60oC and RH 85% to probe ion clusters in the membranes, Figure 31. For [PVBTMA][Br]-b-PMB 250-590-38.7, the ion cluster peak was detected and around 3.8 nm. When the DF of the membrane increases to 70.7%, the intensity of the ion cluster peak decreases and the peak shifts to 2.7 nm which suggests that the distance between clusters get shorter as the DF increasing. For the highest DF of [PVBTMA][Br]-b-PMB 250-590-84.0, the ion cluster peak is totally absent. The absence of ion cluster peak can be the result from the composition changing from low to high PVBTMA content leading to the formation of more homogeneous ion conducting domains. Compared to the conductivity data shown in figure 1c, the conductivity increase from 0.015 S/cm for IEC 0.770 mmol/g (DF is 25%) to 0.040 S/cm for IEC 1.329 mmol/g (DF is 46%) at 90 ^{o}C and RH 95%. More than a two fold increase of the conductivity can be achieved with the IEC value increasing from 0.770 to 1.329 mmol/g. The disappearance of an ion cluster could also be the reason for the increase of conductivity. Therefore, high DF in the ionic domain is another avenue to eliminate ion cluster formation for high ion conductivity and still retain the good membrane property.

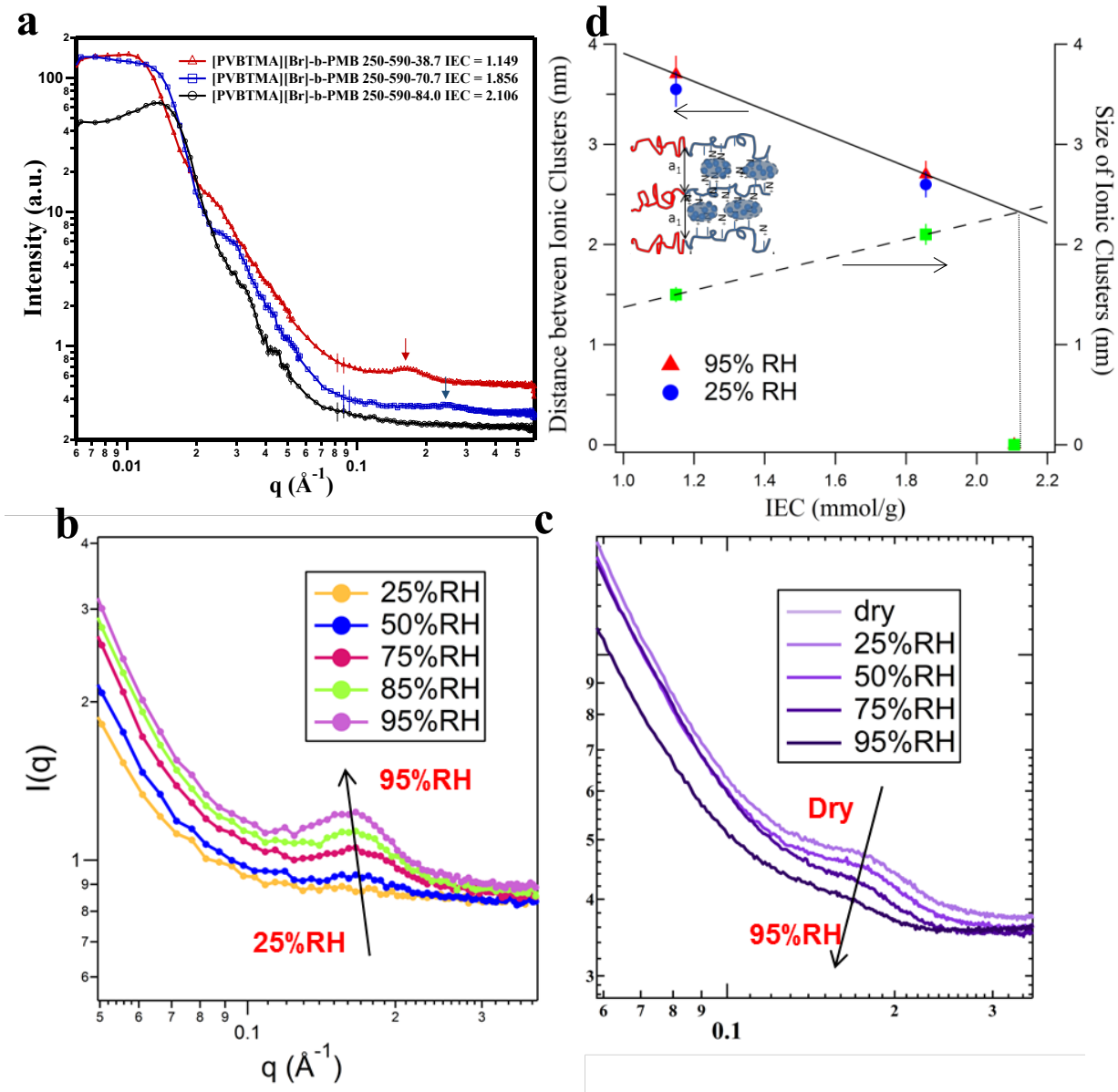

Figure 22. **(a) SANS profile of [PVBTMA]-*b*-PMB 250-590 with different IEC at 60°C and RH 85% using 100% D_2O as humidify. (b) SANS and (c) SAXS spectra of [PVBTMA]-*b*-PMB 250-590-38.7 membrane. (d) Distance between ionic clusters (left axis) and size of the clusters (right axis) as a function of IEC. Solid line is a guide to the eye. Inset is a schematic of the morphology of the block chains and ionomers.**

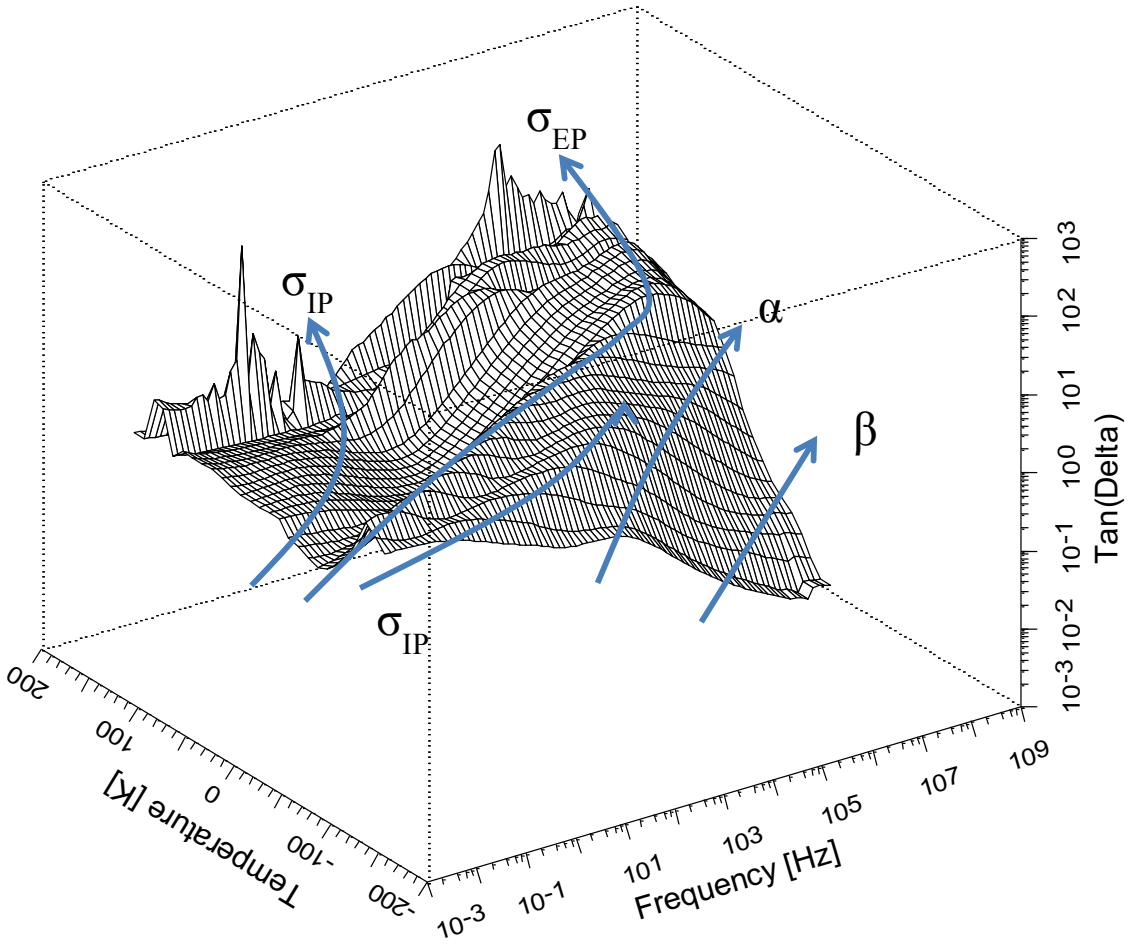

Figure 23. Broadband electric spectroscopy of diblock polymer in bromide form under the condition of water saturation. The ratio of real to imaginary part of the complex conductivity, labeled Tan(Delta), is plotted versus temperature and frequency.

Broadband electric spectroscopy (BES) is a very powerful tool to determine the conductivities, dielectric relaxations and characteristic relaxation times of a material, **Figure 23**. These values, which are determined by fitting the BES profiles over a range of temperatures and frequencies, can be used to elucidate the mechanism of conduction within the material particularly when combined with techniques such as DSC and DMA. In collaborative efforts with Prof. Vito di Noto from the University of Padova in Italy we are undertaking a series of detailed BES investigations of the block copolymers that have been recently prepared. From a highly informative set of initial testing we observe three principal conduction mechanisms that are graphically illustrated below.

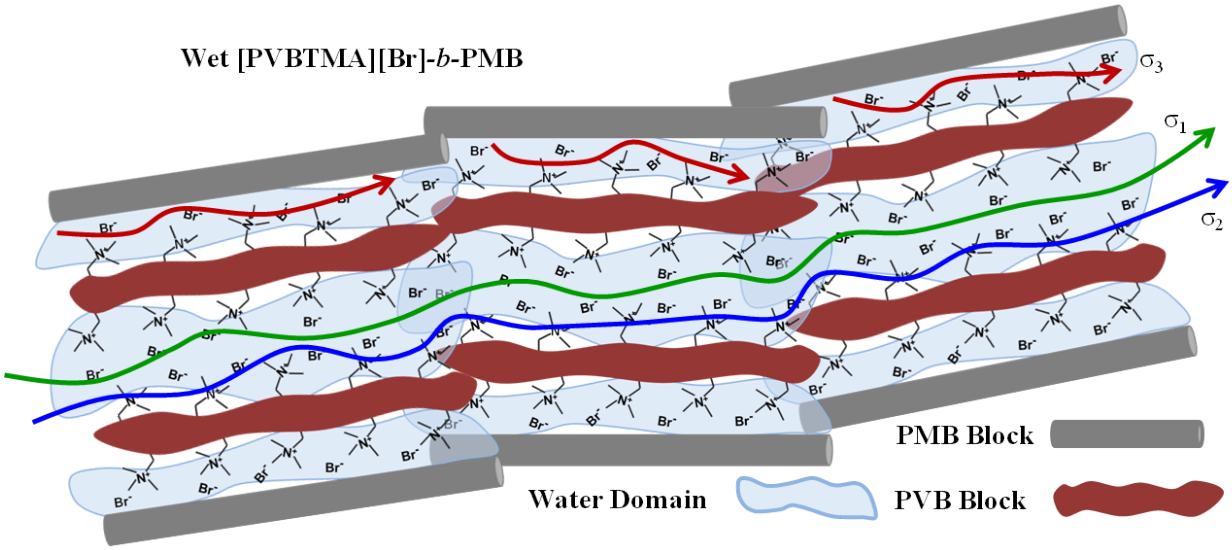

Figure 24 Proposed mechanism of local and long-range conduction in [PVBTMA][Br]-*b* PMB in under wet conditions.

A mechanism of conduction hypothesized from the electrical spectroscopy data indicates that in the hydrated membrane the long range conductivity occurs via two main percolation pathways: one within the water domains and another along the interface between the water and polar domains. In the dry membrane state, conduction along the interface between the PMB hydrophobic and the [PVBTMA][Br] domains also provides an important contribution to the long range charge migration within the polar domains.

3. Optimized Polymer systems

3.1 Polystyrene-block-poly(vinylbenzylammonium salt) (chloride, bicarbonate, and hydroxide).

Polystyrene-block-poly(vinylbenzyl chloride) (PS-b-PVBC) is an attractive material for conversion to an anion exchange membrane through amination; however, the potentially fragile nature of the polystyrene based material limits its application as an alkaline fuel cell membrane. Blends of Poly(2,6-dimethylphenylene oxide) (PPO) and polystyrene (PS) are well studied engineering materials as PPO is compatible with PS in a wide range of compositions. As part of our work on the development of potential alkaline fuel cell membranes, we are studying the preparation of PPO (and brominated PPO) and PS-b-PVBC membrane blends and post functionalization of the blended membrane with trimethylamine (

Figure 25).

Figure 25. Preparation of PPO blended membranes.

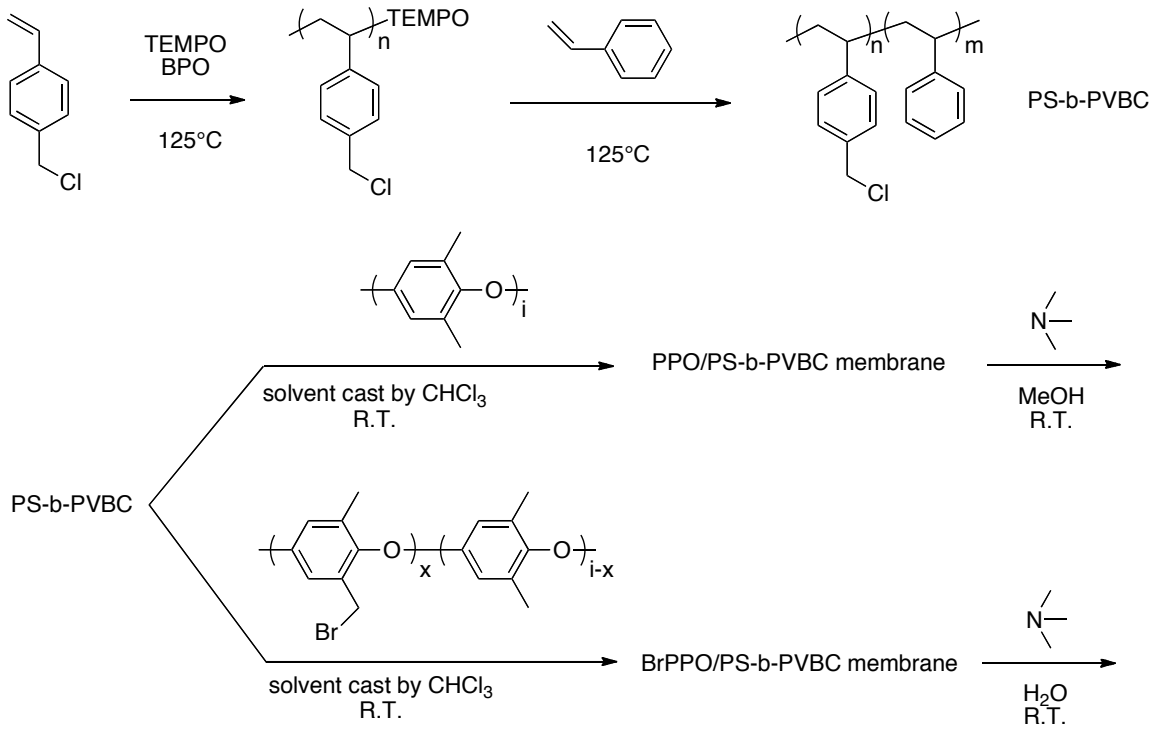

PS-b-PVBC copolymer was prepared with a composition of 32:68 (mass ratio) through a nitroxide mediated radical polymerization. This sample of PS-b-PVBC was used to blend with PPO and the resulting PPO/PS-b-PVBC blended membranes were prepared in different compositions (PPO:PS-b-PVBC = 60:40, 50:50, 40:60, 30:70, and 20:80). Conversion to a quaternized ammonium salt was accomplished by reacting the membrane films with trimethylamine in methanol over 48 hours. The films were characterized by titration to determine the ion exchange capacity (IEC) and a greater than 90% conversion to the benzyltrimethylammonium chloride. Chloride and bicarbonate conductivity were measured under 95%RH at 60°C and are plotted as a function of titrated IEC in **Figure 26**.

The blended membranes qualitatively have much improved mechanical properties compared to membranes produced without PPO and they show good chloride and bicarbonate conductivity. The conductivity increases with increasing IEC, and the same trend is observed in water uptake.

The membranes produced in this case are the result of a compatible blend of PS-PVBC and PPO that is aminated after film formation. The amination results in a conversion of the benzyl chloride groups to benzyl ammonium groups, but because of the high glass

transition temperature of the PPO/PS blend, there is not the ability for the polymer chains to reorganize into ordered domains. As a result, small angle X-ray scattering (SAXS) analysis showed no characteristic morphological features. Annealing was attempted under different conditions in an attempt to approach the glass transition temperature and reorder the morphology. The results in water uptake and conductivity show a marked increase when the membranes are annealed at temperatures above 125 °C and a greater increase when annealed at temperatures above 125 °C in the presence of water (**Figure 27**). In all cases the SAXS analysis shows no evidence of correlated structure formation, while the films do become less transparent after annealing in the presence of water.

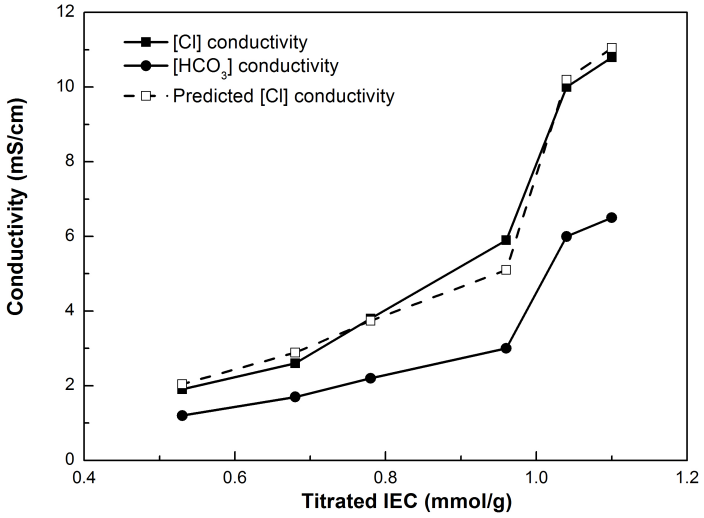

Figure 26. Ion conductivity (chloride and bicarbonate) of PPO blend membranes versus titrated IEC. Closed symbols represent membranes in chloride form; open symbols represent membranes in bicarbonate form. Different IECs represent membranes in different blend composition.

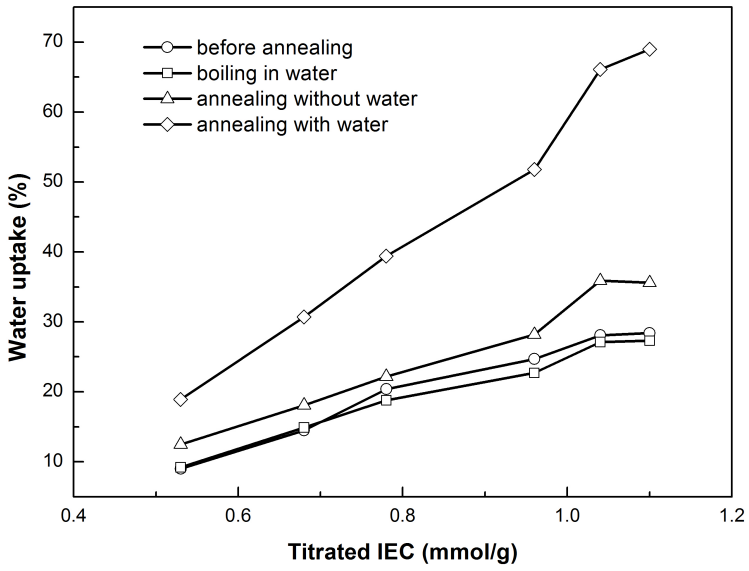

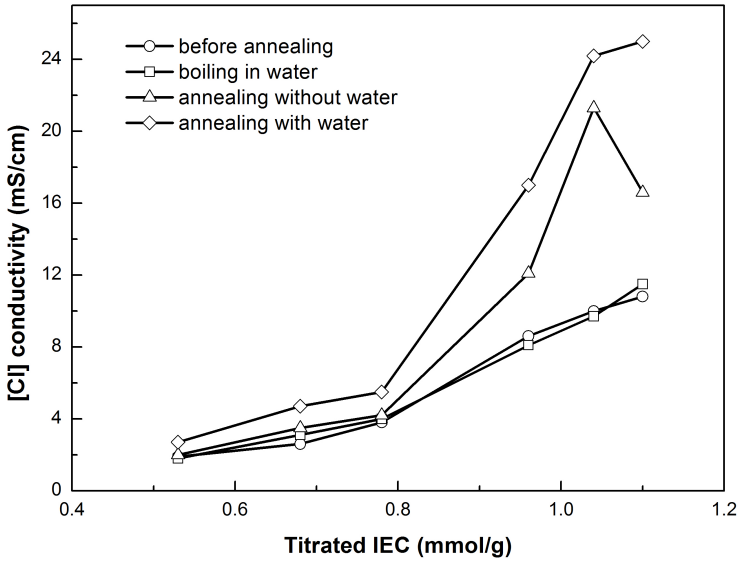

Figure 27. (a) Water uptake (%) of membranes before and after three different fabrication methods versus IEC; (b) conductivity of membranes before and after three different fabrication methods versus IEC.

In addition to the formation of blends with PPO, we are investigating the effect of crosslinking PS-b-PVBC copolymer films to form ammonium crosslinks and subsequently aminating the remaining benzyl chloride groups to form a functional membrane (**Figure 28**). Again, the intent here is to overcome the limitations seen in the brittleness of the polystyrene-based copolymers.

Figure 28. Formation of crosslinked membranes based on PS-b-PVBC.

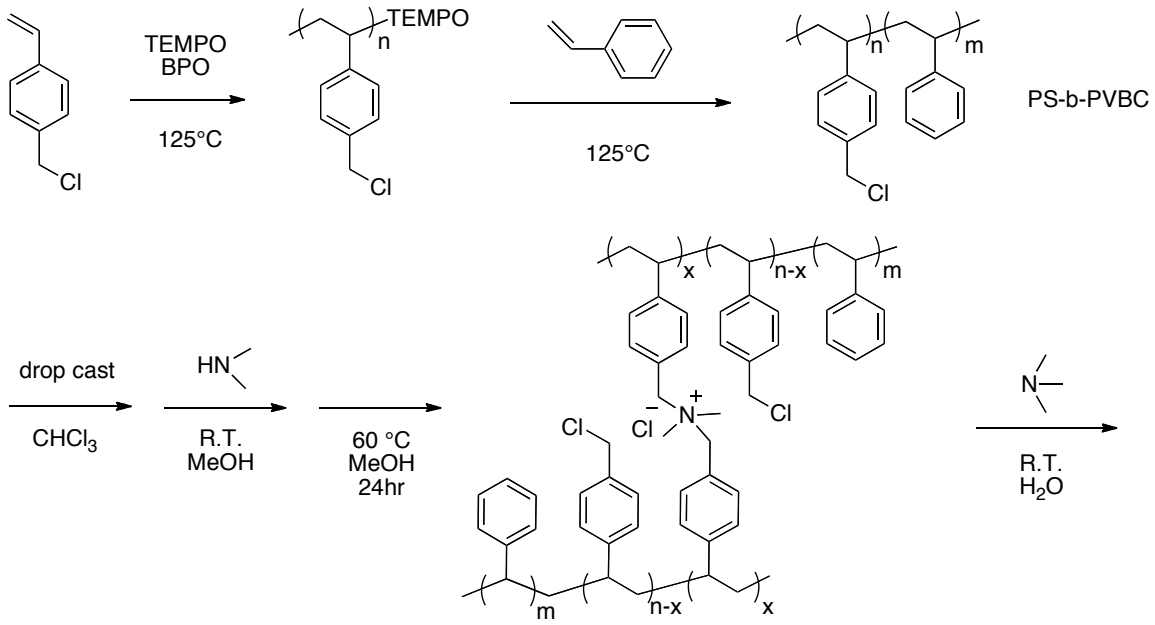

The chains are first reacted with dimethylamine in different amounts to form a defined number of crosslinks. After the remaining benzyl chloride groups are converted to benzyltrimethylammonium chloride groups, the films were characterized to the extent of conversion, IEC, and the chloride conductivity was measured. It is found that the materials show good chloride conductivities and that the conductivities are inversely related to the crosslinking amount and directly related to the IEC (**Figure 29**).

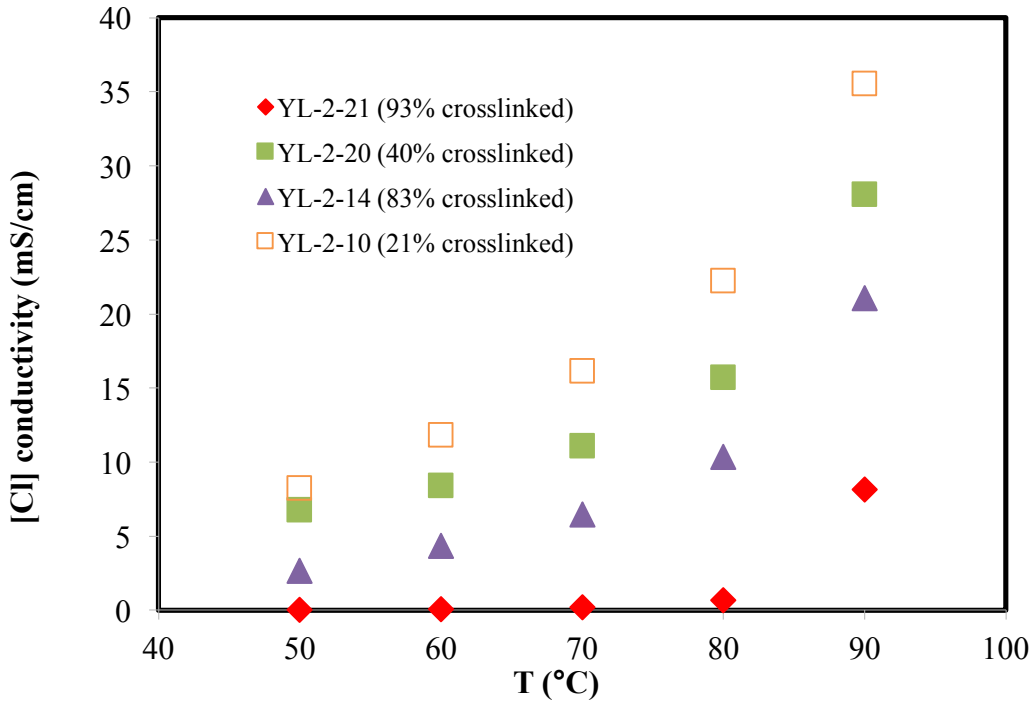

Figure 29. Cl^- conductivity of crosslinked AEM versus temperatures.

Our synthetic efforts are focused on the design and examination of a variety of block copolymers that can provide both an understanding of the ion transport as well as provide mechanically and chemically stable membrane materials. We have developed a procedure to produce a semi-crystalline polyethylene-based copolymer that in many ways is an analogous structure to the semi-crystalline Nafion™ PEM materials. The crystalline nature of the polyethylene provides mechanical stability, while a benzyltrimethylammonium functional block provides a stable linkage for the anion transport. The procedure for the synthesis and membrane fabrication is outlined in the following Scheme (**Figure 30**). Here, a polybutadiene-block-polymethylstyrene is synthesized by anionic polymerization in order to form a high 1,4-polybutadiene enchainment (greater than 90%). Subsequently, the block copolymer is hydrogenated to produce a lightly branched but still semi-crystalline polyethylene. The pendent methyl group can be quantitatively brominated providing a precursor material that can be processed into a membrane film by melt pressing. The resulting membrane can then be aminated as done for other membrane films by reaction with a solution of trimethylamine. The membranes have thus far been examined in the bromide form, but anion exchange can readily be accomplished by established procedures.

Figure 30. Synthesis and preparation of membrane films based on polyethylene block copolymers.

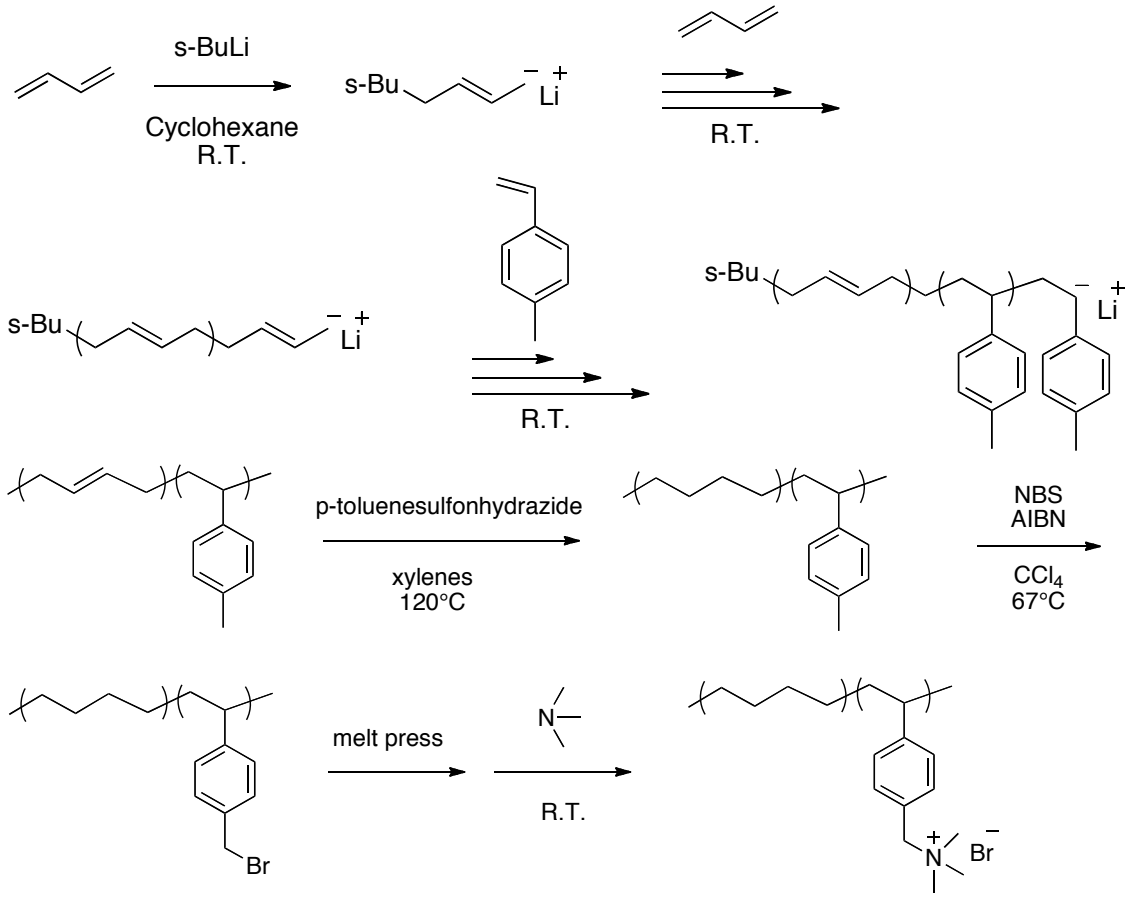

A number of materials have been designed and characterized (Table 1). The water uptake is seen to follow the composition of the copolymer, increasing with the amount of poly(4-methylstyrene) and therefore the amount of ammonium bromide.

Table 1. Characterization of PB-b-P4MS and PE-b-P[VBTMA][Br] block copolymer

membranes	M_n[a] of PB block (g/mol)/PDI	M_n[a] of PB-b-P4MS diblock (g/mol)/PDI	PB : P4MS compostion[b] (wt%)	Water uptake (%)	Theoretical IEC (mmol/g)
A	40k/1.06	61k/1.08	68 : 32	22	1.49
B	47k/1.09	75k/1.13	60 : 40	28	1.80
C	50k/1.08	66k/1.16	77 : 23	12	1.01
D	33k/1.05	68k/1.14	51 : 49	35	2.11

a) determined by light scattering (GPC); b) determined by ^{1}H NMR spectroscopy

These materials when converted to a hydrophilic group are not able to reorganize because of the crystalline nature of the hydrophobic polyethylene block. The domains are therefore expected to remain largely of the same dimensions as what is present after initial melt fabrication. This produces a membrane that should remain dimensionally stable to changes in hydration. This can be seen through SAXS analysis that shows no significant changes with changes in the relative humidity for each of the samples (**Figure 31**).

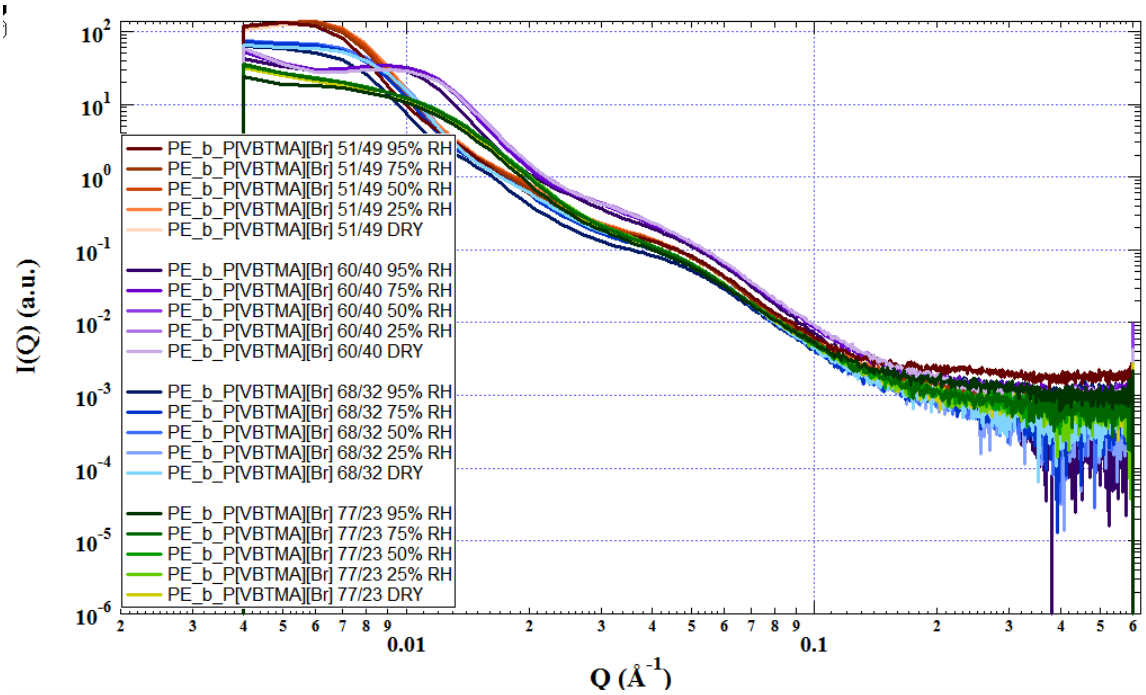

Figure 31. SAXS data of PE-b-P[VBTMA][Br] membranes with different PB and P4MS compositions.

Some demonstration of ordered domains are evident in the SAXS characterization as well as a peak that may be associated with the ionic domains. Further work is necessary to understand the SAXS characterization.

A promising result for these materials is depicted in **Figure 32**, showing the results of conductivity measurements on one sample. A relatively high bromide conductivity is observed under conditions of 60 °C and 95% humidity and interestingly, a low activation energy is calculated from the measurement of conductivity at varying temperature. Here again, further studies are necessary, but the materials thus far show promise for potential application as well as for developing an understanding of transport.

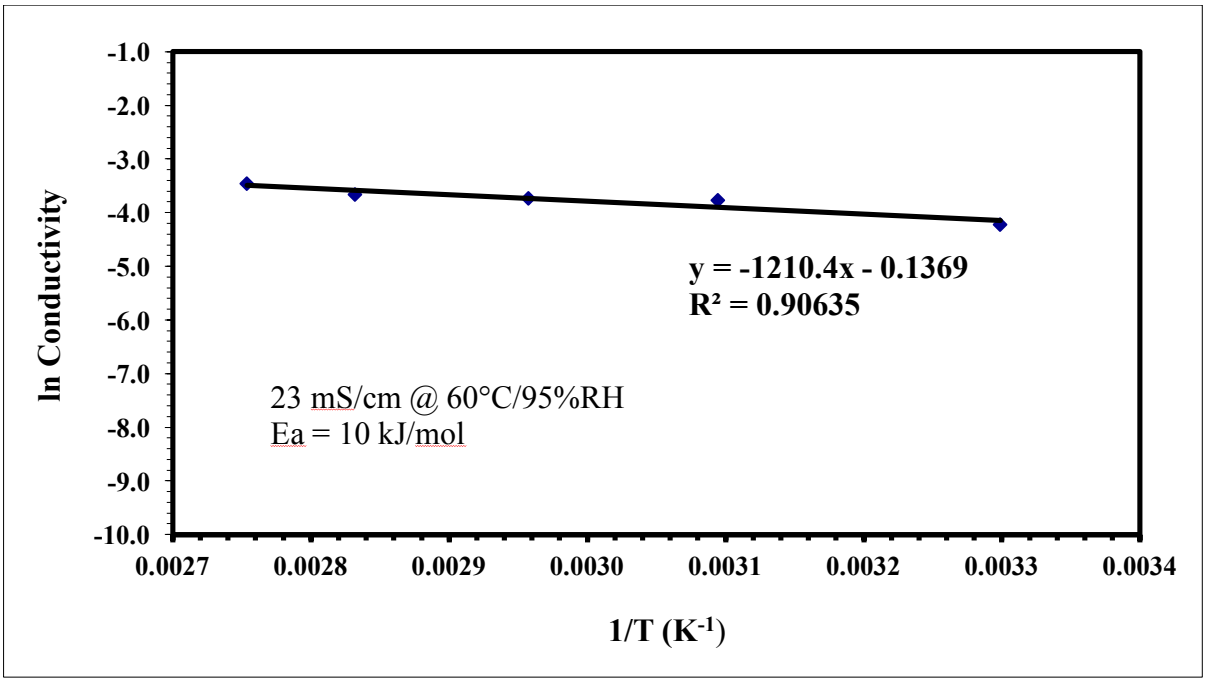

Figure 32. [Br] Conductivity of PE-b-P[VBTMA][Br] with PB : P4MS composition at 60% : 40% (wt%).

Poly(2,6-dimethylphenylene oxide) (PPO) is well-known engineering material that forms strong, thermally and chemically stable films. It has been investigated by number of other groups as a potential anion exchange membrane because the pendent methyl groups can be readily converted into benzylammonium groups. We have taken an approach to produce block and random copolymers of PPO in order to design phase separation into the membranes for potentially improved conductivity. The copolymers are prepared by employing a 2,6-diphenylphenol as comonomer, **Figure 33**. Because the 2,6-diphenyl- and 2,6-dimethylphenols have different reactivities, block and random copolymers can be produced under the appropriate reaction conditions.

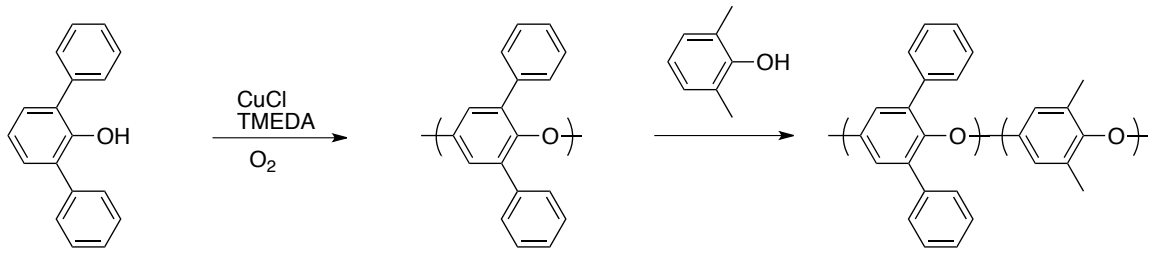

Figure 33. Copper catalyzed oxidative polymerization of 2,6-dimethylphenol and 2,6-diphenylphenol copolymers.

Table 2. Characterization of PPO Copolymers

Sample	% Methyl Rpt Units	Bromine/Methyl Rpt Unit	IEC Th. (meq/g)	IEC Meas. (meq/g)	Water Uptake
Block-1	21	0.76	0.69	0.14	26.5
Block-2	21	0.73	0.67	0.40	7.9
Block-3	24	0.83	0.87	0.51	9.3
Block-4	44	1.05	2.04	0.96	41.6
Block-5	41	0.87	1.61	1.03	30.2
Block-6	45	1.16	2.27	1.09	41.0
Block-7	49	1.16	2.49	1.27	43.6
Ran-1	21	0.99	0.87	0.15	19.1
Ran-2	48	0.83	1.84	1.35	34.4

Gel permeation chromatography and ^{1}H NMR spectroscopy were used to determine the configuration of the copolymers. The chromatograms show a shift of the peak to higher molecular weight and thereby the growth of the second block from the first. While ^{1}H NMR spectroscopy displays chemical shifts for the methyl protons in a minimum number of chemical environments in agreement with a blocky structure. Some samples gave some methyl PPO homopolymer as a minor component of the product polymer due to the high reactivity of 2,6-dimethylphenol. Random copolymerizations are inferred from the combination of gel permeation chromatography and ^{1}H NMR spectroscopy where the NMR spectroscopy indicates different chemical environments for the methyl protons.

Functionalization of the copolymer was carried out in a two-step process outlined in **Figure 34**. First the copolymer was brominated exclusively at the benzylic position using liquid bromine. The bromine was then substituted with a tertiary amine to form a copolymer with quaternary ammonium functionality on only one block. The bromination was carried out using a method developed by Cabasso and coworkers. A dilute solution of polymer in 1,1,2,2-tetrachloroethane was refluxed. Bromine diluted with 1,1,2,2-tetachloroethane was added dropwise to the polymer solution. The low concentration and

high temperature force the bromine reaction through a radical mechanism that prefers to react at the benzylic position on the methyl substituted repeat unit minimizing the side reaction of the bromine on the aromatic rings.

The brominated polymers were characterized with ^{1}H NMR spectroscopy and GPC. The ^{1}H NMR spectrum of brominated block copolymer shows a decrease in the methyl proton signals at 2 ppm and a similarly shaped set of peaks forming at around 4.2 ppm. The chemical shift agrees well with literature values for brominated poly(2,6-dimethyl-1,4-phenylene oxide. The degree of bromination can be calculated from the integration ratio for the two sets of peaks at 2 and 4.2 ppm and is given for each polymer in **Table 2**. GPC of the brominated copolymers exhibited similar shaped peaks as the unfunctionalized copolymers suggesting that no polymer degradation occurred. However, the peaks shifted to longer elution volumes implying the brominated copolymers form smaller random coils in solution. It is hypothesized that this is due to a small reduction in solubility by adding the bromine groups to the polymer thereby causing the copolymer to form a tighter coil in solution.

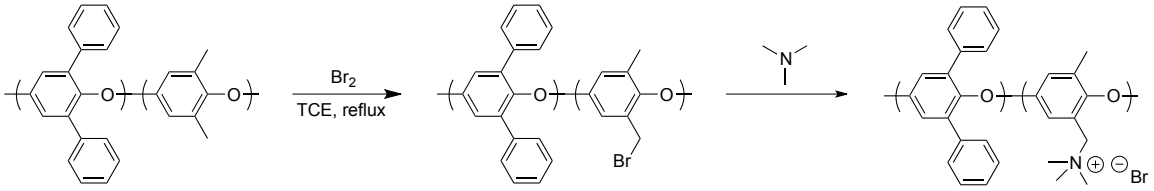

Figure 34. Functionalization of copolymers by first brominating followed by amination.

The final step in functionalization of the block copolymers is the substitution of trimethylamine for the benzyl bromide. The amination reaction was carried out on a film cast from a chloroform solution. The film was soaked in an aqueous solution of trimethylamine for two days, soaked in water for a day, rinsed with copious amounts of water and dried to remove excess amine. The reaction was assumed to be quantitative. The theoretical ion exchange capacity can then be calculated from the composition of the copolymer and the degree of bromination for each sample according to the equation,

$$IEC = \frac{f_{Br}N_{Me}}{(100 - N_{Me})M_{Ph} + N_{Me}(M_{Me} + 78.9f_{Br})}$$

where f_{Br} is the fraction of bromine per methyl substituted repeat unit; N_{Me} is the percent methyl substituted repeat units in the polymer; M_{Ph} is the formula weight of the phenyl substituted repeat unit; and M_{Me} is the formula weight of the methyl substituted repeat unit. The theoretical ion exchange capacity values along with the ion exchange capacity measured by back titration are given in **Table 2**.

The titrated values are all significantly lower than the theoretical calculations most likely due to two reasons. First, some of the polymer could have been extracted from the film once it was fully functionalized, especially for the samples that contain some methyl substituted homopolymer. Some of the amination solutions were evaporated to reveal a small amount of polymer but not enough to account for the total loss in ion exchange capacity. The other possibility is incomplete reaction of the amine with the benzyl bromide. Examination of the FTIR spectra of the brominated and aminated

copolymers suggests this to be likely also. The peak corresponding to the C-Br stretching at 626 cm^{-1} decreases upon amination but does not disappear completely suggesting an incomplete reaction. Preparation of membrane films and measurement of conductivity with temperature and humidity is ongoing for these materials.

Polysulfone materials have been investigated as a promising backbone structure in both proton and alkaline exchange membranes for fuel cell applications. We also have efforts designed to look at functionalized polysulfone as a membrane, but are doing so with the intent of examining alternative cations and in functionalizing the polysulfone where the ammonium functionality is further removed from the proximity of the backbone. Two projects are in progress involving polysulfone. In the first, polysulfone copolymers are made using a benzimidazole monomer that can subsequently be quaternized to an ammonim salt (**Figure 35**).

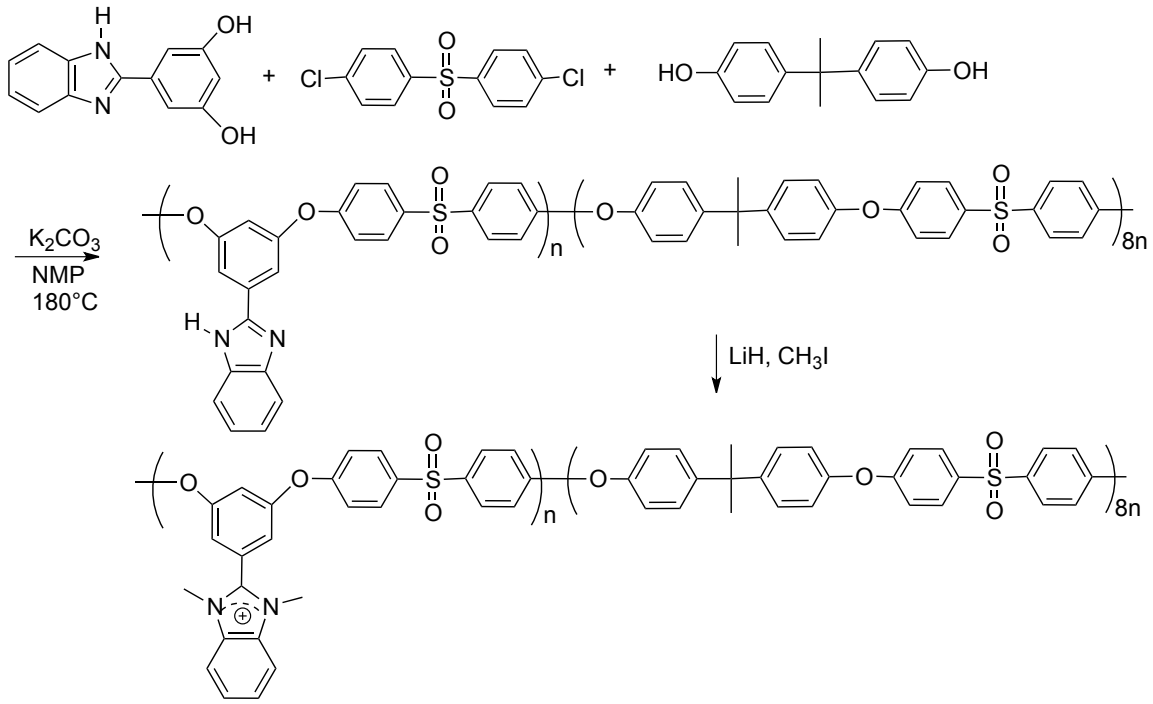

Figure 35. Polysulfone with benzimidazole monomer.

As an initial step, copolymers have been synthesized that have an 8:1 molar ratio of bishenol monomers, while additional polymerizations are being investigated. Benzimidalolium functional polymers have recently appeared in the literature as potential anion exchange membrane materials.[xxxiv] In that work, the benzimidazolium groups are constrained within the backbone, while in our investigation, the benzimidazolium group is pendent to the chain potentially offering improved ion mobility and domain formation.

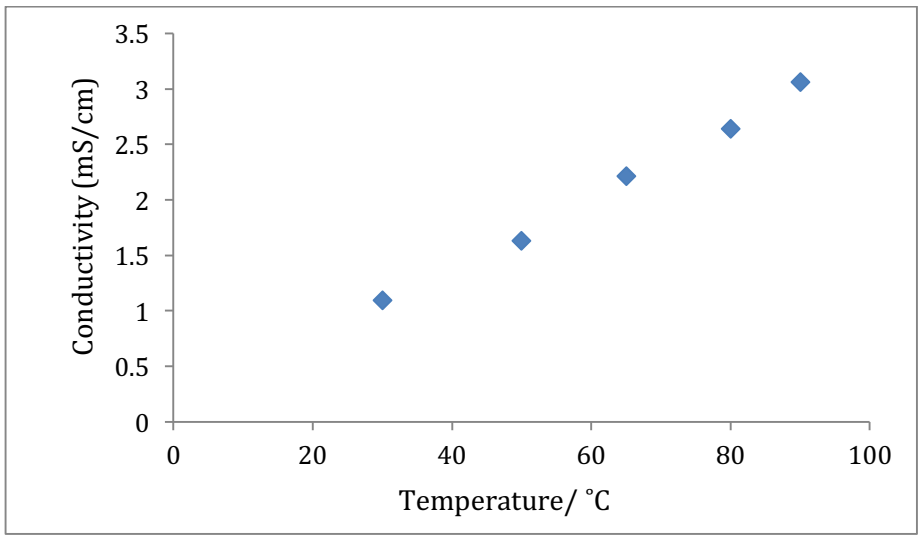

Figure 36. Iodide Conductivity versus Temperature for Benzimidalolium Polysulfone Copolymer.

Only preliminary investigations of conductivity have thus far been conducted, but show promise based on the small IEC that results from the copolymer composition (**Figure 36**). A balance of ionic groups and film-forming polysulfone content is being investigated as new compositions are prepared and analyzed.

In a second approach to investigating polysulfone-based materials, a simple post-polymerization sequence of reactions is designed to functionalize the polymer while removing the functional group from the proximity of the backbone, **Figure 37**. Polysulfone is well-studied to undergo sulfonation upon reaction with chlorosulfonic acid. The chlorosulfonic acid groups can then be converted into cation functional sulfonamide groups by reaction with a trimethylbenzylammonium functional aniline. The resulting arylsulfonamide has been investigated in our laboratories to be an exceptionally chemically stable group under basic conditions. The sequence of reactions leads to a very simple method of cation functionalization, while the functional aniline provides a reagent that can be used to functionalize other types of polymer backbones.

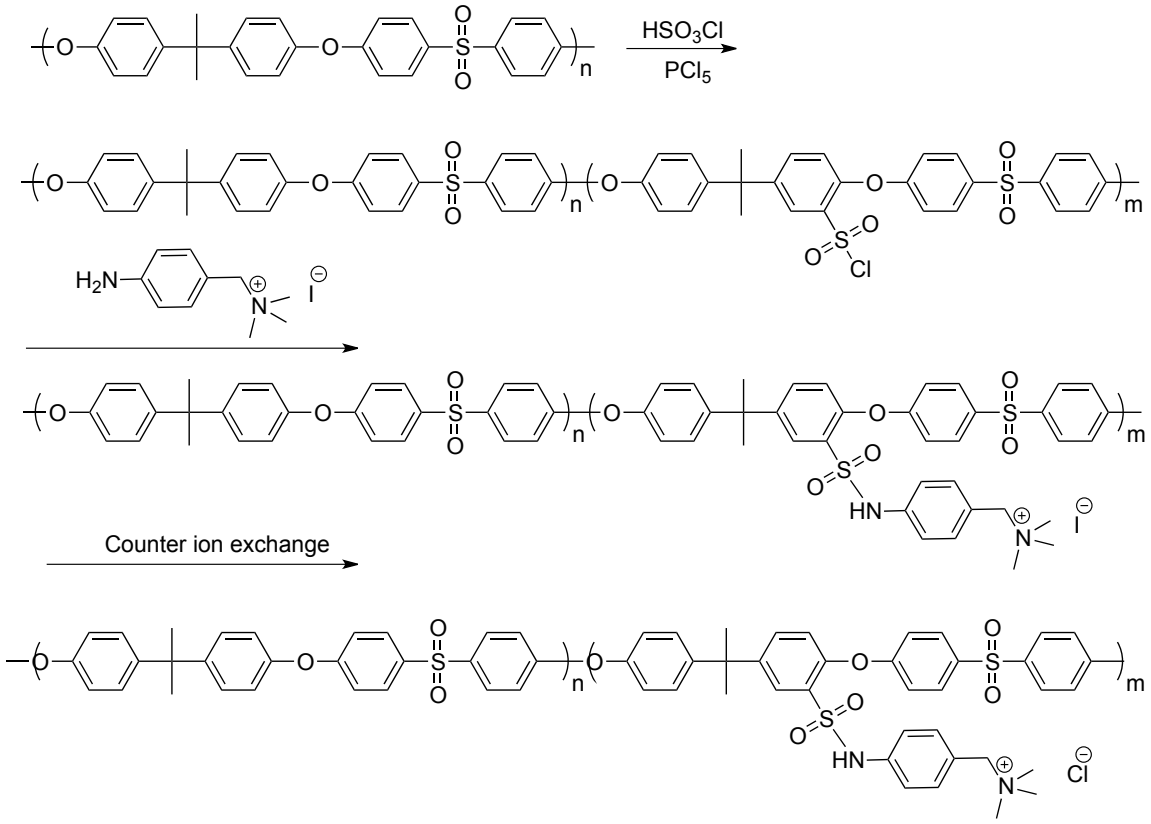

Figure 37. Second approach to polysulfone chemistry.

It is determined that a range of amounts of sulfonyl chloride functional groups can be introduced, resulting in a range of ammonium functionalization. The water uptake is found to increase with the amount of cationic groups (**Table 3**).

Table 3. Characterization of sulfonamide functionalized polysulfones.

Feed Ratio of Polysulfone to Chlorosulfonic acid	**Water Uptake %**	**IEC (mmol·g^{-1}) Theoretical value (Assume qualitative reaction)**	**IEC (mmol·g^{-1}) (Calculated from NMR)**	**IEC (mmol·g^{-1}) Back Titration value**	**Conductivity (mS•cm^{-1}) 95%RH, 90°C**
1:0.25	16.4	0.47	0.21	0.19	3.4
1:0.5	18.1	0.81	0.32	0.31	2.1

1:0.75	27.5	1.06	0.69	0.65	9.0

Initial conductivity measurements are demonstrated in Figure X showing some variability in the correlation of conductivity to the IEC. Research is continuing and efforts are focused at examining more highly functionalized materials.

3.2 Film Casting and characterization of PS-*b*-PVBC block copolymer and corresponding blends

A micrometer blade film applicator was used to cast consistent films of various thickness from the polystyrene-*b*-poly(vinylbenzyl chloride) (PS-*b*-PVBC) block copolymer synthesized by the Knauss group. Blends of polystyrene (PS) and poly(vinylbenzyl chloroide) (PVBC) homopolymers were also cast into membrane as a comparison to the diblock films. Soaking these membranes in trimethylamine replaced the chlorinated sites with trimethylammonium groups producing a cationic, conductive polymer ([PVBTMA][Cl]). Electrochemical impedance spectroscopy was used to determine the in-plane ionic conductivity of the membrane over a range of temperature and humidity conditions. **Figure 38** shows the conductivity results of the diblock films compared to the homopolymer blend films at 95% relative humidity at temperatures ranging from 30-90°C. The diblock films showed significantly higher conductivity than the blended film with a maximum conductivity of 32 mS/cm. The specific conductivity of the diblock films increased significantly as film thickness was decreased while the conductivity of the blended films increased only a small amount with decreased thickness. Initial small angle x-ray scattering of as-cast films did not indicate any microstructure in either the diblock or blended films. Future experiments will anneal the diblock films under various conditions in an attempt to generate a structured morphology in the membrane. Extensional rheology measurements were performed using an ARES G2 rheometer on the blended PS/PVBC and cationic PS/[PVBTMA][Cl] and results indicated that tensile strength, elongation, and film elasticity all decrease with the addition of cation groups to the polymer. Mechanical characterization of the diblock PS-*b*-PVBC and PS-*b*-[PVBTMA][Cl] is ongoing and will be compared to that of the blended films.

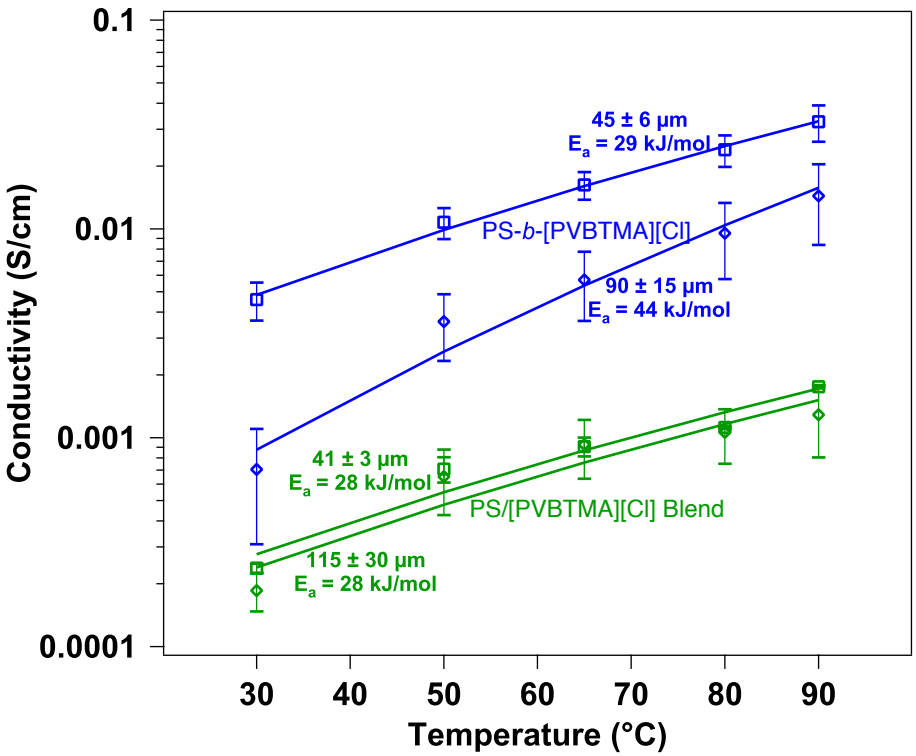

Figure 38 Conductivity of the 70/30 PS-*b*-[PVBTMA][Cl] diblock compared to a blend of 70/30 PS/[PVBTMA][Cl] at 95% relative humidity. The diblock membranes had conductivity an order of magnitude higher compared to the blended films and showed thinner films had a higher specific conductivity than thicker films.

3.3 Poly(ethylene glycol) (mPEG) Grafted AEMs (Graft copolymer)

Proton exchange membranes (PEMs) usually exhibit higher ion conductivity than AEMs, with the primary reason being that the size of proton is much smaller than hydroxide in the AEM. However, the hydration number in the PEM is also much higher than in the AEM. For example, polysulfone-based PEMs show relatively higher hydration number ($\lambda \approx 20$)(9) than common AEMs ($\lambda = 5$ - 10). In order to study the hydration number effect on ion conductivity of AEMs, another AEM system is designed to increase hydration numbers by manipulating the amount of water uptake in a membrane while maintaining the ion exchange capacity relatively constant. mPEG is a hydrophilic polymer that can absorb enough water to increase the hydration number in AEM. The mPEG is a hydrophilic polyethylene glycol with a reactive primary hydroxyl group on one chain end so that it can be readily grafted onto polymer chain pendent benzyl chloride groups(10), (**Scheme 1**).

Scheme 1. Synthesis of mPEG grafted copolymer

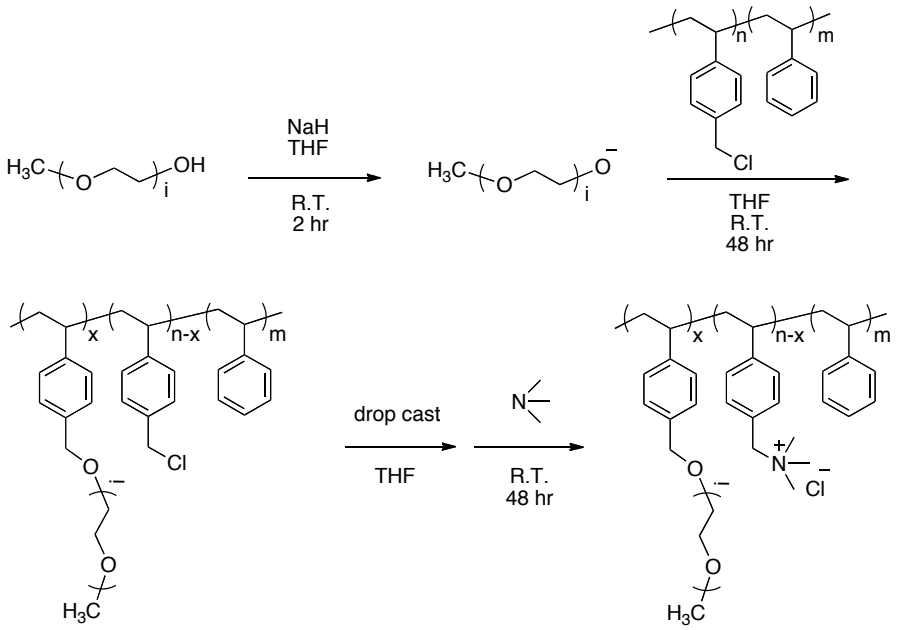

In this study, a PEG grafted membrane is prepared by grafting mPEG to a PVBC-b-PS block copolymer. The membranes are grafted with different mPEG amounts (2.0%, 4.4%, 6.8% and 11.2% by weight). The extent of mPEG grafting reaction was determined by GPC and NMR spectroscopy, not shown. The mPEG is determined to be attached to the polymer backbone as demonstrated by the GPC chromatograms showing no residual unreacted mPEG and an increase in the hydrodynamic volume of the polymer after attachment. In combination with NMR spectroscopy that indicates the composition of mPEG incorporated, it is determined that the grafting reaction occurs in high yield. The remaining benzyl chloride groups in graft polymer are subsequently converted to benzyltrimethyl ammonium cationic groups after film formation to result in an anion exchange membrane.

Membranes are prepared with different amounts of PEG grafts and the water uptake and hydration number are determined for each membrane at room temperature and plotted as a function of titrated IEC. The grafted membranes are compared with a membrane without the PEG graft. The hydration number increases with increased mPEG grafting extent in the membrane and correlates to higher chloride conductivity. The chloride conductivity of mPEG grafted AEMs are also compared at different relative humidity (50%RH, 80%RH and 95%RH). The AEM with higher mPEG grafting extent shows decreased dependence on humidity (**Figure 39** and 9).

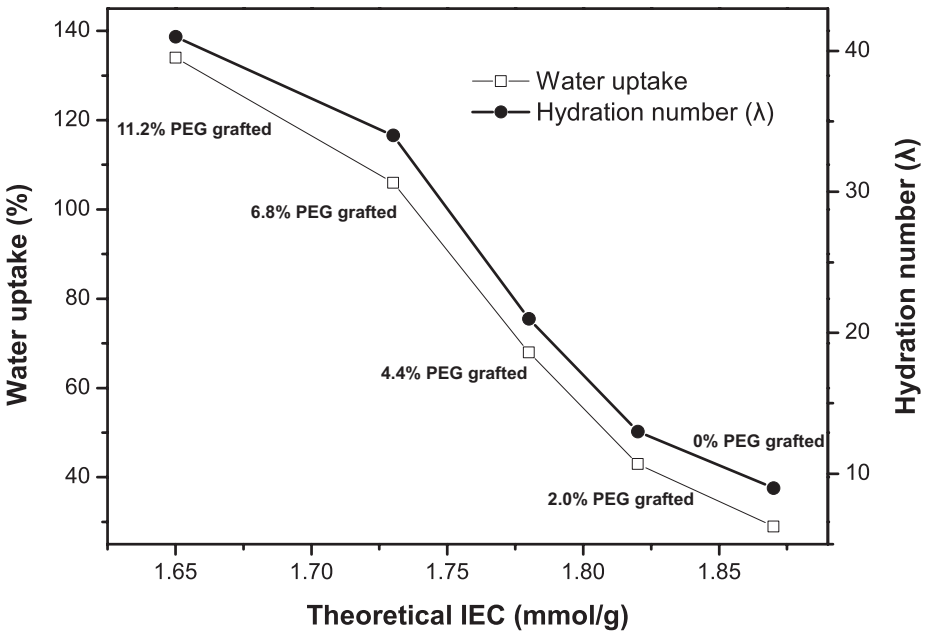

Figure 39. Water uptake and hydration number versus titrated IEC of PEG grafted AEMs

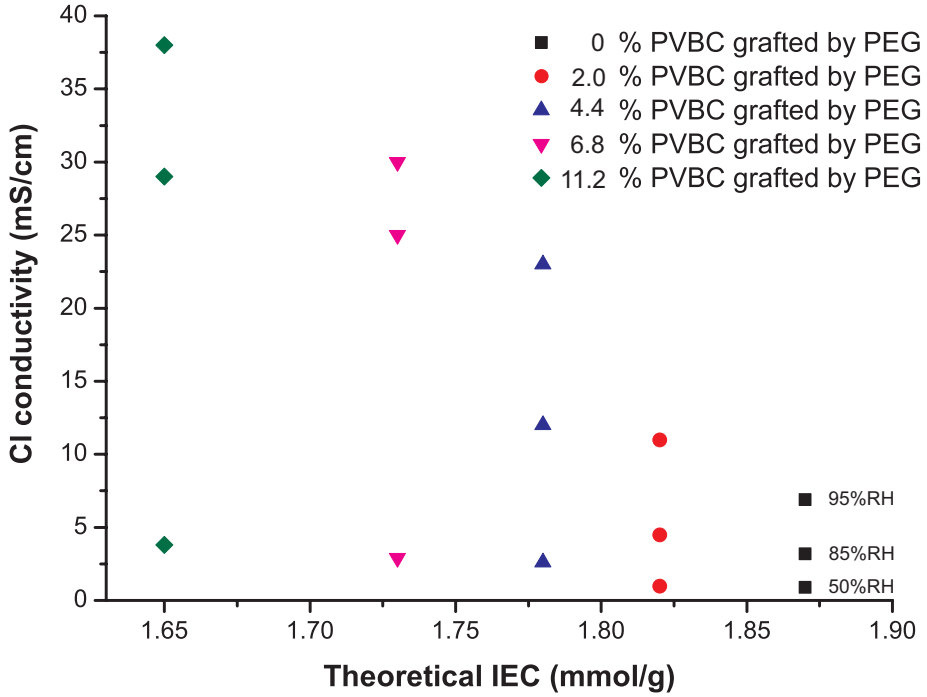

Figure 40. Cl conductivity comparison (50%, 80% and 95%RH) of PEG grafted AEM at 60 °C.

The research is continuing by exchanging the chloride for hydroxide and the hydroxide conductivity is being examined for each of the membranes.

3.4 Poly(phenylene oxide)-b-PVBTMA Copolymers

While the styrenic polymers are a useful system for designing controlled block copolymers and studying the fundamental behavior as alkaline exchange membrane, they

continue to suffer from relatively poor mechanical properties. For property improvement we are continuing to study blends of the styrenics with poly(2,6-dimethyl-1,4-phenylene oxide) (PPO) as reported last year, but we are also studying a number of block copolymer systems that are prepared from engineering polymers and polymers that are known to display good mechanical properties as membranes. In a search for a simple route to engineering polymer membranes, we have developed block copolymers of PPO and polyvinylbenzyl chloride that can be subsequently processed into films and then converted into quaternary ammonium block copolymers.

PPO is known to have good chemical and alkaline stability and other research groups have also begun to examine PPO. However, in most cases the PPO is examined to use the benzylic methyl groups to convert into a benzylammonium group as demonstrated in our own work(11). Another advantage of PPO is that it is monofunctionalized with a phenol chain end. This chain end can be functionalized with an initiating group and used to prepare diblock copolymers. The following scheme depicts the procedure for the preparation of a diblock copolymer with vinylbenzyl chloride. After the copolymer is synthesized, films can be prepared by melt pressing and the resulting film can be reacted with trimethylamine to convert the benzyl chloride groups into anion conducting benzyltrimethylammonium groups.

Scheme 2. Synthesis of PPO-*b*-PVBTMA copolymers

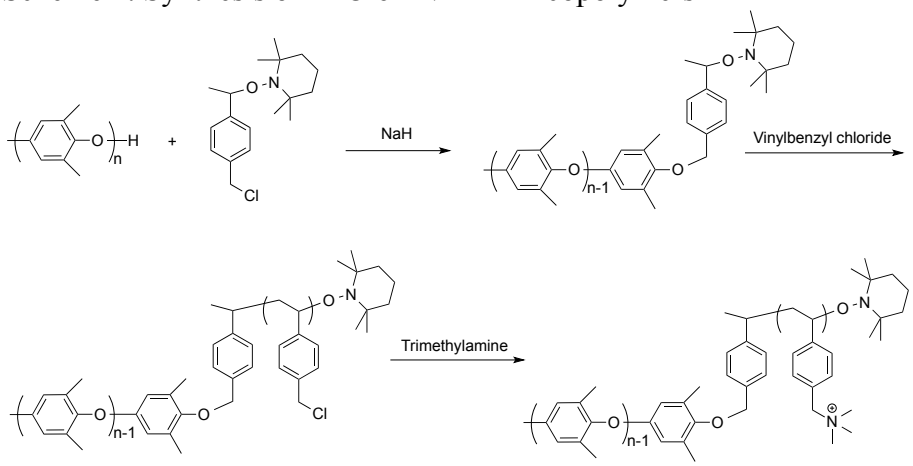

Details of the synthesis procedure are provided. PPO was deprotonated by sodium hydride and a nitroxide functional reactant was introduced. End group analysis was conducted using ultraviolet/visable (UV/Vis) spectroscopy to observe the phenoxide chain end that absorbs between 310nm and 380 nm(12).

PPO-BzEt-TEMPO was employed as a macroinitiator in a nitroxide mediated polymerization of vinylbenzyl chloride to give PPO-b-PVBC block copolymers. A series of block polymers with different PVBC block lengths was prepared in this research. The polymerization was carried out in bulk vinylbenzyl chloride at 125 °C for different reaction times. **Figure 41** shows the GPC curves of the original PPO, the end capped PPO, and two PPO-b-PVBC copolymers with different PVBC block lengths. The shift of the block copolymers in to lower elution volume in

the chromatogram demonstrates the formation of higher molecular weight polymer compared to the PPO homopolymer, suggesting the successful synthesis of PPO-*b*-PVBC copolymers.

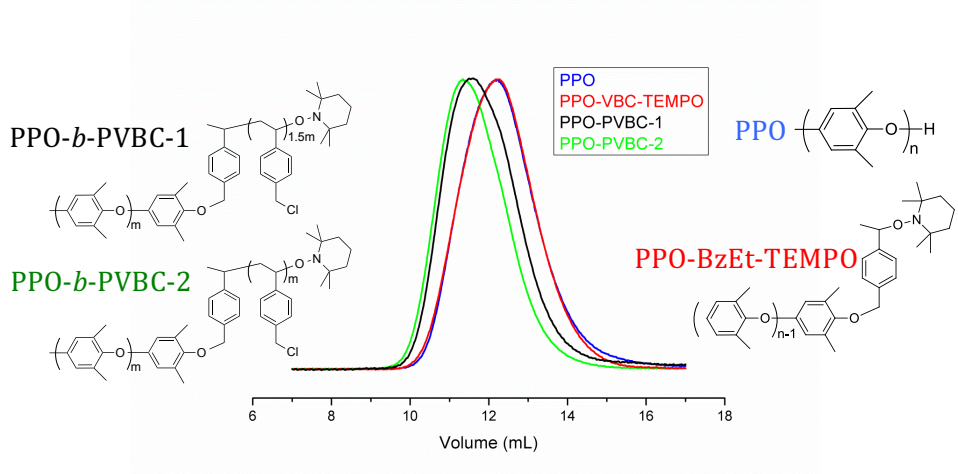

Figure 41. GPC curves of original PPO (blue), end capped PPO (red) and two PPO-*b*-PVBC copolymers (black and green).

The molecular weight can be calculated from ^{1}H NMR spectra based on the distinctive peaks from each block. The NMR spectra exhibit characteristic peaks at δ = 4.5 ppm (a) derived from protons on the benzylic carbon in PVBC as well as the peaks at δ = 2.1 ppm (b) representing protons on the methyl groups in PPO. The quantitative ratio of PVBC block to PPO block was calculated from integration of these two peaks. The molecular weights of each block polymer were calculated based on the repeat units ratio of two block polymers and based on the number average molecular weight of PPO of 20 kg/mol. **Table 4** displays the molecular weight of each block polymer calculated from NMR spectra.

Table 4. Molecular weights of each PPO-*b*-PVBC block copolymer based on NMR spectra.

Sample	PVBC:PPO	Mol. Wt. of PVBC block (kg/mol)	Mol. Wt. of PPO-*b*-PVBC (kg/mol)	Weight percentage of PVBC (%)
PPO-*b*-PVBC1	1: 6.88	3.7	23.7	16
PPO-*b*-PVBC2	1: 4.1	6.2	26.2	24
PPO-*b*-PVBC3	1: 3.34	7.6	27.6	28
PPO-*b*-PVBC4	1: 2.74	9.3	29.3	32
PPO-*b*-PVBC5	1: 2.08	12	32	37
PPO-*b*-PVBC6	1: 1.94	13	33	39

PPO-*b*-PVBC7	1: 1.39	18	38	47
PPO-*b*-PVBC8	1: 1.27	20	40	50
PPO-*b*-PVBC9	1: 1.11	23	43	53
PPO-*b*-PVBC10	1: 0.9	28	48	58
PPO-*b*-PVBC11	1: 0.77	33	53	62
PPO-*b*-PVBC12	1: 0.44	57	77	74

Films were prepared of the block copolymers by solution casting from tetrachloroethane, however some phase separation was observed, possibly from residual homopolymer PPO. The block copolymer and homopolymer PPO have different solubilities and it was observed that a thin film of PPO formed on top of the block copolymer. The block copolymers were however readily melt pressed into films at 240 °C. A high temperature is necessary because of the high T_g of the PPO block. At this temperature it was found that the resulting film was no longer soluble, presumably as a result of crosslinking of a portion of the pendent vinylbenzyl chloride groups. This crosslinking was expected to be advantageous especially for the polymers with high PVBC content.

Table 5. IEC, Water Uptake, and Hydroxide Conductivity of PPO-b-PVBTMA membranes

Sample	Weight Percentage of PVBTMA (%)	Water Uptake (%)	IEC[a] (mequiv/g)	IEC[b] (mequiv/g)	Conductivity[c] (ms/cm)
PPO-*b*-PVBTMA1	19	5	0.98	-	2
PPO-*b*-PVBTMA2	28	11	1.45	-	4
PPO-*b*-PVBTMA3	32	13	1.68	-	5
PPO-*b*-PVBTMA4	37	13	1.91	-	6
PPO-*b*-PVBTMA5	43	32	2.23	1.7	25
PPO-*b*-PVBTMA6	45	33	2.33	1.5	20
PPO-*b*-PVBTMA7	53	50	2.75	1.6	28
PPO-*b*-	56	64	2.89	2.1	36

PPO-*b*-PVBTMA8	59	70	3.06	1.8	45
PPO-*b*-PVBTMA9	64	87	3.30	-	61
PPO-*b*-PVBTMA10	68	95	3.49	2.71	73
PPO-*b*-PVBTMA11	78	174	4.05	-	87
PPO-*b*-PVBTMA12					

[a]Calculated from 1H NMR of PPO-b-PVBC. [b]Titrated values, in which "-" means the titration is under tested. [c]Measured at 20 °C in 18 MΩ water. Teflon stripe was running as background.

The films were suspended in aqueous trimethylamine solution to convert the benzyl chloride groups to benzyltrimethylammonium chloride groups, and the chloride was exchanged for hydroxide. The water uptake and IEC of the membranes was measured in the hydroxide form at room temperature. As expected, both water uptake and conductivity goes up proportional to the increase of weight percentage of PVBTMA or IEC values, except for PPO-*b*-PVBTMA5, which shows a higher conductivity than PPO-*b*-PVBTMA6. This is possibly due to the incomplete quaternization of PPO-*b*-PVBC6, which is also suggested by the lower titrated IEC value compared to PPO-*b*-PVBTMA5.

A wide range of compositions is prepared in the study and the resulting materials display a broad range of IEC and corresponding water uptake and conductivity. The conductivity and water uptake display an expected increase with IEC as depicted in Figure 12. While the polymers with high IECs show impressive conductivities at room temperature, the polymers do swell significantly. However, the materials do not dissolve in water presumably due to the crosslinking that occurs during the melt processing as well as due to the block copolymer nature of the materials. The conductivities are quite high for some of the polymers and further studies are continuing to determine the conductivity with temperature and humidity.

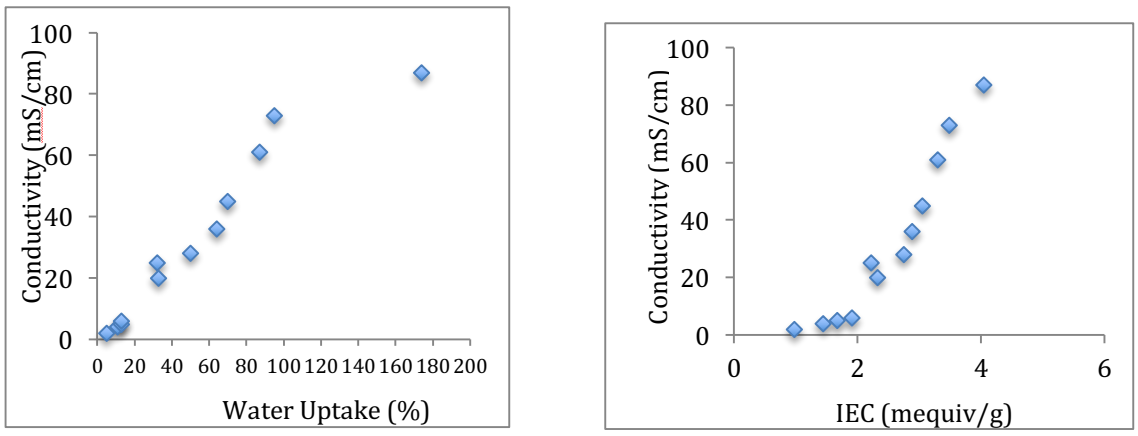

Figure 42. Hydroxide conductivity of PPO-b-PVBTMA at 20 °C in water vs. water uptake, left, and theoretical IEC, right..

3.5 Polyformal block copolymers

As part of our investigation of engineering polymers as components of block copolymers, we are investigating materials that can be formed into distinct block copolymers by condensation polymerization. The polyacetal from the reaction of bisphenol with dibromomethane is also known as polyformal. It is an engineering polymer that is stable in an alkaline environment. In our design, we have prepared polysulfone as a hydrophobic block copolymerized in the polyformal reaction to make multiblock polysulfone-co-polyformal materials. To prepare the polyformal block, we use tetramethylbisphenol A that can subsequently be converted into bromobenzyl and then benzyltrimethylammonium groups. The tetramethyl groups can be converted into as many as four ionic groups per repeat unit. Combined with the fact that the repeat unit of the polyformal is relatively small, the formation of the block copolymers results in segregated hydrophobic-hydrophilic blocks wherein the hydrophilic blocks contain a high concentration of ionic groups. It is anticipated that the high concentration of ionic groups will have a significant effect on the morphology and ionic conductivity. The use of tetramethyl groups has been attempted previously(13), however, the block copolymer in our work specifically designs the high concentration of ionic groups in a hydrophilic block.

A series of polysulfone oligomers ranging in their molecular weight (M_n) from 2,500 to 7,250 g/mol were synthesized from bisphenol A (BPA) and bis(4-chlorophenyl)sulfone (BCPS) via condensation polymerization. The BPA and BCPS were taken up in N-methylpyrrolidone (NMP) in the presence of potassium carbonate in a reactor fitted with Dean-Stark equipment for the azeotropic removal of water. The resulting oligomer molecular weights were controlled by stoichiometric imbalance with BPA being in slight excess, in order to obtain hydroxyl terminated materials. The molecular weights and polydispersity were determined by gel permeation chromatography (GPC) using Wyatt miniDawn light scattering (LS) and Optilab DSP (RI) detectors. The resulting low molecular weight polysulfone materials were designated to serve as the hydrophobic blocks of the copolymer.

Scheme 3. Synthesis of Multiblock polysulfone copoly(formal)

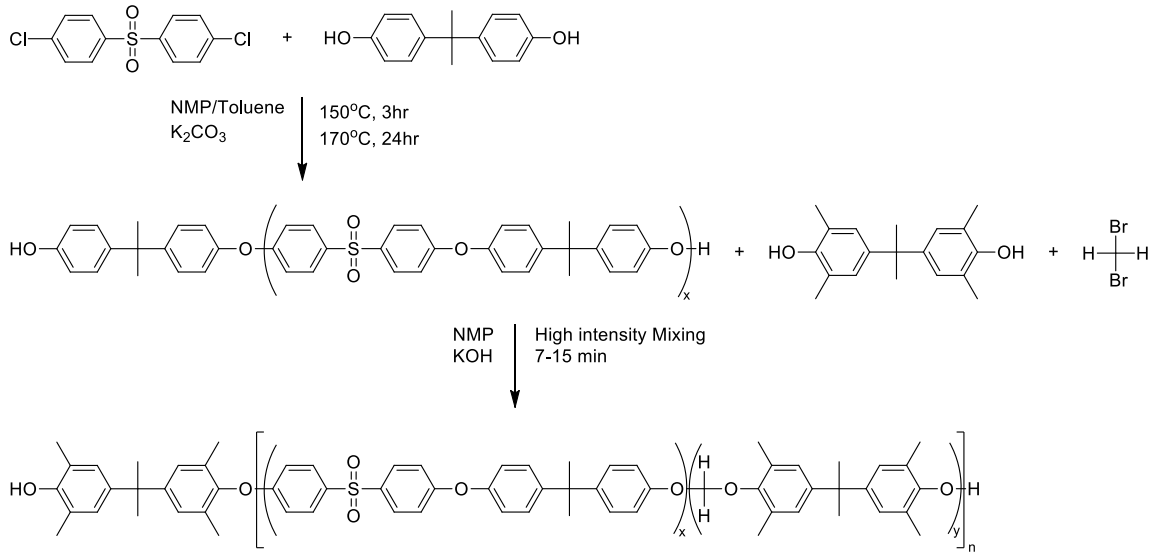

Preparation of the multiblock polysulfone-co-polyformal polymers was accomplished by the nucleophilic substitution reaction of polysulfone oligomers and tetramethyl bisphenol A (TMBPA) with dibromomethane in the presence of potassium hydroxide with high intensity mixing(14). The molecular weights of the polymers obtained are shown below in the following table

Table 6. Molecular Weights of Multiblock Polymers

Material ID[a]	**Planned Polyformal Block MW [g/mol]**	**M_n [g/mol]**[b]	**M_w [g/mol]**	**PDI**	**Weight% Polyformal**[c]	**Average PF Block MW**
PSF2.5PF20	500	34,000	70,000	2.1	19	730
PSF2.5PF30	750	21,000	46,000	2.2	27	900
PSF2.5PF40	1000	52,000	100,000	2.0	33	1100
PSF5.0PF20	1000	12,000	32,000	2.7	18	950
PSF5.0PF30	1500	18,000	61,000	3.3	27	1300
PSF5.0PF40	2000	32,000	103,000	2.8	33	1600
PSF7.25PF20	1450	40,000	82,000	2.1	19	1600
PSF7.25PF30	2175	51,000	116,000	2.2	26	2300
PSF7.25PF40	2900	46,000	107,000	2.3	33	3000

[a] The first number designates the polysulfone block M_n in kg/mol and the second number designates the planned percentage of polyformal in the final material. [b] Molecular weights were calculated from a polystyrene calibration. [c] Calculated from the ^{1}H NMR spectra.

Analysis of the formal linkage protons in the ^{1}H NMR spectra of these materials revealed three, well resolved signals, which provide insight into the block character of the polymers. These signals appear at 5.68ppm 5.49ppm and 5.21ppm, **Figure 43**. Assuming that the signal at 5.50ppm represents both ends of the polyformal block in a multiblock

material, the average block size was calculated from the integral values for signals at 5.49ppm and 5.21ppm using the following formula:

Equation 1. Average Polyformal Block Size Calculation

$$MW = \frac{\int 5.21\,ppm}{\frac{\int 5.49\,ppm}{2}}$$

In making this assumption, the calculated average block molecular weight values are overestimated, due to the inability to determine the number of terminal polyformal blocks contributing to the integral value at 5.49ppm. However, considering the molecular weight increase from the polysulfone starting materials there is significant fraction of the material that is indeed multiblock.

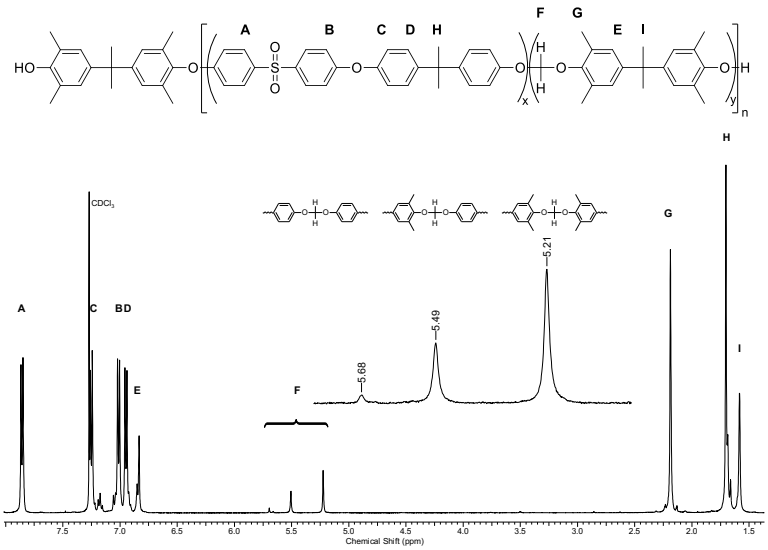

Figure 43. 1H NMR Spectrum of Multiblock Polysulfone Copoly(formal)

The alkaline stability of the poyformal linkages was assessed on a sample of block copolymer. Sample PSF5.0PF30, in powder form was soaked in 5% and 10% KOH solutions at 80°C for eight days. Upon completion, the sample was dried and the molecular weight measured by GPC. Ultimately, there was no observed degradation of the backbone; therefore, this series of materials was determined to be suitable for alkaline fuel cell applications.

Scheme 4. Functionalization of Multiblock Materials

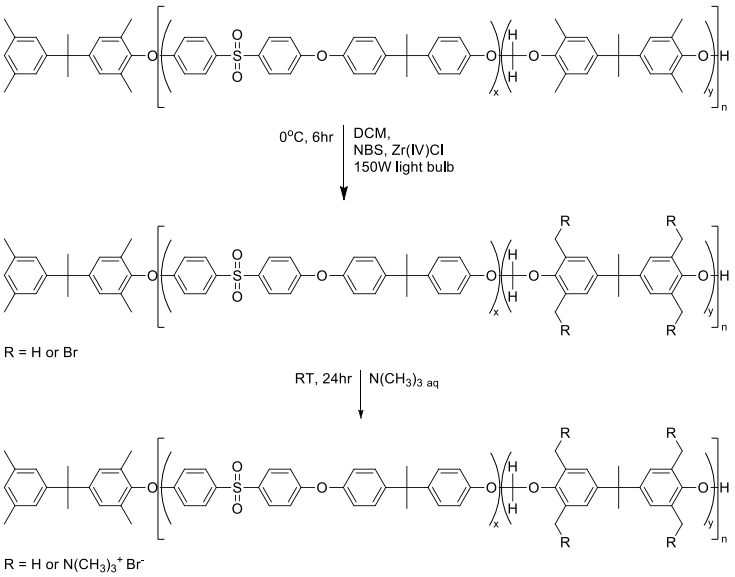

In order for the multiblock polymers to be successfully functionalized as benzyltrimethylammonium (BTMA) species for anionic conductivity, the benzylmethyl groups of the polyformal blocks were halogenated for later substitution. The synthetic method for brominating the benzylic position on the polyformal repeat units was adapted from the literature(15). It was observed that using more common conditions i.e. elevated temperatures and radical initiators, the result was much less selective and ultimately destructive to the polymer backbone. The method used in this study, allows for the bromination at low temperatures with conversion of up to 3.8 bromomethyl groups per repeat unit.

Table 7. Multiblock Bromination Conversion

Sample ID	**Bromomethyl Groups per PF Repeat Unit**[a]	**Degree of Functionality**[b]
PSF2.5PF20	3.82	0.74
PSF2.5PF30	3.52	0.95
PSF2.5PF40	2.49	0.82
PSF5.0PF20	3.14	0.56
PSF5.0PF30	3.22	0.87
PSF5.0PF40	2.56	0.86
PSF7.25PF20	3.23	0.61
PSF7.25PF30	2.63	0.69
PSF7.25PF40	3.04	1.02

[a] Calculated from the ^{1}H NMR spectra. [b] Degree of functionality is defined as the average number of bromomethyl groups per total number of repeat units.

The final conversion of the brominated materials to benzyltrimethylammonium groups was completed in a two step process. First, the soluble brominated polymers were drop cast from 1,1,2,2-tetrachloroethane onto a glass substrate. After complete removal of solvent, the films were suspended in aqueous trimethylamine for 24 hs to complete the

conversion. The brominated films generally were tough, flexible, creasable, and transparent, and upon amination, the material properties remained similar.

Table 8. Membrane Water Uptake and Hydroxide Conductivity

Sample ID	Water Uptake %[a]	λ[b]	Theoretical IEC	IEC[c]	Conductivity / mS cm^{-1} [d]
PSF2.5PF20	10.1	4.3	1.54	1.32	21.0
PSF2.5PF30	45.6	17.1	1.93	1.48	43.5
PSF2.5PF40	23.9	11.8	1.75	1.12	25.0
PSF5.0PF20	4.0	2.2	1.20	1.01	9.3
PSF5.0PF30	8.2	3.2	1.80	1.43	21.7
PSF5.0PF40	16.2	5.7	1.81	1.57	39.0
PSF7.25PF20	6.5	3.6	1.29	0.99	22.7
PSF7.25PF30	10.5	4.6	1.48	1.25	19.5
PSF7.25PF40	14.7	5.6	2.09	1.45	27.3

[a] Calculated form the formula ($mass_{wet}$ − $mass_{dry}$)/$mass_{wet}$ x 100. [b] Calculated from (WU/$mass_{H20}$)x(1000/IEC). [c] Calculated from the titration of chloride. [d] Completed in 18 MΩ water at room temperature.

Membranes were characterized to determine water uptake, ion exchange capacity (IEC) and hydroxide conductivity. The water uptake values for each membrane were quite low, ranging from 4% to a maximum at 45%. The IEC of each membrane was determined to be approximately 20 to 30% lower than the theoretical value calculated from the ^{1}H NMR spectra in the bromomethyl form, indicating that the heterogeneous amination of the membranes is not a complete conversion.

Hydroxide conductivity was measured in high resistivity water at room temperature. The results of three measurements were averaged and are tabulated above. Comparing the IEC values to the conductivity shows that the conductivity increases with increasing IEC value with the exception of the PSF5.0PFXX series. This series of materials had less predictable bromination; therefore, their corresponding IEC and conductivity values did not follow the expected trend. However, all of the conductivity data supported a direct relationship between the degree of functionality and the conductivity, thus as the clustering of BTMA groups increased the conductivity followed.

The hydroxide conductivities and the excellent mechanical properties of the polyformal materials warrant further studies. The materials can be readily produced in large quantities and processing studies are being conducted while research is continuing toward maximizing properties and studying the effect of the block composition.

3.6 Polyisoprene Block Polymers

We present a versatile synthetic approach to obtain solvent processable, crosslinkable copolymers that form robust membranes suitable to use as anion exchange membranes (AEMs). Vinylbenzyl chloride (VBCl), and isoprene were used as building blocks to synthesize polyisoprene-*ran*-poly(vinylbenzyl chloride) (PI-*ran*-PVBCl) copolymers Robust, flexible and ion conducting membranes were obtained through a simple thermal

treatment without addition of any extra crosslinkers. The conductivity properties of the resulting membranes were investigated by impedance spectroscopy. Small angle X-Ray scattering (SAXS) experiments under controlled humidity and temperature was employed to correlate morphology with conductivity properties.

Random copolymers of isoprene and vinylbenzyl chloride (VBCl) were synthesized via nitroxide mediated polymerization, a versatile synthetic technique suitable for polymerization of a wide range of monomers. The versatility of this synthetic technique allowed synthesis of a series of copolymers with varying copolymer compositions through bulk polymerization of isoprene and VBCl monomers. Desired copolymer compositions were achieved by tuning the monomer ratio in the copolymerization reaction. Copolymer compositions were determined from ^{1}H - NMR by comparing the corresponding chemical shifts for allylic protons of isoprene units and benzylic protons of VBCl units: δ 4.7 - 6.0 ppm and at δ 4.5 ppm, respectively. The random character of the PI-*ran*-PVBCl copolymers was confirmed from the matching values of copolymer composition and monomer feed ratio. Reactivity ratios of isoprene and VBCl (1.30 and 0.75, respectively) analyzed from their Q-e values support this result ([xxxv]). A broad dispersity is indicative of possible chain transfer reactions during polymerization, and has also been observed for homopolymerization of isoprene under similar temperature and reaction time conditions ([xxxvi]). Despite their broad dispersity the isolated polymers were soluble in organic solvents. These copolymers were designed to form a covalently crosslinked network structures; therefore, for the purposes of this work a well-controlled molecular weight is not crucial.

Through a simple quaternization reaction of the copolymers in aqueous trimethylamine (TMA) solution, benzyl chloride units were converted to benzyltrimethylammonium (BTMA) cations, with chloride as the counter ion, with a range of ion exchange capacitiesbetween 0.77 and 2.34 mmol/g . Quantitative conversion to BTMA was confirmed by FTIR spectroscopy by monitoring the complete disappearance of the carbon chloride bond vibration band at 1260 cm^{-1}. A qualitative confirmation of complete quaternization is the change in solubility properties of the copolymers. During the quaternization process water insoluble PI-*ran*-PVBCl copolymers became water soluble polyisoprene-*ran*-poly(vinyl benzyl trimethylammonium chloride) (PI-*ran*-P[VBTMA][Cl]) copolymers. This is a strong indication of formation of a hydrophilic polycation. Besides being soluble in water, all of the quaternized copolymers showed excellent solubility in methanol, regardless of their IECs, providing solvent processability and ease of membrane fabrication.

In present work, we have demonstrated the transport behaviors of the AEMs with different IECs and crosslink densities including water diffusion coefficients and anion exchange constants by using time-resolved FTIR-ATR spectroscopy. The data quantitatively show the water diffusion coefficient increases with increasing IEC and decreasing crosslink density. The transport properties are similar to that of Nafion™. The water diffusivities in terms of the hydration level have also been obtained. The results suggest the diffusion coefficient increases with increasing water content. Finally, the transportation of various single anions and mixed anionic pairs within these AEMs were

performed. The ranking of ion transport rate for a series of different anions is NO_3^- > BF_4^- > CO_3^{2-} ≈ HCO_3^-. Therefore, within these cross-linked membranes we have explored fundamental transport properties in real-time enabling the investigation of the water and anion transport mechanisms in AEMs and the correlation of property- to-structure relationships. From these results we are able to have a better understanding on how to further design AEMs access desired optimum performances for AAEMFCs.

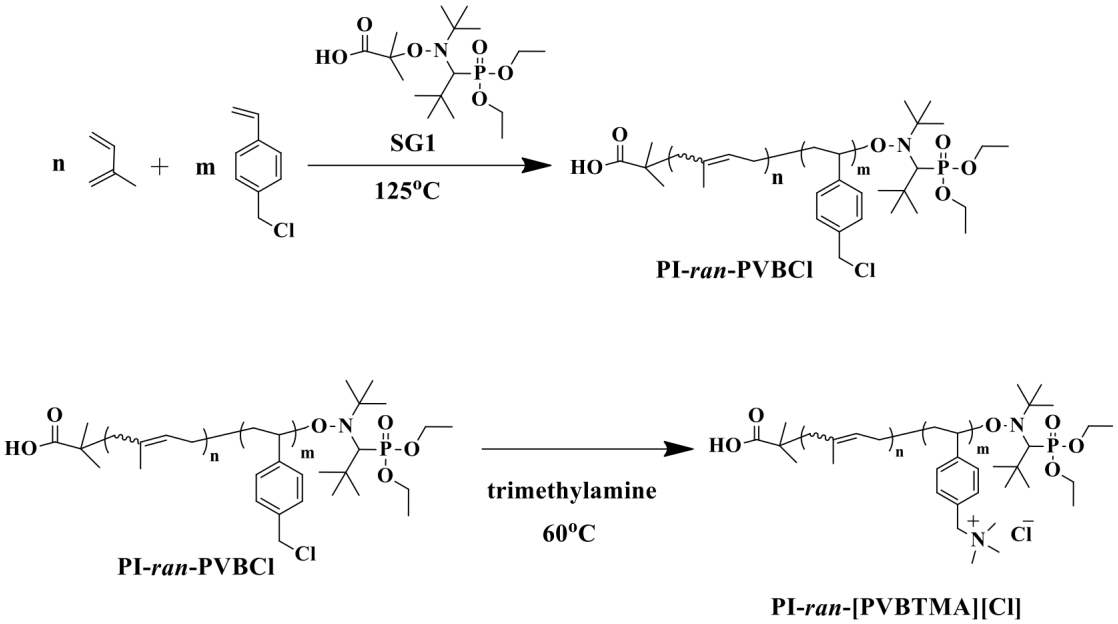

Scheme 5. Polymerization of PI-*ran*-PVBCl (Top), quaternization to PI-*ran*-P[VBTMA][Cl] (bottom)

3.7 Random Co-polymers with isoprene

Our focus is to have a fundamental understanding of ion transport through polymeric media. By designing novel polymers, polymer architectures and monomers, we are developing a better understanding of structure-property relationships, such as the effect of morphology on ion conductivity or the effect of molecular design on alkaline stability. In the recent period of MURI funding we have investigated UV cross-linked anion exchange membranes from solvent processable isoprene containing ionomers.

A series of precursor copolymers poly(isoprene-*random*-vinylbenzyl chloride) (PI-*ran*-PVBCl) was prepared through nitroxide mediated polymerization (NMP) of isoprene and 4-vinylbenzyl chloride (VBCl), as reported previously (Scheme 1). The ratio of the two monomers during the polymerization reaction dictated the final copolymer ratio. The copolymer compositions were determined by analyzing the ^{1}H-NMR spectra comparing the corresponding peak areas for vinylic protons of isoprene and benzylic protons of VBCl. A series of materials were synthesized with varying isoprene to VBCl ratio (Table 1).

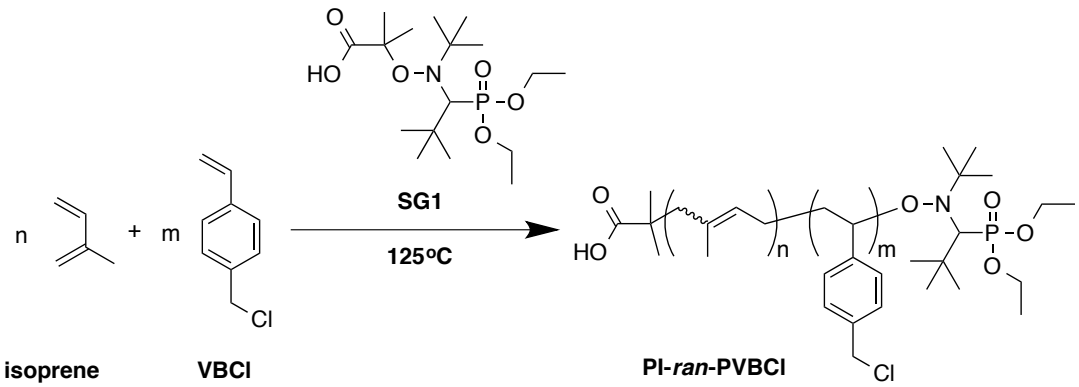

Scheme 6: Polymerization of isoprene and VBCl via nitroxide mediated polymerization to form PI-*ran*-PVBCl .

Table 9 Series of PI-*ran*-PVBCl copolymers, their average molecular weight, dispersity and copolymer compositions, IEC or PI-*ran*-[PVBTMA][Cl]-x after quaternization

Sample	**PI-*ran*-PVBCl**				**PI-*ran*-P[VBTMA][Cl]**
PI-*ran*-[PVBTMA][Cl]-x	**$M_{n,GPC}$[a] (kg/mol)**	***Đ***	**f_{VBCl}[b] NMR(%)**	**f_{VBCl}[c] feed(%)**	**IEC[d] (mmol/g)**
PI-*ran*-[PVBTMA][Cl] 1.37	115	2.91	10.5	11.5	1.36
PI-*ran*-[PVBTMA][Cl] 1.68	55.1	3.10	15.0	15.1	1.68
PI-*ran*-[PVBTMA][Cl] 2.15	69.1	2.83	21.2	25.5	2.15
PI-*ran*-[PVBTMA][Cl] 2.29	68.3	3.57	23.2	26.2	2.29
PI-*ran*-[PVBTMA][Cl] 3.11	68.8	2.89	38.1	40.0	3.11

[a]M_n and *Đ* of PI-*ran*-PVBCl were measured by GPC with respect to narrow linear PS standards. [b]Mole percent of VBCl as analyzed by ^{1}H NMR. [c]Mole percent of VBCl in the monomer feed . [d]IEC of copolymers prior to cross-linking was calculated based on the mole percent of VBCl as analyzed by ^{1}H NMR.

Isoprene tends to isomerize during NMP forming three types of isomers: 1,4-addition, 1,2-addition, 3,4-addition, where 1,4-addition is the dominant isomer. Relative ratios of each isomer can be estimated from ^{1}H-NMR by analyzing the vinyl proton signals. A representative ^{1}H-NMR is shown in Figure 2. Signals δ 4.5-6 ppm are assigned to the vinyl protons of isoprene: The intense peak of the dominant isomer (1,4-addition) overlaps with the peaks of two germinal protons of 1,2-addition (δ 4.75–5.55 ppm), while the single proton of 1,2-addition is observed around δ 5.5 - 5.9 ppm. Protons of 3.4-addition give peaks around δ 4.55–4.75 ppm. For the series of PI-*ran*-PVBCl copolymers listed in Table 1, the relative mole ratios of 1,4-, 1,2- and 3,4-additions were found to be around 90%, 4%, and 6%, respectively.

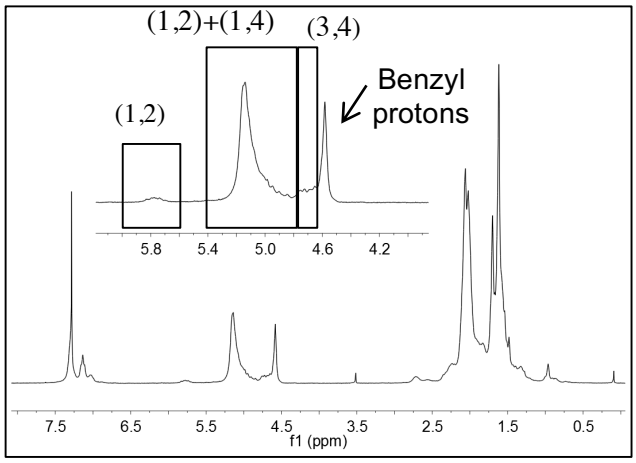

Figure 44: ^{1}H NMR spectrum of PI-*ran*-PVBCl copolymer in $CDCl_3$. Inset is enlarged vinyl proton region of isoprene with regions assigned to corresponding chemical shifts of isomer.

The functional PI-*ran*-PVBCl precursors were quaternized through substitution of benzyl chloride groups by trimethylamine (TMA) to obtain benzyltrimethylammonium (BTMA) cations (Scheme 2). Nearly quantitative quaternization of the functional polymer precursors were confirmed by FT-IR analysis. Upon quaternization water and methanol soluble PI-*ran*-P[VBTMA][Cl] ionomers with moderate to high ion exchange capacities (IECs) were achieved. IEC is dependent on the number of ionic groups. Therefore, theoretical IEC values of the synthesized ionomers can easily be calculated using the copolymer ratios of the corresponding neutral precursors (Table 2).

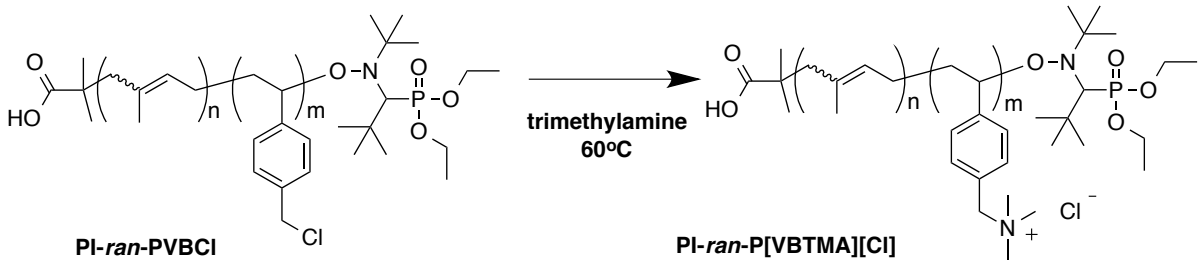

Scheme 7: Quaternization of PI-*ran*-PVBCl to form PI-*ran*-P[VBTMA][Cl] ionomers

Membranes were prepared as drop-cast films from methanol solutions of the ionomers including dithiol cross-linkers and photoinitiator. Dithiol cross-linkers were used to perform thiol-ene chemistry on the double bonds of the isoprene units to render water insoluble robust membranes. It has been reported that the reactivity of the alkenes towards thiol-ene reaction is inversely proportional to the extent of substitution. Using this strategy, two separate sets of membranes were prepared by using two different dithiol cross-linkers with similar molecular weight: 1,10-decanedithiol (DT) and 2,2'-(ethylenedioxy)diethanethiol (EDDT) (Scheme 3). While DT has an intrinsic hydrophobic character due to its aliphatic hydrocarbon structure, two oxygen atoms of EDDT impart slight hydrophilic character to the molecule.

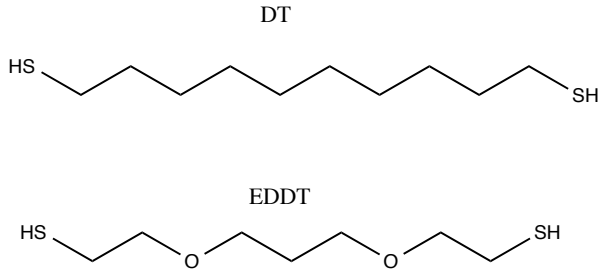

Scheme 8: Chemical structures of 1,10-decanedithiol (DT) and 2,2'-(ethylenedioxy)diethanethiol (EDDT)

The final IEC capacity of the membranes will be lower than their corresponding precursor ionomers, due to increasing total mass of the network by addition of the cross-linkers. Normalized IEC of each membrane was calculated using the IEC of the ionomer and the total mass of the ionomer and the dithiol cross-linker used. The normalized IECs of the membranes were confirmed by Mohr titration. Matching values of the normalized IEC and the titration results qualitatively confirmed efficient cross-linking (Table 3). The titrated IEC values are slightly lower than the normalized IEC values, likely due to incomplete ion exchange of chloride ions with nitrate. This would result in lower chloride concentration of the analyte solution, thus a lower IEC than expected.

Characterization of the UV cross-linked membranes

As mentioned earlier, using the series of ionomers synthesized listed in Table 1, two separate series of membranes were prepared using two different dithiol cross-linkers (Scheme 3). The main difference between the two cross-linkers is the slightly more hydrophilic character of EDDT compared to DT. It is known that water plays a major role for ion conducting membranes, as it was shown that the ion conductivity through polymeric media is highly dependent on presence of water in the system. However, water compromises mechanical stability, since water has a plasticizing effect on ion conducting membranes. Especially at high IECs, membranes usually absorb excess water and become very delicate. The two sets of membrane series were studied and compared to understand the effect of water on structure-property relationship. For future discussions DT will be referred to as hydrophobic cross-linker and EDDT as hydrophilic cross-linker. Analogous to that, membranes prepared with DT and EDDT will be referred to as hydrophobic and hydrophilic membranes, respectively.

Table 10: Normalized and titrated IEC values, % water uptake, chloride conductivity, average d-spacing under dry and hydrated environment

PI-*ran*-P[VBTMA][Cl]-x	Cross-linker	IEC_{Norm}	IEC_{tit}	w.u.[a] (%)		$\sigma_{b\ 60^oC}$ (mS/cm)	$\sigma_{b\ 90^oC}$ (mS/cm)	d_{dry} [c] (nm)	d_{wet} [d] (nm)
PI-*ran*-P[VBTMA][Cl] 1.37	DT	0.79	0.66	15.2	10.7	3.3	9.6	4.8	5.0
PI-*ran*-P[VBTMA][Cl] 1.68	DT	1.09	0.96	20.8	10.6	7.2	15.3	4.8	5.2
PI-*ran*-P[VBTMA][Cl] 2.15	DT	1.47	1.38	39.6	15.0	6.8	15.9	5.1	5.4
PI-*ran*-P[VBTMA][Cl] 2.29	DT	1.60	1.50	56.7	19.7	10.2	21.1	4.7	4.9

PI-*ran*-P[VBTMA][Cl] 3.11	DT	2.38	2.19	335	78.2	17.2	33.7	3.8	4.4
PI-*ran*-P[VBTMA][Cl] 1.37	EDDT	0.83	0.70	25.0	16.8	5.1	13.0	4.0	4.6
PI-*ran*-P[VBTMA][Cl] 1.68	EDDT	1.13	0.88	38.0	18.7	8.2	15.8	3.7	4.8
PI-*ran*-P[VBTMA][Cl] 2.15	EDDT	1.53	1.42	67.3	24.4	19.6	37.1	3.6	NA
PI-*ran*-P[VBTMA][Cl] 2.29	EDDT	1.66	1.48	115	38.5	7.1	11.1	5.4	5.5
PI-*ran*-P[VBTMA][Cl] 3.11	EDDT	2.45	2.28	437	99.0	n.d.	n.d.	3.4	NA

[a] Water uptake [b] Conductivity measurements are collected at 95% relative humidity [c]Average distance between ionic clusters as determined from SAXS at 60 ^{o}C at dry conditions [d]Average distance between ionic clusters as determined from SAXS at 60 ^{o}C at 95% relative humidity

Water Uptake

Water uptake properties of both series of membranes were investigated. Both of the series of membranes showed low to moderate water uptake and lambda values for IECs between 0.8 – 1.5 mmol\g and moderate to high water uptake at higher IECs. (Table 2, Figure 45) Membranes prepared with the hydrophobic cross-linker (DT) had water uptake values around 15-57 wt% for IECs below 1.6 mmol/g, that corresponds to 10-20 water molecules per cation. Excessive water uptake at the highest IEC limit (2.4 mmol/g) resulted a water uptake as high as 335 wt%.

Membranes with hydrophilic cross-linker (EDDT) showed a similar trend of water uptake as the membranes with hydrophobic cross-linker: moderate to high water uptake for membranes with IEC below 1.66 mmol/g, and excessive water uptake for the highest IEC (2.45 mmol/g) membrane. They showed comparably higher water absorbtion than the membranes with hydrophobic cross-linker at similar IECs. Overall, the water uptake values were 1.5 – 2 times higher compared to the membranes cross-linked with DT. For example, membranes with EDDT with IEC around 1 mmol/g absorbed water almost twice as much than the membranes with DT. This trend was observed for almost all other IECs. This difference of the water uptake profiles of the two series of membranes confirmed the increase in hydrophilic character of the membranes by incorporation of electron-rich oxygen atoms to the polymer network.

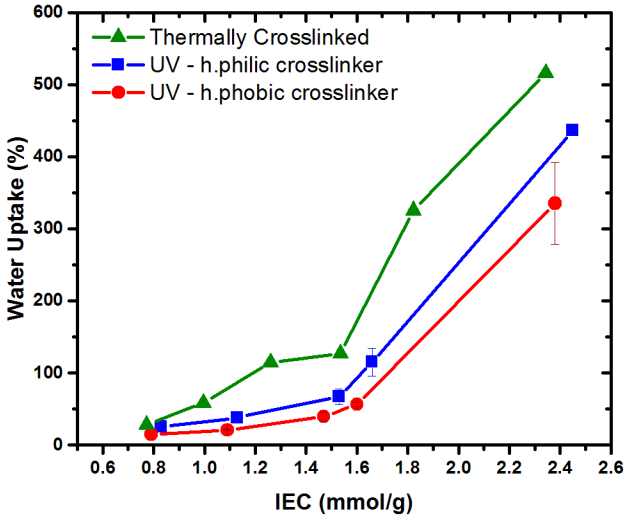

Figure 45: Water Uptake profile of thermally cross-linked (triangles) and UV cross-linked hydrophilic (squares) and hydrophobic (circles) membranes. Lines are drawn as a guide to the eye.

In both of the series the highest IEC membranes (2.4 mmol/g) experienced excessive water uptake. Precursors for the highest IEC membranes are composed of around 60 mol% isoprene and 40 mol% VBTMA. Considering that the cross-linkable units consist of only 8 – 10 mol% of the hydrophobic units, the cross-link density would presumably be not sufficient to prevent extreme water absorbtion. At this IEC, hydrophilic membrane swelled comparably more than the hydrophobic membrane. While the hydrophobic membrane maintained its integrity, the hydrophilic membrane was soft and fragile, such that it was hard to grip the membrane. This is presumably due to incorporation of absorbed water into the cross-linked network. In other words, water was not only absorbed by the highly hygroscopic BTMA cations, but also by the hydrophilic EDDT, that forms the cross-linked network together with isoprene. Therefore, the absorbed water will diffuse into the cross-linked network. Due to plasticizing effect of water on the cross-linked network, delicate membranes were obtained. Thus, where water goes is as important as how much water is absorbed.

Ion Conductivity

Ion conductivity of the UV cross-linked membranes was studied under humidity and temperature controlled environment. Chloride ion conductivities were measured at 95% relative humidity. Conductivity values at 60 and 90 ^{o}C are reported in Table 2 and Figure 6.

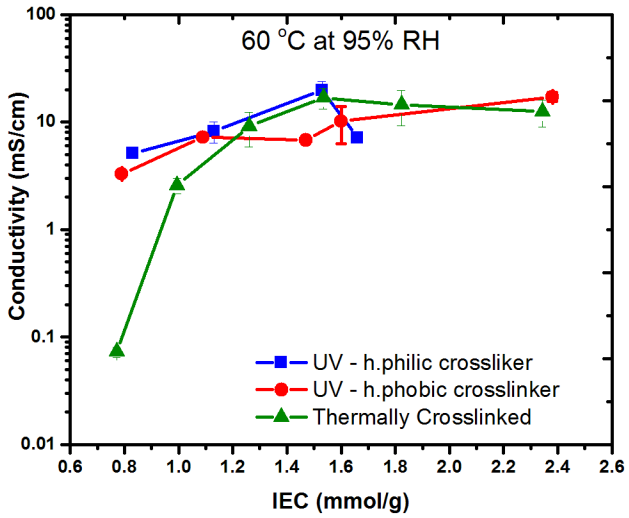

Figure 46: Ion conductivities of thermally cross-linked (triangles) and UV cross-linked hydrophilic (squares) and hydrophobic (circles) membranes. Lines connect data points as a guide to the eye.

Hydrophobic membranes showed a monotonic increase of conductivity with increasing IEC. Conductivity values stayed within two orders of magnitude for the studied IEC range. Highest conductivity was achieved from the highest IEC membrane (IEC 2.38 mmol/g). At 90 °C chloride ion conductivities as high as 33.7 mS/cm was observed. While the conductivity values stayed within two orders of magnitude, nearly five-fold increase was observed as IEC was increased from lowest to highest IEC (Table 2).

Conductivity of the hydrophilic membranes increased gradually until IEC reached 1.5 mmol/g, where the highest conductivity was reached (19.6 mS/cm at 60°C, 37.1 mS/cm at 90°C,95% RH). A substantial decrease in conductivity is observed beyond this IEC limit. Conductivity values collected for the membrane with IEC 1.66 mmol/g was almost as low as the lowest IEC (0.83 mmol/g) membrane. For the highest IEC membrane, data collection was not possible due to fragile nature of the membrane. This is presumably due to the fragile character of these membranes at this high IEC values, as explained previously. Especially the highest IEC membrane became very soft upon immersion to water such that the membrane was not easy to grip and mount to the instrument. Thus, data collection was difficult, and impossible for the highest IEC membrane.

For the range of IECs around 1.5 mmol/g and below, hydrophilic membranes show slightly higher conductivity values than their hydrophobic analogues. Hydrophilic membranes reached their highest conductivities at IEC 1.53 mmol/g, while the hydrophobic membranes showed two to three times lower conductivity values at an equivalent IEC (1.47 mmol/g). This difference is likely due to higher water uptake of hydrophilic membranes, as well as due to more uniform distribution of water within the membrane. Water has a profound effect on ion conductivity through polymeric medium, as water provides the necessary environment to render ion transport. As discussed earlier, absorbed water molecules are drawn into the cross-linked network by the hydrophilic EDDT cross-linker. Thus, the water molecules presumably are not localized around BTMA moieties, as it would be the case in hydrophobic membranes, where the hydrophobic cross-linked network would likely repel water. Therefore, ions can be

transferred easily between BTMA moieties via delocalized aqueous medium. Hydrophobic membranes showed as high conductivities as the hydrophilic membranes only at their highest IEC limit (2.38 mmol/g). While this could be explained by increasing water uptake, thus lambda values, with increasing ion content, the amount of water molecules ($\lambda = 78$) to render this conductivity is much higher than it is for the hydrophilic membrane at IEC 1.47 mmol/g ($\lambda = 24$). When hydrophobic membranes absorbed similar amount of water (IEC 1.6 mmol/g, $\lambda = 19.7$) to hydrophilic membranes at IEC 1.47 mmol/g, the obtained conductivity values were still lower than the hydrophilic membranes, despite the higher IEC.

It was found that the diffusion coefficient of the conducting ion approximates its dilute solution diffusivity limit, when ion conducting membranes are sufficiently hydrated. It is also known that conductivity is a function of diffusion coefficient, and they are directly proportional. Therefore, it would be not possible to increase the conductivity further by increasing the IEC, once the dilute solution conditions are reached. The conductivity of the hydrophobic membranes at the highest IEC is presumably collected at the dilute solution conditions, and thus highest conductivity possible was observed at this IEC.

While these observations emphasize the role of water present in ion conducting membranes, it also shows that the distribution of water within the membrane plays a critical role for efficient ion transport through polymeric medium. However, excess water absorption is not desirable to not to loose mechanical stability.

Morphology

Morphology of the UV cross-linked hydrophobic and hydrophilic membranes were investigated with small angle X-Ray scattering (SAXS) under environmentally controlled conditions. Figure 7 and Figure 8 show the SAXS scattering patterns of the UV cross-linked hydrophilic and hydrophobic membranes, respectively, at 60^{o}C under dry and 95% relative humidity conditions. Membranes in both of the series showed a scattering peak around 0.1 – 0.2 Å^{-1} reminiscent of the ionomer peak of hydrated Nafion®. The electron density contrast is rendered by the chloride ions. Therefore, these scattering peaks were attributed to phase separation of BTMA cations presumably to form ion clusters.

When dry, hydrophobic membranes showed an average d-spacing between ion clusters in the range of 3.8-5.1 nm. Lack of scattering at lower scattering angles is somewhat unexpected and indicates lack of scattering for larger features. Smallest average d-spacing was observed from the highest IEC membrane, as an expected result of high BTMA concentration of the precursor copolymer. The precursor copolymer for this membrane has the highest BTMA concentration, thus the average distance between the clusters would be the closest. Unexpectedly, the largest average d-spacing was observed from the membrane with IEC 1.47 mmol/g.

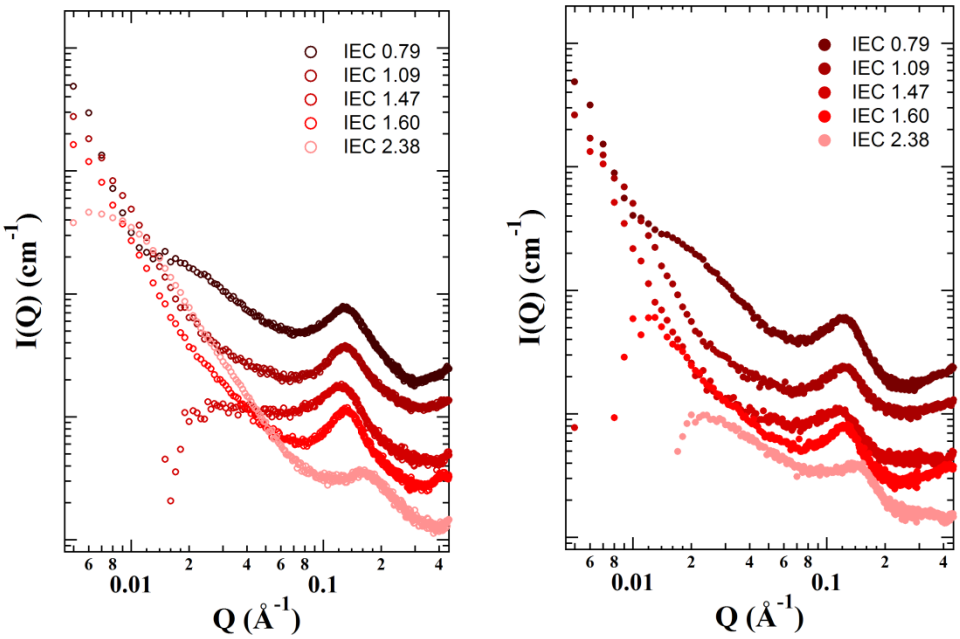

Figure 47: SAXS data for UV cross-linked PI-*ran*-P[VBTMA][Cl] hydrophobic membranes at dry (left) and 95% RH (right) environment. Spectra are offset on y-axis for clarity.

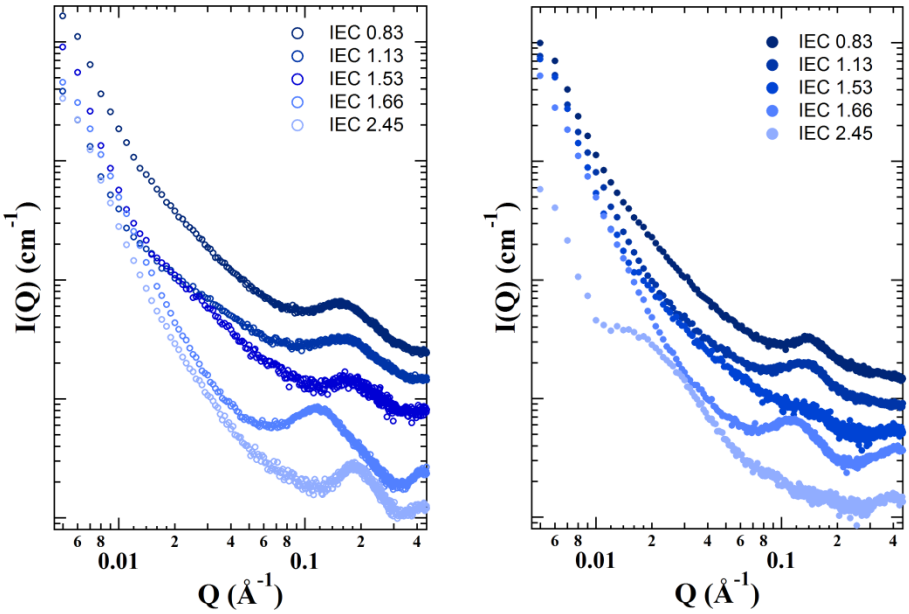

Figure 48: SAXS data for UV cross-linked PI-*ran*-P[VBTMA][Cl] hydrophilic membranes at dry (left) and 95% RH (right) environment. Spectra are offset on y-axis for clarity.

When hydrated a slight shift of the scattering peaks toward higher scattering angles was observed, indicative of the swelling of the membranes as the hygroscopic ion clusters absorb water. The change in average d-spacing is most pronounced for the highest IEC membrane. This is presumably due to high water uptake of the membrane at this high IEC, as well as the reduced volume fraction of the cross-linked network, thus reduced support surrounding the ionic clusters.

The peak intensities and peak width at full width half maximum stay rather similar upon hydration. This indicates that the ion clusters do not undergo a significant rearrangement to form well-defined clusters. Freedom of the ion clusters are presumably restricted by the well cross-linked hydrophobic matrix around them. Therefore, swelling of the clusters and thus the membranes are limited.

When dry, d-spacing of hydrophilic membranes decreased with increasing IEC, with the exception of the membrane with IEC 1.66 mmol/g. This decrease of d-spacing is an expected result of increased ion concentration, and it was observed previously for the thermally cross-linked membranes prepared using similar ionomers. The unexpected large d-spacing of the membrane with IEC 1.66 mmol/g is not clear.

As the relative humidity is increased to 95%, a shift of the scattering peak towards lower scattering angles was observed, similar to the hydrophobic membranes. This shift was more pronounced compared to the hydrophobic membranes, indicating that hydrophilic membranes swelled more than the hydrophobic membranes, presumably due to higher water uptake of the hydrophilic membranes. Peak intensity of the membranes decreased remarkably after hydration. Scattering of the membranes with IECs 1.53 mmol/g and 2.45 mmol/g disappeared almost completely upon hydration. The shoulder at lower scattering angles obtained from the membrane with IEC 2.45 mmol/g suggested formation of a large-scale phase separation. Absence of scattering peaks indicates uniform distribution of chloride ions within the hydrated membranes. This is presumably due to the hydrophilic character of the EDDT cross-linker, by which the water molecules are drawn toward the cross-linked network surrounding the ion clusters. Thus, dissociated chloride ions can diffuse out from the ion clusters into the cross-linked network. This also explains decreasing intensity of scattering peaks with increased water content in the membrane.

Correlation of Morphology with Ion Conductivity

In our previous discussion we found a strong correlation between morphology and ion conductivity of the thermally cross-linked PI-*ran*-P[VBTMA][Cl] membranes. It was shown that ion conductivity was greatly enhanced when the average d-spacing between ionic clusters was below a critical distance. This distance was found to be around 5 – 5.6 nm for hydrated membranes. For both of the UV cross-linked membrane series the average d-spacing was found to be below 5.4 nm when hydrated (Table 2). Conductivity and SAXS measurements were performed under similar environmental conditions. As it was discussed before, the highest conductivity of the hydrophilic membranes series was measured at IEC 1.54 mmol/g, while hydrophobic membranes exhibited almost 3 times less conductivity at a similar IEC. This difference was attributed to a uniform distribution of water molecules within hydrophilic membranes. At this IEC scattering peak was absent for the hydrated hydrophilic membranes, while hydrophobic membranes at similar IEC showed a peak corresponding to an average d-spacing around 5.4 nm. This observation implies uniform distribution of chloride ions through the membrane, thus supports uniform distribution of water molecules in the hydrated membrane. This is a very important information as it suggests that absence of an ion cluster, thus a homogenous distribution of conducting ions, improves ion conductivity. Beers and Balsara hypothesized that ion clusters obstruct ion transport through ion conducting membranes. Their study on ion conducting block copolymers indicated that absence of ion clusters would be an effective way to enhance conductivity of hydrated ionomers.

Cluster-free block copolymers were achieved by confining the conducting block in an average d-spacing less than 12 nm. However, is not easy to achieve robust block copolymer membranes with narrow average d-spacing, since molecular weight is one of the factors that influences extent of phase separation. Our observations showed that a cluster-free hydrated membrane could be achieved through random copolymers by assistance of a hydrophilic non-conducting network surrounding the ionic moieties without sacrificing the necessary high molecular weight to obtain robust membranes.

Comparison of UV cross-linked membranes with their thermally cross-linked equivalents

UV cross-linked membranes were prepared to have a final IEC that would match with the IECs of the thermally cross-linked analogues of these PI-*ran*-P[VBTMA][Cl] ionomers, that were previously prepared by our group. It was observed that at a similar IEC both of the UV cross-linked membrane series absorbed comparably less water then their thermally cross-linked equivalents (Figure 5). While the hydrophilic UV cross-linked membranes absorbed more water than the hydrophobic membranes, their water uptake values were still lower than the thermally cross-linked membranes. Therefore, UV cross-linked membranes swelled comparably less than the thermally cross-linked membranes. These observations suggested that UV cross-linking allowed better control over cross-link density rendering a well-cross-linked network.

It is important to point out that, compared to the thermally cross-linked membranes at their highest IEC, the UV cross-linked hydrophilic membrane at the highest IEC was more fragile despite its lower water uptake value. This is presumably due to plasticizing effect of water that is absorbed by the EDDT units into the cross-linked network, as discussed earlier. This underlines the importance of water management in ion conducting membranes. While water is an important element for efficient ion conductivity, it might not be a desired component for the non-ionic network to sustain robustness of the membrane. Also, the thermally cross-linked membrane was formed from a PI-*ran*-P[VBTMA][Cl] with 24 mol% isoprene, while its UV cross-linked equivalent consists of 38 mol% isoprene. Thus, UV cross-linked membrane contained less available cross-linking sites. This compositional difference might be another reason for the fragile nature of hydrated UV cross-linked hydrophilic membrane.

When ion conductivities were compared**,** the most remarkable difference of the UV cross-linked membranes from their thermally cross-linked analogues is their equivalent or higher conductivity values despite their comparably lower water uptake (Figure 6). Especially at the lowest IEC limit, both hydrophilic and hydrophobic UV cross-linked membranes show almost two orders of magnitude higher conductivities than the thermally cross-linked membrane with IEC 0.77 mmol/g (0.07 mS/cm at 60 ^{o}C, 0.26 mS/cm at 90 ^{o}C). At this IEC thermally cross-linked membranes absorb around 30 wt% water. While the hydrophilic membranes absorb similar amount of water at a similar IEC, hydrophobic membranes still absorb half of the amount of what thermally cross-linked membranes absorb. This observation strongly suggests that efficient ion conductivity cannot only be explained by the extent of water uptake or ion concentration.

SAXS results showed that the average d-spacing values obtained from the UV cross-linked membranes were smaller than those of thermally cross-linked membranes with equivalent IECs. At the lowest IEC hydrated thermally cross-linked membranes had an average d-spacing around 6 nm. Lowest IEC UV cross-linked membranes formed clusters with an average d-spacing 5.0 and 4.6 nm for hydrated hydrophobic and hydrophilic

membranes, respectively. For the thermally cross-linked membranes a critical average d-spacing was suggested, below which a percolated ion network would form. Our findings with the UV cross-linked membranes strongly support this hypothesis. Therefore, large difference between the conductivities of thermally and UV cross-linked membranes can be explained by formation of ion clusters with an average d-spacing around and below 5 nm. This is a very important observation, since it shows that high ion conductivities could be achieved at low IECs if the necessary morphology is achieved. This is especially important to make robust ion conducting membranes, since mechanical properties of hydrated membranes are largely affected by the composition of the membrane and thus absorbed water.

Other important findings of SAXS results are the differences of change in peak intensity and peak position with the change in relative humidity. Scattering peaks of thermally cross-linked membranes became sharper and more intense with inclusion of water, indicating formation of better-defined ion clusters. UV cross-linked membranes, on the other hand, showed a decreased intensity, such that some membranes did not scatter when hydrated. Peak shift of the UV cross-linked membranes was relatively less pronounced compared to thermally cross-linked membranes. This indicates a well-cross-linked network formation for UV-crosslinked membranes with more confined ionic clusters.

Studies at Colorado School of Mines compared thermally and UV crosslinked membranes by studying their mechanical properties. UV cross-linked hydrophobic membranes and two thermally crosslinked membranes were compared (3 hours and 24 hours crosslinked). In general, UV cross-linked membranes showed more strength when hydrated, suggesting that thiol-ene cross-linking was an efficient way of preparing AEMs. With collaboration with Prof. Vito Di Noto from University of Padova Italy broadband electric spectroscopy data is collected. After detailed analysis we are hoping to have a better understanding of ion transport through these UV crosslinked systems.

3.8 Polysulfone Block Polymers

Because of the encouraging results from PPO-*b*-PVBTMAx films, we have extended the research to polysulfone block copolymers to take advantage of the good thermal and mechanical properties and the solubility properties for ease of processing.[xxxvii] In order to have good control over the copolymer synthesis, we synthesized dihydroxy terminated polysulfone (PSf) using excess bisphenol A. As a result, triblock copolymers were synthesized by growing poly(vinyl benzyl chloride) (PVBC) block from both ends of the polysulfone. The PSf-PVBCx polymers were then either solvent cast or melt pressed into films followed by quaternization in aqueous trimethylamine. The following scheme presents the synthetic route for PSf-PVBTMAx triblock copolymers.

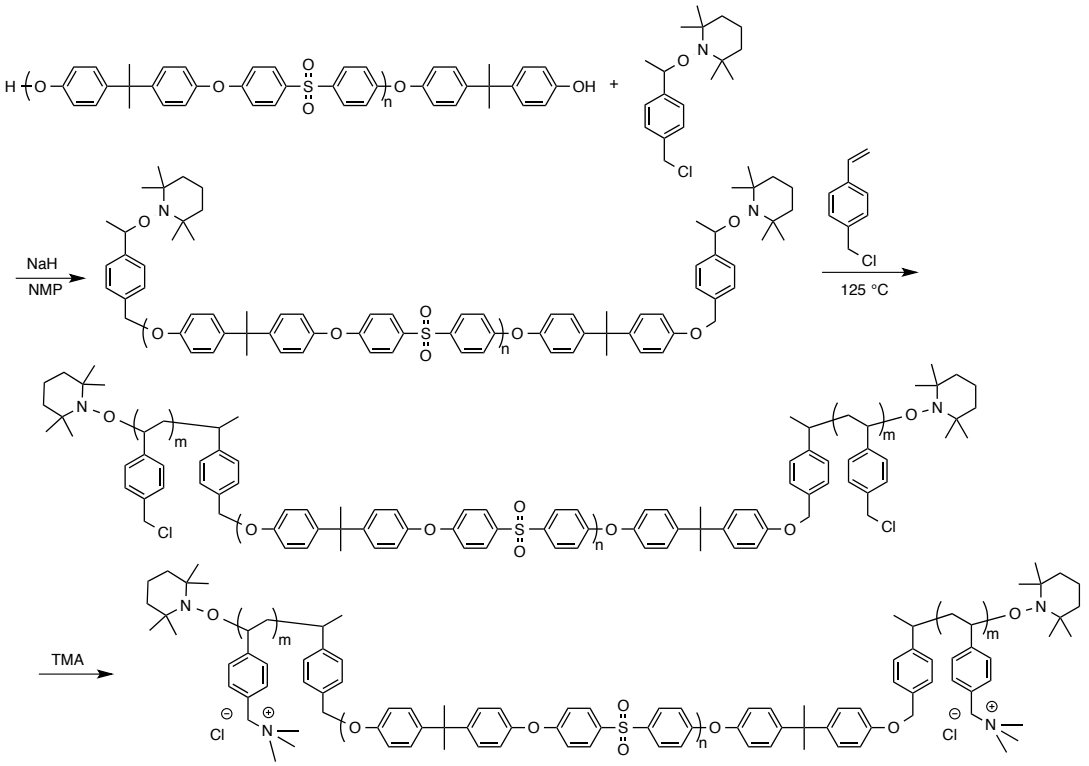

Scheme 9. Synthetic route of PVBTMA-PSf-PVBTMA triblock copolymers

The confirmation of the end capping of polysulfone was conducted by both proton nuclear magnetic resonance (^{1}H NMR) spectroscopy and ultraviolet/visable (UV/Vis) spectroscopy. ^{1}H NMR spectra comparison showed the existence of characteristic peaks from the end-capping agent, alkoxyamine, in the spectrum of end-capped polysulfone. The UV/Vis spectra comparison of the original polysulfone and end-capped polysulfone demonstrates the successful end capping of polysulfone by the absence of phenoxide group absorbance in the range from 310 to 340 nm.[xxxviii]

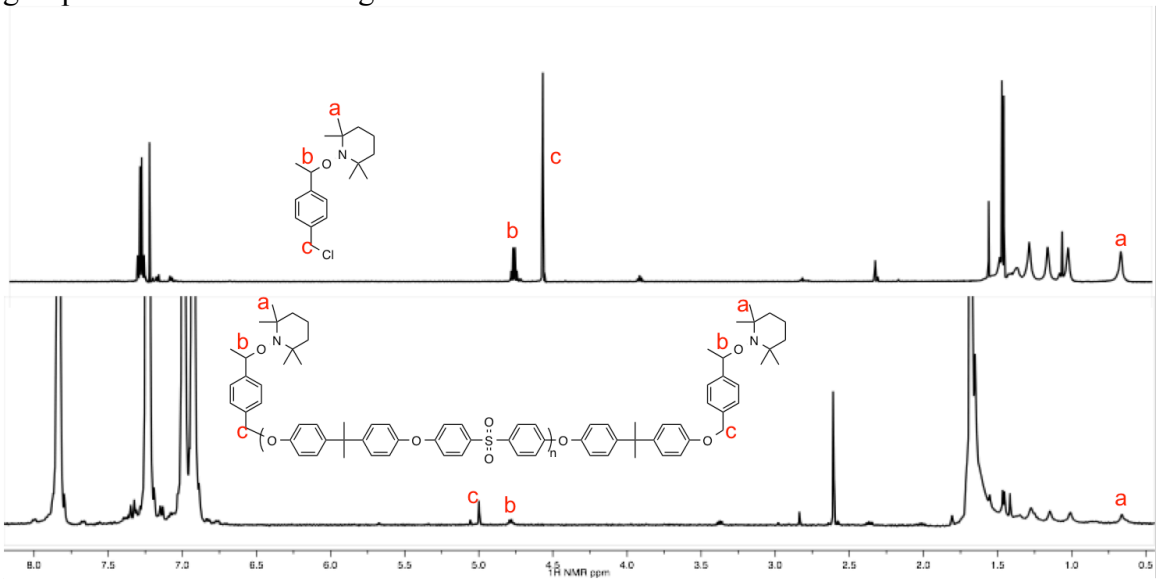

Figure 49. ^{1}H NMR spectra of Cl-BzEt-TEMPO (upper) and end-capped polysulfone (lower) measured in $CDCl_3$.

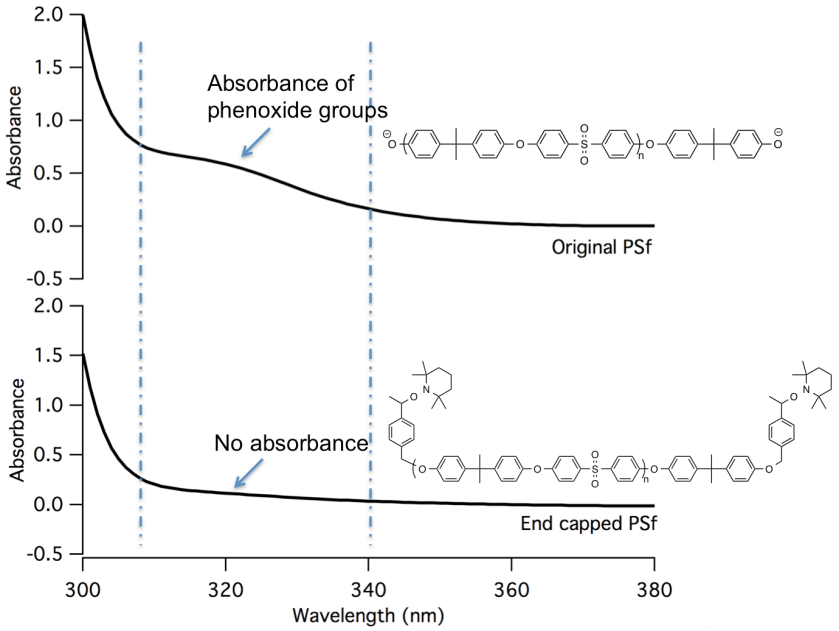

Figure 50. UV-Vis spectra of basified original polysulfone (upper) and end capped polysulfone (lower).

A series of PVBC-PSf-PVBC triblock copolymers were synthesized by initiating PSf-BzEt-TEMPO macroinitiator in vinylbenzyl chloride through nitroxide-mediated polymerization. The PVBC block length was controlled by the reaction time with the polymerization carried out in bulk vinylbenzyl chloride at 125 °C. The figure below displays the GPC traces of the end-capped polysulfone and five PVBC-*b*-PSf-*b*-PVBC triblock copolymers with different PVBC lengths. The block copolymers have shorter retention times compared to the end-capped polysulfone indicating the successful synthesis of the triblock copolymer with higher molecular weight.

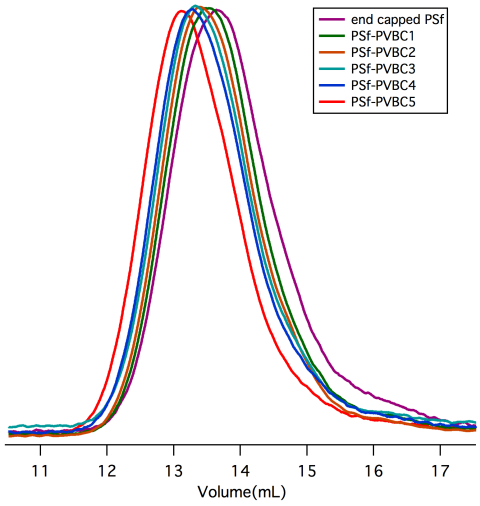

Figure 51. GPC traces of end capped polysulfone and five PVBC-*b*-PSf-*b*-PVBC triblock copolymers.

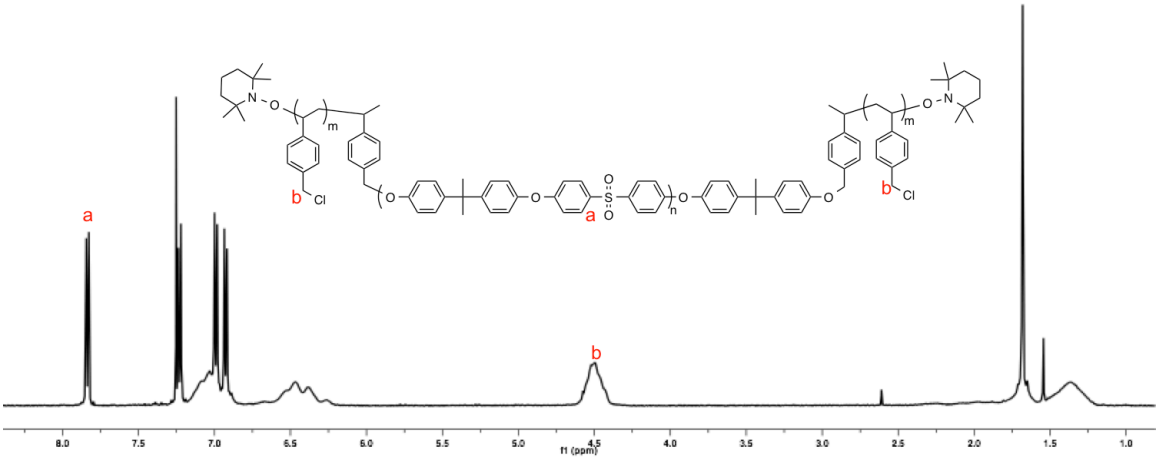

Figure 52. ^{1}H NMR spectrum of PSf-PVBC5 in $CDCl_3$.

The PSf-PVBC copolymers were also characterized by 1H NMR spectroscopy, from which the molecular weight can be calculated based on the distinguishable peaks from each block. The proton NMR spectrum of a representative triblock copolymer, PSf-PVBC5, depicts the characteristic peaks for the polysulfone block and the PVBC block. Peak "a" at chemical shift of 7.8 ppm stems from aromatic protons adjacent to the sulfone groups in the polysulfone block and peak "b" at 4.5 ppm derives from protons on the benzylic carbon in PVBC block. The quantitative ratio of PVBC block to polysulfone block was calculated from the integration of these two peaks. Based on the polysulfone number average molecular weight of 30 kg/mol and the block ratio obtained from NMR spectra, the molecular weight of the PVBC block was calculated. The following table displays the molecular weight of each block copolymer calculated from NMR spectra.

Table 11. Molecular weights of each PSf-PVBC block copolymer based on NMR spectra.

Sample	m : n*a*	Mn (NMR)*b*		*DP*n *b* of PVBC	Weight percentage of PVBC *b* (%)
		Mn of PVBC block (kg/mol)	Mn of PSf-PVBC (kg/mol)		
PSf-PVBC1	1: 1.08	11	41	73	27
PSf-PVBC2	1: 1.64	17	47	111	36
PSf-PVBC3	1: 2.38	25	55	161	45
PSf-PVBC4	1: 2.67	28	58	181	48
PSf-PVBC5	1: 4.08	42	72	276	58

*a*m : n depicts the block ratio of Polysulfone to PVBC. *b*Determined by proton NMR from the integrations of methylgroups of PPO and benzylic methylene groups of PVBC.

The PVBC-PSf-PVBC triblock copolymers were processed into films prior to quaternization through two methods: solvent casting and melt pressing. Solvent cast films were prepared by drop casting 10 wt% polymer in chloroform solution onto clean microscope glass slides. The glass slide was held at room temperature for a couple of hours before drying in a vacuum oven overnight at 50 °C. Melt pressed films were prepared by pressing the copolymer powders into films at 200 °C in a hot press. The press temperature was determined from TGA and DSC measurement shown below, exceeding the *T*gs of both PVBC and polysulfone phase, yet avoiding degradation. The solvent cast and melt pressed films were then immersed in 45 wt% aqueous trimethylamine solution to generate ammonium chloride functionalized films.

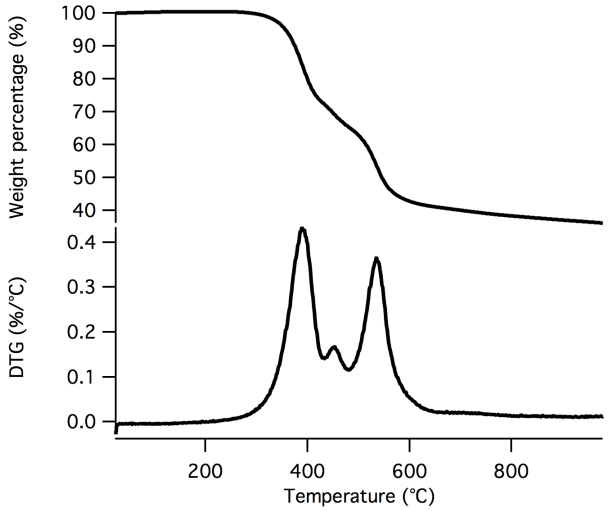

Figure 53. TGA (upper) and DTG (lower) thermograms of PSf-PVBC5 (fPVBC: 58 %) under flowing nitrogen at a heating rate of 10 °C/min.

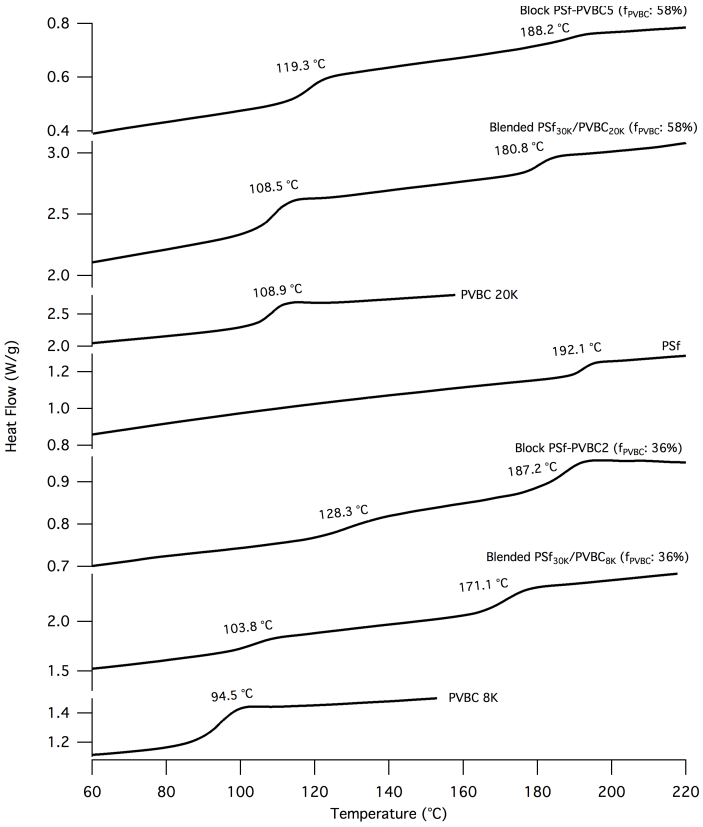

Figure 54. DSC thermograms of block copolymers PSf-PVBC2 and PSf-PVBC5, blended polysulfone and PVBC (8 kg/mol) with 36 % weight percentage of PVBC, blended polysulfone and PVBC (20 kg/mol) with 58 % weight percentage of PVBC, homopolymer PVBC (8 kg/mol), PVBC (20 kg/mol) and homopolymer polysulfone (30 kg/mol).

The differences between solvent cast films and melt pressed films were studied by solubility tests. The results are summarized in the following table. The PSf-PVBC powder and solvent pressed PSf-PVBC films have the same solubility while the melt pressed PSf-PVBC films could not be dissolved in any solvents examine, instead swelling in the solvents that could dissolve PSf-PVBC powder. The insolubility is expected from the crosslinking between benzyl chloride groups and/or the residual TEMPO-functional chain ends during hot pressing.

Table 12. Solubility test to PSf-PVBC powder, the solvent casted PSf-PVBC films and the corresponding PSf-PVBTMA films, melt pressed PSf-PVBC films and the corresponding PSf-PVBTMA films

	$CHCl_3$	1,2-dichloro-benzene	1,1,2,2-tetrachloro-ethane	THF	toluene	DMF	NMP	MeOH	H_2O
PSf-PVBC (powder)	+	+	+	+	+	+	+	–	–
PSf-PVBC films (solvent cast)	+	+	+	+	+	+	+	–	–
PSf-PVBC films (melt press)	–/swell	–/swell	–/swell	–/swell	–/swell	–/swell	–/swell	–	–
PSf-PVBTMA films (solvent cast)	–/swell	–/swell	–/swell	–/swell	–/swell	–/swell	–/swell	–/swell	–/swell
PSf-PVBTMA films (melt press)	–/swell	–/swell	–/swell	–/swell	–/swell	–/swell	–/swell	–/swell	–/swell

Membranes were converted to hydroxide counterion through soaking in aqueous sodium hydroxide solution. The water uptake of the membranes was measured in the hydroxide form at room temperature. The following table summarizes weight percentage of PVBTMA block, water uptake, ion exchange capacity (IEC) and dimensional swelling of the PSf-PVBTMAx films in water at 20 °C. As expected, increasing weight percentage of PVBTMA and concomitant increased IEC values lead to increased water uptake from the higher weight percentage of the hydrophilic PVBTMA blocks. Compared to the water uptake and dimensional swelling for the solvent cast membranes, the melt pressed membranes with the same PSf-PVBC precursor showed slightly lower IEC values and water uptake. The dimensional swelling showed that solvent cast membranes swelled more significant in the through-plane direction, indicating an anisotropic microstructure in the cast membrane, while pressed membranes greatly reduced swelling in this direction and the swelling became more evenly distributed in the three directions, indicating that a more isotropic microstructure dominated in the pressed membrane.

Table 13. Weight Percentage of PVBTMA(OH), IEC, Water Uptake and Dimension Swelling of PSf-PVBTMA Membranes

	Weight percentage of PVBTMA (OH)	IEC (meq/g)a	Melt pressed films						Solvent cast films (cast from chloroform)					
			IEC*b*	Water uptake /%	λc	Length swelling/ %	Width swelling/ %	Thickness swelling/ %	IEC*b*	Water uptake/%	λc	Length swelling/ %	Width swelling/ %	Thickness swelling/ %
PSf-PVBTMA1	32	1.61	1.43	11.9	4.6	0.22	0.65	2.6	1.56	34.8	12.4	1.7	1.9	7.8
PSf-PVBTMA2	42	2.08	1.91	32.1	9.3	7.2	5.8	1.5	2.01	58.1	16.1	5.7	7.2	22.2
PSf-PVBTMA3	50	2.51	2.35	53.3	12.6	15.7	16.2	2.7	2.46	98.2	19.9	10.8	6.1	28.4
PSf-PVBTMA4	54	2.65	2.38	71.5	16.7	14.3	17.6	6	2.53	120.2	26.4	11.2	11.8	36.9
PSf-PVBTMA5	64	3.12	2.87	125.2	24.2	30.5	27.4	10.6	3.02	238.1	43.8	11.9	12.4	123

The SAXS data at 60 °C for both cast and pressed membranes of PSf-PVBTMAx was investigated under dry and 95 % RH conditions. The following figure depicts the SAXS profiles for PSf-PVBTMA1 membranes prepared from solvent casting (a) and melt pressing (b). PSf-PVBTMA1 was chosen as a representative case to compare the SAXS pattern for cast membranes and pressed membranes. The cast membrane PSf-PVBTMA1 showed a strong scattering peak at 0.014 $Å^{-1}$ under dry condition, corresponding to a domain spacing of 44.8 nm. Under 95% RH the cast membrane PSf-PVBTMA1 showed a peak at 0.011 $Å^{-1}$ matching with a domain spacing of 57.1 nm. The shift of the scattering peak to lower angle at higher humidity indicates the ionic domain expansion after water absorption. A single scattering peak suggests the presence of periodic but lack of long range ordering within the membrane. Another diffuse scattering peak at 0.032 $Å^{-1}$ only appeared under wet conditions but not dry conditions.

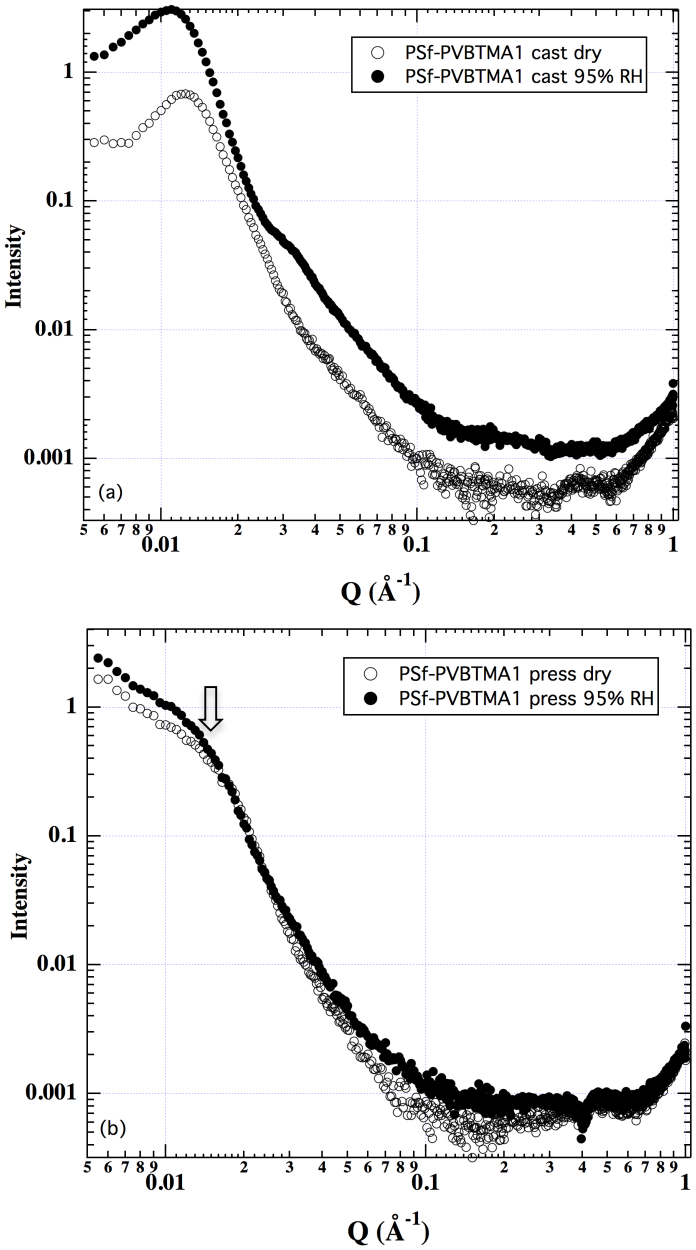

Figure 55. SAXS profiles of PSf-PVBTMA1 membrane (a) in chloride form prepared from cast PSf-PVBC1 film(a) and pressed PSf-PVBC1 film (b). The open dots stand for dry membrane at 0 % RH and the solid circles represent the humidified membrane at 95 % RH.

The following figure displays the ionic conductivity in chloride, hydroxide and bicarbonate forms for the PSf-PVBTMAx membranes (solvent casting and melt pressing prepared) measured in water at 20 °C, 60 °C and 80 °C. The conductivities for different counter ions all increased with increased temperature. The hydroxide conductivity showed higher values than the chloride and bicarbonate conductivity for each PSf-PVBTMAx sample due to the higher aqueous diffusion coefficient of hydroxide ion,[xxxix,xl] while the chloride conductivity and bicarbonate conductivity showed similar

values for each sample at the same temperature. Studies on conductivity with different counter ions show similar behavior in previous studies.[xli,xlii]

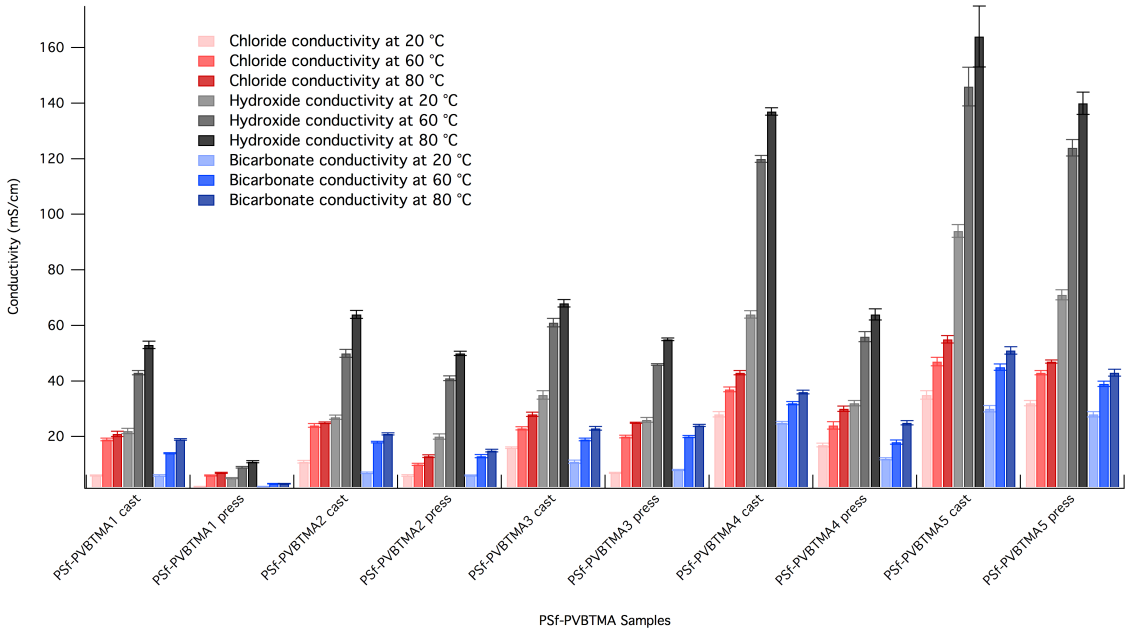

Figure 56. Conductivity of PSf-PVBTMAx membranes in their chloride forms (red series), hydroxide forms (black series) and bicarbonate forms (blue series) in water at 20 °C, 60 °C and 80 °C.

3.9 Functionalization of 3M Ionomer with quaternary ammonium cations

The first year and a half of this project was dedicate to the functionalization of a commercial perfluorocarbon ionomer with various quaternary cations (methyl, ethyl, trimethylbenzyl) as possible anion exchange membrane polymers. These materials were characterized by extent of functionalization, conductivity, water uptake, and polymer organization to determine the impact of cation species on AEM performance. Polymer synthesis conditions were constant for all cation species, however the resulting polymers had large differences in extent of functionalization (IECs ranged from 0.33 to 0.72 meq/g) with the smaller cation species functionalizing to a larger degree. It is suspected that steric hindrance limited the final alkylation step of the larger cationic species. These polymers displayed significant degradation upon exposure to hydroxide; so all characterization was performed in the chloride form to prevent bias from polymer instability. Membranes were cast on to Teflon blocks from DMAc solvent for membrane characterization. Conductivity of the membranes ranged from 0.6 to 4.8 mS/cm with the methyl ammonium polymer having the largest conductivity followed by trimethylbenzyl and ethyl ammonium polymers respectively. Water uptake was generally low with the highest at 8% for the methyl ammonium polymer, followed closely by the trimethylbenzyl and ethyl ammonium at 7.1 and 6.6% respectively. While the total water uptake was similar for all species, the large differences in IECs resulted in large differences in lambda, with values ranging from 6 to 11 waters per cation group. The large differences in lambda suggest different solvation structures for the different cations. Small angle x-ray scattering experiments suggested ionic aggregation, 37 – 42 Å,

independent of cation species but slight differences in long-range order with cation species. Diffusion of water through the methyl ammonium membrane was relatively high 1.6×10^{-5} cm^2/s and indicated restriction over a range of diffusion times, 6 – 700 ms. **Table 14** summarizes the results of the characterization for the functionalized perfluoroquaternary ammonium polymers. This study highlighted the importance of considering cation species with respect to performance and synthetic route for new anion exchange membrane polymers.

Table 14 Summary of the IEC, conductivity and corresponding activation energy, water uptake, and diffusion coefficient for PFQA polymer membranes. The conductivity and water uptake are for saturated conditions at 60°C. The diffusion coefficient was measured at 80%RH and 25°C.

Cation Species	IEC	σ	Ea	WU	λ	D
	(meq g^{-1})	(mS cm^{-1})	(kJ mol^{-1})	(%)		(cm^2 s^{-1})
Methyl	0.72±0.02	4.8±0.1	36±5	8.0±0.2	6.2±0.2	1.6×10^{-5}
Trimethylbenzyl	0.52±0.02	3.3±0.2	59±5	7.1±0.1	7.6±0.3	-
Ethyl	0.33±0.01	0.6±0.5	50±14	6.6±0.1	11.0±0.4	-

4. Incorporation of Novel Cations.

4.1 Sulfonium

Similar to quaternary nitrogen or phosphorus, tertiary sulfur (sulfonium) bears one unit of positive charge, and thus is a candidate for the cationic functional group in HEMs. Trialkylsulfonium based molten salts have already been used as electrolytes, [xliii] indicating that sulfonium is a feasible cationic functional group. However, conventional sulfonium cations (e.g., trialkyl or arylalkyl sulfonium) are less chemically and thermally stable than ammonium, [xliv] limiting their applications in HEMs. By contrast, triaryl sulfonium is much more stable (up to 300 °C)[3], largely due to conjugation between the *p* and *d* orbitals of the sulfur atom and the π electrons of the benzene rings[xlva,xlvi]. Electron-donating aryl substituents improve sulfonium's stability through charge delocalization, and are also expected to enhance the basicity of triarylsulfonium hydroxide[3b,xlvii].

We designed diphenyl(3-methyl-4-methoxyphenyl) tertiary sulfonium (*MeO*TAS), a novel cationic group containing methoxyl and methyl substituents (Figure 57). The methoxyl substituent increases electron density, while the methyl substituent provides a linkage to the polymer backbone. The *MeO*TAS-functionalized polysulfone HEM (PSf-*MeO*TASOH) shows excellent thermal stability, acceptable hydroxide conductivity, and good chemical stability.

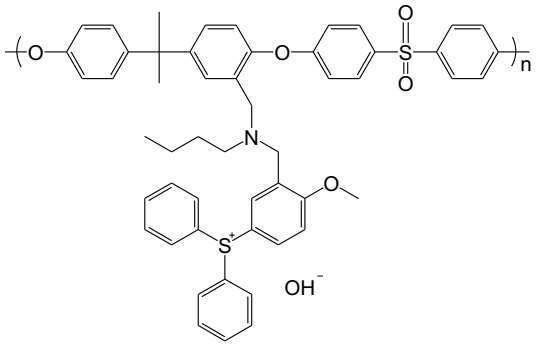

Figure 57. Chemical structure of *MeO*TASOH-functionalized polysulfone (PSf-*MeO*TASOH).

PSf-*MeO*TAS was synthesized by a nitrogen-bridge strategy in three major steps (**Figure 58**): 1) synthesis of diphenyl(3-methyl-4-methoxyphenyl) sulfonium chloride by condensation of diphenyl sulfoxide and 2-methylanisole, followed by bromination and anion exchange; 2) synthesis of butylaminated polysulfone (PSf-BA) through chloromethylation and amination to introduce the nitrogen bridge; and finally 3) the reaction between the bromomethyl group of diphenyl(3-bromomethyl-4-methoxyphenyl) sulfonium chloride and the butylamine group of PSf-BA to incorporate the *MeO*TAS cation into the polysulfone backbone. The high purity of all synthesized compounds was confirmed by ^{1}H NMR spectroscopy (see Figure 59 for an example), showing a degree of functionalization of 46%. PSf-*MeO*TASOH HEMs are transparent, flexible, and robust (Figure 60).

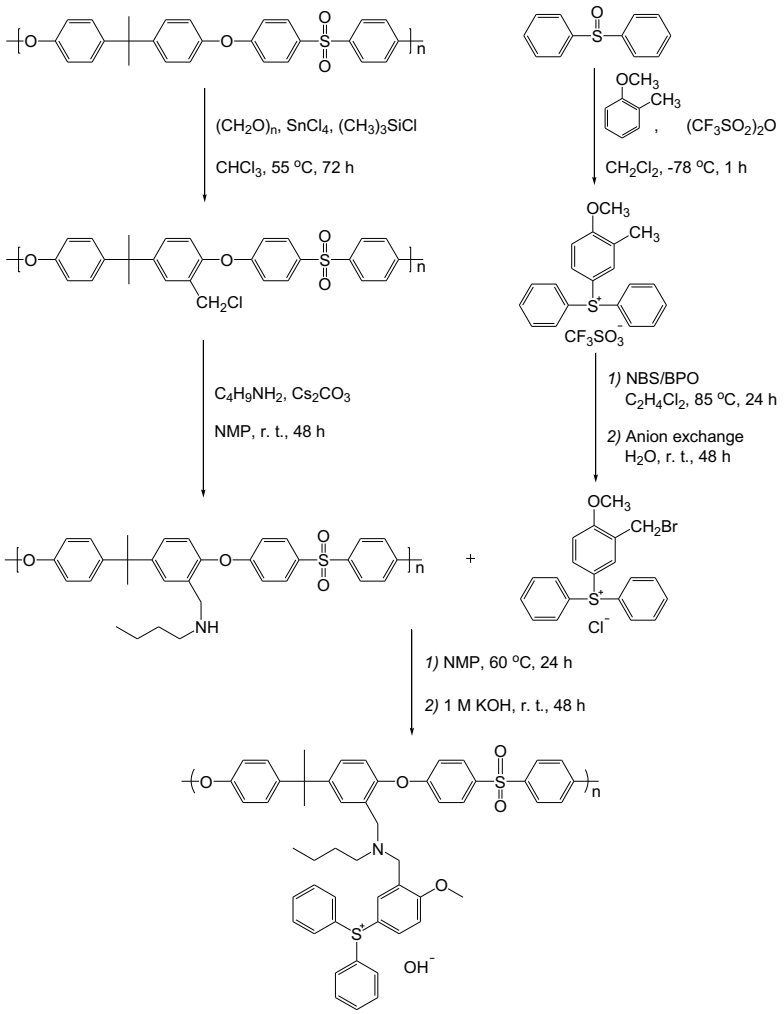

Figure 58. Synthesis of *MeO*TASOH-functionalized polysulfone (PSf-*MeO*TASOH).

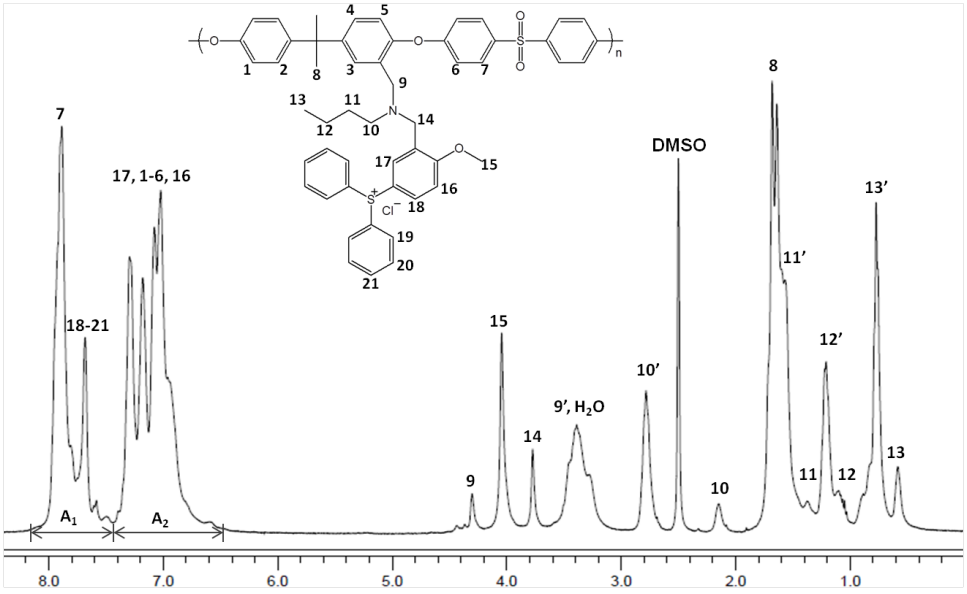

Figure 59. ^{1}H NMR spectrum of MeOTAS chloride functionalized polysulfone (PSf-MeOTASCl) in DMSO-d6.

Figure 60. Photographs of PSf-*MeO*TASOH HEMs.

The PSf-*MeO*TSOH HEM shows excellent thermal stability (Figure 61). Under the same test conditions, the onset decomposition temperature T_{OD} (Table 15) was much higher for PSf-*MeO*TSOH (242 °C) than for HEMs based on ammonium (140−170 °C)[xlviii] or phosphonium (178 °C)[xlix] with the same polysulfone backbone. This T_{OD} (with *ca.* 1% weight loss) is also higher than those of guanidinium-based poly(arylene ether sulfone) (185 °C, 5% loss)[l] and imidazolium-based polyfluorene (200 °C, 4% loss).[li]

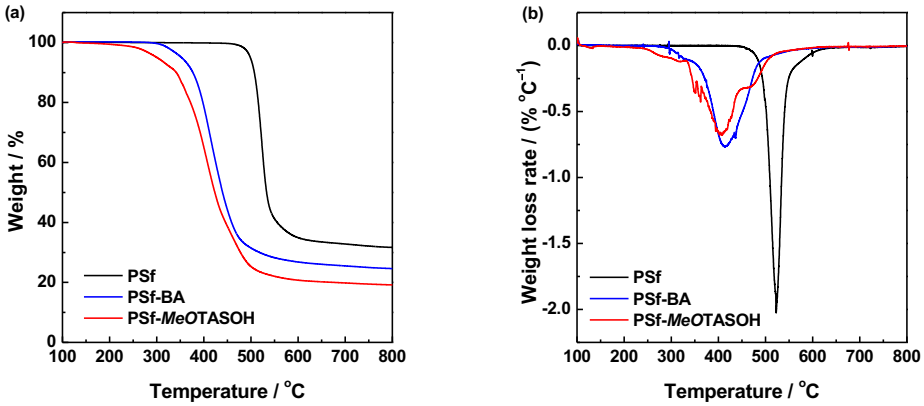

Figure 61. Thermogravimetric analysis (TGA) curves (a) and derivative thermogravimetric (DTG) curves (b) for pristine PSf (black line), butylaminated PSf (PSf-BA) (blue line), and PSf-*MeO*TSOH (red line). Test conditions: nitrogen atmosphere, flow rate of 20 mL min^{-1}; heating rate of 10 °C min^{-1}.

With an ion exchange capacity (IEC) of 0.69 mmol g^{-1}, PSf-*MeO*TASOH shows 27% water uptake and <5% swelling ratio at RT. The hydroxide conductivity is 15 mS cm^{-1}, which meets the basic requirement of HEM fuel cells (>10 mS cm^{-1}).[lii] Generally, the conductivity increases almost linearly with ionic group density (IEC), so IEC-normalized hydroxide conductivity (Table 16) is a more objective measure of intrinsic conductivity[7]. PSf-*MeO*TASOH shows a high IEC-normalized conductivity (22 mS g cm^{-1} mmol^{-1}) that is close to that of ammonium-based HEMs (19 mS g cm^{-1} mmol^{-1}),[liii] indicating similar basicity. PSf-*MeO*TASOH is more intrinsically conductive than imidazolium-based

HEMs (8.4 mS g cm^{-1} $mmol^{-1}$), [liv] but not phosphonium-based ones (39 mS g cm^{-1} $mmol^{-1}$). [lv] Note that there is significant room to improve the hydroxide conductivity of PSf-*MeO*TSOH by increasing the IEC. Additionally, we intend to introduce more methoxyl groups onto the aryl rings, which should increase sulfonium's basicity and thus raise the conductivity.

Polymer	T_{OD} [a] (°C)	T_{FD} [b] (°C)
PSf	476	523
PSf-BA	308	414
PSf-*MeO*TASOH	242	406

[a] T_{OD}, onset decomposition temperature.
[b] T_{FD}, fastest-weight-loss decomposition temperature.

Table 15. Thermal decomposition temperature of pristine PSf, butylaminated polysulfone (PSf-BA), and PSf-*MeO*TASOH.

PSf-*MeO*TASOH also shows good alkaline stability, which is critical for fuel cell operation. ^{1}H NMR spectra (Figure 62) show that PSf-*MeO*TASOH remained stable after immersion in 1 M KOH at 60 °C for 10 days, whereas commercial ammonium-based FAA membranes became brittle due to severe degradation. In a long-term 30 day test, PSf-*MeO*TASOH remained stable in 1 M KOH at RT.

HEM	IEC[a] mmol g^{-1}	HC[b] mS cm^{-1}	HC_{IEC}[c] mS g cm^{-1} $mmol^{-1}$
PSf-*MeO*TASOH[d]	0.69	15.4	22.3
PSf-TASOH[e]	0.68	7.7	11.3

[a] IEC, theoretical ion exchange capacity based on the degree of functionalization. [b] HC, hydroxide conductivity measured in water at 20 °C. [c] HC_{IEC}, IEC-normalized hydroxide conductivity. [d] Degree of functionalization: 46%. [e] Degree of functionalization: 44%.

Table 16. Ion exchange capacity, hydroxide conductivity, and IEC-normalized hydroxide conductivity of PSf-*MeO*TASOH and PSf-TASOH HEMs at RT.

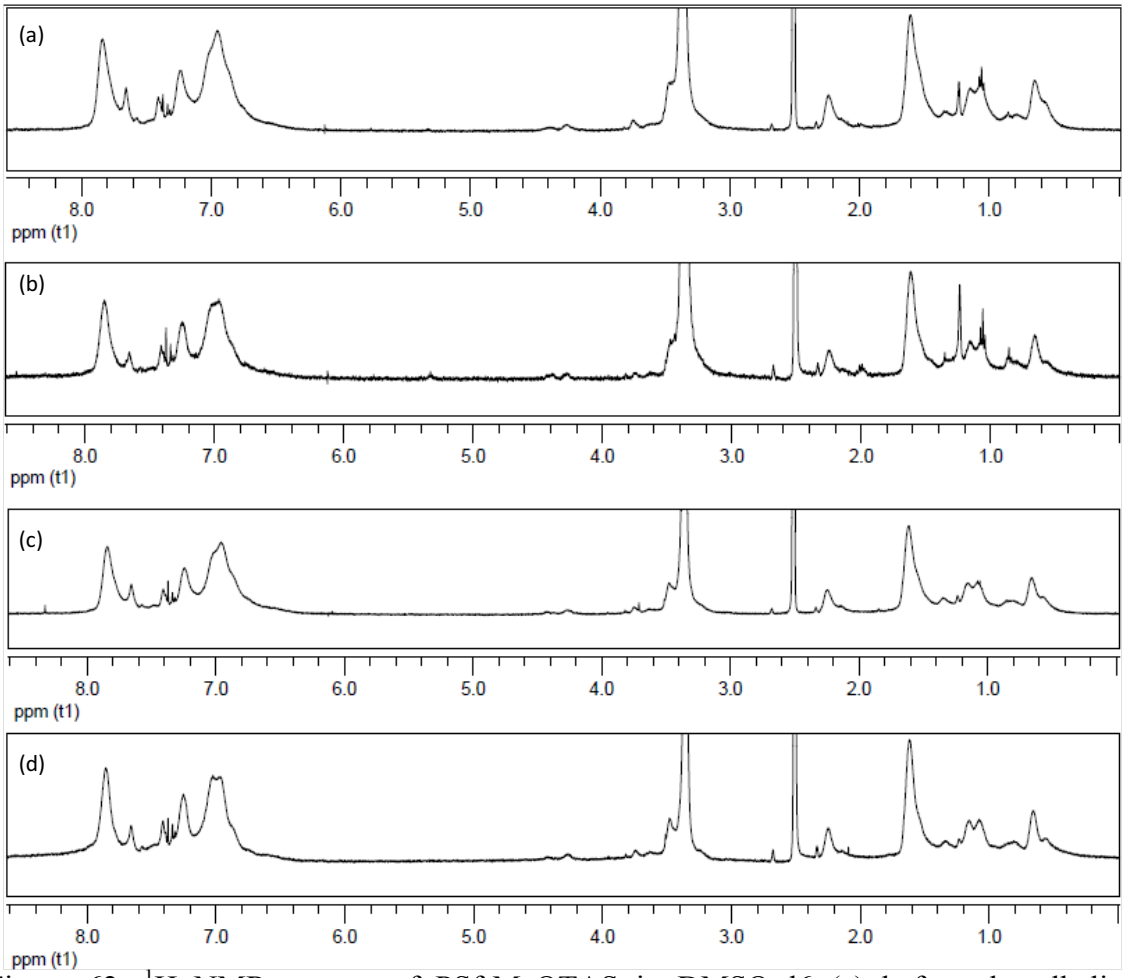

Figure 62. ^{1}H NMR spectra of PSf-MeOTAS in DMSO-d6 (a) before the alkaline stability test, (b) after 1 day, (c) after 5 days, and (d) after 10 days. Test conditions: 1 M KOD/D2O, 60 °C.

4.2 Phosphonium cations

The cationic group is the key part of hydroxide exchange membranes (HEMs), controlling fundamental properties such as conductivity, solubility, and stability. We studied the alkaline stability of a series of phosphonium cations and propose a multi-step degradation mechanism for $TPQP_{Bn}$ cation. Inspired by the new mechanism, a superior quaternary phosphonium-based cation (*9Me*TPP_{Me}) with excellent alkaline stability was developed.

Long-term alkaline stability test on model molecules

To mimic the aromatic backbone structure and activated halide functionality of chloromethylated polysulfone, we selected benzyl chloride as the quaternizing agent to be attached to the phosphine precursor. The small-molecule model $TPQP_{Bn}Cl$ (Figure 15b) was synthesized by reacting tris(2,4,6-trimethoxyphenyl) phosphine with benzyl chloride. Although the model compound was prepared in the chloride form, subsequent degradation testing rapidly and irreversibly converted it to the hydroxide form ($TPQP_{Bn}OH$) with no need for a separate ion exchange step. For a benchmark, we prepared a second model molecule based on the benchmark benzyl trimethyl ammonium

hydroxide cation (BTMA). The synthesis is analogous to that of $TPQP_{Bn}Cl$: trimethyl amine was reacted with benzyl bromide to yield the ammonium bromide salt, BTMABr (Figure15a). As with the QP model compound, BTMABr converts trivially to BTMAOH during alkaline degradation testing.

A 1 M alkaline solution was prepared by dissolving KOD in a 5:1 (vol) mixture of CD_3OD/D_2O. (The purpose of the methanol is to accelerate degradation.) The QP (or QA) model compound was added to the alkaline solution to obtain a molar ratio of 30 KOD: 1 model (*i.e.*, 0.033 M). A similar quantity of 3-(trimethylsilyl)-1-propanesulfonic acid sodium salt ($TMS(CH_2)_3SO_3Na$) was also added to serve as an internal standard. The mixture was held at 80 °C for 58 days, with NMR (^1H and, for the QP model, ^{31}P) spectra taken periodically. Both model molecules degraded substantially over the test period (raw NMR data in Figure 16, summary of degradation rate in Figure 17). The QP model compound degraded less than the QA model (59% vs. 82% after 20 days) judging by the gradual decrease in area of the largest model peak as compared to the constant area of the largest internal standard peak.

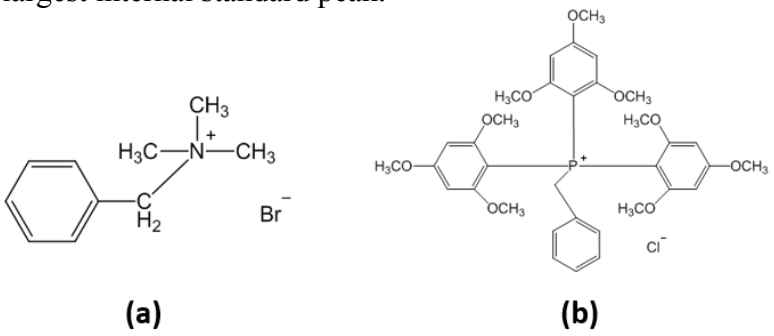

Figure 63. Chemical structures of (a) $TPQP_{Bn}Cl$ and (b) BTMABr.

(a)

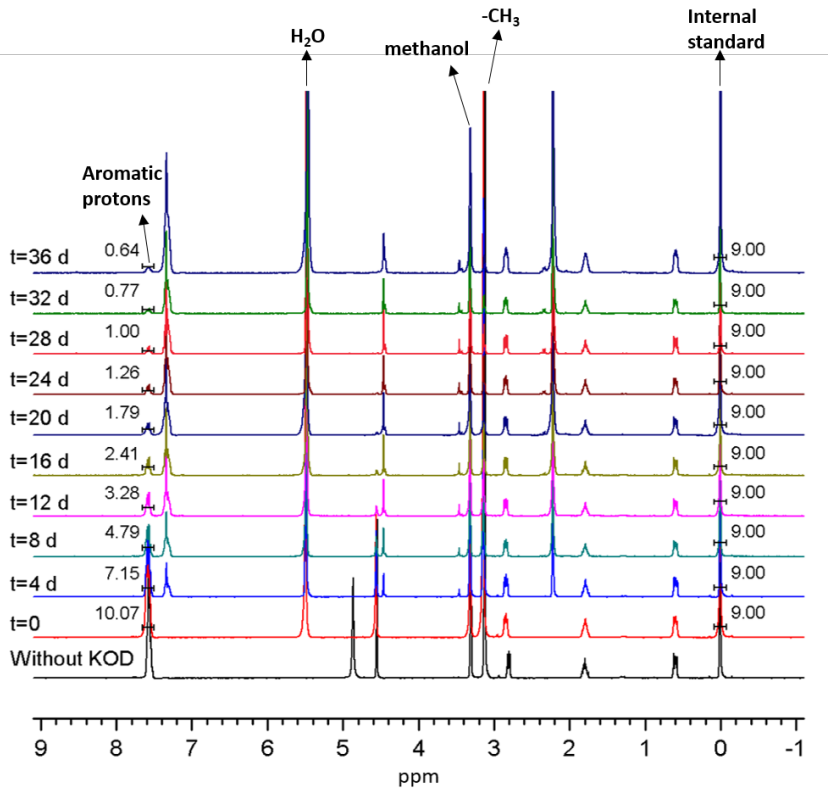
H2O
methanol
-CH3
Internal standard
Aromatic protons
t=36 d
0.64
9.00
t=32 d
0.77
9.00
t=28 d
1.00
9.00
t=24 d
1.26
9.00
t=20 d
1.79
9.00
t=16 d
2.41
9.00
t=12 d
3.28
9.00
t=8 d
4.79
9.00
t=4 d
7.15
9.00
t=0
10.07
9.00
Without KOD
9 8 7 6 5 4 3 2 1 0 -1
ppm

(b)

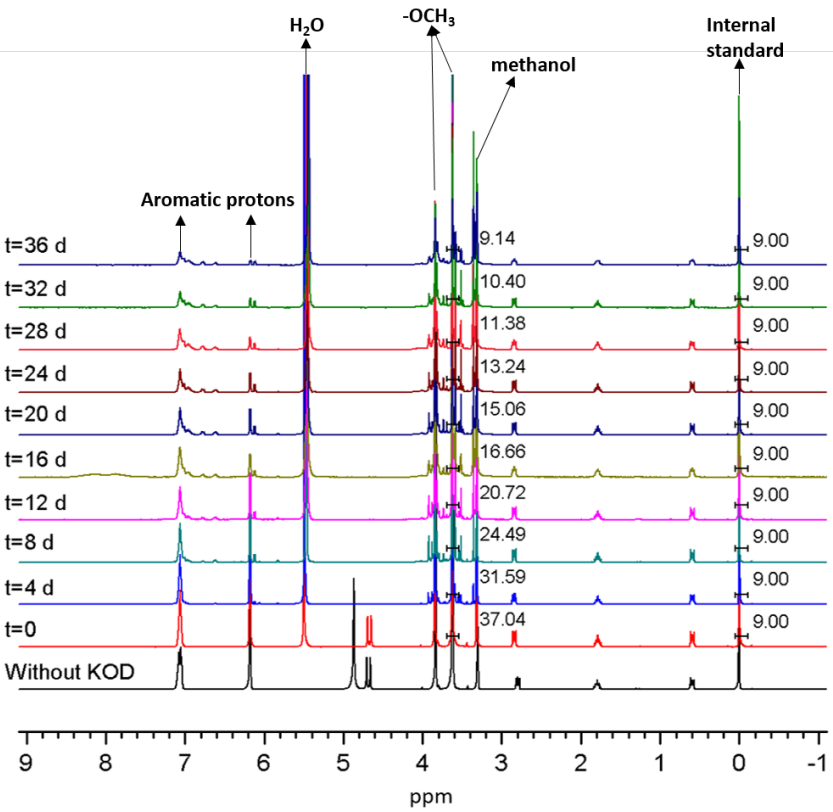
H2O
-OCH3
methanol
Internal standard
Aromatic protons
t=36 d
9.14
9.00
t=32 d
10.40
9.00
t=28 d
11.38
9.00
t=24 d
13.24
9.00
t=20 d
15.06
9.00
t=16 d
16.66
9.00
t=12 d
20.72
9.00
t=8 d
24.49
9.00
t=4 d
31.59
9.00
t=0
37.04
9.00
Without KOD
9 8 7 6 5 4 3 2 1 0 -1
ppm

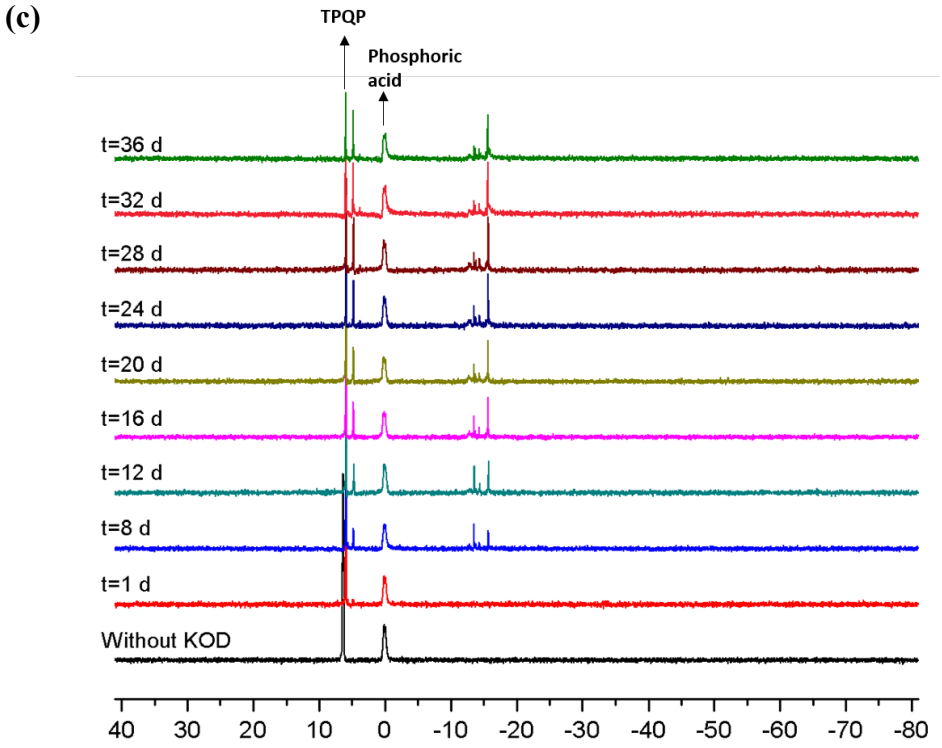

Figure 64. ^{1}H NMR spectra for (a) QP and (b) QA models during degradation test. (c) ^{31}P NMR spectra for QP model during degradation test.

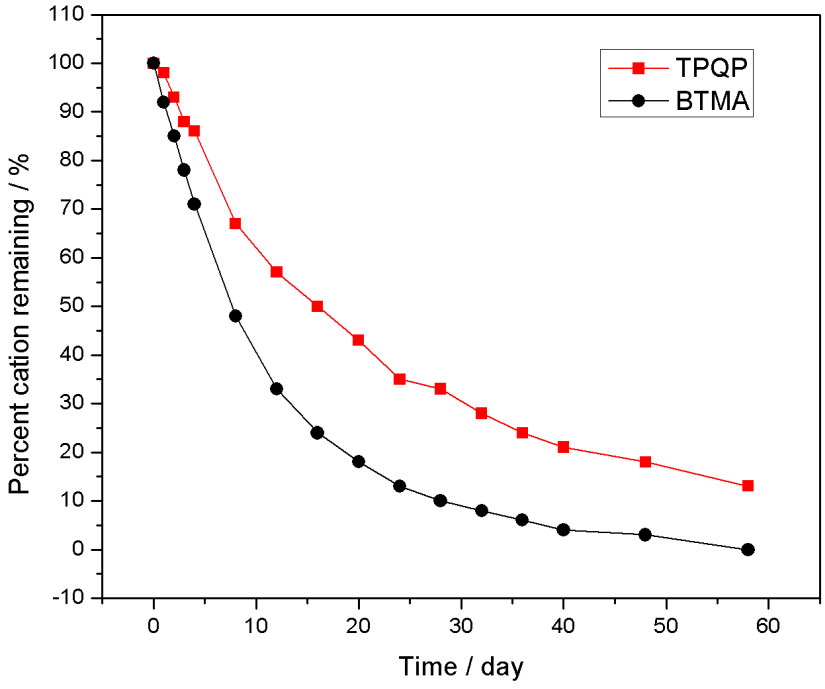

Figure 65. Plots of degradation rate of QP and QA models in 1 M KOD solution at 80 ^{o}C.

Identification of the degradation mechanism of three molecules analogous to the QP model.

Three "analogs", triaryl phosphonium salts similar to the $TPQP_{Bn}$, were synthesized using the same method by which the $TPQP_{Bn}$ was prepared. They were chosen for their simplicity and similarity to $TPQP_{Bn}$, with ring substituents of varying degrees of electron donating capability. The QP analogs are shown in Figure 18. In an alkaline durability test, the three analogs degraded into the corresponding phosphine oxide and toluene (Figure 19). The products were confirmed by adding phosphine oxide (synthesized separately) and toluene (as purchased) to the reaction mixture, and noting that the new NMR peaks overlapped perfectly with the suspected degradation products. As expected, changing the ring substituent from –H (weakly electron donating) to –Me to –OMe (strongly electron donating) increased the alkaline stability. However, all three analogs completely degraded unacceptably quickly (within a week) even at room temperature. The plots of cation lifetime (Figure 20) shows that $TPQP_{Bn}$ is much more stable than its three analogs.

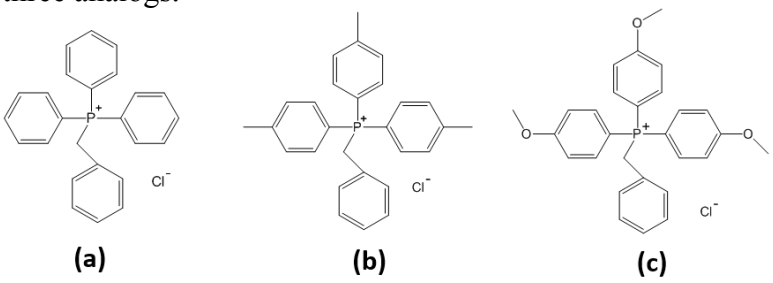

Figure 66. Chemical structures of three analogs of QP model: (a) TPPCl, (b) *3Me*TPPCl and (c) *3MeO*TPPCl.

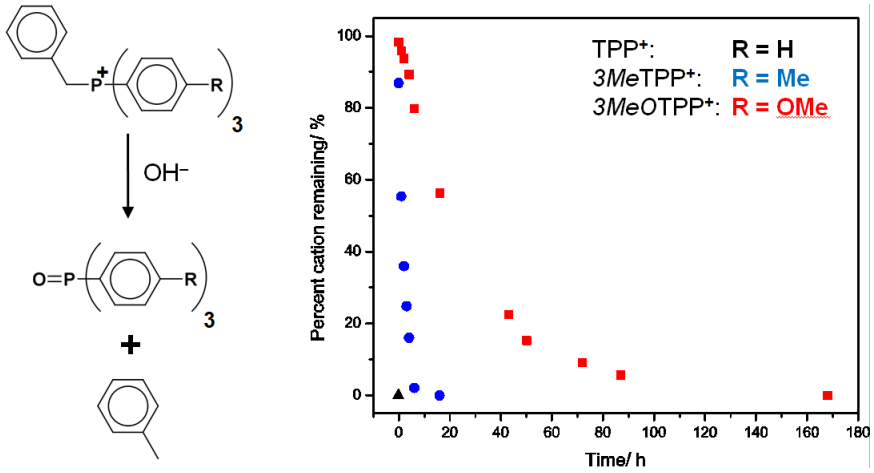

Figure 67. Analogs of the QP model. Degradation of 0.033 M phosphonium salt in 1 M KOD (solvent: 5 CD_3OD : 1 D_2O) into toluene and the corresponding phosphine oxide at 20 °C was calculated from change in area of ^1H NMR peaks.

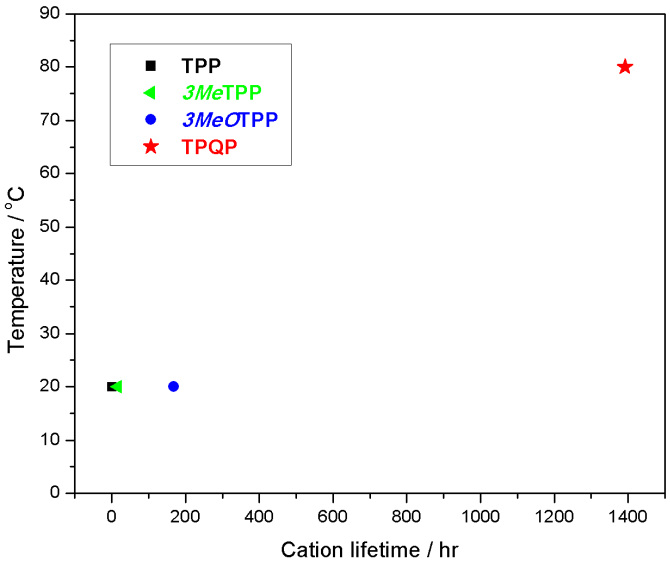

Figure 68. Plots of cation life time of QP model and its analogs.

Identification of the major degradation mechanism of the QP model.

The QP model was subjected to the same durability test as its analogs, but at elevated temperature (80 °C vs 20 °C) due to its expected superior stability. After 58 days, it still had not degraded completely (Figure 20). Despite the similarity of the QP model to its analogs, neither phosphine oxide nor toluene was produced by its degradation (Figure 21). To account for this unexpected behavior, we proposed a novel multi-step mechanism (Scheme 4), including ether hydrolysis, inner salt formation, ketone rearrangement and further hydrolysis.

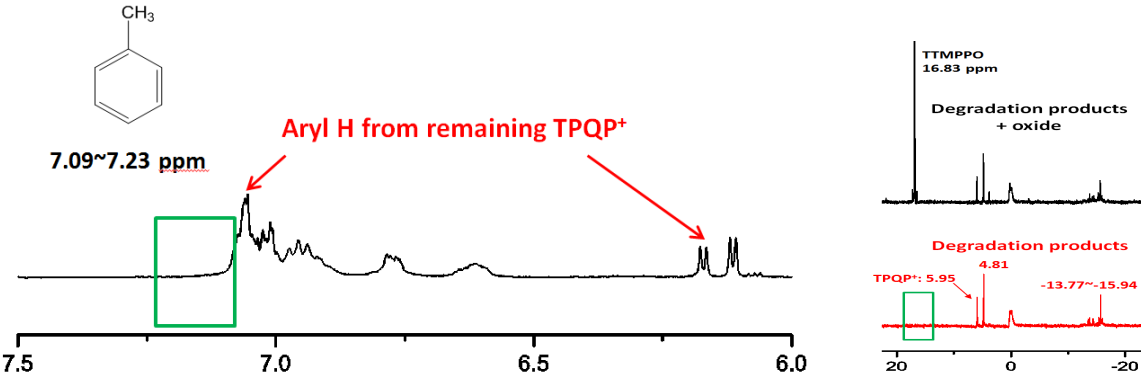

Figure 69. Evidence that the QP model degrades by a different mechanism. Top: ^{1}H NMR spectrum showing no trace of toluene from 7.09 to 7.23 ppm. Right: ^{31}P NMR showing no trace of phosphine oxide (TTMPPO) at 16.83 ppm. The green boxes indicate where the missing species would be found, if present.

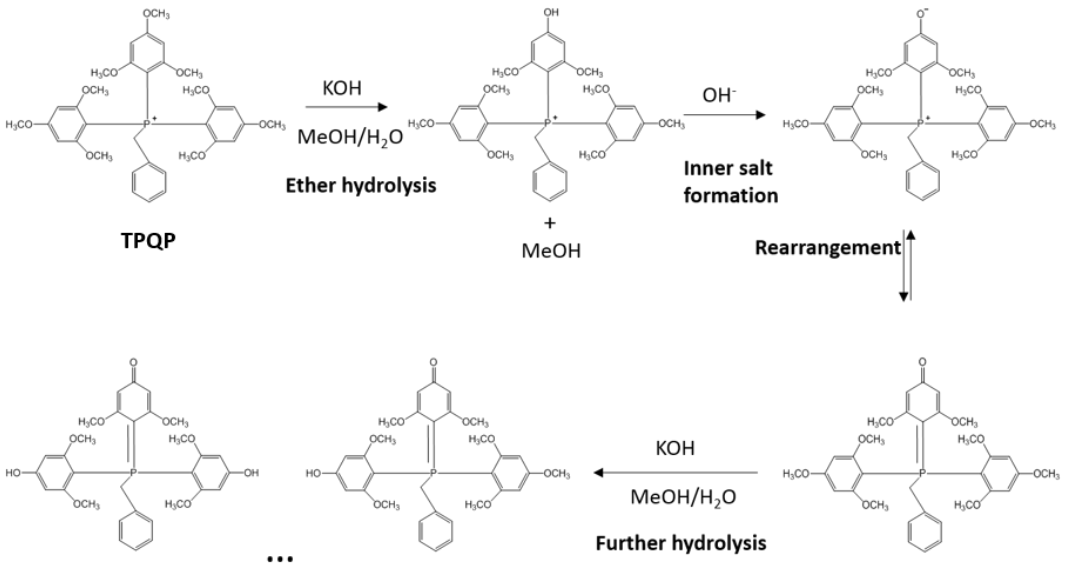

Scheme 10. Proposed degradation mechanism of $TPQP_{Bn}OH$ in alkaline environment.

Verification of the degradation mechanism of the QP model compound.

To verify the proposed mechanism, we tested each step individually.

Step 1 (ether hydrolysis): Literature suggests that anisole (methoxybenzene) degrades into phenol (hydroxybenzene) in base at high temperature, producing methanol. Unfortunately, (deuterated) methanol is already present in our test solution (as the solvent), rendering detection of the formation of a small quantity by ^{1}H NMR impossible. We solved this issue by changing the solvent from deuterated methanol to deuterated ethanol for one test (Figure 22). Methanol is clearly produced over time, confirming that ether hydrolysis takes place.

Step 2 (inner salt formation): Acid was added to the degradation products to force the back reaction from ylide to alcohol (Figure 23). The proximity of the resultant alcohol peak to the QP model peak in the ^{31}P spectrum is expected due to the strong structural similarity of these species near the phosphorus center.

Step 3 (ketone rearrangement): Typical of aryl ketones, the reaction mixture turned orange during degradation. Additionally, FTIR spectroscopy identified a characteristic ketone absorption peak (Figure 24).

Step 4 (further hydrolysis): The ^{31}P spectrum suggests that multiple similar products form after ketone rearrangement, consistent with statistical hydrolysis of the remaining methoxyl substituents into hydroxyl groups.

This mechanism demonstrates that due to the strong electron-donating ability of nine methoxyl groups, the essential structure of $TPQP_{Bn}$ becomes much less susceptible to OH^- attack so that the overall alkaline stability of $TPQP_{Bn}OH$ is enhanced. However, the methoxyl groups on benzene ring could undergo ether hydrolysis to from hydroxyl group in base, which becomes the weak point of $TPQP_{Bn}$. Therefore, finding a balance between the electron density on P center and the alkaline stability of substituents on benzene ring is critical for a superior phosphonium based cation.

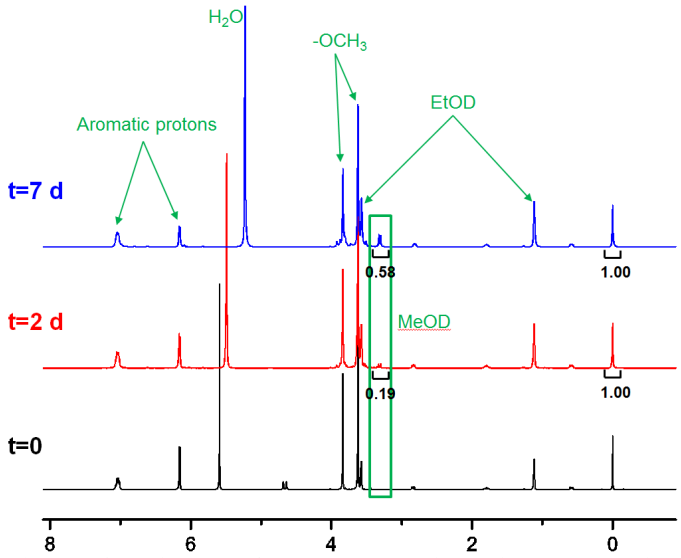

Figure 70. Evidence of ether hydrolysis during degradation. Another degradation test was performed in ethanol instead of methanol, resulting in the ^{1}H NMR spectra shown above. The methanol production peak is boxed in green.

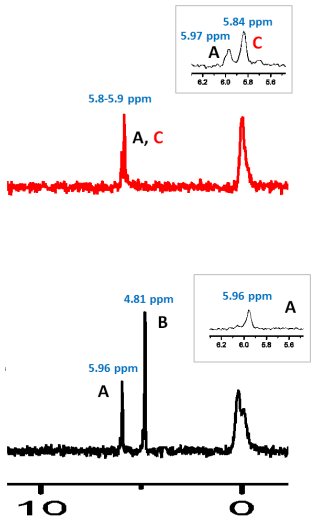

Figure 71. Evidence of ylide formation during degradation. Bottom: 31P spectrum of degradation products, showing the QP model (A) and the ylide degradation product (B). Top: Same spectrum after addition of HCl. The acid protonates the ylide, eliminating peak B and generating an alcohol peak (C).

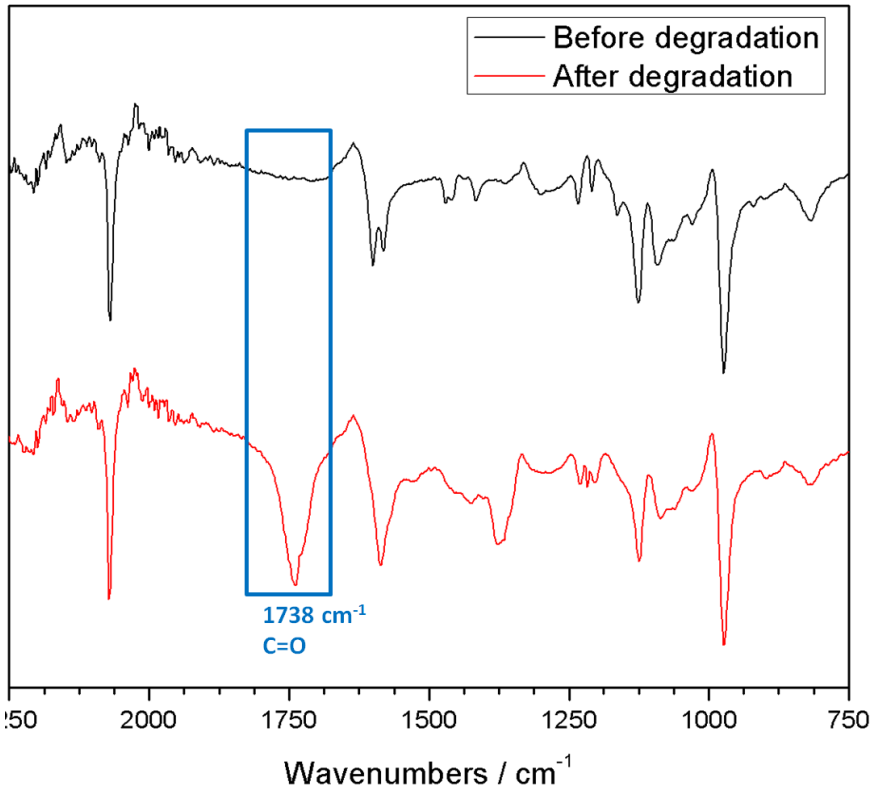

Figure 72. Evidence of ketone formation during degradation. This FTIR spectrum shows a characteristic ketone peak only after degradation.

Design of a superior quaternary phosphonium-based cation.

We designed an improved cation "9Me-QP" (Figure 25b) that contains no OMe groups and therefore should not undergo the same degradation. Specifically, we replaced all nine OMe groups by functionally similar Me ($-CH_3$) groups, aiming to preserve the steric and electronic properties responsible for QP's strong performance as a hydroxide ion conductor. In principle, the new cation, either in small molecule (model) form or when attached to a polymer chain, can be prepared in the same manner as $TPQP_{Bn}$: by quaternization with a benzyl halide (BnX). However, an alternate approach was required to synthesize the 9Me-QP model, as described in the following subtask.

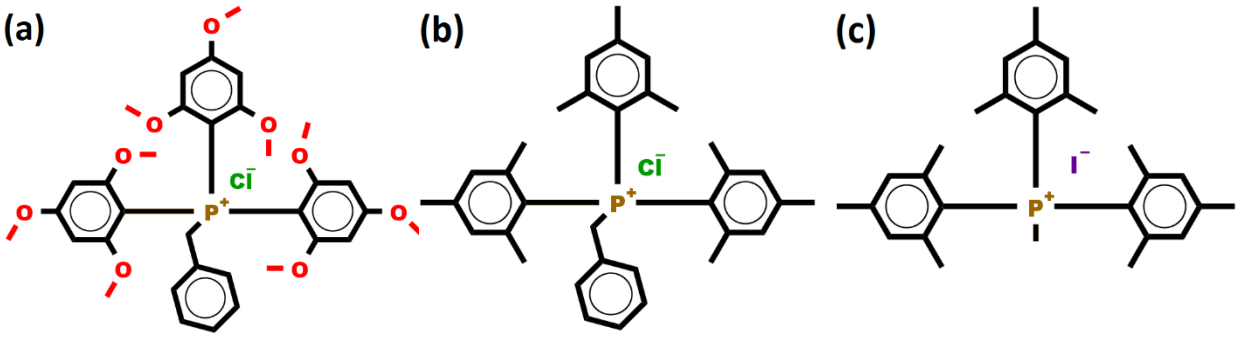

Figure 73. Structures of (a) the original QP model ($TPQP_{Bn}Cl$), (b) the desired 9Me-QP model (*9Me*TPP_{Bn}), and (c) the actual 9Me-QP model we synthesized (*9Me*TPP_{Me}).

Synthesis of the 9Me-QP model.

Initially, we attempted to synthesize the 9Me-QP model (*9Me*TPP_{Bn}) (Figure 25b) by quaternization with BnCl. No reaction occurred, so we tested two other benzyl halides (BnBr and BnI) under a variety of conditions, to no avail. Finally, we achieved quaternization with MeI (Figure 25c, Scheme 5). The ^{1}H NMR spectrum of the resultant model cation (*9Me*TPP_{Me}) is shown in Figure 26a; the ^{31}P NMR spectrum, a single peak at 7 ppm, is shown in Figure 26b. Both confirm the synthesis of the *9Me*TPP_{Me}. We anticipated the concern that any superior durability of *9Me*TPP_{Me} could be attributed to the switch from a benzyl to an alkyl, and accordingly prepared a control version of $TPQP_{Bn}$ ($TPQP_{Me}$). The ^{1}H NMR spectrum of $TPQP_{Me}$ is shown in Figure 27a; the ^{31}P NMR spectrum, a single peak at -3.8 ppm, is shown in Figure 27b. Both confirm the synthesis of the $TPQP_{Me}$.

The phosphine precursors of TPQP and 9Me-QP show significantly different quaternizabilities. There are two possible explanations: (1) *Electron density of P atom*. ^{31}P NMR spectroscopy suggests that electron density at P atom is lower for the 9Me-QP precursor than for the TPQP one (-37 ppm *vs*. -70 ppm in $CDCl_3$), implying lower nucleophilicity. However, this electron deficiency cannot fully explained why raising temperature did not kickstart the reaction or why quaternization with the alkyl halide was so strongly preferred. (2) *Sterics*. Due to their rigidity, the Me groups of 9Me-QP are more sterically hindering than the OMe groups of TPQP, to the extent that the 9Me-QP phosphine precursor reacts with a methyl halide but not with a bulkier benzyl halide. Despite OMe's larger size, C-O bond rotation allows the trailing methyl substituent to give way to reacting species.

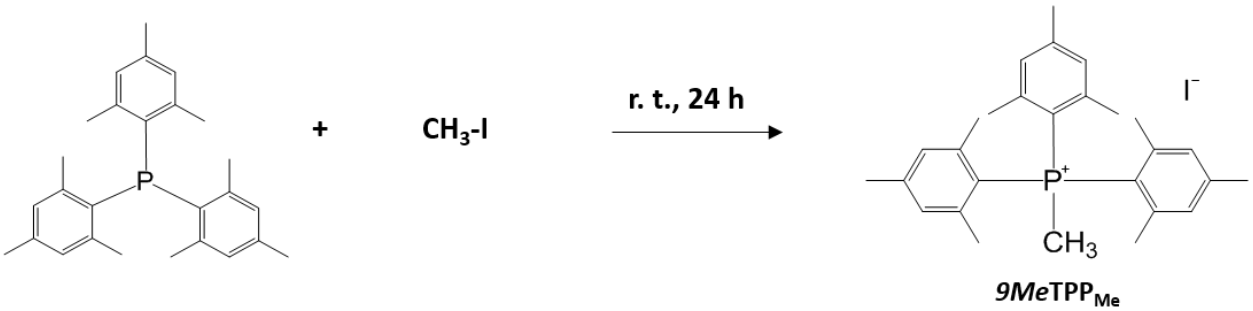

Scheme 11. Successful quaternization reaction with methyl iodide to form the 9Me-QP model compound.

(a)

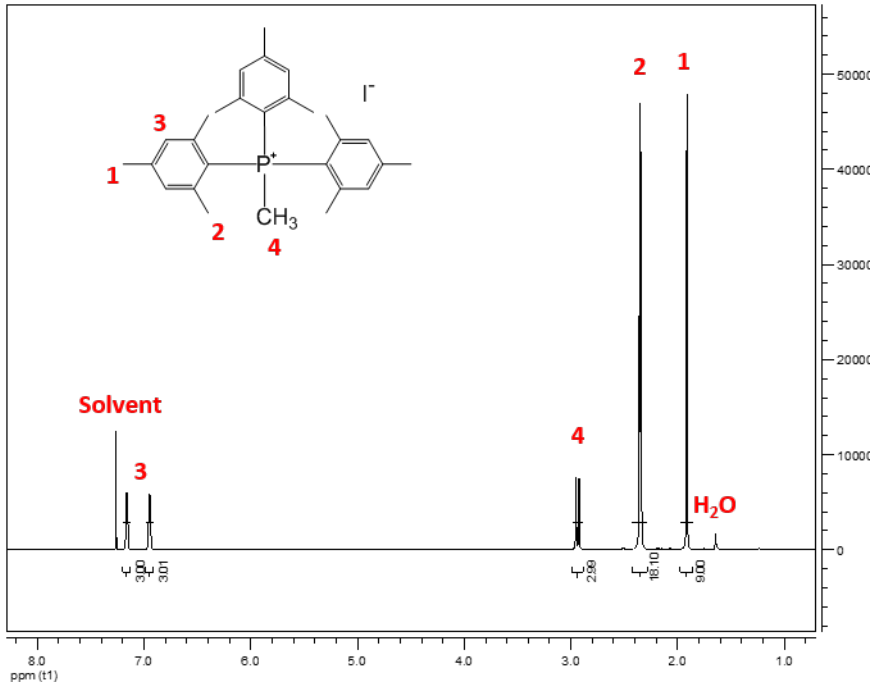

(b)

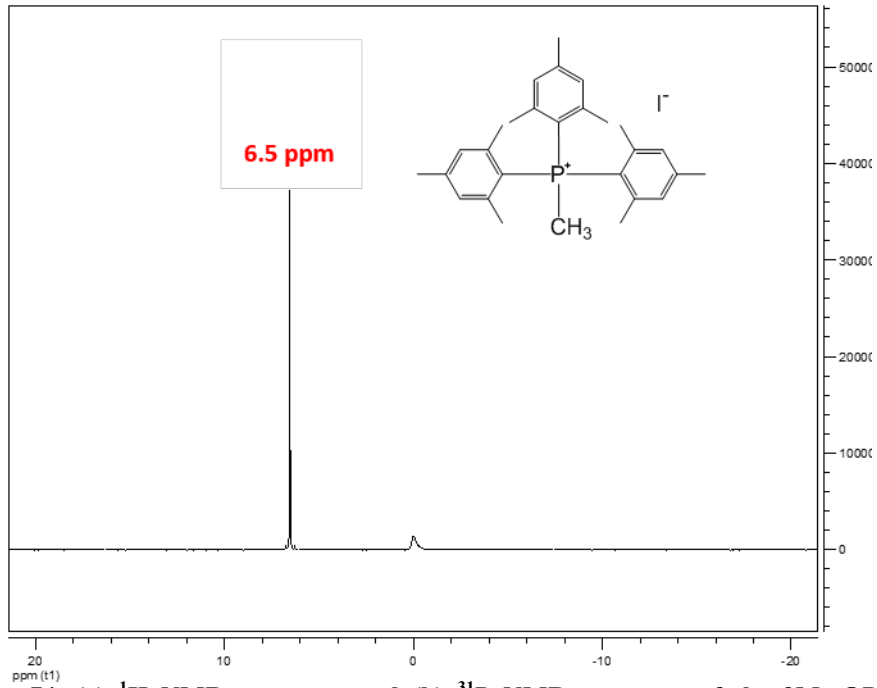

Figure 74. (a) ^{1}H NMR spectrum and (b) ^{31}P NMR spectrum of the 9Me-QP model compound (*9Me*TPP_{Me}) in $CDCl_3$.

(a)

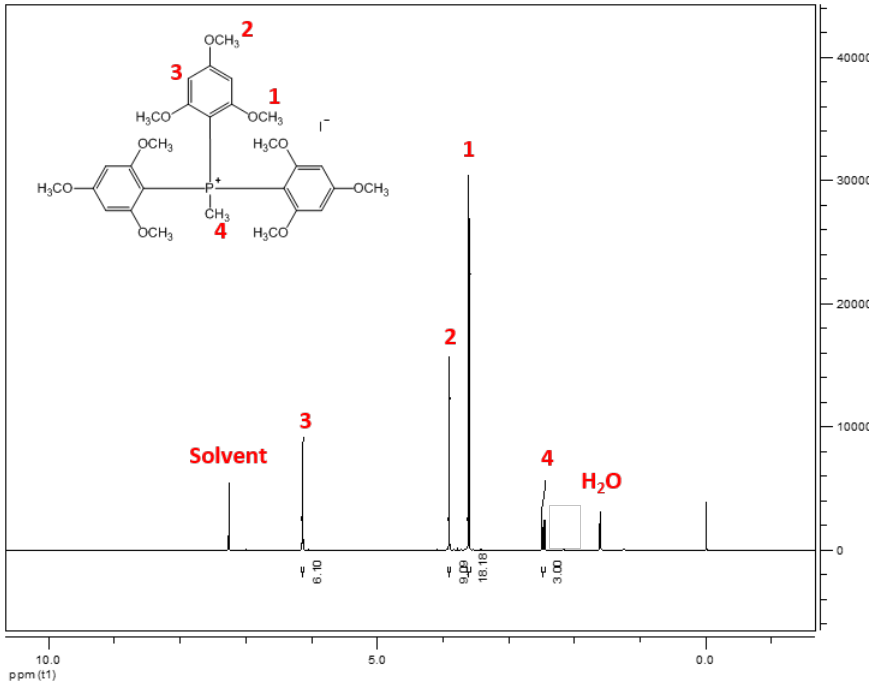

(b)

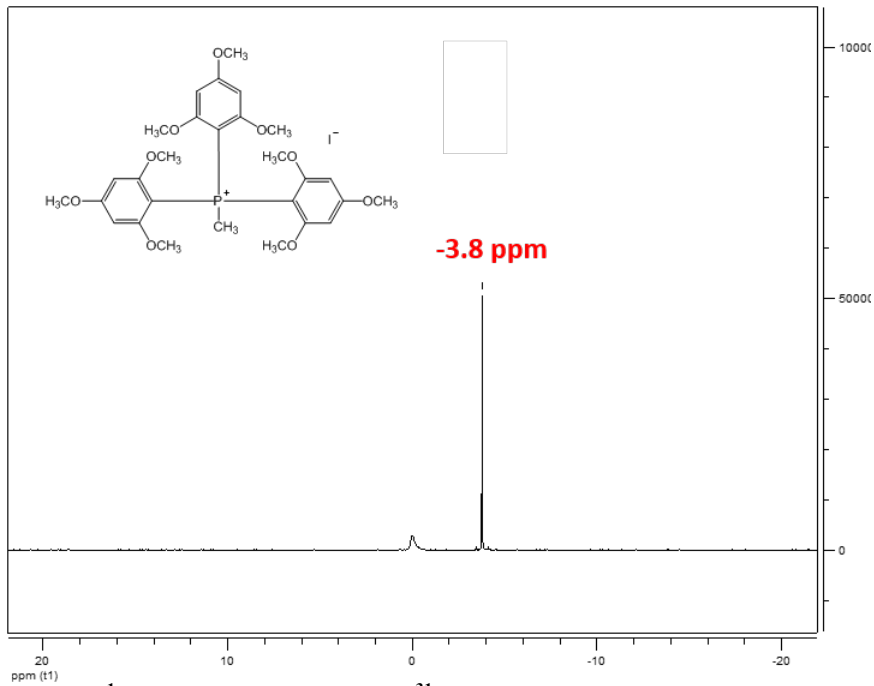

Figure 75. (a) ^{1}H NMR spectrum and (b) ^{31}P NMR spectrum of the TPQP$_{Me}$ in CDCl$_3$.

*Degradation of the the 9Me-QP model (*9Me*TPP$_{Me}$).*

We quantified the stability of *9Me*TPP$_{Me}$ by our standard procedure: 30 mM phosphonium salt in 1 M KOD (solvent: 5 MeOD : 1 D_2O) at 80 °C. ^{1}H NMR and ^{31}P NMR spectra (Figure 28) were taken periodically. After 108 days, 85% of *9Me*TPP$_{Me}$ remained, whereas after 60 days, 14% of TPQP$_{Me}$ remained (Figure 29). *9Me*TPP$_{Me}$ is substantially more stable than TPQP$_{Me}$.

While $TPQP_{Me}$ degraded slightly less than $TPQP_{Bn}$ over 60 days (86% *vs*. 88% degradation), the difference is insignificant compared to the improvement of *9Me*TPP_{Me} (15% *vs*. 86% degradation). Thus, the switch from benzyl halide to methyl halide quaternization is not the major reason for the superiority of *9Me*TPP_{Me}. Since the phosphine oxide is the sole degradation product (Figure 28), we propose that *9Me*TPP_{Me} degrades only through an oxidation mechanism. The enhanced alkaline stability of *9Me*TPP_{Me} not only comes from the stable substituents on benzene ring, but more importantly the significant steric hindrance of nine methyl groups that protects the P center from OH^- attack.

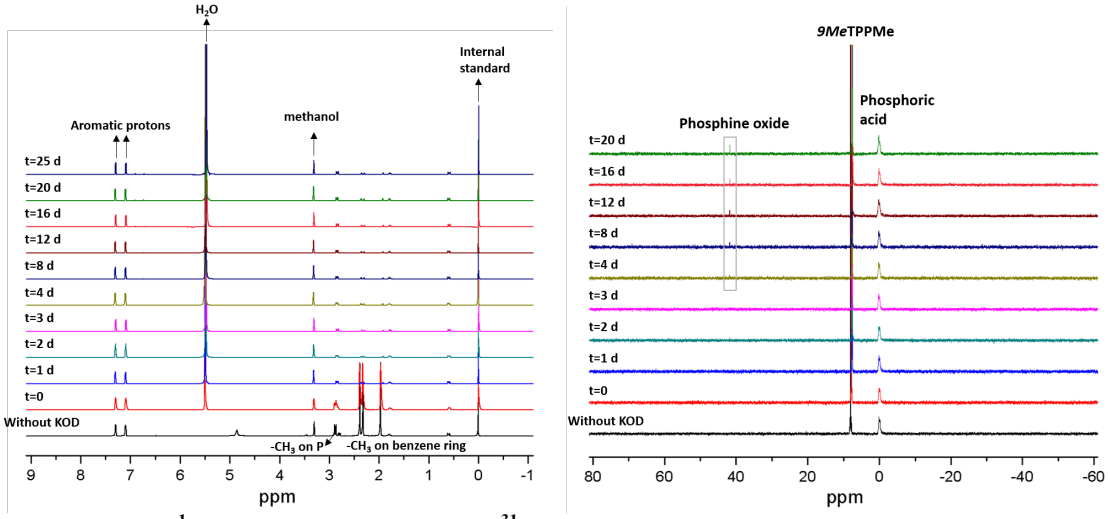

Figure 76. Left, ^{1}H NMR spectra and Right, ^{31}P NMR spectra for *9Me*TPP_{Me} during degradation test.

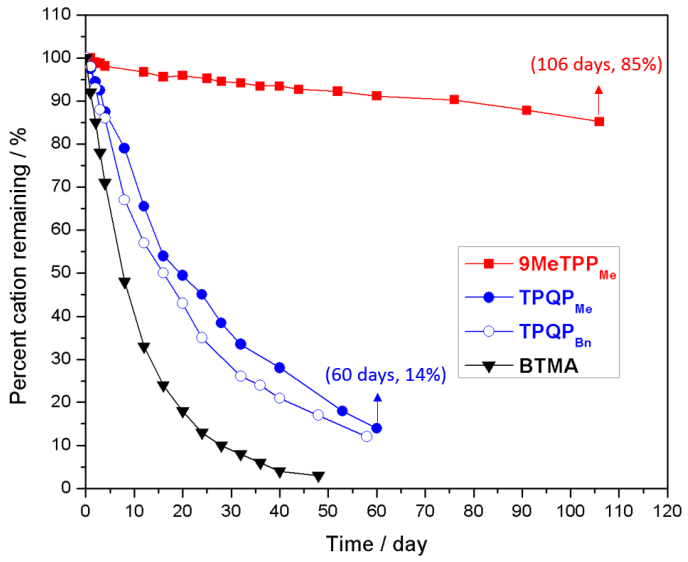

Figure 77. Degradation of *9Me*TPP_{Me}, $TPQP_{Me}$ and $TPQP_{Bn}$ under the same accelerated test conditions: 30 mM phosphonium salt in 1 M KOD (solvent: 5 MeOD : 1 D_2O) at 80 °C. Percent cation remaining was calculated from ratios of NMR integrals.

Synthesis of 9Me*TPP$_{Me}$ functionalized polymer.*

We propose three strategies to link the new cation *9Me*TPP$_{Me}$ to a polymer backbone. For Strategy 1 & 2, polysulfone was taken as the typical backbone, but these two strategies can be analogically applied to other aromatic polymers. For Strategy 3, poly(4-bromostyrene) was taken as the typical backbone, but this strategy can be analogically applied to any other polymer containing bromobenzene.

Strategy 1 (Scheme 6): One methyl on benzene ring of *9Me*TPP$_{Me}$ was brominated by using NBS as the brominating agent and BPO as the initiator to give a bromomethyl group. The reaction between bromomethylated *9Me*TPP$_{Me}$ and the aminated polymer gave us the *9Me*TPP$_{Me}$ functionalized polymer.

Strategy 2 (Scheme 7): The acylating agent 4-iodobutanoyl chloride was synthesized by reacting 4-Iodobutyric acid with thionyl chloride. Then the polymer backbone was acylated by 4-iodobutanoyl chloride to introduce alkyl iodide group. Finally, the acylated polymer was quaternized with the corresponding phosphine to introduce *9Me*TPP$_{Me}$. The C=O bond can be easily reduced to –CH_2 by hydrosilanes in the presence of triflic acid.

Strategy 3 (Scheme 8): Triarylphosphine with eight methyl groups and one vinyl group was synthesized as the precursor. Then Heck reaction was carried out to attach the precursor to the polymer backbone. Finally, the phosphine on polymer backbone was quaternized with CH_3I to introduce *9Me*TPP$_{Me}$.

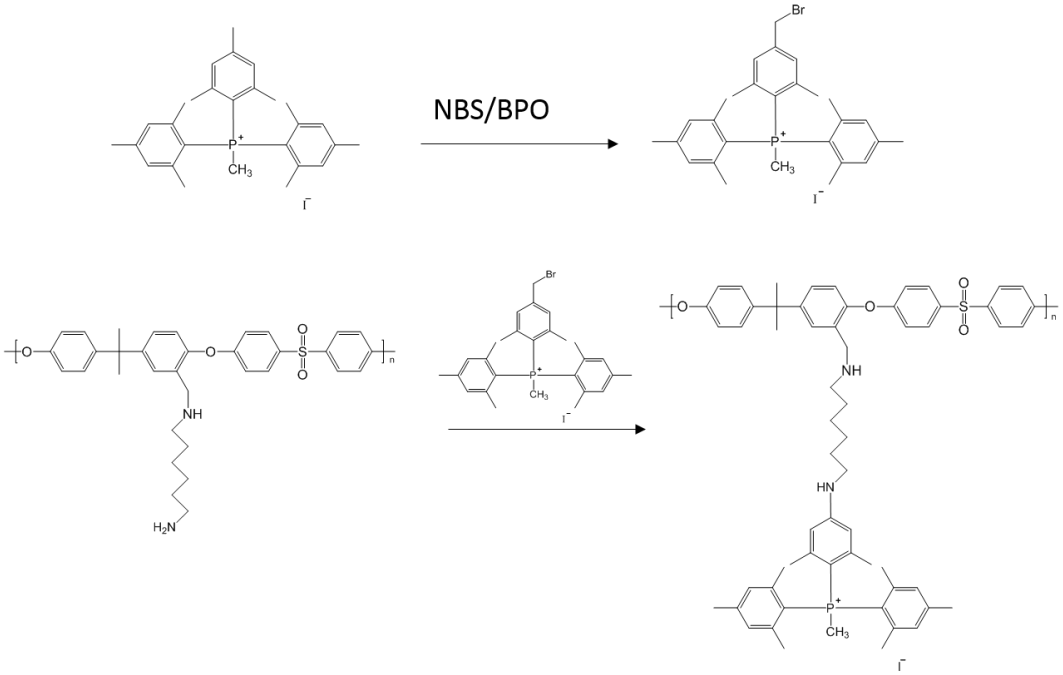

Scheme 12. Strategy 1 for attaching *9Me*TPP$_{Me}$ to an aromatic polymer backbone.

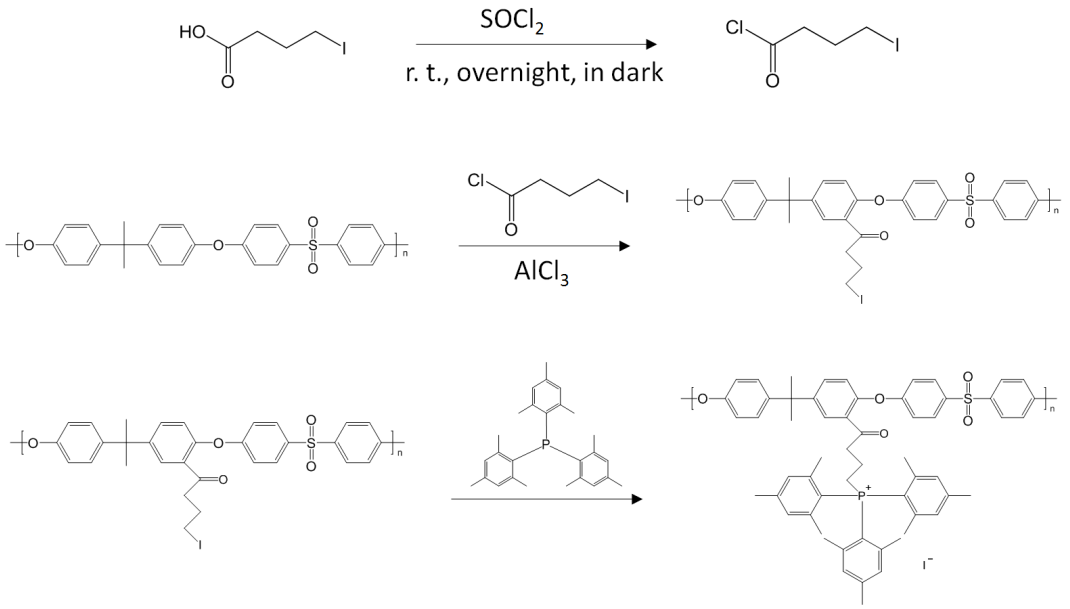

Scheme 13. Strategy 2 for attaching *9Me*TPP$_{Me}$ to an aromatic polymer backbone.

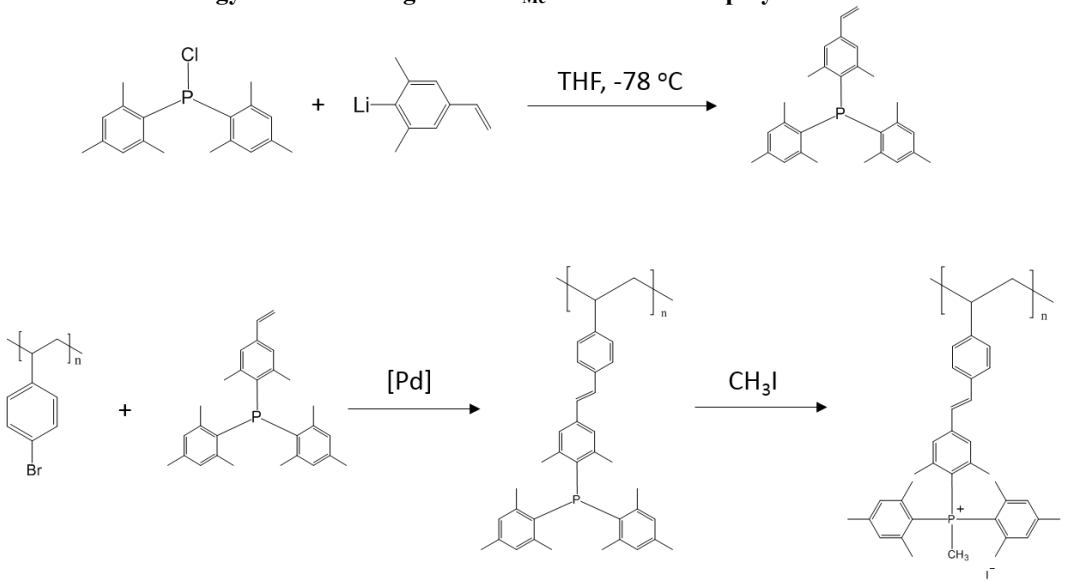

Scheme 14. Strategy 3 for synthesizing *9Me*TPP$_{Me}$ functionalized polymer.

In conclusion, the alkaline stability of a series of phosphonium cations have been studied. TPQP$_{Bn}$ shows better stability than the ammonium benchmark BTMA$_{Bn}$. Its unique degradation mechanism demonstrates that the strong electron-donating ability of the nine methoxyl groups on benzene rings can effective prevent the P center from falling apart, but the methoxyl group itself can undergo ether hydrolysis and trigger another type of degradation. *9Me*TPP$_{Me}$ shows excellent alkaline stability, much better than TPQP$_{Me}$ and TPQP$_{Bn}$ because by replacing the methoxyl group with methyl group, we not only eliminating the substituent degradation, but also introduce huge steric hindrance around the P center. Beneficial from its excellent alkaline stability, *9Me*TPP$_{Me}$ would be a very promising candidate for the cationic group served in HEMs.

4.3 Cobaltocenium

Previously, we designed a cobaltocenium-based HEM and synthesized it by a nitrogen-bridge method analogous to the one described in the sulfonium section. The three major synthetic steps in this nitrogen-bridge approach are: amination of chloromethylated polymer, bromination of bis(pentamethyl)cobaltocenium(III) chloride, and incorporation of brominated bis(pentamethyl)cobaltocenium(III) chloride into the aminated polymer. The first two steps were accomplished with better than 95% conversion.

This year, we focused on the final incorporation step, designing a model reaction (**Figure 78**) to confirm its feasibility. We chose hexamethylenediamine (HDA) as the linking molecule because it simultaneously has sufficient molecular length (6 carbon atoms between the amino groups) and one of the highest basicities among diamines (pK_b = 3.0). The first step of the model reaction is the synthesis of benzyl hexamethylenediamine (Bn-HDA) (**Figure 78**, top); the second is the synthesis of benzyl hexamethylenediamine bis(pentamethyl)cobaltocenium hydroxide (**Figure 78**, bottom). The products were confirmed by ^{1}H NMR spectroscopy (Figure 79), with more than 95% conversion obtained in both cases. The success of this model reaction strongly confirmed the feasibility of the proposed synthetic route. Following this route, we completed our synthesis of the novel cobaltocenium-based HEM by incorporating the cobaltocenium cation into a polysulfone matrix.

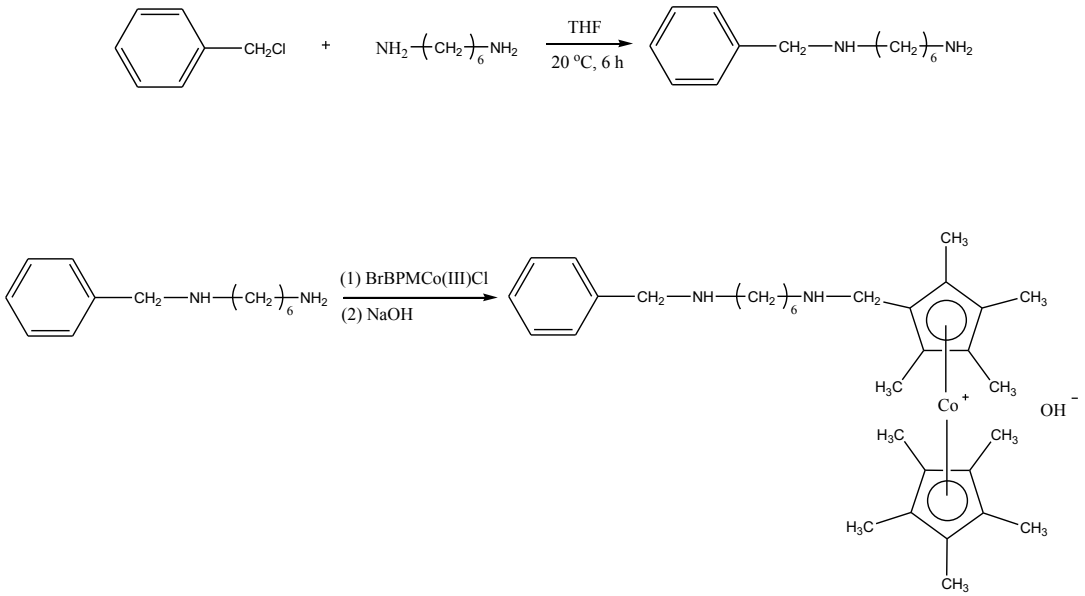

Figure 78. Synthesis of model molecules benzyl hexamethylenediamine (top) and bis(pentamethyl)cobaltocenium(III) hydroxide-linked benzyl hexamethylenediamine (bottom).

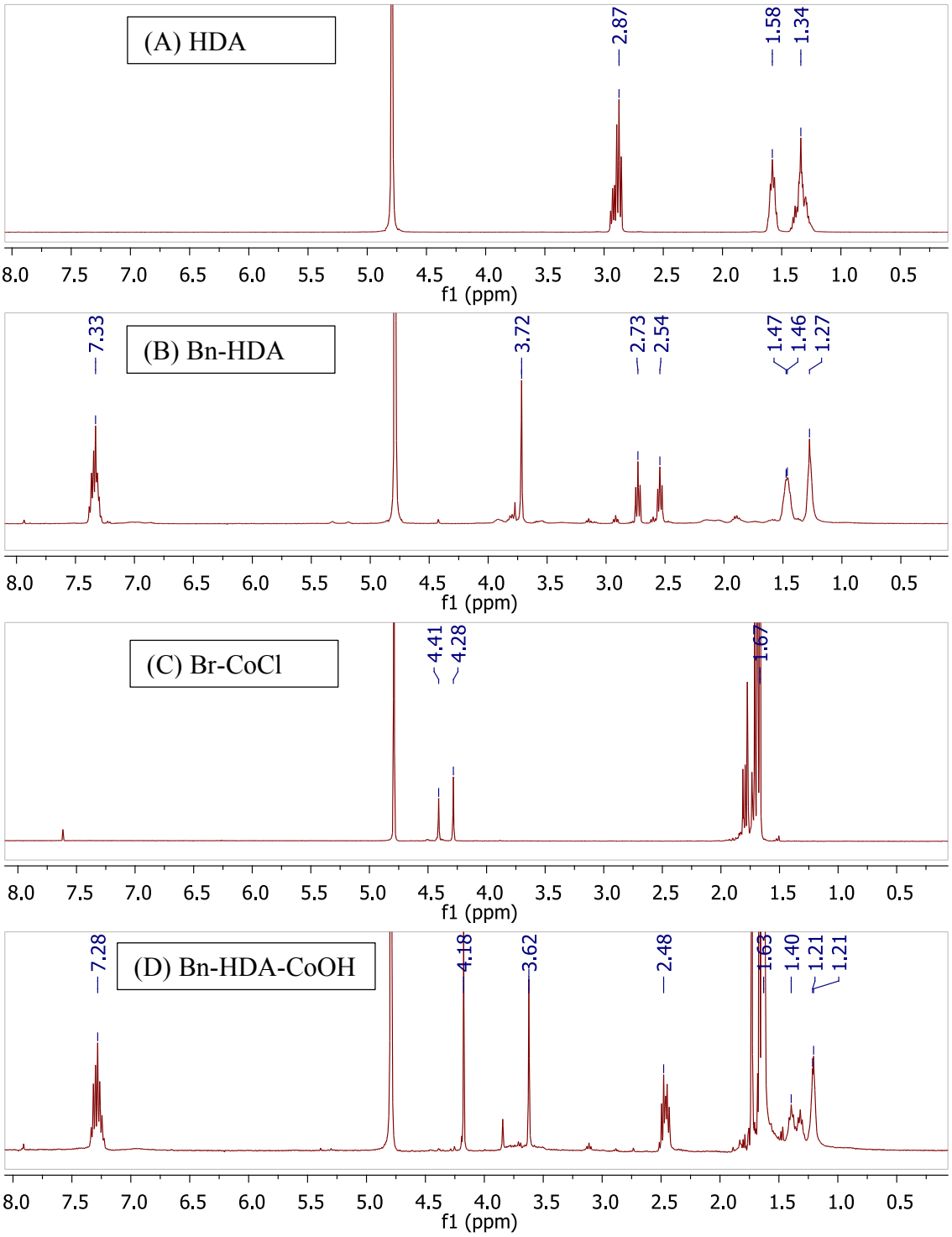

Figure 79. ^{1}H NMR spectra of model reaction species (A) hexamethylenediamine, or HDA; (B) benzyl hexamethylenediamine, or Bn-HDA; (C) brominated bis(pentamethyl)cobaltocenium chloride, or Br-CoCl; and (D) benzyl hexamethylenediamine bis(pentamethyl)cobaltocenium hydroxide, or Bn-HAD-CoOH.

We prepared cobaltocenium-based polysulfone membranes, which show deep yellow color and are uniform, flexible, and robust. SAXS analysis showed that the cobaltocenium membranes are amorphous and have a uniform microstructure.

We investigated the stability of cobaltocenium under aggressive conditions, both as a small molecule and in a polymer membrane. The bis(pentamethyl)cobaltocenium salt shows at least 1000 hours of durability at 140 ^{o}C in 1 M NaOD solution with only about 1.8% degradation, assuming methanol is the final degradation product (3.33 ppm, Figure 80). On the other hand, the cobaltocenium-based membrane shows at least 2000 hours of durability at 100 ^{o}C in 1 M KOH solution, with no changes in morphology, color, flexibility, or conductivity. This observed high stability is consistent with what has been reported previously (stable up to 176 ^{o}C in alkaline conditions[lvi,lvii]), confirming the potential of the cobaltocenium cation system.

The membranes show decent hydroxide conductivity: 10 and 22 mS/cm were obtained with degrees of chloromethylation of 100% and 123%, respectively. As with the sulfonium-based membranes, we believe the conductivity has room to improve considering the relatively low ion exchange capacity (currently 1.1-1.2 mmol/g).

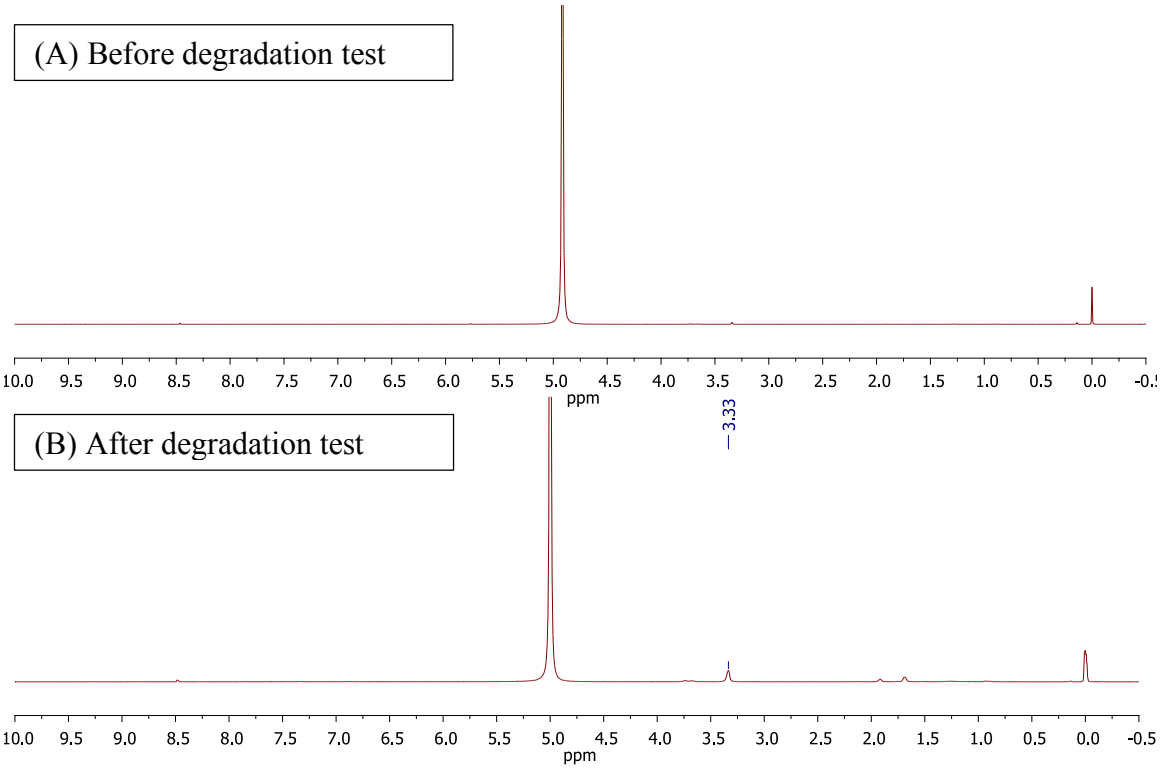

Figure 80. ^{1}H NMR spectra of model cation (A) before the degradation test, and (B) afterward. Test conditions: 140 ^{o}C, 1 M NaOD/D_2O, 1000 hours.

4.4 Stabilized and sterically hindered imidazolium cations

Recently, imidazolium-functionalized HEMs were widely studied due to their high ionic conductivity. [lviii] However, the most commonly used imidazolium hydroxide salts are unstable in alkaline solution. Herein, we demonstrate that imidazolium hydroxide can be stabilized by sterically protecting the C(2) position (α carbon with respect to both nitrogen atoms) and increasing the aromaticity of the imidazolium ring. Then, we use this strategy to prepare novel hydroxide exchange membranes with greatly enhanced alkaline stability.

Figure 81 outlines the synthetic route to the novel imidazole N-methyl-4,5-dimethyl-2-(2,4,6-trimethoxyphenyl)-imidazole (TMIM). 4,5-dimethyl-2-(2,4,6-trimethoxyphenyl)-1H-imidazole (TMIM-H) was prepared by reacting 2,4,6-trimethoxybenzaldehyde, 2,3-butanedione and ammomium acetate in methanol. TMIM-H reacted quickly with MeI under NaH in THF, giving TMIM in 95% yield. The chemical structures were confirmed by 1H NMR (Figure 82).

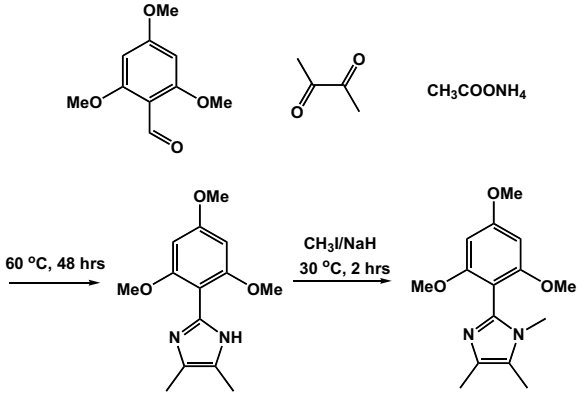

Figure 81. Synthesis of N-methyl-4,5-dimethyl-2-(2,4,6-trimethoxyphenyl)-imidazole (TMIM).

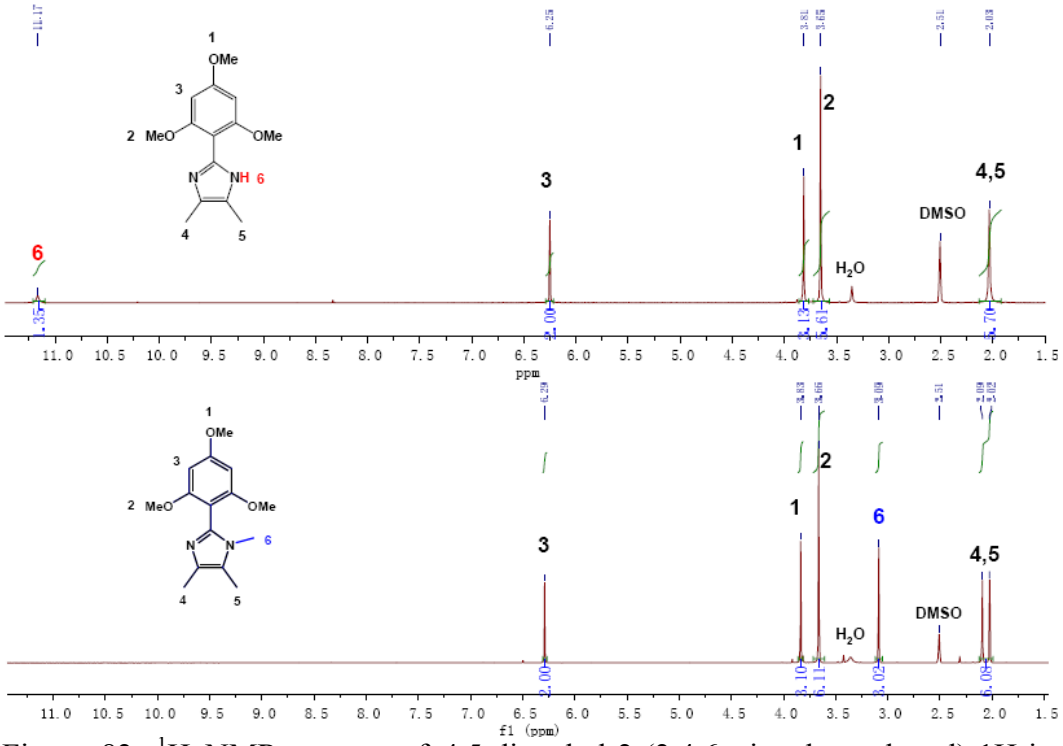

Figure 82. ^{1}H NMR spectra of 4,5-dimethyl-2-(2,4,6-trimethoxyphenyl)-1H-imidazole and N-methyl-4,5-dimethyl-2-(2,4,6-trimethoxyphenyl)-imidazole (TMIM).

On the basis of reported decomposition mechanisms of imidazolium salts, we hypothesized that crowding the reactive C(2) position with bulky, strongly electron-donating groups would hinder OH^- nucleophilic attack, thus increasing the alkaline stability. We compared our novel imidazolium hydroxide (TMIMOH) with the most commonly used one (IMOH), both synthesized as shown in **Figure 83**. The chemical stability of these model compounds was analyzed by ^{1}H NMR using D_2O as the solvent. TMIMOH showed very high thermal resistance. It was found to be stable in 1 M NaOD/D_2O at 100 °C; no change was detected after 48 h (Figure 84). IMOH, on the other hand, was only stable below 40 °C under the same conditions (Figure 85).

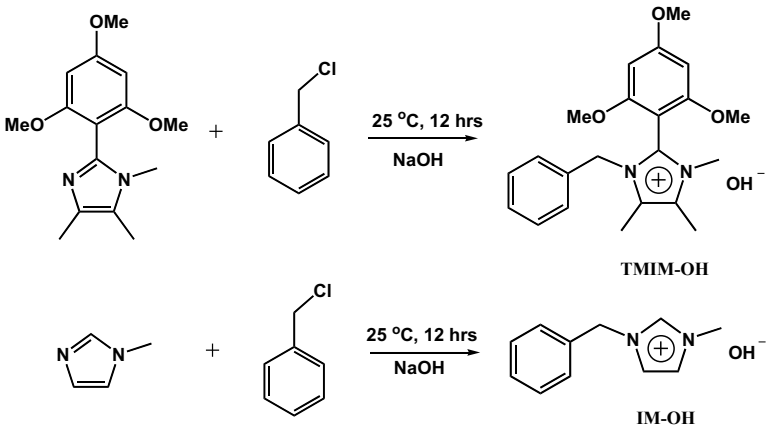

Figure 83. Synthesis of the model compounds.

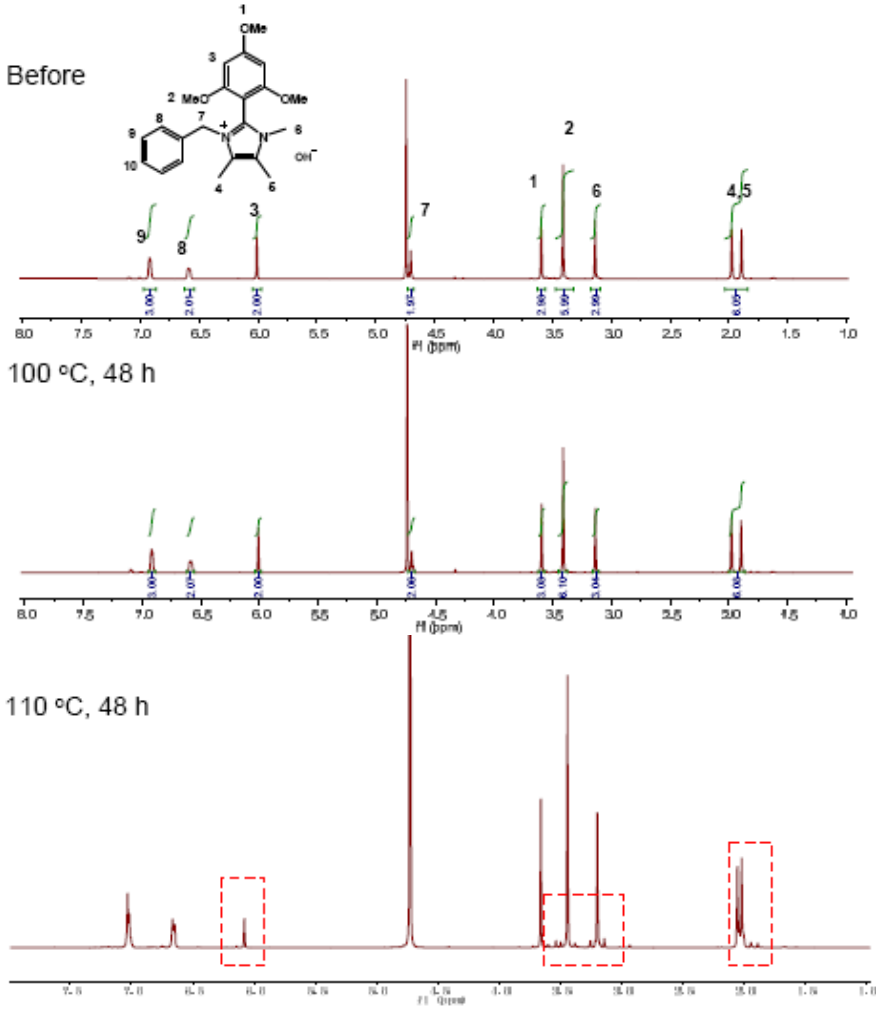

Figure 84. ^{1}H NMR spectra of TMIM-OH in 1M NaOD/D_2O after 48 h.

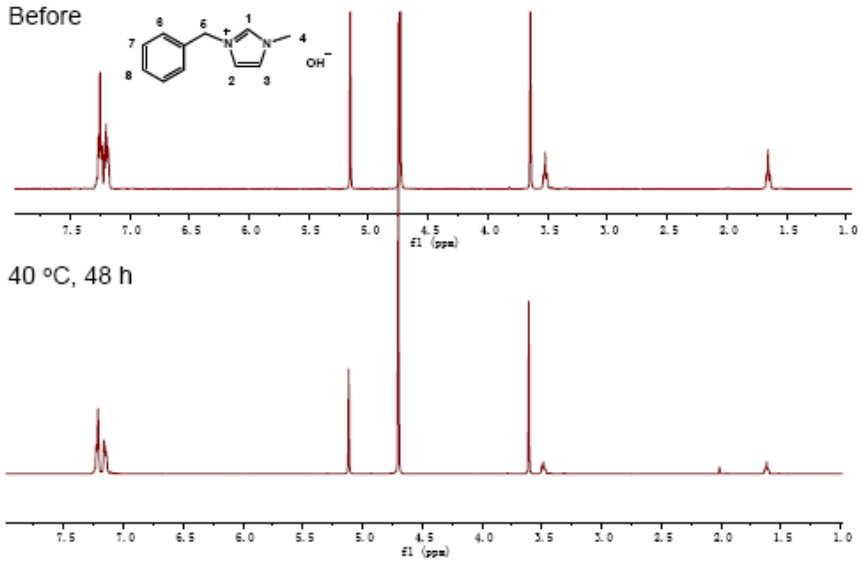

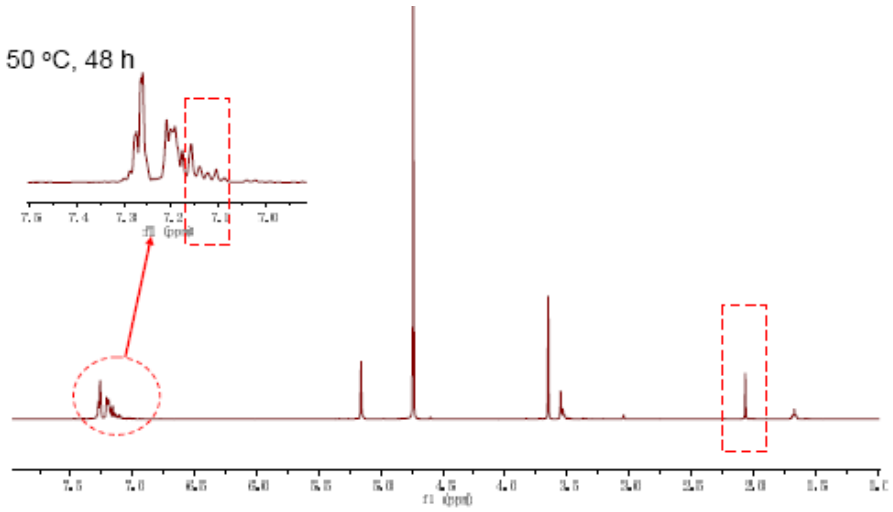

Figure 85. ^{1}H NMR spectra of IM-OH in 1 M NaOD/D_2O after 48 h.

Solvent-processable imidazolium-functionalized PPO (PPO-TMIMOH) was synthesized by the chloromethylation-Menshutkin two-step method (**Figure 86**). The membrane is transparent, flexible, and mechanically strong and exhibits high hydroxide conductivity (34 mS/cm). PPO-TMIMOH membrane also has outstanding stability, retaining flexibility and 95% of initial ionic conductivity even after immersion in 1 M NaOH at 80 °C for 48 h. By contrast, PPO-IMOH membrane becomes brittle and retains only 22% of its initial 32 mS/cm, indicating the degradation of cationic groups.

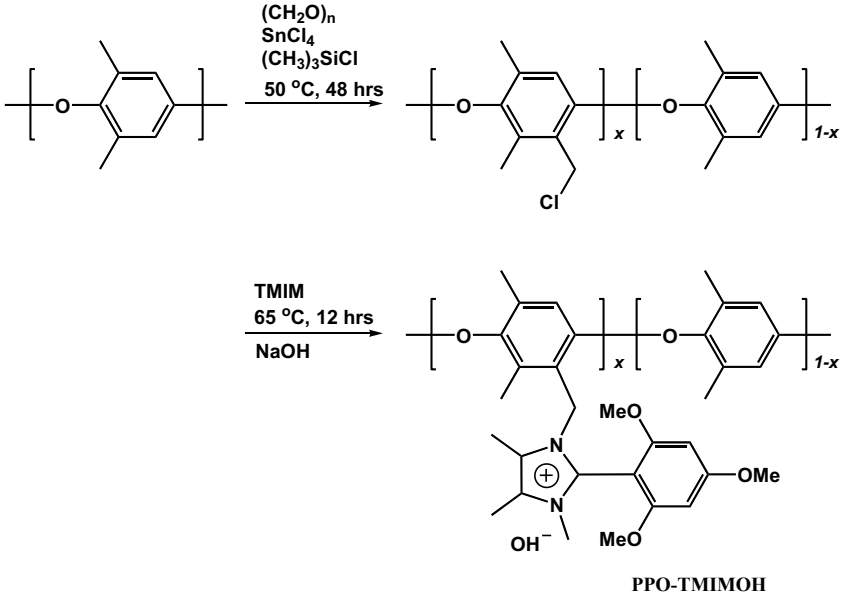

Figure 86. Synthesis of TMIM-based PPO hydroxide exchange membrane.

4.5 Strung cation architecture

Hydroxide exchange membranes have intrinsically lower ionic conductivity than proton exchange membranes under similar conditions, because the mobility of OH^- is lower than that of H^+(16). High IEC is necessary for HEMs to achieve high OH^-

conductivity. However, high IEC usually leads to excessive water uptake, decreasing the morphological stability and mechanical strength. This general trade-off between high hydroxide conductivity and low water uptake has been a great bottleneck in designing high-performance HEMs. Chemical cross-linking (17), physical reinforcement (18), and block-copolymer architecture (22) have been utilized to overcome the tradeoff (viz., lower water uptake while maintaining high hydroxide conductivity), but these techniques often bring challenging problems, such as reduced flexibility, lowered stability, and/or decreased micro-compatibility.

We provide a novel design that can efficiently overcome the conductivity/swelling trade-off: Stringing cations on side-chains of HEM polymers to create highly concentrated yet ordered hydrophilic domains, while still allowing the polymer backbone to form hydrophobic domains. Upon membrane formation, the cation strings as well as absorbed water constitute the hydrophilic phase and the polymer main-chain constitutes the hydrophobic phase, establishing an ideal bi-continuous membrane micro-structure. The hydrophilic phase provides high hydroxide conductivity; the hydrophobic phase provides mechanical stability and suppresses water uptake.

One example based on our cation string design is a strung quaternary ammonium hydroxide exchange membrane (SQAPS, **Scheme 17**). Briefly, SQAPS was synthesized by three major steps: (1) synthesis of small-molecule cation string (QACM-4, **Scheme 15**); (2) synthesis of tertiary-amine-functionalized polysulfone (TAPS, **Scheme 16**); and (3) attaching the small-molecule cation string to the tertiary-amine-functionalized polysulfone backbone, followed by membrane casting (SQAPS, Scheme 5). With similar IECs, the cation string HEM (SQAPS-30, 2.82 mmol/g) shows a 3-fold reduction in water uptake (53% vs. 160% at 20 ^{o}C) and a slight increase of hydroxide conductivity (67 vs. 58 mS/cm at 20 ^{o}C) when compared with normal quaternary ammonium-functionalized poly(aryl ether sulfone) without cation string structure (QAPS-75, 2.76 mmol/g).

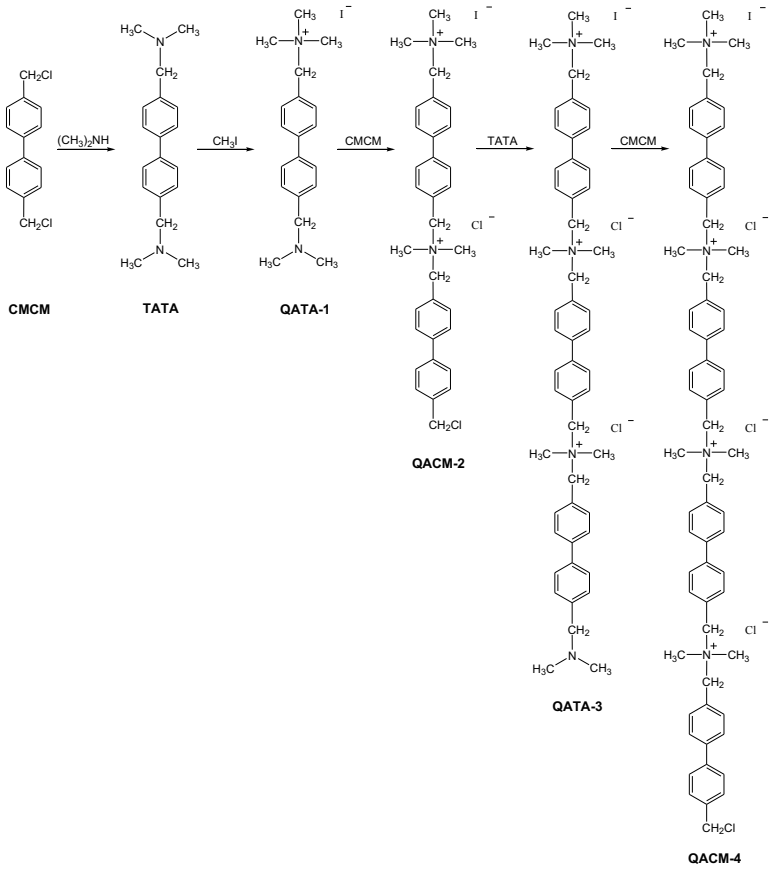

Scheme 15. Synthesis of the small-molecule quaternary-ammonium string.

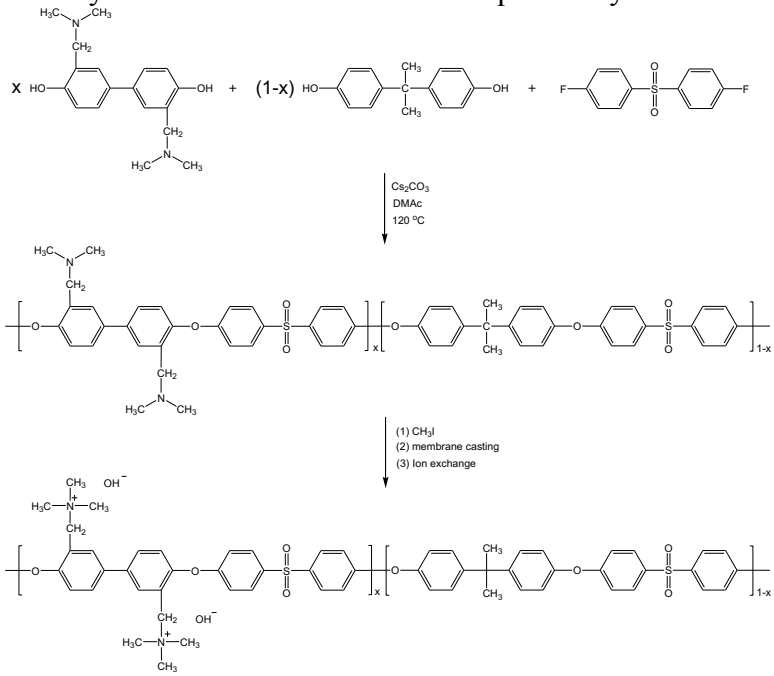

Scheme 16. Synthesis of the tertiary-amine-functionalized polysulfone (TAPS-x) and normal quaternary-ammonium polysulfone (nQAPS-x)

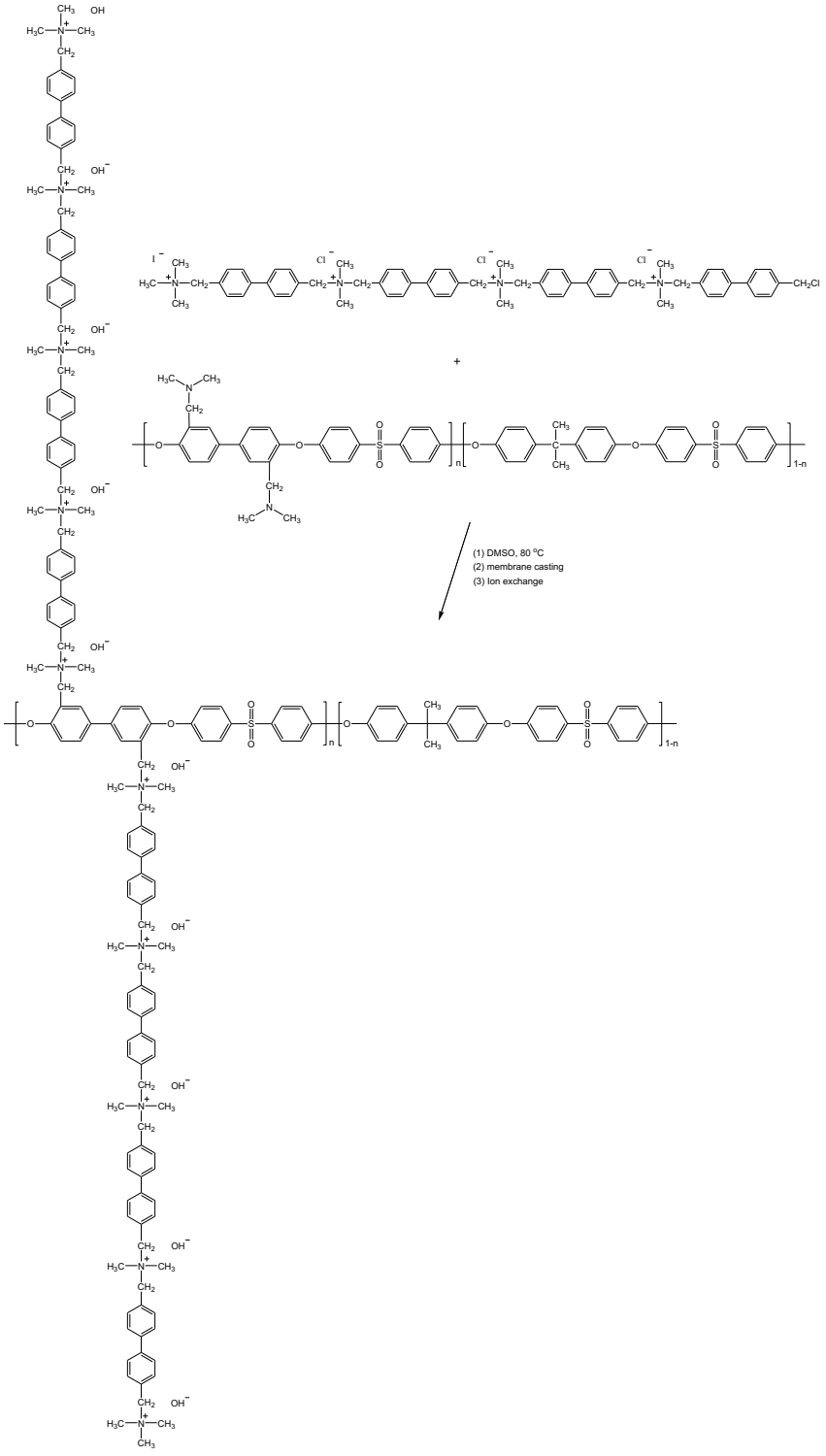

Scheme 17. Synthesis of the strung-quaternary-ammonium polysulfone (SQAPS-x)

4.6 Spiro C6 cations

Much of our focus has been on developing methods for functionalization of membranes with benzyltrimethylammonium cations, partly because of the ease of attachment, but

also because the group can be alkaline and thermally stable when attached to the right polymer backbone with the appropriate tether. Some alkaline exchange membranes that bear benzyltrimethylammonium cations have shown decreased conductivity performance over time while at high temperature and under alkaline conditions.[5] Recently, spirocyclic ammonium cations composed of five or six membered rings have indicated significantly higher alkaline stability up to temperatures as high as 160°C in 6M NaOH.[6] The stability has been reported to be a result of the preferred conformation of the ring structures and their inability to easily adopt a conformation that allows Hoffman elimination or substitution transition states. While the stability of the spirocyclic and similar ring-containing ammonium cations has been demonstrated with small molecule model structures, the attachment of such structures to stable backbones to result in processible materials for the preparation of membranes has not been shown. Our most recent research is directed at the development of membranes with improved alkaline stability by utilizing such cationic functional groups.

Poly(diallyldimethylammonium chloride) (PDADMAC) is a common cationic polymer material used in water treatment membranes, flocculants, and biomaterials.[7,8] PDADMAC is commonly synthesized from diallyldimethylammonium chloride (DADMAC) through radical cyclopolymerization. While PDADMAC is a common polymer, very little work has been done to prepare block copolymers of PDADMAC with a hydrophobic block. There have been several reports in which the DADMAC monomer has been polymerized by reversible addition fragmentation chain-transfer polymerization (RAFT)[9,10],[9,10] where homopolymers with low polydispersity have been obtained, indicating the feasibility of block copolymer synthesis. A similar monomer, diallylpiperidinium chloride (DApipCl), has been shown to easily polymerize by free radical cyclopolymerization and produce polymers containing spirocyclic ammonium cations.[11] However, no further investigation of PDApipCl is present in the literature.

Scheme 18. Polymerization of Diallylammonium Chloride Salts

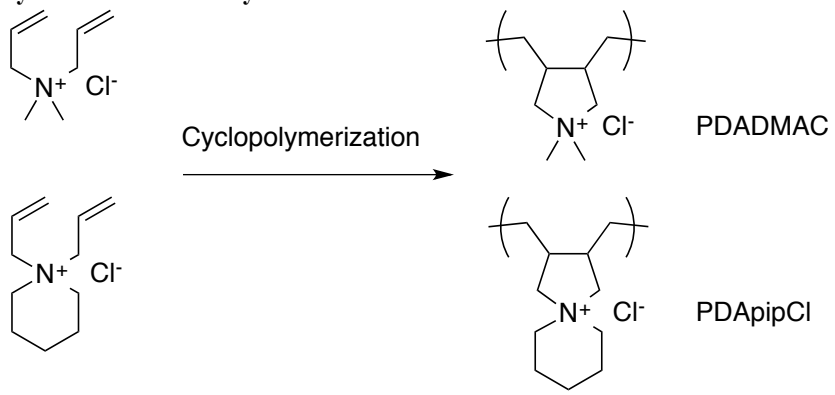

In the present work, we propose that a membrane consisting of a polysulfone backbone with random poly(diallylpiperidinium hydroxide) grafts will have improved alkaline stability of the ammonium cations and ultimately a longer lifetime when compared to the more traditional benzyltrimethylammonium functionalized membranes. The approach we are taking is to functionalize high molecular weight polysulfone (or poly(2,6-dimethyl-1,4-phenylene oxide) (PPO)) with RAFT chain transfer agents (CTAs). PDAPipCl will then subsequently be grafted from the polysulfone backbone producing a

spirocyclic ammonium functionalized graft copolymer. Controlling the reaction time will allow control over the conversion and ultimately IEC, conductivity and water uptake.

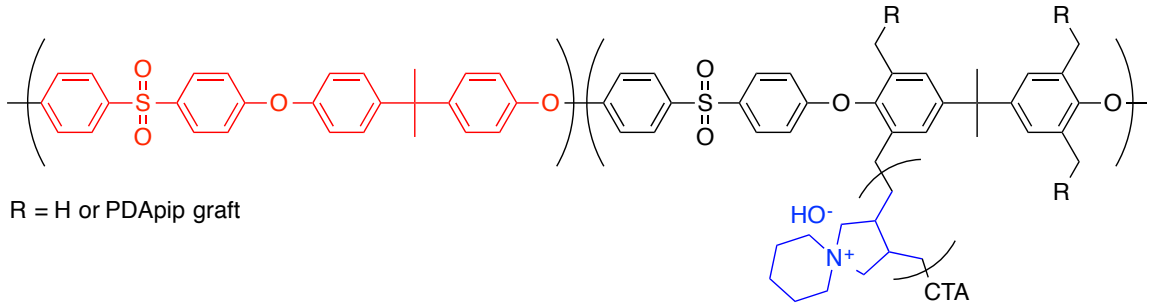

Figure 87. Polysulfone-PDApipOH Graft Copolymer

The polysulfone-graft-PDAPipCl) copolymers are expected to be mechanically robust, as a result of the polysulfone backbone, and to phase separate into hydrophilic PDAPipCl domains and hydrophobic polysulfone domains. Ultimately, these materials are expected to show enhanced alkaline stability under harsh alkaline fuel cell operating conditions.
Synthesis of the *N,N*-diallylpiperidinium chloride (DApipCl) monomer was readily accomplished in two steps. First, piperidine was reacted with allylbromide in the presence of sodium hydroxide. The recovered *N*-allylpiperidine was purified by distillation and further reacted with allylchloride. The final *N,N*-diallylpiperidinium chloride salt crystallized from the reaction mixture thus the DApipCl monomer was recovered without further purification. Structural analysis of the obtained DApipCl confirmed the presence of two allyl moieties and is shown below in the following figure.

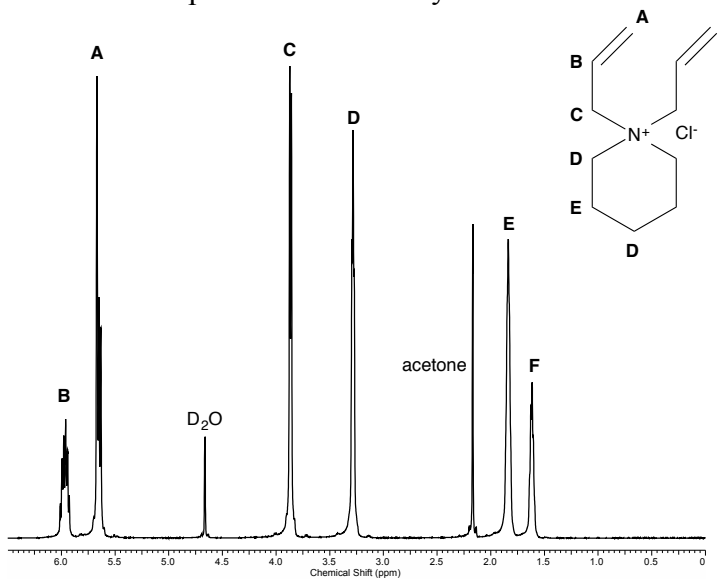

Figure 88. ^{1}H NMR Spectrum of *N,N*-diallylpiperdinium chloride (DApipCl)

Synthesis of the PDApipCl homopolymer under both free radical and RAFT conditions has been accomplished. Free radical polymerization was of the DApipCl monomer in DMSO was successful and the resulting material structure was determined by ^{1}H NMR spectroscopy and is shown below.

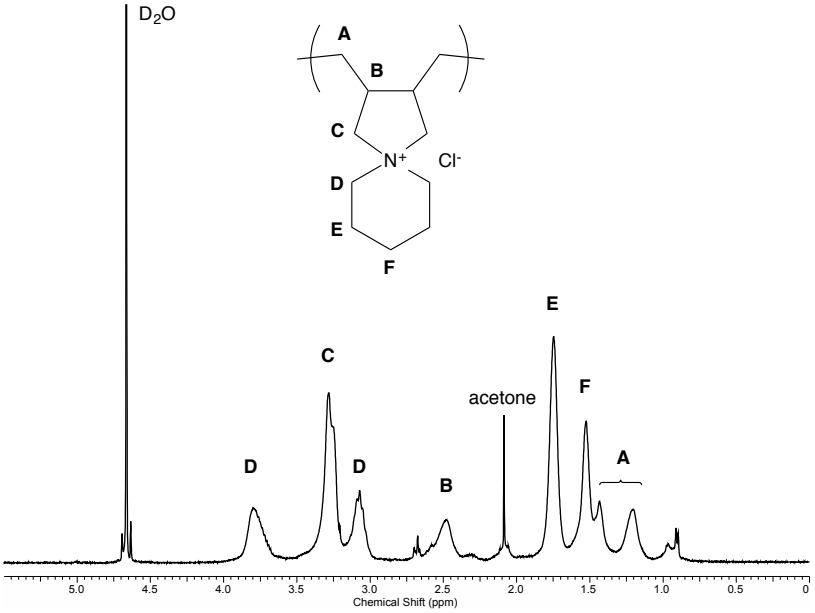

Figure 89. ^{1}H NMR Spectrum of Poly(diallypiperdinium chloride) (PDApipCl)

The solubility of PDApipCl in DMSO is limited. Under free radical polymerization conditions the homopolymer readily precipitates out of the reaction mixture. Polymerizing DApipCl under RAFT conditions in DMSO was precluded due to limited solubility. However, when the RAFT polymerization of DApipCl is carried out in methanol, solubility is no longer a problem. Structural analysis, shown in the figure below, of the PDApipCl homopolymer generated under RAFT conditions with the benzylethylxanthate (BEX) CTA, clearly indicates xanthate end groups and a successful polymerization.

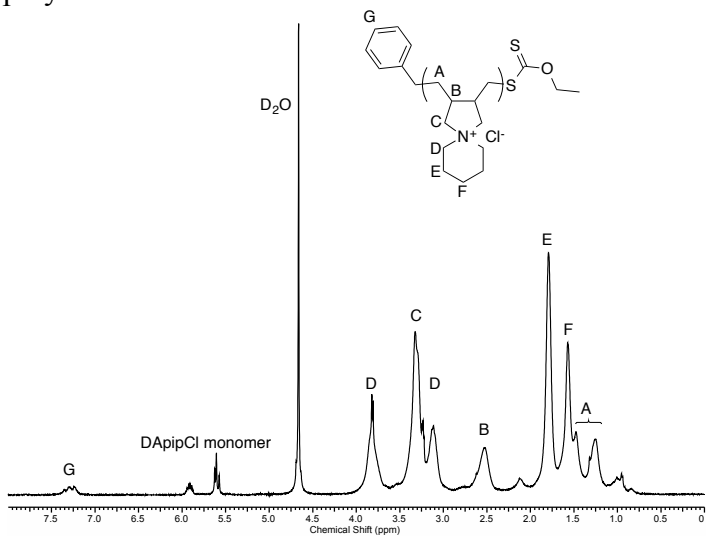

Figure 90. PDApipCl Homopolymer with BEX CTA End Group

Numerous reports on the structural determination of PDADMAC have shown that the DADMAC monomer ring closes to produce *cis* and *trans* 5 membered rings. The cyclopolymerization of DApipCl produces a spirocylic material in which the repeat units are bridged by 5 membered rings.

Polysulfone containing tetramethylbisphenol A repeat units and PPO polymers can easily be modified to contain a variety of CTAs. Modification proceeds by first brominating the benzylmethyl groups followed by substitution with a corresponding dithioacid, shown in the scheme below. Currently we are investigating two different CTAs, BEX, and benzylpropanoic acid trithiocarbonate (BPATC).

Scheme 19. CTA Functionalization of Polysulfone and PPO Materials

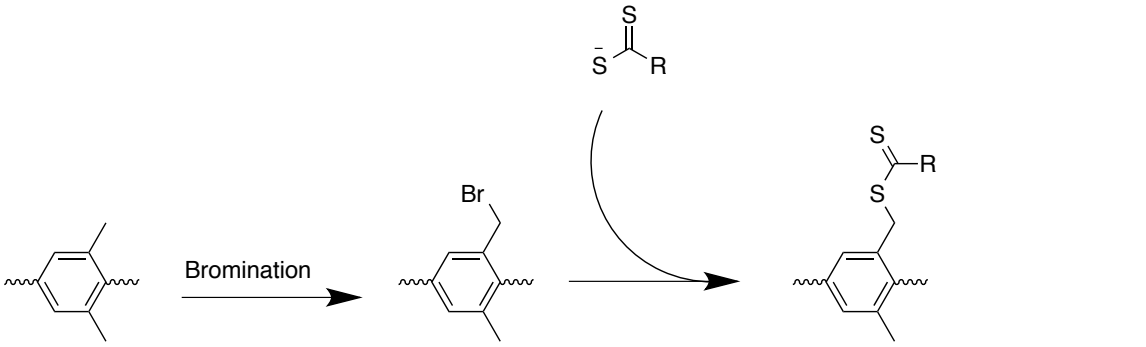

R = OCH_2CH_3 or SCH_2CH_2COOH

Synthesis of the polysulfone-PDApipCl and PPO-PDApipCl graft copolymers currently has met limited success. The two main challenges have been employing a CTA capable of polymerizing DApipCl, and solubility of the amphiphilic polymer. High molecular weight polysulfone has been functionalized with a variety of CTAs including dithiobenzoates, trithiocarbonates and xanthates. The latter two CTAs have shown the most promise in their ability to produce the homopolymer, and the dithiobenzoates fail due to the stability of the RAFT intermediate radical being far greater than the propagating polymer. Solubility is currently the largest obstacle. The only common solvent for the polysulfone and PPO macro RAFT agents and PDApipCl is *N*-methylpyrrolidone (NMP). However, the solubility of DApipCl in NMP is limited to approximately 1 M at elevated temperatures. It was determined that DApipCl solubility can be dramatically improved with the addition of a small amount of methanol. Through several experiments we have concluded that concentrated solutions, up to 25% (w/v), of the polysulfone macro CTA and PDApipCl can be prepared from NMP with 10% methanol. Although, we have found conditions in which both the macro CTAs and PDApipCl monomer can be dissolved, RAFT polymerization still is a challenge due to solubility changes as the reaction proceeds. The challenges notwithstanding, we have been able to graft a small amount of PDApipCl from a polysulfone macro CTA, shown the figure below, and we estimate approximately 2 repeat units have been grafted. Current work is focused on improving the conversion such that a conductive membrane, with an IEC of at least 1 is obtained.

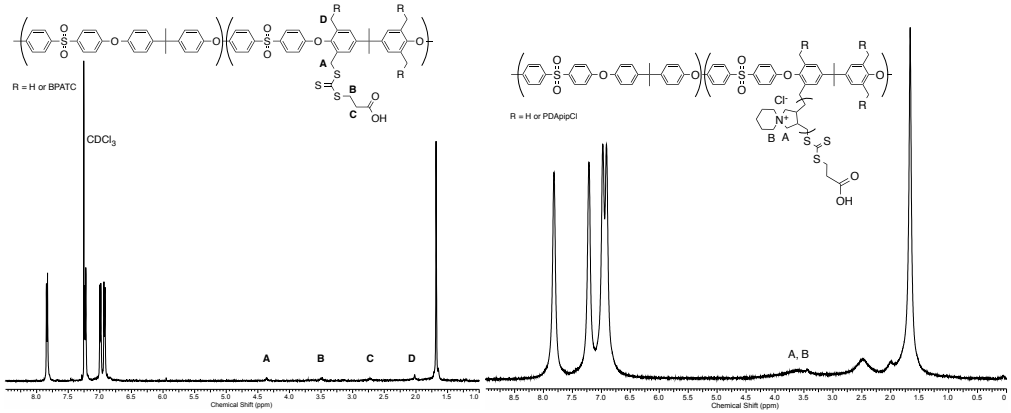

Figure 91. (Left) BPATC Functionalized Polysulfone, (Right) Polysulfone-graft-PDApipCl Copolymer

4.7 C6 cations from hydrogenation of pyridine

In another approach to prepare piperidinium functional polymers, we are examining the hydrogenation of poly(4-vinylpyridine) to a poly(vinylpiperidine) that can be quaternized by reaction with alkyl halides. As a design, we are investigating the synthesis of polyethylene-b-poly(4-vinyldimethylpiperidinium) for anion exchange membrane applications, with the general structure of the block copolymer shown in the figure below.

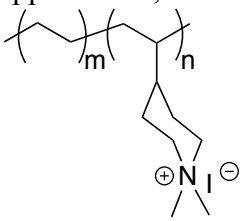

Figure 92. The Designed Block Copolymer Polyethylene-b-Poly(4-vinyldimethylpiperidinium iodide)

Several reasons motivate us to pursue this polymer. Semicrystalline polyethylene is expected to have excellent chemical resistance and mechanical properties, remaining stable in strong base. We have shown in previous reports that a polyethylene-b-poly(vinylbenzyltrimethylammonium hydroxide) polymer shows excellent mechanical properties and good conductivities with low water uptake. Changing the cationic functionality to the piperidinium functional group should improve the long-term alkaline stability compared to the benzyltrimethylammonium group at relatively high temperatures.[12]

The synthetic route toward the target polymer is shown in the following scheme. Sequentially polymerizing 1,3-butadiene and 4-vinylpyridine prepares a new block copolymer, polybutadiene-block-poly(4-vinylpyridine), that after hydrogenation yields polyethylene-block-poly(4-vinylpiperidine). In a final step, the polymer can be processed into films and then reacted with methyl iodide to produce the target polymer polyethylene-block-poly(4-vinyldimethylpiperidinium).

Scheme 20. The Synthetic Route of Polyethylene-b-Poly(4-Vinylpiperidinium iodide)

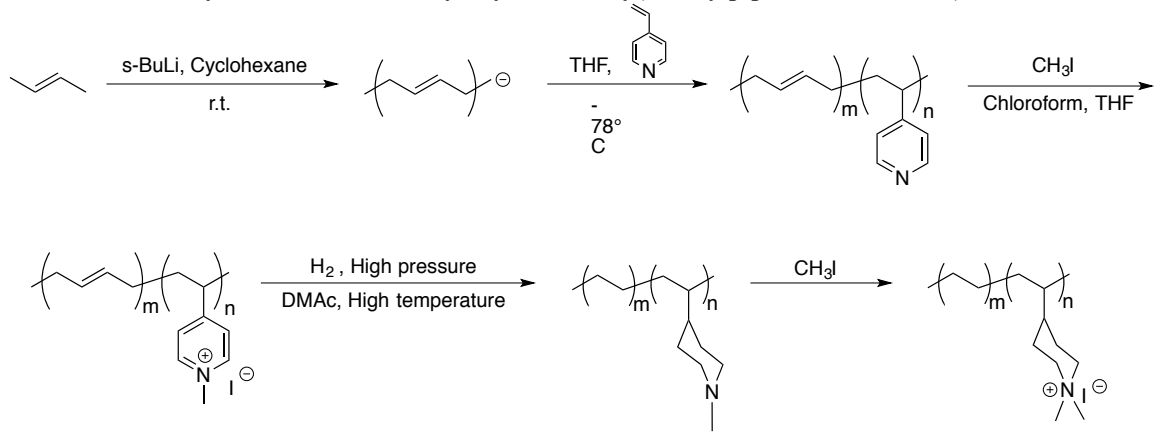

We have so far successfully synthesized polybutadiene-block-poly(4-vinylpyridine) through anionic polymerization. The molecular weight was targeted to yield a polybutadiene block of approximately 70,000 g/mol and a poly(4-vinylpyridine) block of approximately 20,000 g/mol. Due to the difference in solubility of the two very different polymer blocks, the block copolymer was found to be insoluble in most common solvents making it difficult to characterize the molecular weight through GPC measurement. However, the polymer is soluble enough to characterize by NMR spectroscopy. The polybutadiene-block-poly(4-vinylpyridine) copolymer was washed in boiling methanol and hexanes to remove any impurities. The ^{1}H NMR spectrum of the polymer is shown in Figure 7. In this spectrum, peaks "a" and "b" respectively correspond to the protons on the pyridine ring; peak "c" refers to the two protons on the double bonds of the polybutadiene; peak "d" corresponds to the four protons on the methylene group of the polybutadiene. The integration of peak "a" or "b" to peak "c" reflects the mole ratio of hydrophilic to hydrophobic polymer blocks. The integration of the peaks was the same as the feeding mole ratio of monomers, proving the high conversion of the reaction in the formation of block copolymer.

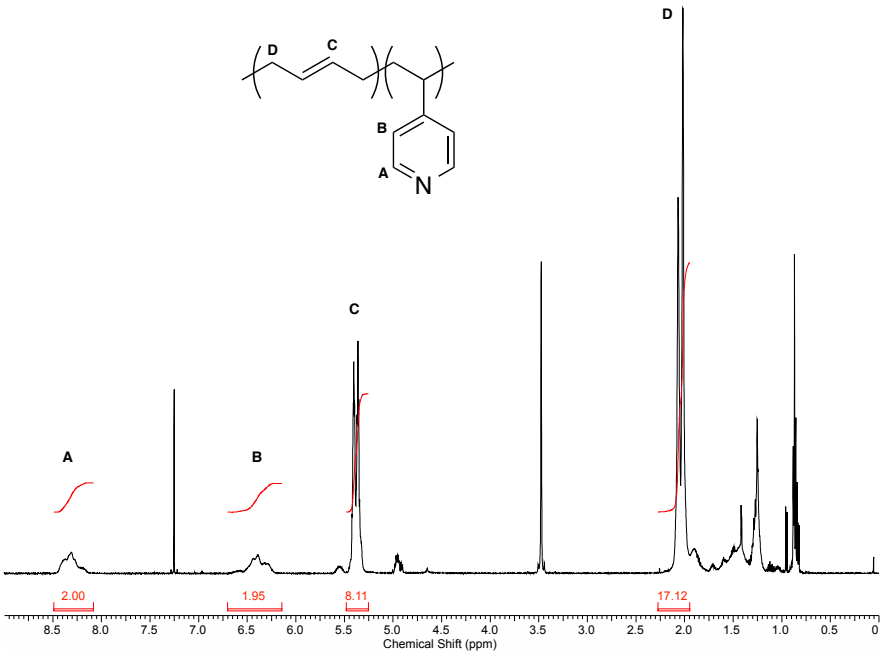

Figure 93. ^{1}HNMR of Block Copolymer Polybutadiene-block-Poly(4-vinylpyridine) in $CDCl_3$ at 25°C

Previous studies have shown that methylated poly(4-vinylpyridine) can be hydrogenated under milder conditions compared to poly(4-vinylpyridine), so we have synthesized polybutadiene-block-poly(N-methyl-4-vinylpyridinium) to make the hydrogenation process easier.[13] We hydrogenated the polybutadiene-poly(N-methyl-4-vinylpyridinium) block copolymer try to obtain the polyethylene-block-poly(N-methyl-4-vinylpiperidine). Because the hydrogenated block copolymer is insoluble most solvents, its structure cannot be determined by ^{1}HNMR spectroscopy. In order to show the resulting polymer structure, infrared spectroscopy was employed. The IR spectrum of polybutadiene-block-poly(N-methyl-4-vinylpyridinium), which is shown in the top figure below, was compared to that of the hydrogenated block copolymer (bottom figure). Figure 94 shows a peak at 3005.88 cm^{-1}, which correspond to C-H bonds of the pyridine ring, the peaks at 1640.78 cm^{-1}, 1573.26 cm^{-1}, and 1518.12 cm^{-1} also correspond to the "C=C" bond or "C=N" bond. These peaks are characteristic peaks demonstrating that the polybutadiene blocks and poly(N-methyl-4-vinylpyridinum) blocks are present in the cpolymer. Figure 95 shows there are no peaks above 3000 cm^{-1} thus, it supports that the pyridinium rings in block copolymer were fully hydrogenated to form piperidine rings. However, a peak around 1640 cm^{-1} remains indicating that some double bonds remain in the partially hydrogenated block copolymer. Figure 96 indicates three possible polymer structures "a", "b", and "c". Structure "a" represents the target polymer, and structures "b" and "c" are the possible unsaturated products remaining after hydrogenation. We believe that the remainder of unsaturated material resides in the polybutadiene block, therefore further hydrogenation is required.

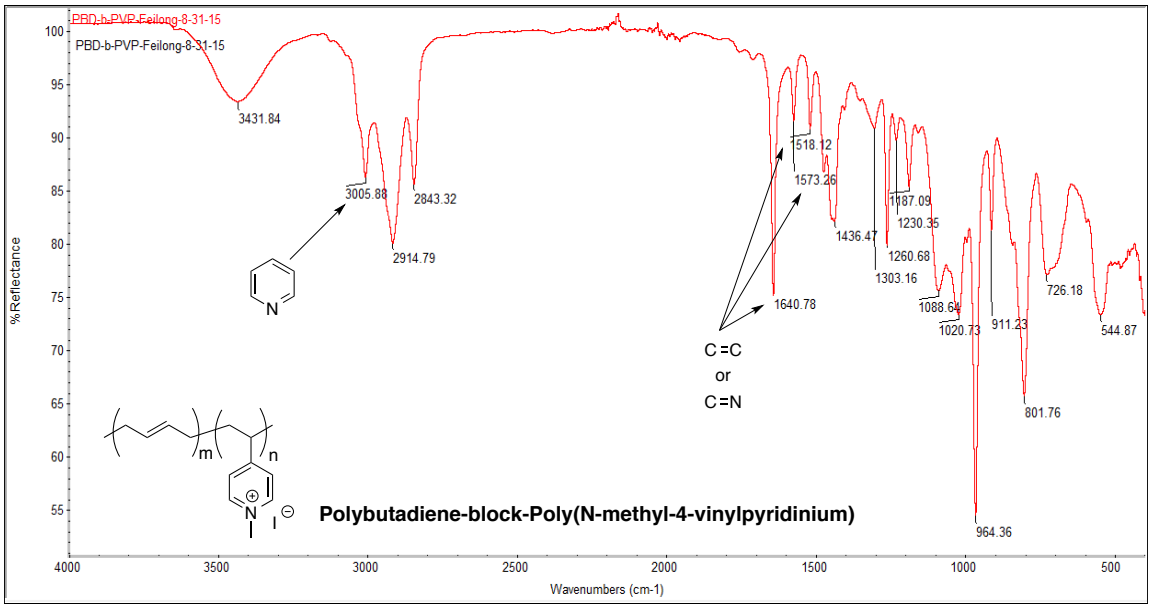

Figure 97. IR Spectrum of Polybutadiene-block-Poly(N-methyl-4-vinylpyridinium iodide).

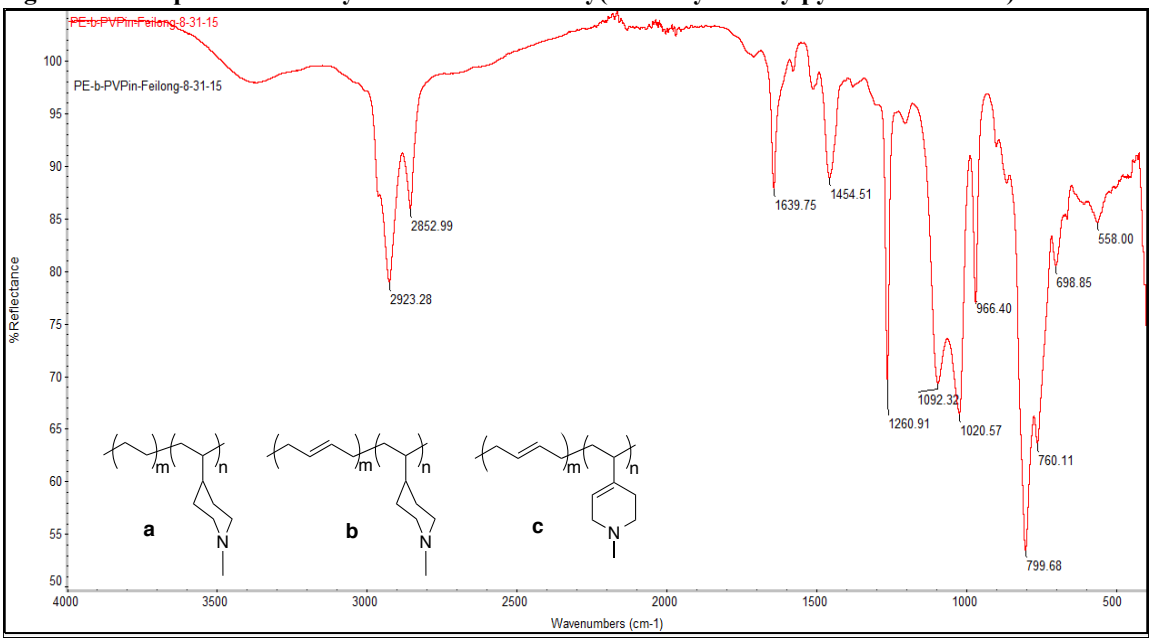

Figure 98. IR Spectrum of Hydrogenated Polybutadiene-block-Poly(N-methyl-4-vinylpyridinium iodide)

A mild hydrogenation procedure, Scheme 21, in which p-toluenesulfonyl hyrazide is used, can reduce polybutadiene to polyethylene. Currently, we are applying these reaction conditions to determine that the source of unsaturation is the polybutadiene block and to completely reduce the block copolymer. We will analyze the resultant material with FT-IR, which will indicate full hydrogenation if the peaks between 1500 and 1700 cm^{-1} are no longer present.

Scheme 22. Further hydrogenation.

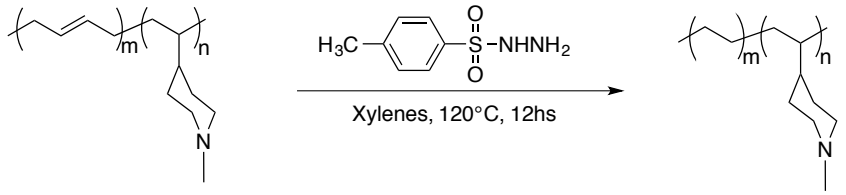

The incompletely reduced copolymer is a very tough, ductile material, and we anticipate that the further reduction, followed by film preparation and quaternization will lead to mechanically strong membranes. The combination of the stable and mechanically strong polyethylene backbone with a stable ammonium cation is anticipated to produce the superior membranes.

4.8 C6 cations via quaternization

Polyisoprene-r-polyvinylbenzyl chloride based random polymer and poly vinylbenzyl chloride-b-polycyclooctene-b-polyvinylbenzyl chloride triblock polymer backbones were studied, Scheme 1. Selection of these backbones was due to both polyisoprene and polycyclooctene having low Tg so making the polymers flexible and elastic to handle. It was envisioned that the random materials would act as an ionomer and the triblock material as a membrane. The random polyisoprene-polyvinylbenzyl chloride based random polymers after functionalizing with trimethyl ammonium or methyl piperidinium cations, gave materials with high ion exchange capacities (IEC), >3.0 mmol/g, and these high IECs led to materials with compromised mechanical strength, i.e. not suitable for membrane formation, but with the chemical stability needed for use in electrodes. The polyvinylbenzyl chloride-co-polycyclooctene triblock functionalized with methyl piperidinium had IECs as high as 2.0 mmol/g and gave a phase separated lamellar morphology leading to a higher conductivity and good membrane forming properties at least in the dry state.

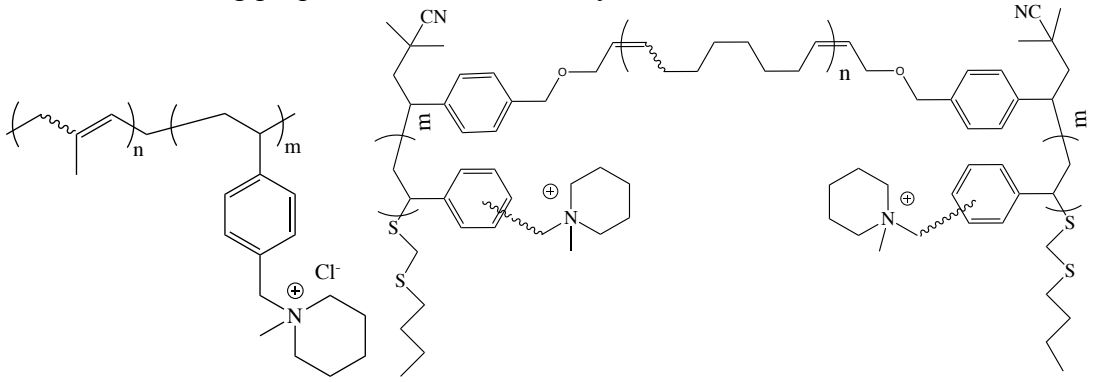

Scheme 23. Polyisoprene-r-polyvinylbenzyl chloride based random polymer, left, and polyvinylbenzyl chloride-b-polycyclooctene-b- polyvinylbenzyl chloride triblock, right.

Cation selection

Four cation species were studied in this project, the standard trimethylbenzyl ammonium cation which is known to have substandard chemical stability but is the standard benchmark due to its ease of stability and common usage. Tris(2,4,6-trimethoxyphenyl) phosphonium (TTMPP) was selected as it is bulky and contains

electron-donation functional group which is thought to be make it more hydroxide stable than the benchmark benzyl trimethyl ammonium cation. Dimethylpiperidinium has been recently proposed to be very chemically stable due to the geometric constraint of the six-membered ring on the elimination transition state. Dimethylpyrrolidinium is also thought to have high stability due to β proton in the non-anti-periplanar position. The chlorinated polymers where therefore quatenized to give, benzyl trimethyl ammonium (BTMA) benzyl TTMPP, benzyl methylpiperidinum (MPRD), and benzyl methyl pyrrolidinium (MPY) cations. The first materials described below all had moderate IECs of around 1.3 meq g^{-1}.

We compare the chemical durability of PCMS-PCOE-PCMS-MPRD to the polymers that with same polycyclooctene triblock backbone but have been functionalized with methylpyrrolidinium, tris(2,4,6-trimethoxyphenyl) phosphonium and trimethyl ammonium (Figure 2). Membranes were soaked in 1 M KOH at 80 °C for 14 days and 30 days respectively. Compared to the 1st generation BTMA cation functionalized polymer, the 2nd generation cation functionalized films with the saturated ring cations show improved durability. But, both PCMS-PCOE-PCMS-MPY and PCMS-PCOE-PCMS-TTMPP degraded faster than PCMS-PCOE-PCMS-MPRD. PCMS-PCOE-PCMS-MPRD has 15.8% loss in IEC after 14 days, and 42% loss in IEC after 30 days, which is much more stable compared to BTMA which degrades 25% after 4 days by soaking in 1 M KOH at 80°C.

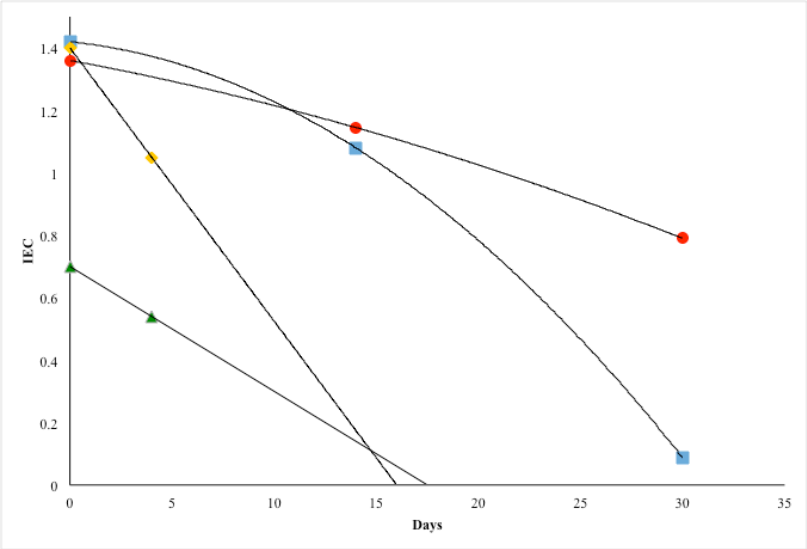

Figure 2. Comparison of durability between 1st geneartion cation functionalized PCMS-PCOE-PCMS-BTMA (diamonds) and 2nd generation cation functionalized PCMS-PCOE-PCMS-MPRD (circles), PCMS-PCOE-PCMS-MPY (squares) and PCMS-PCOE-PCMS-TTMPP (triangles) by soaking in 1 M KOH at 80°C.

The hydroxide conductivity (Figure 3) of the films was measured under a CO_2 free environment, using UHP nitrogen gas. We noticed PCMS-PCOE-PCMS-TTMPP gave a lower conductivity due presumably to degradation above at 70°C while conductivities of PCMS-PCOE-PCMS-MPRD, PCMS-PCOE-PCMS-MPY keep increasing from 30°C to 80°C due to the higher stabilities. Note that we have seen in the past that it is possible to maesure the hydroxide conductivity of well phase separated polymers with BTMA cations at temperatures <80°C. PCMS-PCOE-PCMS-MPRD (IEC=1.36 mmol/g) had the

highest conductivity, 95 mS/cm at 80°C, than PCMS-PCOE-PCMS-MPY (IEC=1.42 mmol/g), even though IEC is slight smaller.

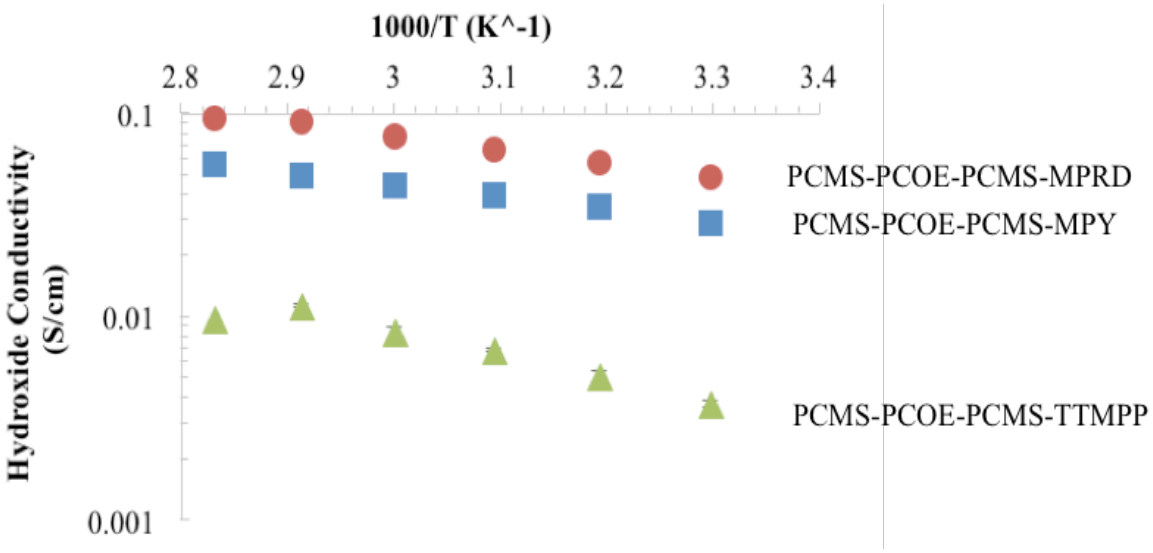

Figure 3. Comparison of hydroxide conductivities betwen PCMS-PCOE-PCMS-MPRD, PCMS-PCOE-PCMS-MPY and PCMS-PCOE-PCMS-TTMPP.

None of the films described above survived testing at ProtonOnSite, because the films became too mechanically weak when swollen in water. We decided to solve this problem by cross-linking the hydrophobic bock of the polymer by photo-crosslinking the residual double bonds with a dithiol. Much work was needed to optimize this process as too much crosslinking resulted in a material that was too brittle. The right level of crosslinking actually enabled us to also increase the IEC of the material. Below we reveal the methods and properties of these films.

Procedure of membrane generation and fabrication

Triblock Copolymer Quaternization with MPRD

A 250 mL conical flask was charged with 50 mL of MPRD (pure) and purged with dry Nitrogen for 15 min. Precursor triblock copolymer ($(PCMS)_{107.5}$-$(PCOE)_{344}$-$(PCMS)_{107.5}$, *ca* 2 g) was then added to the flask with vigorous stirring to dissolve the copolymer in MPRD at room temperature. The flask was sealed under a nitrogen environment for 72 h with no active purge. The pale yellow gel was precipitated in MeOH, washed with MeOH, and then dried in the oven at 30 °C under vacuum overnight. Yield ($(PCMS)_{107.5}$-$(PCOE)_{344}$-$(PCMS)_{107.5}$ w/MRRD) : Yield 2.58 g.

Photo-Cross-Linking

All membranes were prepared by drop-casting from a chloroform solution. ($(PCMS)_{107.5}$-$(PCOE)_{344}$-$(PCMS)_{107.5}$ w/MPRD, 1.64 g) was totally dissolved in chloroform (*ca* 80 mL) at 45 °C for 3 days. Photoinitiator solution (IRGACURE 2959, 0.082 g, 5 % wt of polymer) was then added to the polymer solution. Dithiol cross-linker (110 μL, DT, 7.5 %) was added relative to the total amount of PCOE units as UMass described. The reaction mixture was stirred at room temperature under dark condition for 5 min. The polymer solution was drop cast on a Teflon sheet, covered with a piece of watch glass, and slowly evaporated the solvent overnight in the dark. Cross-linking of the membranes was achieved by exposure to UV light (Fusion UV systems, Inc. belt speed at

3, 7 runs). These membranes were peeled off the substance and soaked with DI water to remove excess DT.

Thin film fabrication

Membrane fabrication methods we used include solvent drop cast, using micrometer applicator and automatic film coater. We have cast freestanding, uniform films via modification of the cast procedure. Polymer was dissolve in chloroform solvent and thoroughly stirred for 1 h. Then polymer solution was filter with a needle filter and drop cast on a piece of pre-cleaned Teflon substrate. Due to the low boiling point of chloroform, we have control the solvent evaporation rate by covering a watchable petri dish on top of polymer solution. After the membrane was dried overnight, it was peeled off and moved to the vacuum oven for a second over night drying stage. Uniform films as thin as 40 μm membrane and >300 cm^2 were cast for these studies (Figure 4).

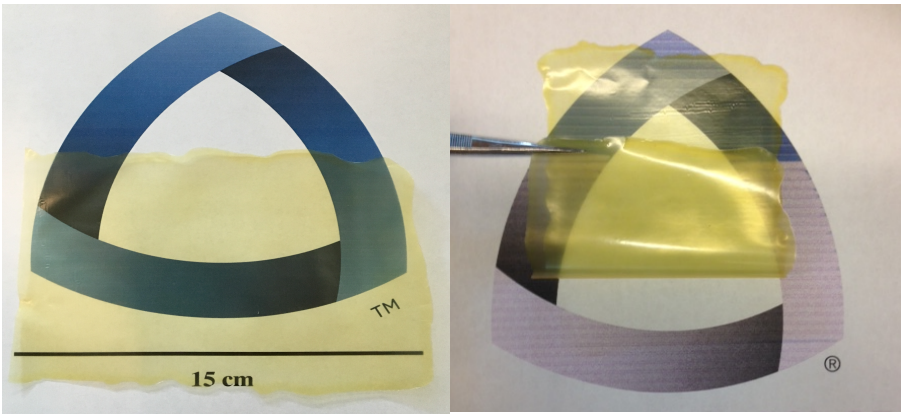

Figure 4. Visual image of cross-linked 40 microns thick membrane

Adjustment of IEC and mechanical property

Based on the fact that MPRD quaternized polyvinylbenzyl chloride-co-polycyclooctene triblock polymer had the highest chemical stability, OH^- conductivity and flexibility, this materials was further refined. In order to attach more cationic groups, we also modified the functionalization procedure. We firstly applied a more compatible solvent, that better dissolved the piperidinium triblock polymer allowing adequate contact of the amine solution to the benzyl chloride groups; Secondly we modified the functionalize procedure into post dithiol functionalization that soaking the membrane into amine solution as the last step. The obtained membrane has improved ion exchange capacity of IEC=2.0 mmol/g with very high Cl^- conductivity over 100 mS/cm at 90 °C, 95% RH.

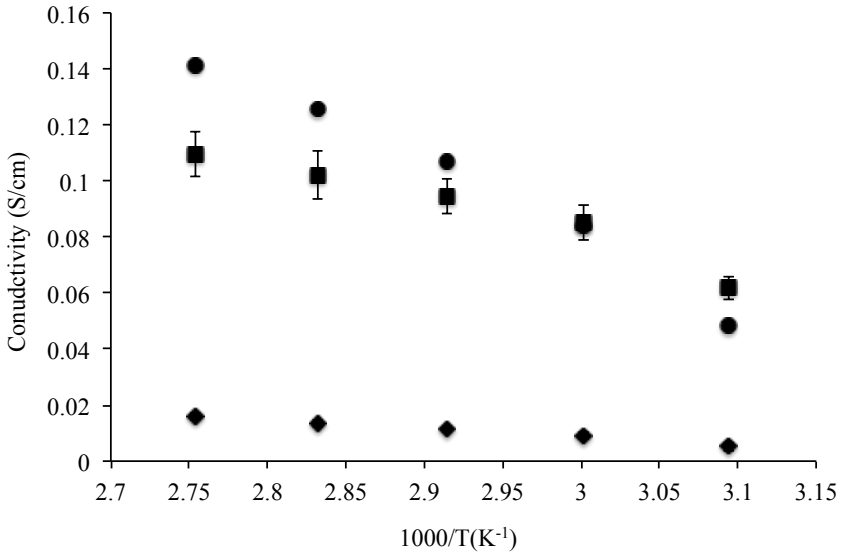

Figure 5. Improved conductivity of piperidinium functionalized triblock membrane produced via modified functionalization procedure (with DCM solvent, square; post functionalization, round) compared to the conductivity of membrane produced with original method (diamond)

The membrane with high IEC value is mechanically weak as to a large extent of water absorption. To solve mechanic problem, we have photo crosslinked the hydrophobic domain with dithiol and thermal crosslinked hydrophilic domain of the polymer. The obtained membrane withholds water absorption and dimensional swelling with improved mechanical strength in humid condition. Obtained membrane is thicker for stretch and allowed to operate at mild temperatures above ambient without melting.

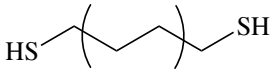

1,10-decanedithiol

From the degradation study of the DT crosslinked materials, 80°C and 1M KOH, (Figure 6), we can see with the same MPRD cation, the triblock copolymer is more hydroxide stable than random polymer, 75% vs <40% remaining after 30 days. This is presumably as it has a well-defined phase separated lamella structure, as proven by HRTEM and SAXS (not shown).

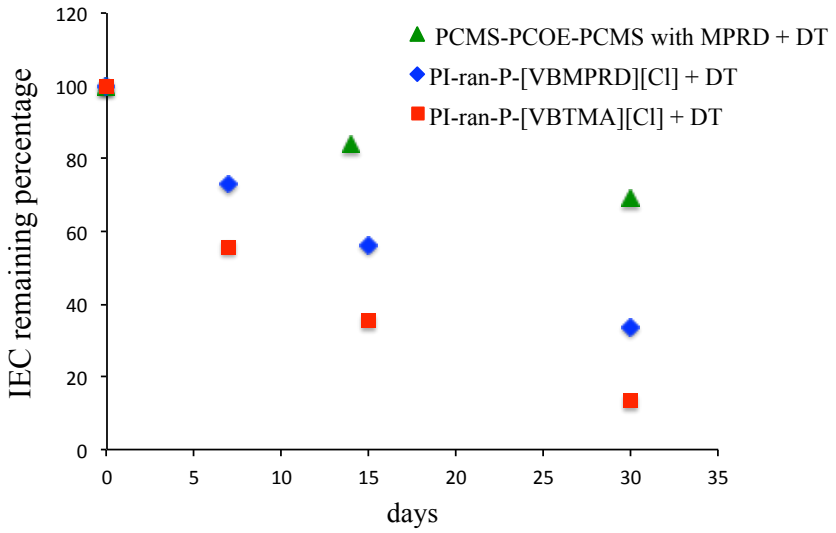

Figure 6. Comparison of durability between random PI-ran-P-[VBMPRD][Cl]+DT, PI-ran-P-[VBTMA][Cl]+DT and triblock PCMS-PCOE-PCMS with MPRD+DT by soaking in 1 M KOH at 80°C.

5. Physical Chemistry Studies

5.1 Influence of AEMS on Carbon based anions

We have studied the reaction of hydroxide counter anions in the quaternized polymeric membranes into the equilibrium of carbonate and bicarbonate ions with air by FTIR. This is in fact verified using different anionic membranes. **Figure 99** shows the increase in absorbance over time for certain time and then the absorbance levels out to a constant absorbance. The most convincing logic for this phenomena could be that the hydroxyl counter anions in quaternized ammonium polymeric membrane uptake carbon-dioxide from the atmosphere and form the dynamic equilibrium of carbonate and bicarbonate anions. **Figure 100** shows a 3 dimensional plot of spectra vs frequency over time. This shows the distinct peaks for carbonate and bicarbonates.

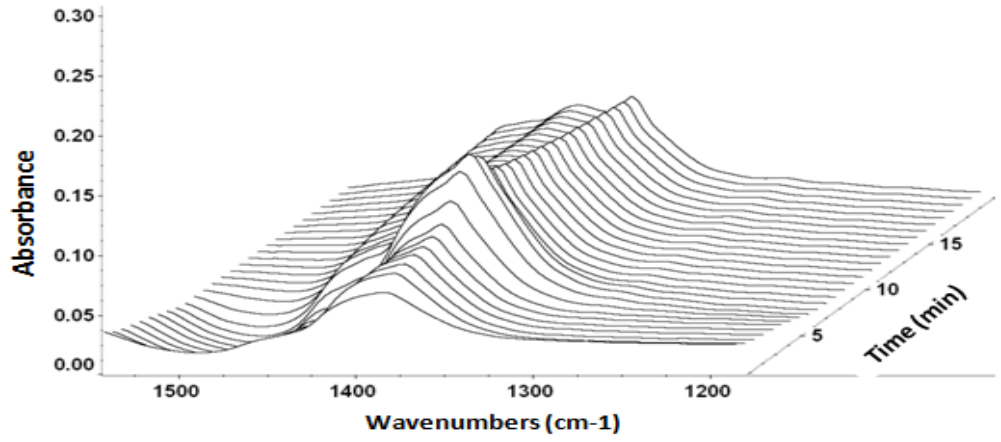

Figure 99 Real time ATR spectra collected for quaternized PEI membrane with hydroxyl as counter anions using FTIR spectroscopy show distinct increase in absorbance intensity over time for carbonate and bicarbonate ions at constant vibrational frequency

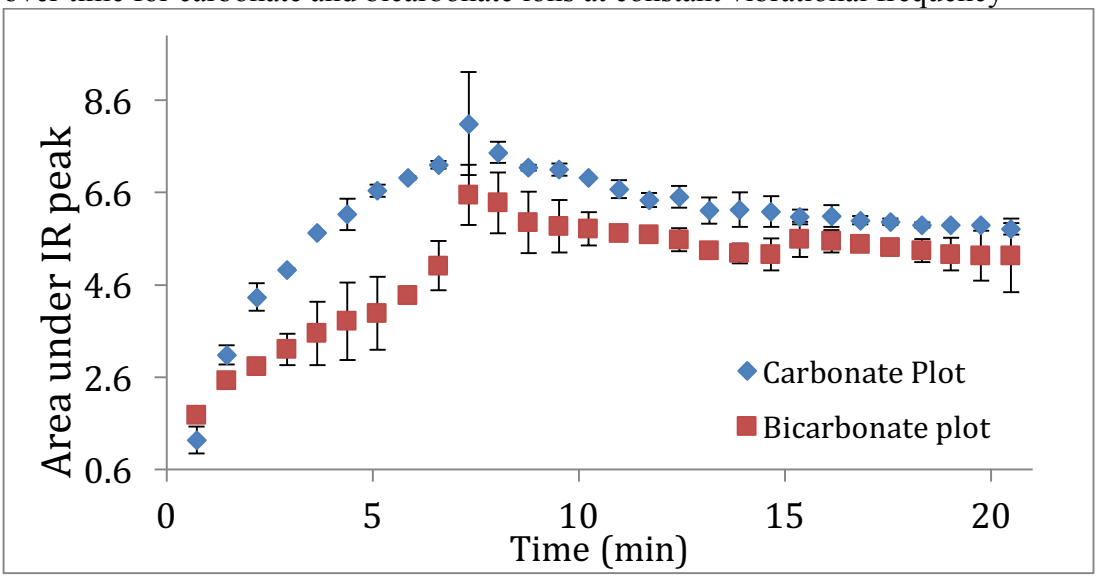

Figure 100 shows the integrated area under IR spectra (shown at Fig 2) at wavenumbers 1380 and 1450 cm-1 collected for quaternized PEI membrane in OH form. Blue-carbonate and Red represent bicarbonate

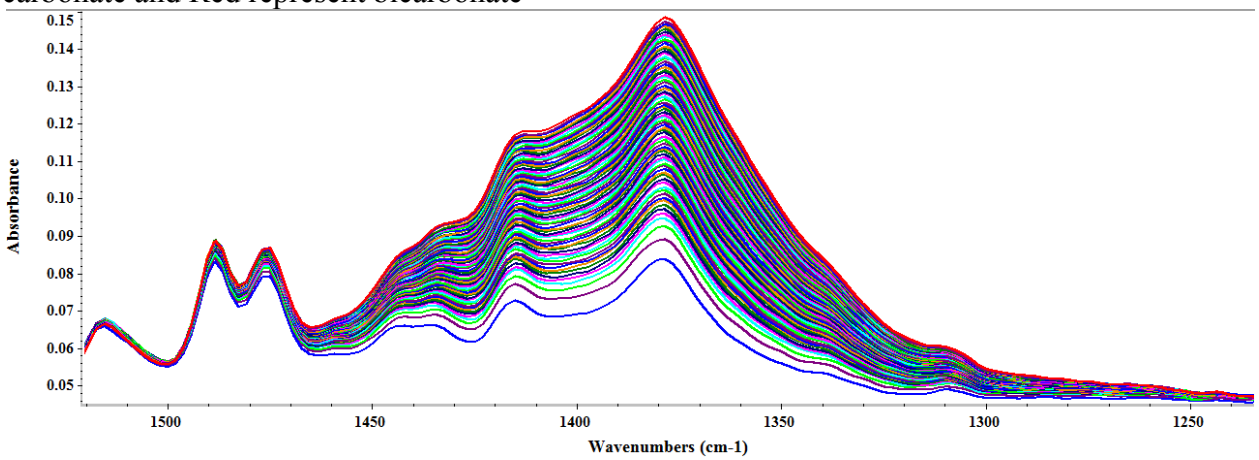

Figure 101 Real time spectra ATR spectra collected for quaternized sulfonyl Diels-Alder poly(phenylene)(SDAPP) (Hibbs' membrane) with hydroxyl as counter anions using FTIR spectroscopy

In order to understand this phenomenon, it is important to understand the environmental conditions in which the experiments are performed. We are in the process of designing a novel setup to control temperature and RH. All physical parts are nearly assembled; the major remaining task is to connect them up to a LabView console.

We are studying the process of CO_2 uptake in hydroxide-form AAEMs, which results in a dynamic mixture of hydroxide, carbonate, and bicarbonate anions. The conductivity results for Fumasep FAA, a commercial membrane, are shown in **Figure 102** with activation energies given in Figure 141.

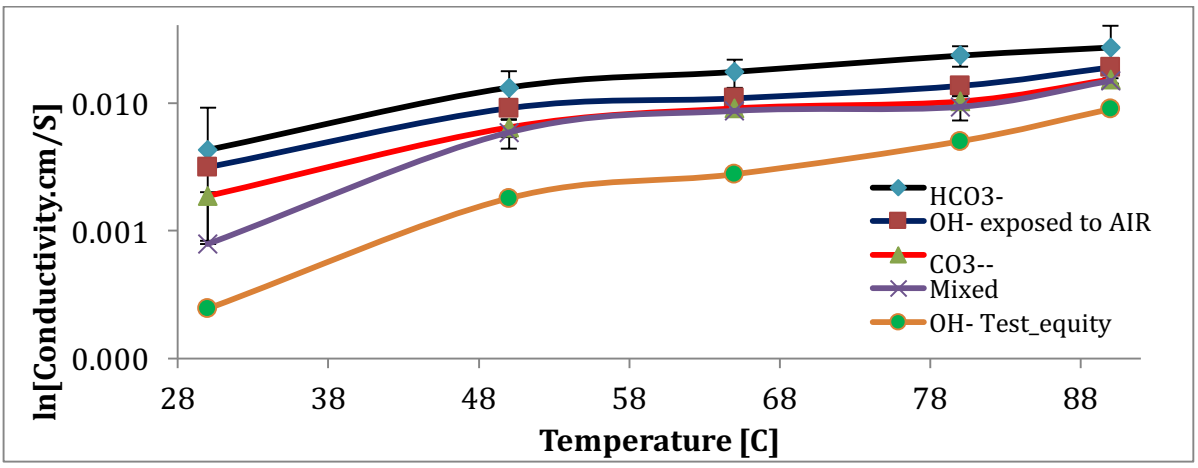

Figure 102 Conductivity of FUMASEP FAA membranes over temperature

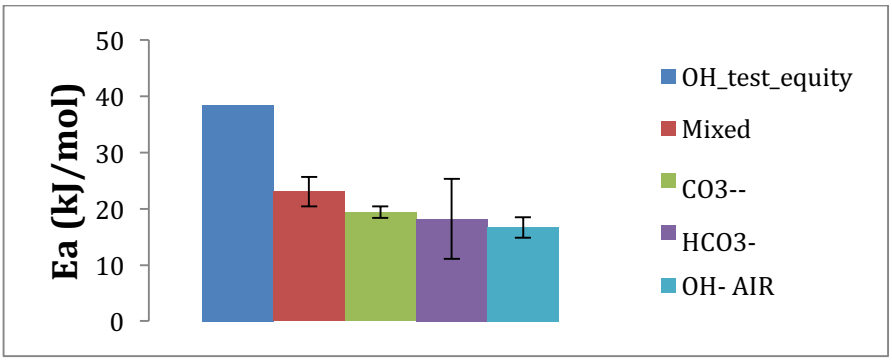

Figure 103 Activation energy for the conductivity of the Fumasep FAA membrane when it is with the given counter anion.

5.2 1,4,5-trimethyl-3-benzyl-2-(2,4,6-trimethoxyphenyl)imidazolium Functionalized AEM

We studied a modified imidazolium functionalized AEM-1,4,5-trimethyl-2-(2,4,6-trimethoxyphenyl) imidazo- lium functionalized polyphenylene oxide (PPO-TMIM) (Figure 38). The materials were in two imidazolium cation functionalization degrees, 33% and 46%, PPO-TMIM-0.33 and PPO-TMIM-0.46, with calculated IECs of 1.53 and 1.82 meq/g respectively. We compared its chemical stability with an unsubstituted imidazolium cation, PPO-IM, which had a calculated IEC = 2.20 meq/g.

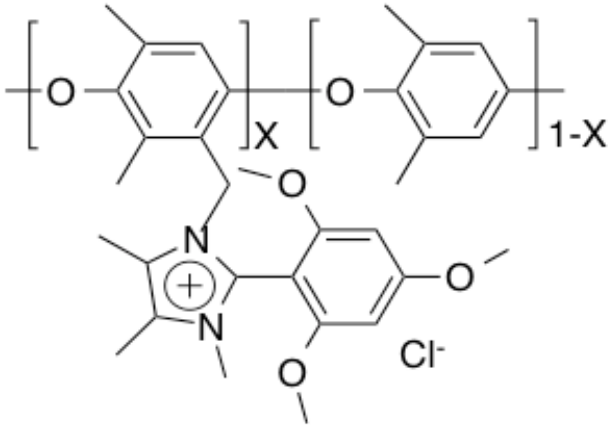

Figure 104. Structure of 1,4,5-trimethyl-2-(2,4,6-trimethoxyphenyl) imidazolium functionalized polyphenylene oxide.

The thermal stability of the polymer was tested by TGA, **Figure 105**. Mass loss evolves over three stages with the highest weight loss rate at temperatures of 50 ℃, 240 ℃ and 392 ℃ (PPO-TMIM-0.33) or 370 ℃ (PPO-TMIM-0.46). From 30℃ to 130℃, weight loss of PPO-TMIM-0.33 and PPO-TMIM-0.46 are 5% and 6%, which is attributed to bound water. The second weight loss correlates with the onset decomposition temperature at 217 ℃ is attributed to 1,4,5-trimethyl-2- (2,4,6-trimethoxyphenyl) imidazolium degradation by nucleophilic attack of chloride anions on 1-methyl through S_N2 reaction [19, 30]. This onset decomposition temperature is higher than quaternary ammonium and unmodified imidazolium cations reported earlier [20] . Final degradation starting at 352℃ is resulted from the decomposition of PPO aromatic chains [18].

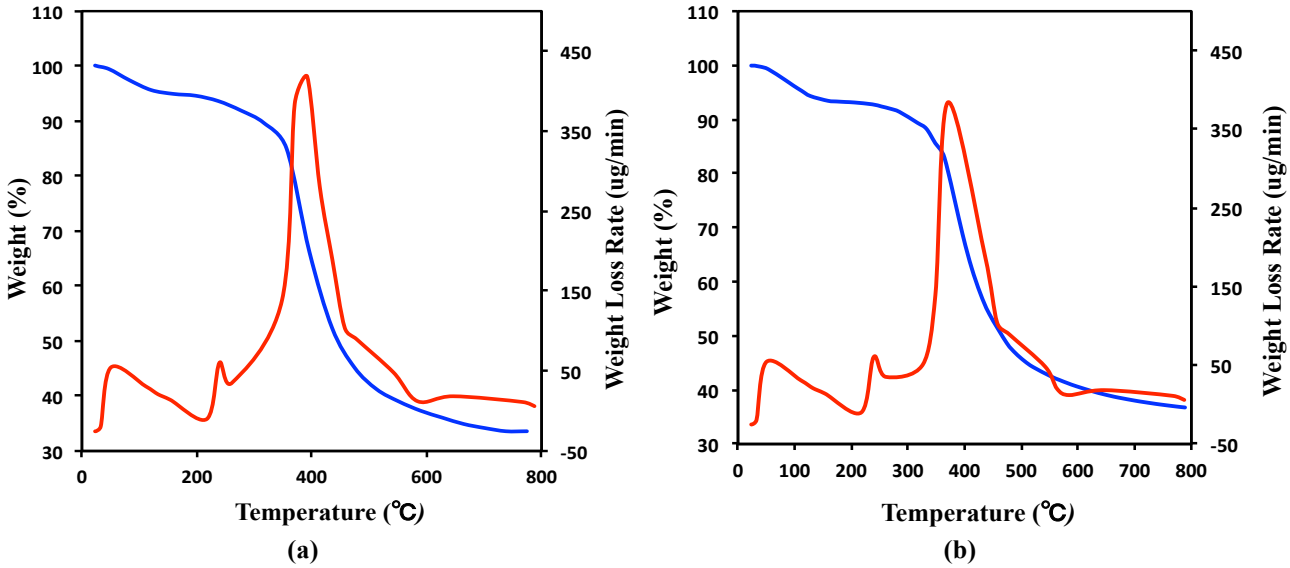

Figure 105. Thermal gravimetric analysis curves and derivative thermal gravimetric curves of 1,4,5-trimethyl-2-(2,4,6-trimethoxyphenyl) imidazolium functionalized polyphenylene oxide. (a) PPO-TMIM-0.33, (b) PPO-TMIM-0.46

Table 17. IEC value and related properties of PPO-TMIM-0.33, PPO-TMIM-0.46.

Sample Designation	IEC (mmol/g)	T_d (°C)	Water Uptake (%)	Conductivity (S/cm)	Ea (kJ/mol)
PPO-TMIM-0.33	1.49	240	17	0.016	15±2
PPO-TMIM-0.46	1.74	240	22	0.023	-

Water sorption for PPO-TMIM-0.33 and PPO-TMIM-0.46 are 17% and 22% (**Figure 106**) respectively, corresponding to λ value of 6.3 and 7 under 95% RH at 60 °C. Hydration number of PPO-TMIM-0.33 and PPO-TMIM-0.46 are almost the same under 40% RH while only 10% difference at 95% RH. The contribution of water uptake to the morphology of the membrane and conductivity will be discussed in the following part.

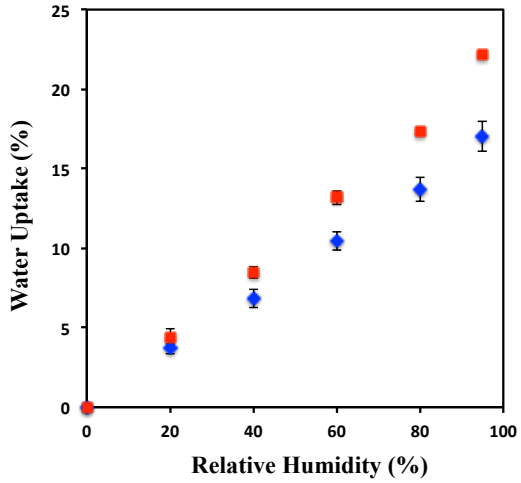

Figure 106. Water uptake of 1,4,5-trimethyl-2-(2,4,6-trimethoxyphenyl) imidazolium functionalized polyphenylene oxide. (■ PPO-TMIM-0.46, ◆ PPO-TMIM-0.33), left %, right, λ.

From SAXS patterns, **Figure 107** taken under dry to saturated conditions, no ordered structures (e.g. lamellae) were observed. However, an ionomer peak at d spacing around 3nm is observed. The position of ionomer peak shifts to lower q as humidity increases, i.e., the ionomer domain size increase with water uptake. For PPO-TMIM-0.46, a peak with d spacing from 10 nm to 32 nm at 95 RH indicating the formation of a new morphological phase from hydrophobic and hydrophilic domains reordering. Both ionomer and crystalline bumps become more distinct after soaking the membrane into DI water.

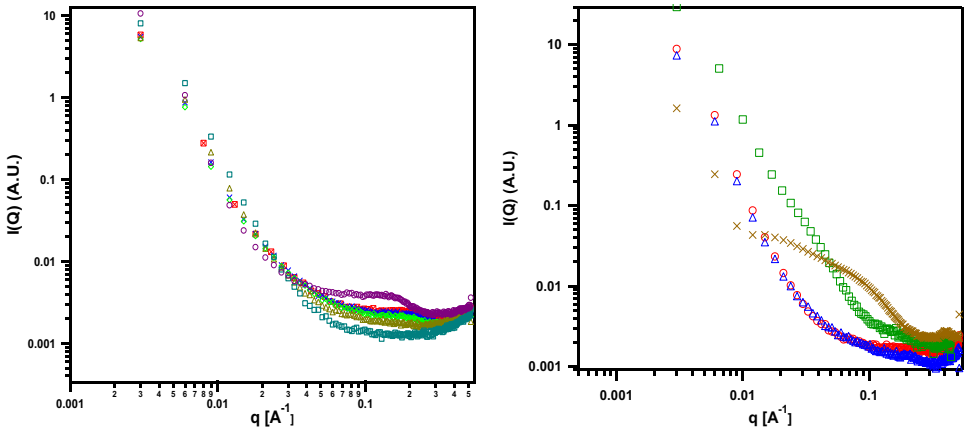

Figure 107. SAXS patterns of 1,4,5-trimethyl-2-(2,4,6-trimethoxyphenyl) imidazolium functionalized polyphenylene oxide.(a) PPO-TMIM-0.33 and (b) PPO-TMIM-0.46 ⊠ dry, × 25 RH, ◇ 50RH, △ PPO- 75RH, □ 95RH, ○ soaked

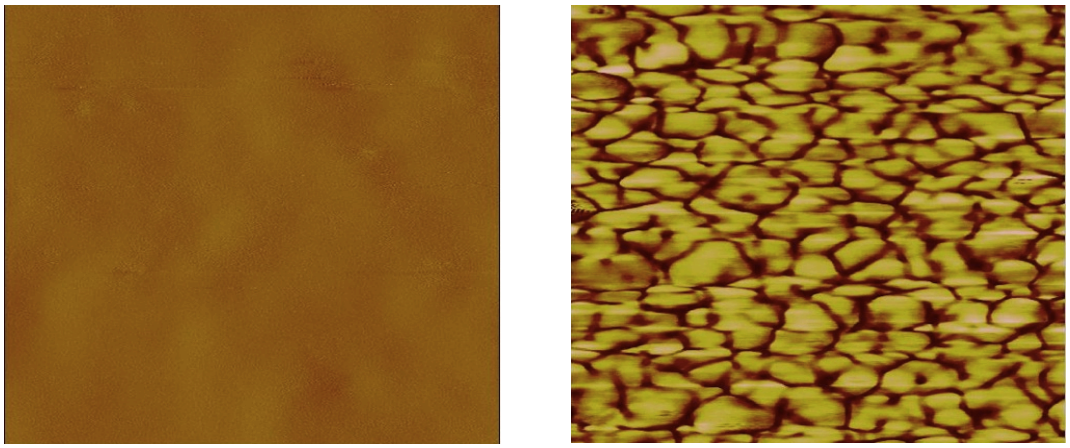

(a) (b)

Figure 108. AFM tapping mode phase images of 1,4,5-trimethyl-2-(2,4,6-trimethoxyphenyl)imidazolium functionalized polyphenylene oxide (PPO-TMIM-0.46) ((a) dry, (b) wet), Scan boxes are 500 nm × 500 nm.

The effect of relative humidity on morphology is furthered exhibited in AFM. The darker cluster increases at high humidity, therefore, the dark areas were assigned to the hydrophilic domains of PPO unit with pendent 1,4,5-trimethyl-2-(2,4,6-trimethoxyphenyl) imidazolium groups containing water, while the bright yellow domains representing hard cluster of hydrophobic PPO backbone, which is consistent with similar imidazolium functionalized AEM [18, 33]. No distinct grains or clusters were observed the membrane is dry. However, by absorbing water, Figure 108(b) displays a clear phase separation by hydrophilic and hydrophobic groups aggregating into isolated domains, which is similar with crystalline (10 nm to 32 nm) and ionomer (3 nm) domain size exhibited in SAXS pattern. The phase separation of the humidified membrane is expected to help to facilitate anion transport.

We also studied the transport behavior inside the polymer by using of PFG-NMR. In order to investigate the diffusion property, we use Mitra equation to provide insights into phase complexities such as the overall size under which water molecules move freely or the tortuous ion conducting pathways in the membrane. Furthermore, the diffusion coefficient D_0, when only Brownian motion occurs, can be obtained from extrapolation of D to t_d=0.

$$= D_0[1 - \frac{4}{9\sqrt{\pi}} \cdot \frac{S}{V} \cdot \sqrt{D_0 \cdot t_d}]$$

where S/V is the surface-to-volume ratio of the porous material. From Figure 40, D_0 of PPO-TMIM-0.46 and PPO-TMIM-0.33 calculated according to Equation (1) are 1.4×10^{-6} cm^2/s and 1.6×10^{-6} cm^2/s, respectively, which are lower than the bulk water diffusion coefficient 2.3×10^{-5} cm^2/s at 25 °C.[59] Our nanometer-scale clusters observed in SAXS

and AFM (shown in report last year) make water transport in the hydrophilic domains at t_d=0 much slower than the bulk water transport, which is due to the effect from the hydrated polymeric environment inside the channels.[60]

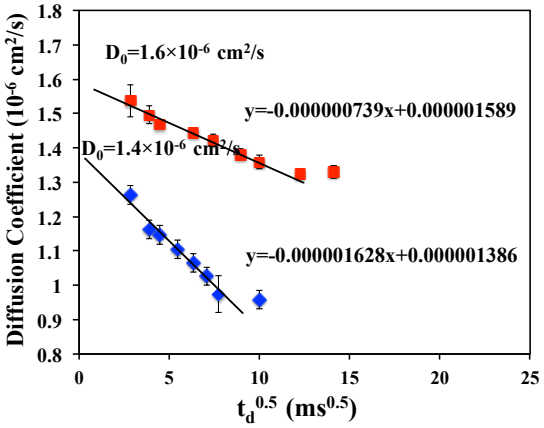

Figure 109. Water self-diffusion coefficients of 1,4,5-trimethyl-2-(2,4,6-trimethoxyphenyl) imidazolium functionalized polyphenylene oxide versus the square root of the diffusion time. The measurement was taken under 80% RH at 26 ℃. (■ PPO-TMIM-0.33, ◆ PPO-TMIM-0.46)

S/V in the Mitra equation can be obtained from the slope in Figure 40. R_c, the reciprocal of S/V, is a critical parameter that designates the structure length scale within which intra-domain transport is dominant.[61],[62] From Table 4, we observed that R_c of both PPO-TMIM-0.46 and PPO-TMIM-0.33 are much larger than cluster sizes shown in AFM and SAXS. By comparing R_c values between PPO-TMIM-0.46 and PPO-TMIM-0.33, it is noticed that even though PPO-TMIM-0.33 embraces a lower water uptake, R_c of PPO-TMIM-0.33 is still larger than that of PPO-TMIM-0.46. The tortuosity of the membrane is calculated from the Equation.[63]

$$D_\infty = D_0 \alpha^{-1}$$

where α is the tortuosity. From Table 4, the tortuosity of PPO-TMIM-0.33, calculated by Equation (2), is smaller than that of PPO-TMIM-0.46. Smaller tortuosity designates a less morphological barrier for transport. The smaller cluster sizes of PPO-TMIM-0.33 observed in AFM (in the report last year) give rise to more junctions of dark domains so that promote transport pathway connections. Hence, PPO-TMIM-0.33, which embraces a smaller tortuosity, makes itself into a larger critical length scale and possesses a weaker dependence on diffusion time, even though it has a lower water uptake. The diffusion length, which relates the diffusion coefficient, D, to the diffusion time, t_d, is calculated according to the Equation.[64]

$$< a^2 >^{1/2} = \sqrt{2Dt_d}$$

where $<a^2>^{1/2}$ is the diffusion length. By plotting the diffusion coefficient versus diffusion length (Figure 41), the fully restricted domain size is observed when the diffusion coefficient levels off. We noticed that fully restricted length scales of PPO-TMIM-0.33 and PPO-TMIM-0.46 are 6.3 μm and 3.4 μm, respectively, which are in line with the R_c values, 6.7 μm of PPO-TMIM-0.33 and 2.6 μm of PPO-TMIM-0.46, obtained from Mitra equation. Thus, the length scale of intra-domain transport of water molecules extends into the micron scale.

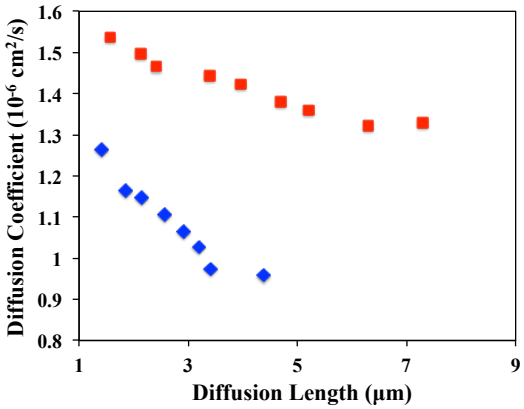

Figure 110. Water self-diffusion coefficients of 1,4,5-trimethyl-2-(2,4,6-trimethoxyphenyl) imidazolium functionalized polyphenylene oxide versus diffusion length. (■ PPO-TMIM-0.33, ◆ PPO-TMIM-0.46).

Table 18 Surface/volume ratio, R_c and tortuosity for 1,4,5-trimethyl-2-(2,4,6-trimethoxyphenyl) imidazolium functionalized polyphenylene oxides.

sample designation	S/V (μm^{-1})	R_c (μm)	tortuosity (α)
PPO-TMIM-0.33	0.15	6.7	1.18
PPO-TMIM-0.46	0.39	2.6	1.47

Figure 112 shows the conductivity results of PPO-TMIM-0.33 and PPO-TMIM-0.46 under 95RH, from 50 ℃ to 90 ℃. PPO-TMIM-0.33 exhibits a linear Arrhenius behavior within the whole temperature scale indicating a dominated water-assisted ion hopping transport, whereas PPO-TMIM-0.46 is more like Vogel-Tamma-Fuleher (VTF) mechanism with polymer chain movement dominated ion transport [38]. The difference is consistent with Wever's [39] work. Even though hydration numbers are similar, conductivity of PPO-TMIM-0.46 is significantly larger than that of PPO-TMIM-0.33 which is probably contribute to large amount of water sorption facilitate anionic group transfer via providing sufficient bridged transport medium. Conductivity of PPO-TMIM-0.46 and PPO-TMIM-0.33 under 95% RH at 90 ℃ are 23 mS/cm and 16 mS/cm respectively that are comparable with other imidazolium functionalized AEM mentioned in introduction [20-23]. The Tokuyama company reported in plane conductivities for A201 and A901 membranes at 23℃, 90% RH as 38 mS cm^{-1} and 42 mS cm^{-1} respectively [4].

From IEC normalized conductivity, it is found PPO-TMIM-0.46 is still higher than that of PPO-TMIM-0.33. The reason probably attributes to the smooth pathway from ordered ionomer and crystalline structure or more free volume generated from chain movement as discussed above. Activity energy of PPO-TMIM-0.33 is 15±2 kJ/mol that is slight lower than other imidazolium AEM [21] indicating a less sensitivity of conductivity versus temperature variation [40].

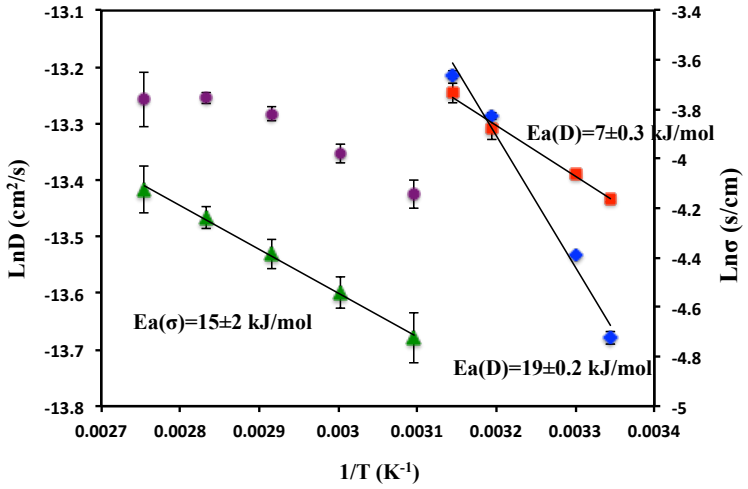

Figure 111. Calculated natural logarithm of conductivity and natural logarithm of water self-diffusion coefficient versus inverse of temperature. The measurements were performed at Δ=20ms (●PPO-TMIM-0.46, ▲ PPO-TMIM-0.33, ■PPO-TMIM-0.33, ◆PPO-TMIM-0.46)

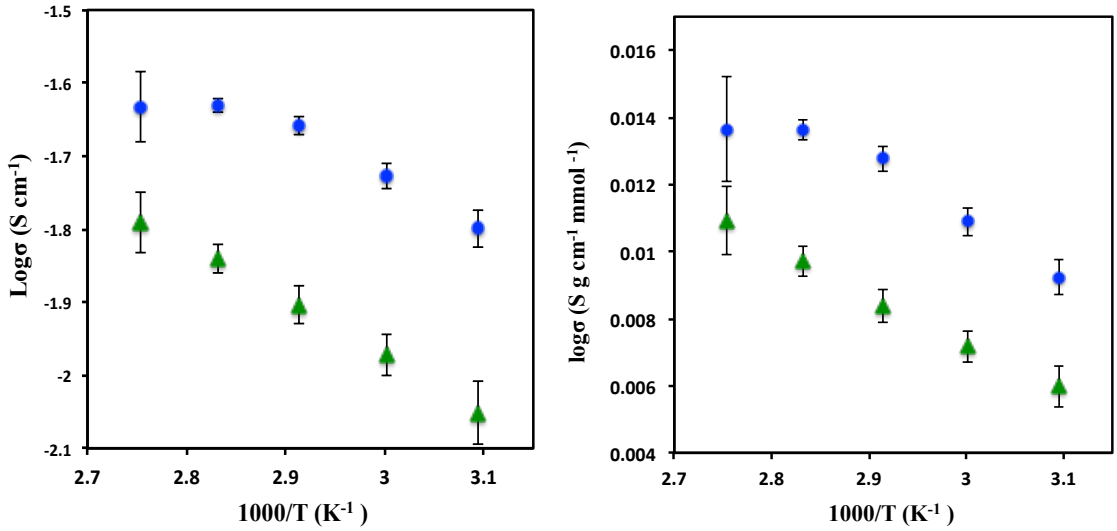

Figure 112. In-plane conductivities and normalized conductivitiesof 1,4,5-trimethyl-2-(2,4,6-trimethoxyphenyl) imidazolium functionalized polyphenylene oxide. (● PPO-TMIM-0.46, ▲ PPO-TMIM-0.33)

Chemical stability measurements were performed by treating PPO-TMIM and PPO-IM in 1 M sodium hydroxide solution at 80 °C. The degradation of cationic groups were determined in terms of the IEC based on the titration of Cl^- form membranes. The degradation processes are shown in Figure 39. Initial measured IECs of PPO-TMIM-0.46 and PPO-IM were 2.0 and 1.9 meq/g. The IEC of substituted PPO-TMIM polymer decreases more slowly initially than that of PPO-IM and both showed a higher IEC at the end than the minimum values recorded. After 24 h of hydroxide treatment at 80 °C, the IEC of PPO-TMIM was unchanged from the initial value, whereas the IEC of PPO-IM

had decreased by 25%. It is possible that the minimum value of the IEC is the true value for the degraded film and that the gradual recovery of the IEC is due to entrapped salt that can not be easily washed from the film, nethertheless the PPO-IM polymer is clearly quite unstable under the test conditions. Other AEMs recently reported also display this degradation phenomenon.[65] The enhanced bacisity of the modified imidazolium due to the electron donating methyl and trimethoxyphenyl groups as well as the static effect from the large trimethoxyphenyl group efficiently prevent nucleophilic OH^- attack on the α-C position of the imidazole ring as compared to the unsubstituted imdazolium cation. This improved long term stability of PPO-TMIM was also demonstrated by Wang[66] under the same degradation conditions.

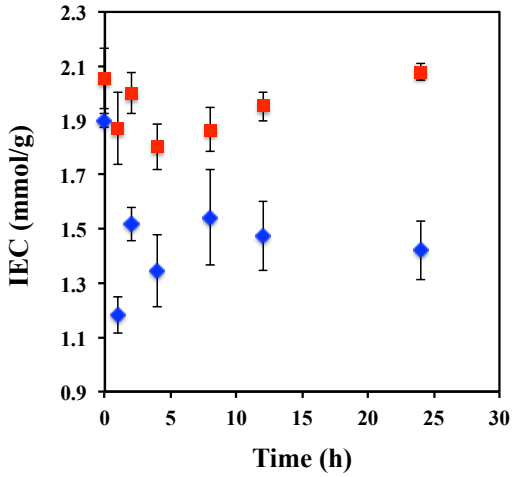

Figure 113. IEC of 1,4,5-trimethyl-2-(2,4,6-trimethoxyphenyl) imidazolium functionalized polyphenylene oxide (■ PPO-TMIM-0.46) and unsubstituted imidazolium functionalized poly phenylene oxide (◆ PPO-IM) during the alkaline stability test at 80 °C in 1 M KOH

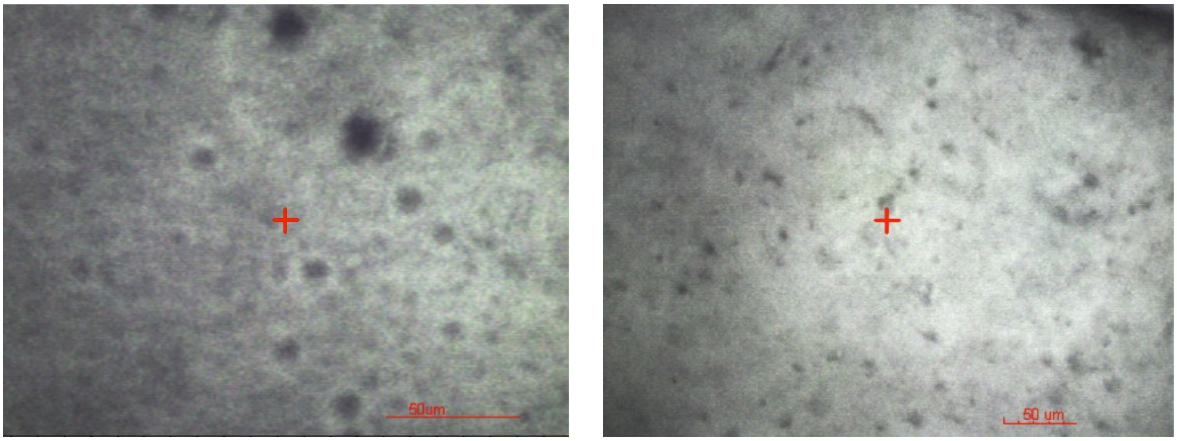

Figure 114 Visible microscope images of 1,4,5-trimethyl-2-(2,4,6-trimethoxyphenyl) imidazolium functionalized polyphenylene oxide ((a) PPO-TMIM-0.33, (b) PPO-TMIM-0.46).

We used visible microscopy to verify that the membrane had morphological features on the micron scale (Figure 114). Both PPO-TMIM-0.33 and PPO-TMIM-0.46 display small

circular patterns ca. 5 µm and larger black dots at ca. 10-15 µm that might compose of smaller length scale structures. These micron order of magnitude lengths and nanoscale domains shown in SAXS and AFM (as in report last year) compose a hierarchical structure. Thus, the interconnected hydrophilic channels facilitate water-molecule transport into a larger length scale (on the micron scale, Figure 114) beyond the dimensions observed in SAXS and AFM (on the nanometer scale).

The self-diffusion coefficients of water for the two polymers as a function of temperature are shown in Figure 43. Both the PPO-TMIM-0.46 and PPO-TMIM-0.33 diffusion coefficients increase along with temperature. The low IEC sample shows a linear relationship with an E_a of 7± 0.3 kJ/mol, while the high IEC sample displays a non-linear, convex, super-Arrhenius behavior. The membrane with higher water uptake, PPO-TMIM-0.46, shows a larger diffusion coefficient at a higher temperature (above 40 °C), which is in line with the conductivity result in Figure 44, even though the water diffusion does not necessarily exhibit a linear relation or proportionality to conductivity.[59]

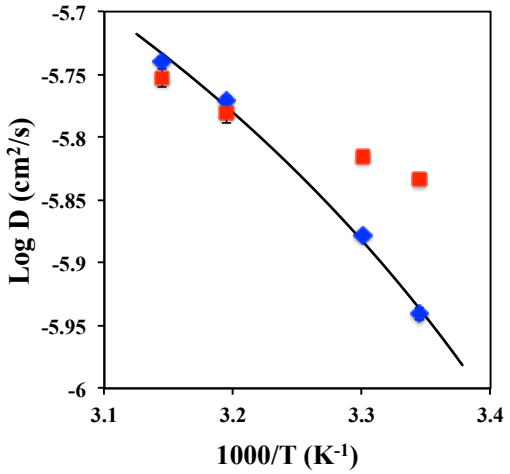

Figure 115. Arrhenius plot of water self-diffusion coefficients under 80% RH. The measurements were performed at Δ=20 ms. (■ PPO-TMIM-0.33, ◆ PPO-TMIM-0.46).

We can fit both the ionic conductivity and water diffusion data for the high IEC polymer to the Vogel-Tammann-Fulcher (VTF) equation shown below.[67,68,69,70]

$$\sigma(T) = \sigma_0 \exp\left(-\frac{b}{T - T_0}\right) \quad D(T) = D_0 \exp\left(-\frac{b}{T - T_0}\right)$$

where σ_0 and D_0 are the conductivity and diffusion coefficients at infinite temperature, b is a constant related to the entropic barrier to free volume creation, T_0 is the temperature at which the mobility of ions and the conductivity drop to zero. Based on the three-parameter fit by using of Mathematica (Table 5), T_0 from the PFG NMR water diffusion coefficient and the EIS Cl^- conductivity data fits are similar, ca. 240 K which is nominally considered 50K lower than the T_g of the material.[71,72] We assign this to the T_b, 290 K, of the hydrophilic phase. The b value obtained is higher, 132 K, for ionic conductivity of Cl^- than for water diffusion from PFG-NMR, 100 K, indicating that Cl^- is energetically less mobile than H_2O in the channel. The maximum conductivity of Cl^- is calculated to be 0.075 S/cm and of water diffusion 7.1×10^{-6} cm^2/s which is an order of

magnitude smaller than for free water at room temperature, 2.3 x10^{-5} cm^2/s, again indicative of the highly hindered transport in these polymers.

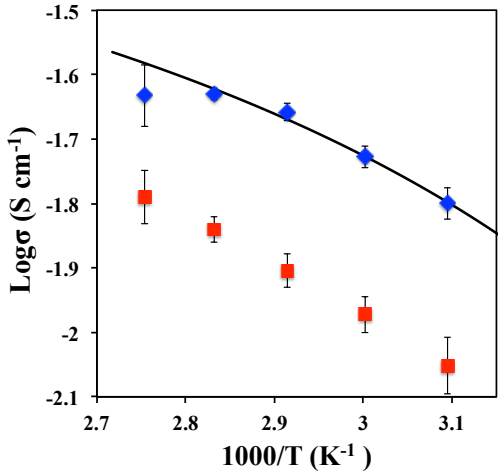

Figure 116. Cl^- form conductivities of 1,4,5-trimethyl-2-(2,4,6-trimethoxyphenyl) imidazolium functionalized polyphenylene oxide under 95% RH. (■ PPO-TMIM-0.33, ◆ PPO-TMIM-0.46)

Table 19 Parameters of VTF regression of PPO-TMIM-0.46 on both conductivity and diffusion coefficients versus temperatures

VTF regression	σ_0 (S/cm), D_0 (cm^2/s)	b (K)	T_0 (K)
conductivity	0.075	132	238
diffusion coefficient	7.1×10^{-6}	100	244

5.3 Fluoride Transport

To understand the fluoride ion transport through aqueous as well as membrane systems, we have employed the state of the art technique of Pulse field Gradient Stimulate spin Echo – Nuclear Magnetic resonance (PGSTE-NMR). We considered 3 different types of chemistries for this ion transport study as show in in Table 20.

Membrane	Chemical composition	IEC (meq/gm)
PE-b-PVBTMA	Diblock copolymer of polyethylene(60%) and Polyvinyl benzyl trimethyl ammonium (40%) (from Prof. Knauss group)	1.71
S-80	ETFE based radiation grafted benzyltrimethylammonium(36)	1.77
TMAC6PP	Poly(phenylene) based AEM with six carbon side chain tethered cations(45)	2.42

Table 20: Different AEMs studied for fluoride diffusion

Self-diffusion coefficients of anions (^{19}F) were determined with a pulsed field gradient stimulated echo (PGSTE) NMR technique. The diffusion coefficients were determined by fitting the measured data to the Stejskal -Tanner equation(46)

$$\left(\frac{S}{S_0}\right) = \exp\left[-\gamma^2 G^2 \delta^2 \left(\Delta - \frac{\delta}{3}\right) D\right],$$

Eq. 1

where S_0 is the signal amplitude, γ is the gyromagnetic ratio, G is the gradient strength, δ is the length of gradient pulse (1 ms) and Δ is the time between pulses.

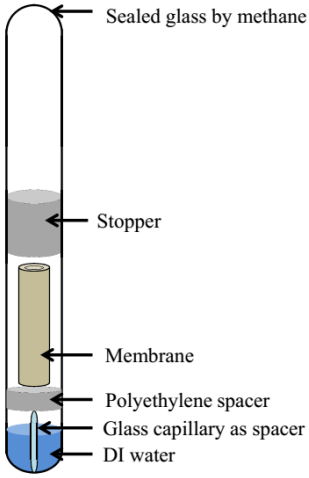

Figure 117: Schematic representation of the NMR tube for diffusion measurements.

The experiments were carried out using a Bruker AVANCE III NMR spectrometer and 400MHz (^1H frequency) wide bore Magnex magnet. ^{19}F (376.02 MHz) diffusion measurements were made using a 5 mm Bruker single-axis DIFF60L Z-diffusion probe. The 90° pulse length was on the order of 5 µs. The range of gradient strength was 0-500 G/cm, which was incremented in 16 steps. The maximum value of the gradient was chosen such that the signal decays completely. The Bruker TopSpin software package was used to control the spectrometer and to analyze the data.

Figure 117 shows the schematic of the NMR tube showing the actual arrangement. The tube was maintained at saturated conditions of humidity by the water at the bottom of it.

AEMs were exchanged to the fluoride form by keeping in 2.5M Benzyl Trimethyl ammonium fluoride at room temperature in a pressure bomb @ 500PSI for 10 days. The exchanged membranes were thoroughly washed with DI water for 24 h and dried before using. The actual percentage of exchange was determined by burning the fluoride exchanged sample membrane in oxygen and determining the fluoride content by fluoride ion sensetive electrode. This was done by Galbraith Labs (Knoxville, TN, USA).

Figure 118 shows the diffusion of fluoride in 0.92M aqueous solution of TMA, TEA and BMA fluorides. We can see that the anion transport is affected by the presence of cations in the solution. Increased size of cations causes the anions to move at a slower pace. The effect of the size of cation on fluoride transport increases at elevated

temperatures and it can be seen from **Figure 118**. We think that this kind of behavior can propagate to membrane systems where bulky quaternary ammonium groups will hinder the movement of anions to a greater extent.

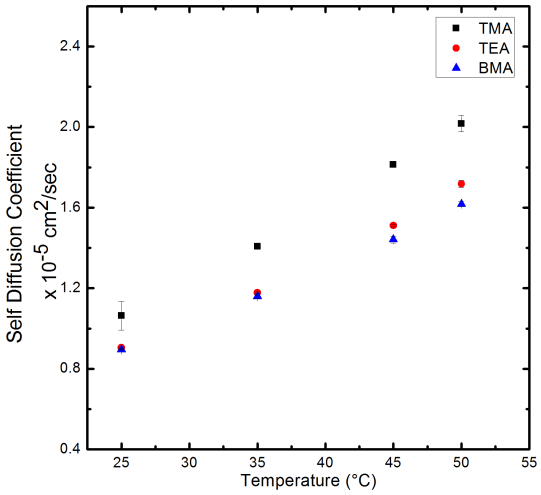

Figure 118: Fluoride ion diffusion in aqueous solutions with different quaternary ammonium cations: Tetra methyl ammonium (TMA, Black), Tetra ethyl ammonium (TEA, Red), Benzyl trimethyl ammonium (BMA, Blue). Conc. of solution = 0.92M

Extending this approach to the membrane system we studied the fluoride diffusion in 3 different types of AEMs. Figure 119 shows the fluoride ion diffusion occuring in the TMAC6PP membrane sample, as a function of temperature and diffusion time (Δ). At 30°C the average value of self diffusion of fluoride ion in the membrane was found to be 0.35 x $10^{-5}$$cm^2$/sec. The effect of diffusion time was not prominent at this temperature. As temperature was raised to 55°C the effect of diffusion time on self diffuison became prominent. The thermal motion of ions increases with temperature and the restricted diffusion effects come into picture. The ions are almost immobile at lower temperatures thus we don't see any effect even after increasing the diffusion time. But as the temperature is increased the ions become much more mobile and we start to see the effect of increased diffusion time on the self diffusion coefficient. Thus restricted diffusion becomes prominent at higher temperatures. Thus we can say that there are narrow water channels present in the membrane resulting into slower diffusion at extended diffusion times.

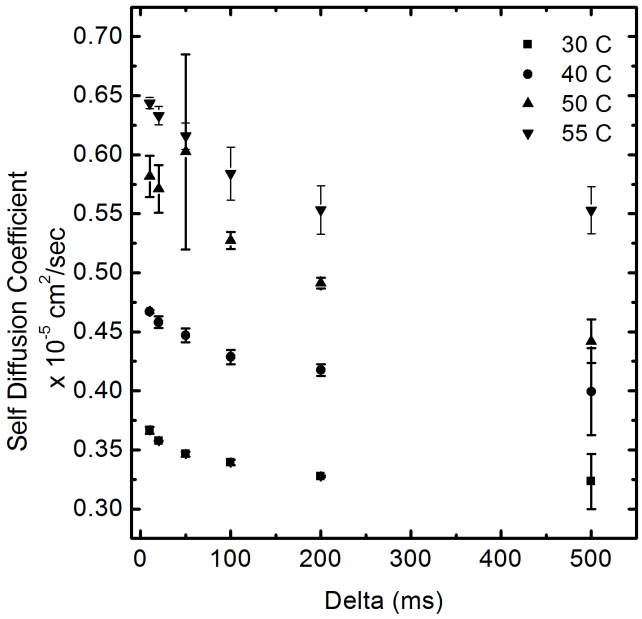

Figure 119: Fluoride diffusion in TMAC6PP membrane as a function of diffusion time.

Figure 120 shows the fluoride diffusion in the block copolymer of PE and PVBTMA. Our previous SAXS experiments have shown presence lamellar structure in this AEM. We see a really small effect of increasing the diffusion time on actual diffusion coeffcient in the studied diffusion time, which can mean that the channel are wide enough for the passage of ions such that we don't see any effect of changing diffusion time.

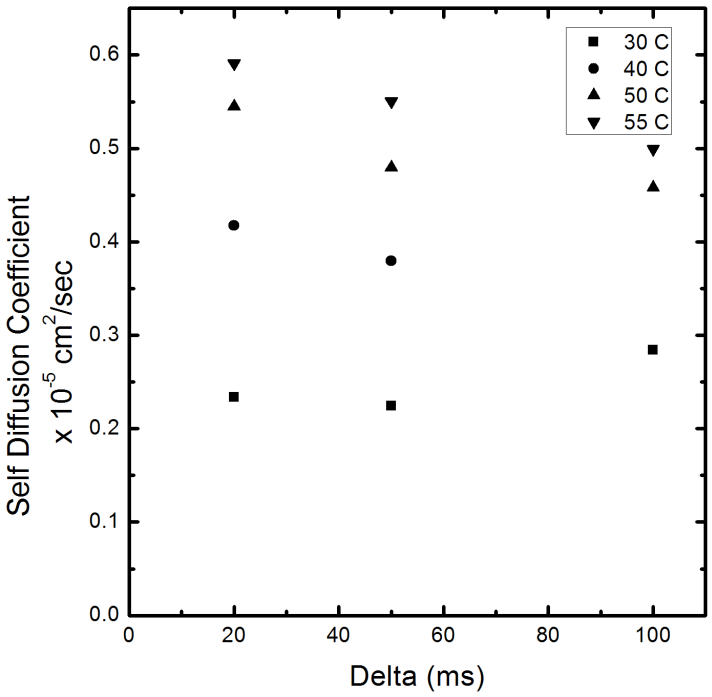

Figure 120: Fluoride diffusion in PE-b-PVBTMA membrane as a function of diffusion time (Delta)

Figure 121 shows the fluoride diffusion for the radiation grafted ETFE polymer, it can be seen here that the diffusion is not affected by changing diffusion times. Also it is worth noting that the self diffusion coefficients are considerably higher than the two other AEMs studied here. This suggests that the movement of anions is not confined, thus showing a higher degree of freedom for diffusion. This kind of behaviour can tell us about lack of defined channels in the membrane confirming the random grafting of the quaternary ammonium groups.

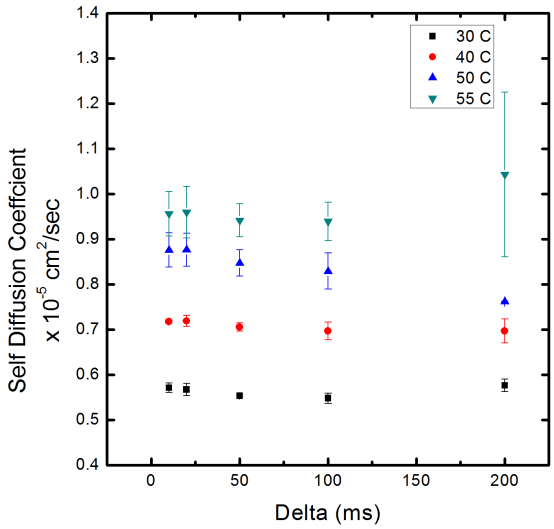

Figure 121: Self diffusion of fluoride ions in S-80 AEM as a function of diffusion time (Δ, ms)

Understanding ion transport by fluoride ion diffusion offers a simple solution to avoiding the detrimental effects of the caustic OH^- ion. It's a technique, which can further strengthen the results of a SAXS experiment as well as presence of water channels. We were able to confirm the random grafting of the ETFE based AEM using the PGSTE-NMR technique. Many other factors like hydrophobicity, hydrophilicity, chemistry, morphology affect the overall ion transport in an AEM thus making it challenging to compare all 3 membranes across the board.

5.4 Hydroxide ion conductivity and IR water study on the ETFE-g-PVBTMA anion exchange membrane.

In most cases, a hydroxide form (when hydroxide ions are counter anions for cationic polymer membranes) of AEM is not stable when it is exposed to air. Hydroxide ions (OH^-) in the membrane react with carbon-dioxides (CO_2) from air to give a combination of carbonates (CO_3^{2-}), bicarbonates (HCO_3^-) and residual OH^-.

Sustained high conductivity is crucial for fuel cell applications. However, the rapid reaction of OH^- in the membrane with atmospheric CO_2 makes conductivity measurement in pure OH^- form extremely difficult. For this reason, few studies report pure OH^- conductivity in AEMs but rather OH^- conductivity of AEMs exposed to air. Many researchers even report OH^- conductivity of membranes measured in water when exposed to air(53-55). When an OH^- form of AEM is exposed to atmospheric CO_2, the membrane is no longer has exclusively pure OH^- anions but rather a combination of CO_3^{2-}, HCO_3^- and residual OH^-. Previous reports showed the conductivity performance of a OH^- form of AEM decreases over time(56). In this report, we study the conductivity performance of one AEM in different counter anionic forms including a controlled pure form of OH^- as the function of temperature and relative humidity. A dynamic conductivity performance of pure OH^- form in an AEM when exposed to atmospheric CO_2 was studied under a controlled environment conditions. Also, the water absorption kinetics of Poly(Ethylene-

co-tetrafluoroethylene) radiation grafted polymer membrane (ETFE-g-PVBTMA) are elucidated in this study.

The detailed synthetic route of the polymeric membrane is published by Varcoe et al(57). In short, the irradiation poly(Ethylene-co-tetrafluoroethylene) was grafted into vinyl benzyl chloride to make a membrane. The grafted membrane was then immersed in aqueous trimethyl ammonium for 4 h to make a poly(ethylene-co-tetrafluoroethylene) grafted poly(vinyl benzyltrimethyl ammonium) membrane (ETFE-g-PVBTMA).

The in-plane conductivity of a ETFE-g-PVBTMA membrane was measured in different anionic forms. The chloride form of the membrane was soaked in 1 M aq. solutions of sodium carbonate, sodium bicarbonate and sodium hydroxide separately for 12 hours to exchange the anion association in the membrane. All forms of the membrane samples except OH^- form were washed and then soaked in 18 MΩ deionized (DI) water for 2 hours while exposed to air but the OH- form was washed with DI water inside a glovebox to prevent the exposure to atmospheric CO_2. Membranes were then washed until the solution was at a neutral pH of 7.0. Impedance spectra were collected over a frequency range of 0.3 Hz to 100 kHz. A 4-probe test cell with platinum electrodes connected to a BioLogic VMP3 Potentiostat was used for the measurements. The test cells were placed in a TestEquity (Solatron 1007 H Model) environmental chamber to control the relative humidity and the temperature of the sample environment. However, to prevent the exposure to atmospheric CO_2, OH^- form of the membrane was rinsed and washed with degassed DI water in a CO_2 free glovebox. The membrane was loaded in a air tight cell inside the glovebox before it was taken out for the conductivity measurement. Ultra High Pure (UHP) nitrogen gas was used to control relative humidity for the pure OH^- form conductivity measurement at different temperature and RH using the BekkTech setup(58) by Fuel Cell Technologies Inc®. For the real time conductivity measurements the membrane when the pure form of OH^- membrane was exposed to CO_2, the N_2 gas was swapped to compressed air. The conductivity was calculated by measuring the membrane resistance in different anionic forms using an electrochemical impedance spectroscopy. The impedance spectra collected using EIS were fit to Nyquist plots using EC-Lab software to obtain the membrane resistances. The conductivity was calculated from:

$$\sigma = \frac{l}{R\,w\,t}$$

where l is the distance between two electrodes, R is the resistance, w and t are the width and thickness of the membrane.

A Dynamic vapor sorption(DVS)-advantage instrument by Surface Measurement System™ was used to measure the sorption and desorption of water vapor by the membrane at 30°C as function of relative humidity. The membrane sample was equilibrated for 3.0 hours at 0%RH to measure dry mass and then equilibrated at 1.5 hours each at 20, 40, 60, 80 and 95%RH before further water uptake measurements. The water uptake (WU) and λ (number of water molecules per quaternary ammonium group)

was calculated as: $WU = (m_{rh} - m_{dry})/m_{dry}$ and $\lambda = WU/(IEC \times MW_{H2O})$ where m_{rh} is the mass of membrane at specific %RH and m_{dry} is the mass of membrane at 0%RH, IEC is ion exchange capacity of the membrane (1.78 ± 0.02 for this ETFE-g-PVBTMA membrane).

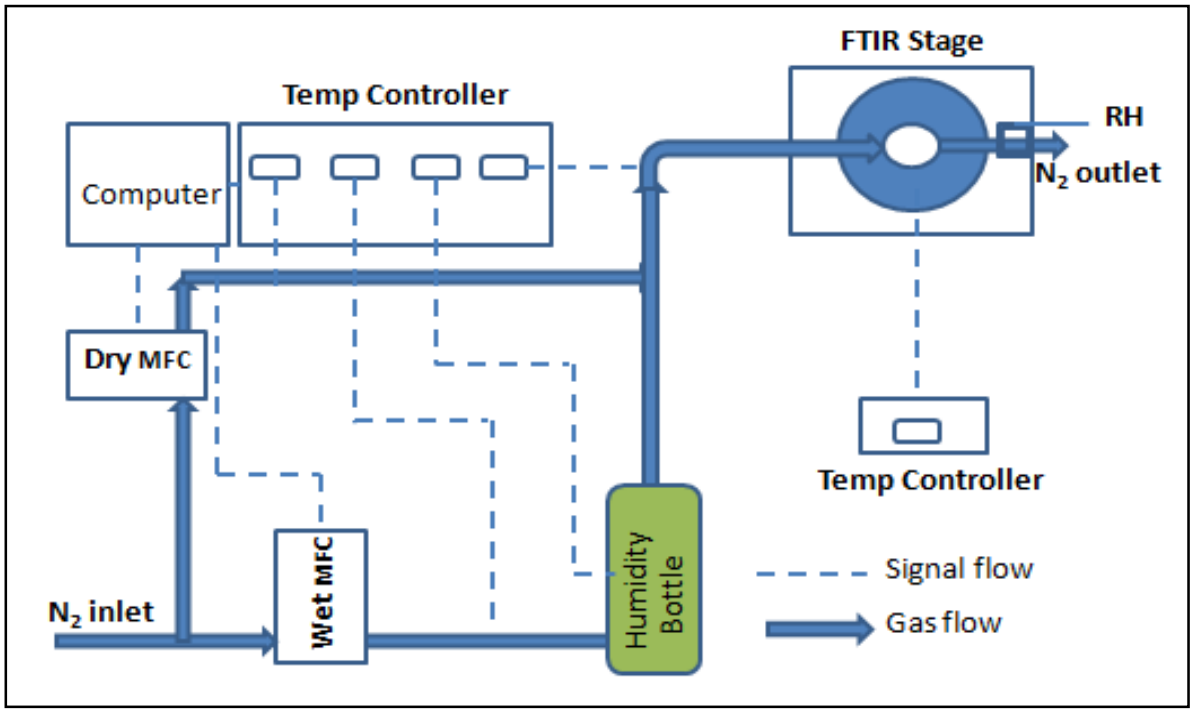

Figure 122 A schematic of a custom-built environmental control setup for the FTIR microscope.

A FTIR microscope was used for collection of IR spectra at different conditions of temperature and %RH. The humidity of the membrane was controlled using a custom designed environmental control set up (Figure 122). Basically the system was used to control the relative humidity inside the sample containing stainless steel oven by adjusting the ratio of the flow of dry and wet N_2 (N_2 bubbled through DI water) using mass flow controllers (MKS Instrument Inc.). The flow rates of the gas were controlled using a Labview software. The sample oven was heated using a Thermo Fisher one channel temperature controller while the humidity bottle and all gas flow lines were heated using a 4 channel E&M temperature controller. A MCT cooled detector with a transmission technique was used to collect spectra with 256 scans and a resolution of 8 cm^{-1}.

Ionic conductivity measurements for the ETFE-g-PVBTMA membrane in OH^-, Cl^-, CO_3^{2-} and HCO_3^- forms were performed as a function of temperature at constant relative humidity of 50, 80 and 95%. The OH^- form of the membrane had a very promising conductivity values at every conditions of temperature and hydration level among the anion forms of the AEM tested. At 80°C and 95%RH, the OH^- conductivity value (~132 mS/cm) was still lower than the Nafion(59) performance at similar conditions but reasonably higher than most AEMs(50). The membrane OH^- conductivity values well

above 100mS/cm (112, 120 and 132 mS/cm for 60, 70 and 80°C; respectively) for any temperature at 60°C and above at 95%RH was higher than values reported for a stable most AEMs. The temperature effect on membrane conductivity seem to be lower at temperature above 60°C compared to the temperature effect on conductivity below 60°C. The lower activation energy for the OH^- form compared to other anionic forms also indicated a weaker temperature dependency of conductivity at temperature higher than 60°C. The conductivity of CO_3^{2-} and HCO_3^- forms of the AEM were very comparable at all conditions of temperature and RH. A previous conductivity study on the membrane in HCO_3^- form showed a similar results(60). The lower conductivity of Cl^- form of the membrane was counterintuitive as it was expected to have a higher conductivity value than CO_3^{2-} and HCO_3^- forms due to its smaller hydration size (Table 21). A lower water uptake at 30°C and 80%RH in Cl^- form indicated not sufficient water molecules are present in membrane for ionic conduction(Figure 126).

The membrane changed its color from a light transparent brown color to dark black during OH^- conductivity measurements and even during OH^- ion exchanged inside the glovebox but the color change of the membrane had no effect in the conductivity performance. The membrane however didn't turn dark in other anionic forms. No obvious evidences of chemical degradation was found under the IR study of the membrane (Figure 125). Our previous ATR IR study on poly(ethyleneimine) AEMs showed the fast kinetics reaction of OH^- with CO_2 when the membrane was exposed to air(61).

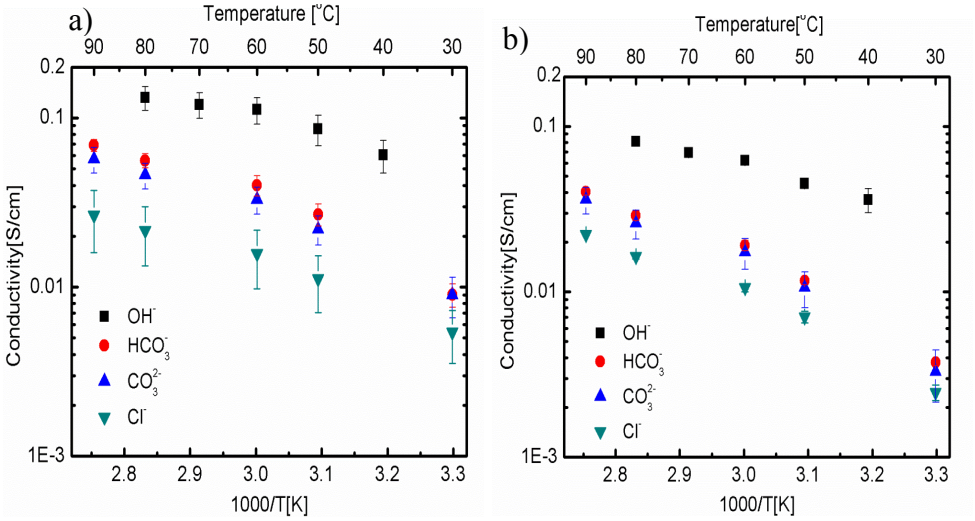

Figure 123 In-plane conductivity of a ETFE-g-PVBTMA membrane in HCO_3^-, CO_3^{2-}, Cl^- and OH^- forms as a function of temperature at a constant humidity a) 95 and b) 80% RH

Tokuyama(62) and Yanagi(63) have also shown that the OH^- form of AEM is unstable in atmospheric CO_2 and uptake of atmospheric CO_2 is rapid (on the order of minutes). Previous researchers have assumed that exposure to CO_2 reduces the conductivity of OH^- form AEMs to the values similar to the CO_3^{2-} and HCO_3^- forms(64). However, the decrease in conductivity performance of OH^- form of membrane when exposed to air was found to be slower than the OH^- conversion time seen in ATR kinetic

study. One of the reasons for the difference could that the ATR spectra collection only consider the surface of the membrane (5 µm deep) compared to whole membrane during the conductivity measurement. The conductivity of the membrane in anionic forms increased with increased in temperature as expected (**Figure 123**). Very few groups have been able to measure a pure form of OH^- conductivity in AEMs due to the fast reactions of OH^- and CO_2 during measurements in air. In fact most groups measure the conductivity while the AEMs are soaked in water(65-67). We found out that the conductivity difference is huge and comparison of conductivity of a membrane measured in water does not represent the situation when the membrane conductivity measurement are performed in controlled environment.

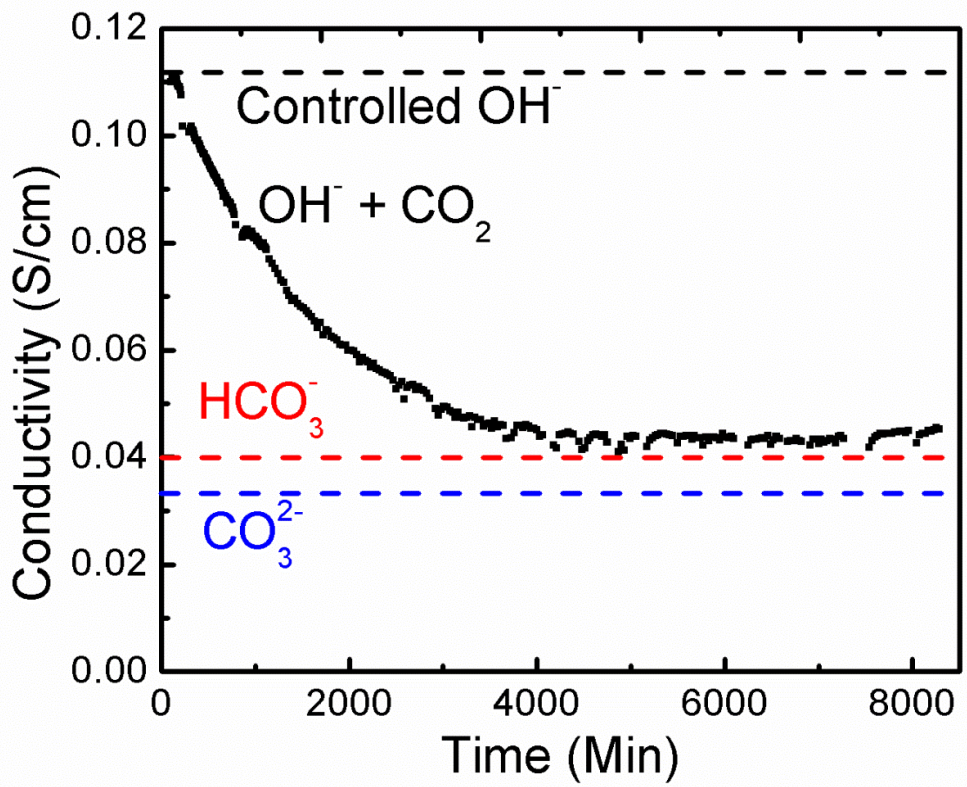

Figure 124. A real time conductivity measurement of a ETFE-g-PVBTMA membrane in OH- form when exposed to compressed air under a controlled environment. Dotted lines represent pure ionic conductivity. All conductivity were measured at 60°C and 95%RH.

A dynamic conductivity measurement of OH^- form of the membrane showed a decreasing trend of conductivity with the exposure time to compressed air (Figure 124). The initial conductivity value of ca. 110mS/cm at 60°C and 95%RH decreased to level out to about ca. 43.0 mS/cm in 3430 min. The membrane degradation was not observed in IR study of the membrane before and after the conductivity measurements (**Figure 125**), so the decrease in performance was believed to be entirely due to the reaction of carbon-dioxide and OH^- to form CO_3^{2-} and HCO_3^- according to the reactions Rxn 1 and Rxn 2.

$$OH^- + CO_2 \rightarrow HCO_3^- \qquad \textbf{Rxn 1}$$

$$OH^- + HCO_3^- \leftrightarrow CO_3^{2-} + H_2O \qquad \textbf{Rxn 2}$$

Rxn 1 is an irreversible forward reaction while the Rxn 2 is an instantaneous reversible reaction(68). The decrease in OH^- form of membrane conductivity approached the conductivity of HCO_3^- form. The leveling conductivity values closer to HCO_3^- form of conductivity indicated Rxn 1 to be a dominating reaction in the presence of excess CO_2. A slight higher conductivity of OH^- air exposed in long time was believed to be due to residual OH^- form in the membrane. The quantitative analysis of anions in the membrane will be part of future work.

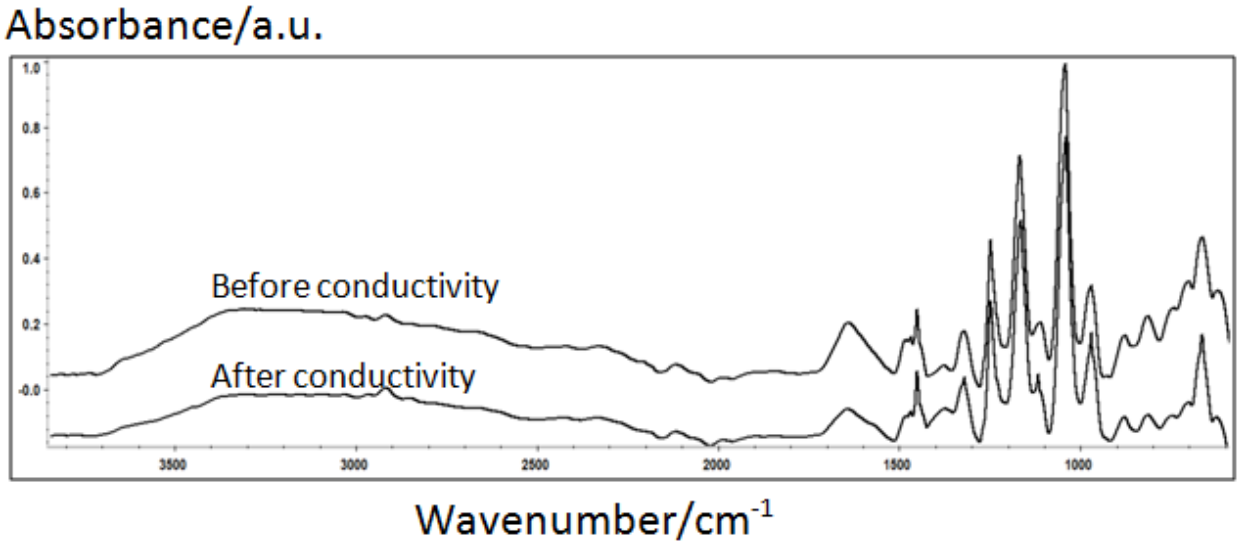

Figure 125. IR spectra collected for ETFE-g-PVBTMA in OH^- form before and after OH^- measurement

The ionic conductivity values at different temperature at constant %RH were fitted to a Arrhenius equation to calculate an ionic transport activation energy (Table 21).

Table 21. Ionic activation energies calculated by fitting the temperature dependency of conductivity using Arrhenius equation as a function of temperature at 95%RH. A linear regression analysis was performed to calculate errors on activation energy

Anions		OH^-	HCO_3^-	CO_3^{2-}	Cl^-
Ea(kJ/mol)		18.7 ± 2.2	28.9 ± 1.5	27.8 ± 2.2	23.6 ± 3.8
Hydration Number	*Literatures*	4.0(67)	6.9(68)	8.7(69)	-
	Measured	-	-	-	3.7 ± 0.2
Hydrated Radius (Å)		3.00(67, 70)	3.64(68, 69)	3.94(69, 70)	3.32(70)

The lowest activation energy for OH^- form of anion indicated the conductivity dependency to be the lowest or even the lowest energy barriers for anion transport among the anions tested. A slight non-linear behavior of natural logarithmic of conductivity dependency on inverse of temperature indicated a slight deviation from Arrhenius behavior of conductivity dependency on temperature. Conductivity of anion in the membrane could be affected by a polymer segmental motion in addition to an activation

energy. A slightly non linear Arrhenius fitting indicated the possibility of Vogel-Tamann-Fulcher (VTF) behavior in which polymer segmental motion contribute for the ions transport across the membrane(71). Activation energy for both CO_3^{2-} and HCO_3^- was comparable. A difference in activation energy among anions corresponded to the hydration radius for OH^- and Cl^-. The OH^- being the smallest anionic size had the lowest activation energy and HCO_3^- had the highest activation energy. Conductivity was highly dependent on the presence of water. The conductivity of the membrane in all anionic forms increases with increasing relative humidity from 50 to 95%. A λ (λ is the number of water molecules per quaternized ammonium group) of about 4(WU ~12 wt%) (Figure 126) at 95%RH and 30°C to give a stable hydrated solvation of Cl^- was found to be consistent with the hydrated OH^- in solution study by Mark E. Tuckerman et al(72).

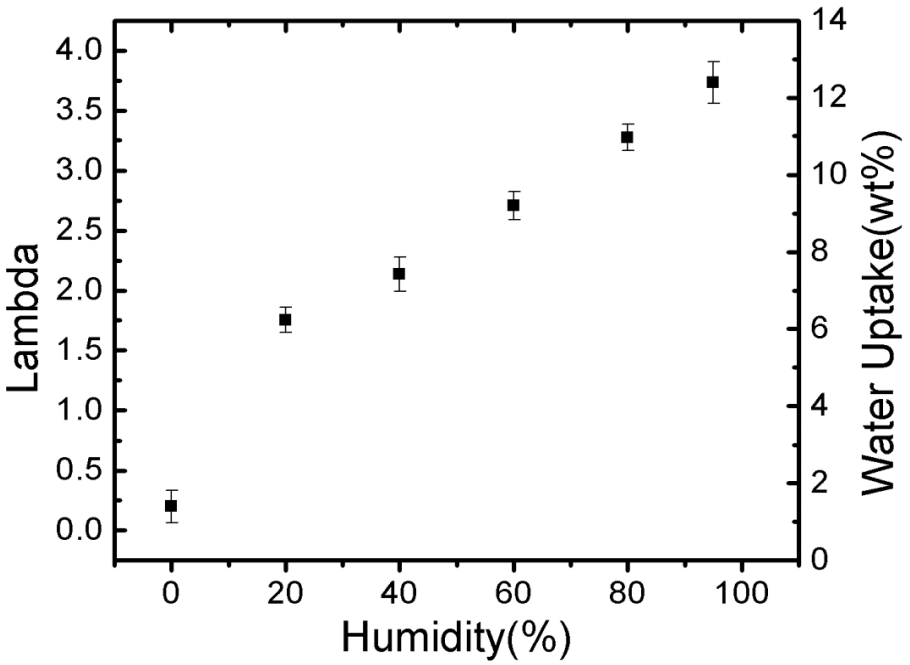

Figure 126. Water uptake (and Lambda) for a ETFE-g-PVBTMA membrane in Cl^- form as a function of %RH at 30°C.

A dynamic spectra that were collected every few minutes during a saturated N_2 gas flow through the membrane at 30°C. An integrated area under the curve at the -O-H stretching region(range 3700- 2960 cm^{-1}) (**Figure 127**) was used over time to see the equilibrated area to confirm the complete saturation of the membrane. A very similar time (~67 minutes) scale was observed for the membrane saturation during the DVS study under similar conditions of temperature and saturated N_2 gas flow (**Figure 128**). Using both the FTIR environment setups and the DVS, the membrane showed a nonlinear water uptake with an initial faster water uptake and a slower as it approached the saturation conditions.

A study of the IR spectra collected at different humidity at 30°C showed a few interesting H_2O polymer interactions (**Figure 129**). An expanded -O-H stretching region (3650- 3000 cm^{-1}) showed an increased in water absorption intensity with the increase

in %RH from 0 to 95. A IR peak shift from 3381 cm^{-1} at 0%RH to 3406 cm^{-1} %RH indicated an increase in -O-H stretching frequency(**Figure 130**a) and a similar behavior was observed in H-O-H bending region 1700-1550 cm^{-1} (**Figure 130**b). In fact, IR wavenumber intensity at ~1580 cm^{-1} decreased while peak intensity at 1643 cm^{-1} increased with the increase in hydration level. The lower H-O-H bending frequency at the lower hydration level shifted towards the H-O-H higher frequency approaching bending frequency of free water molecules at 1643 cm^{-1} (69). Both the -O-H stretching and H-O-H bending showing lower vibration frequency that increased over time indicated at least two extreme frequency of distinct water molecules. When the first few molecules of H_2O was introduced (lower hydration levels), they are tightly bonded to quaternized ammonium group until the ammonium group is surrounded by a layer of water molecules. The tightly bonded H_2O molecules form a inner solvation layer with a lower both stretching and bending frequency of vibration. With the introduction of more H_2O molecules, the interaction of water molecules to quaternized ammonium group decreased as H_2O molecules are farther away. This makes the outer solvation layer with both vibration and bending frequency approaching the free H_2O molecules. Similar interaction behavior was seen in -C-H stretching region (**Figure 130**c). With the increase in the hydration levels, -C-H groups had higher stretching frequency. This could be due to the greater segmental motion that enhances the stretching frequency at the higher hydration levels. However, it'd be hard to tell exactly if the -C-H stretching is originated from backbone or from the side chains without theoretical calculations.

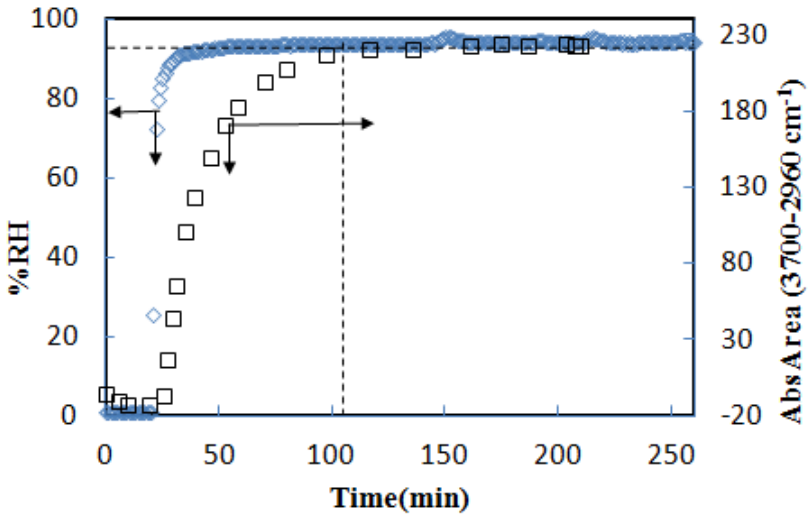

Figure 127. Membrane saturation time was measured using the custom built humidity control system for FTIR microscope. The 100 SCCM of wet N_2 gas was used to saturate the membrane while taking ATR spectra at 30°C. Absorption area under O-H stretching IR peak at the range 3700-2960 cm^{-1} was integrated over time. It took the custom set up ~75 minutes to saturate the membrane.

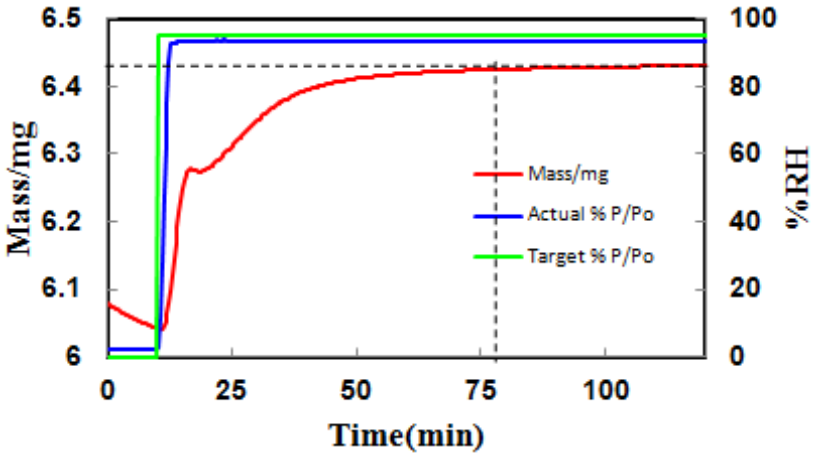

Figure 128 Membrane saturation time measured using a DVS setup. It took the set up ~67 minutes before the membrane was saturated.

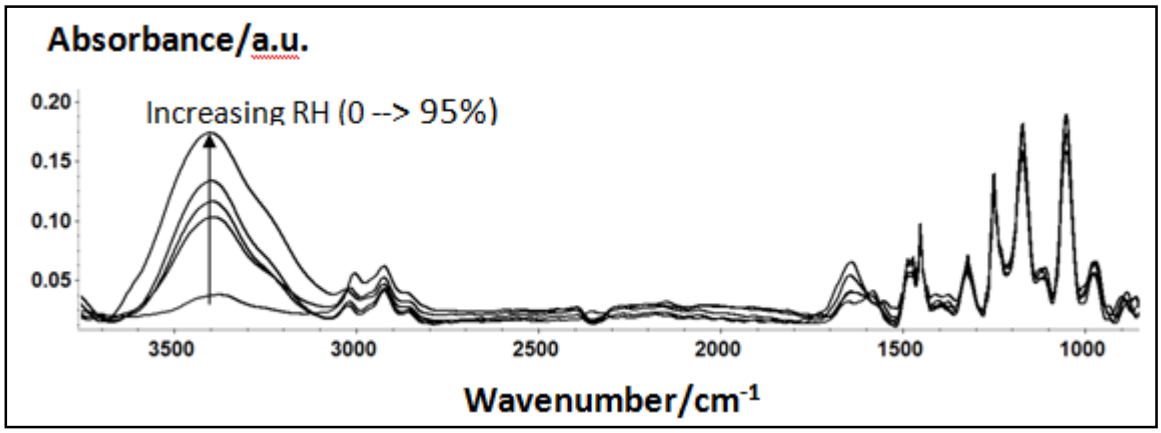

Figure 129 IR study of the membrane as a function of %RH(0, 25, 50, 75 and 100%) at 30°C

a) b) c)

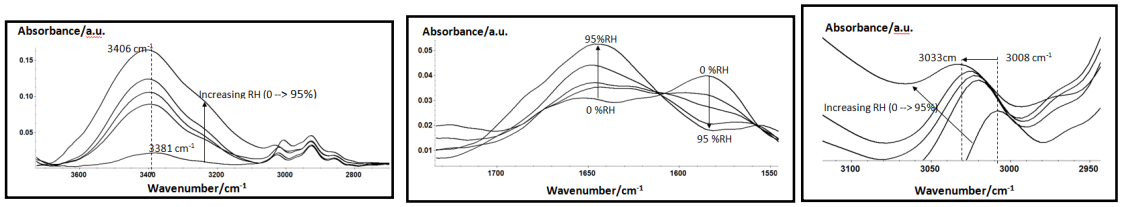

Figure 130 IR water study on the membrane: Expanded region for a) O-H stretching b) H-O-H bending frequency c) -C-H stretching region.

In-plane conductivity was measured for a EFTE-g-PVBTMA membrane in HCO_3^-, CO_3^{2-}, Cl^- and OH^- forms. The membrane was chemically stable in OH^- form at extreme conditions of temperature and humidity. The stability of the membrane was tested by IR studies and no degradation was observed during controlled OH^- conductivity measurement in extreme conditions of temperature and humidity. In fact, the high OH^-

conductivity even at relatively drier conditions (80% and 60°C) made the membrane closer to its proton analogy performance to fuel cell applications. We observed that the air exposed OH^- form of AEMs perform poorly compared to pure form of OH^- conductivity but approached the conductivity of pure form of HCO_3^- over time. The OH^- ions react with CO_2 to form counter ions mixture of HCO_3^-, CO_3^{2-} and OH^-. In the membrane, the presence of these counter anions decreases the ionic mobility reducing the conductivity performance of hydroxide form of AEMs. The IR water study showed water interactions with both the hydrophilic and the hydrophobic polymer blocks indicating at least two different types of water molecules.

5.5 Polyphenylene Oxide co-Polymers

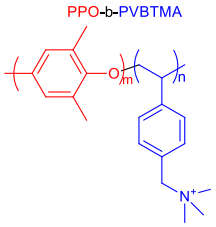

Figure 131:.Schematic of the Polyphenylene Oxide –b- Polyvinyl Benzyl Trimethyl ammonium polymer membrane, IEC= 2.7 meq/gm dry polymer

We used Pulse field Gradient Spin Echo Nuclear Magnetic Resonance technique (PGSE NMR) for studying the transport/self diffusion of fluoride ions in the membrane.[Error! Bookmark not defined.] Fluoride ions serve as a good characterization tool for AEMs because they have similar size to that of a hydroxide ion and they are NMR active and they do not degrade the cations in the film like the hydroxide ions. Figure 132 shows fluoride diffusion as a function of diffusion time and temperature. It can be seen in the figure that as we increase the diffusion time, the restriction comes in to the picture and lowers the diffusion of fluoride ions, showing presence of tortuous channels in the membrane. Behavior of diffusion on a millisecond time scale reflects the cavities and tortuosity present in the membrane and we can characterize the sub micron feature size using Mitra's equation for this AEM.[73] The size of the features inside of the membrane was found to be between 30 nm to 43 nm thus proving the presence of nanometer size channels in the membrane for water and ion transport. Even though the IEC of the membrane is 2.7, lambda value was found to be 4.7 at 60°C from Dynamic Vapor Sorption experiments, showing that the membrane doesn't swell much even at such high IEC.

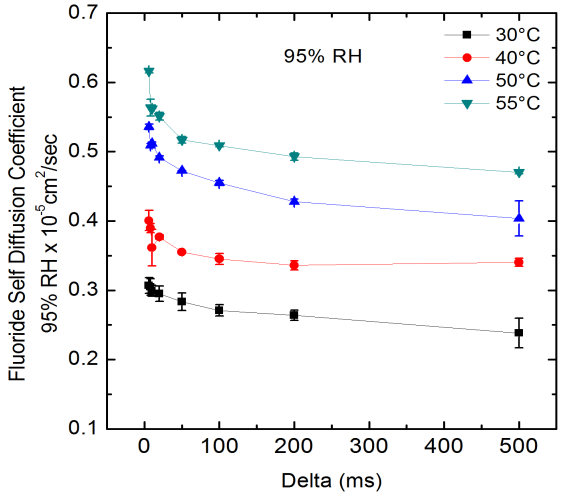

Figure 132. Fluoride Diffusion in PPO-b-PVBTMA[F^-] AEM under saturated humidity environment

The conductivity of this membrane was measured under 95% relative humidity condition using electrochemical impedance spectroscopy as shown in Figure 133. The Fluoride conductivity was 30.5 mS/cm @ 60°C. The conductivity and the fluoride diffusion follows an Arrhenius behavior with an activation energy of 15.6 and 20.5 kJ/mol respectively, showing lower temperature dependence of these two transport properties. Thus low water uptake, low activation energy and high conductivity of this membrane makes it an interesting material for applications in anion exchange membrane electrochemical energy conversion devices.

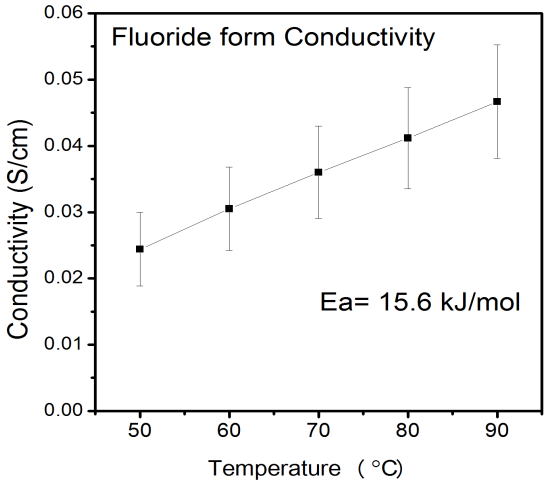

Figure 133. Fluoride Conductivity of PPO-b-PVBTMA[F^-] under 95% Relative Humidity.

5.6 Polyethylene Co-Polymers

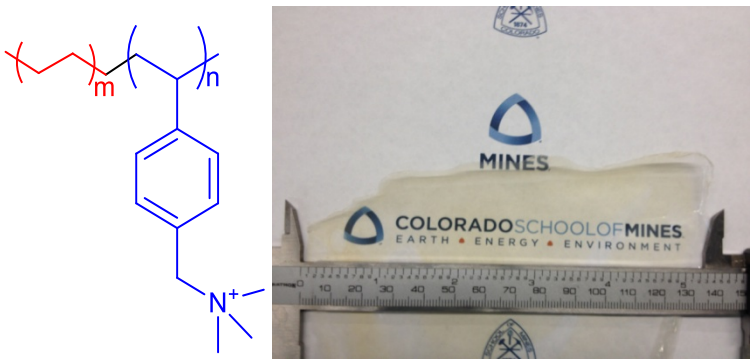

Figure 134. PE-b-PVBTMA[Br^-] structure with picture of the thin (20um) transparent AEM on the right

The polymer [PE-b-PVBTMA[Br^-]] is solvent processable and has excellent mechanical properties. We were able to solvent cast 20µm thin and robust AEM films from this polymer.

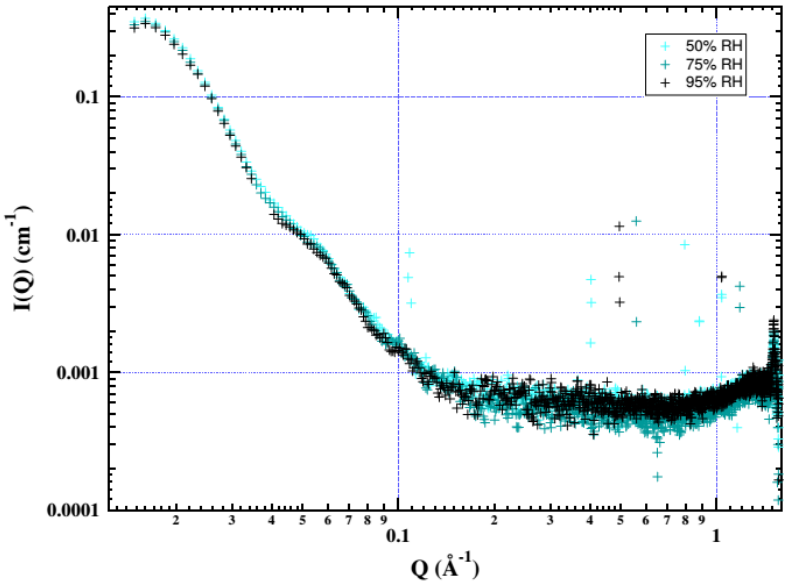

Figure 135. ASAXS pattern of PE-b-PVBTMA[I^-] AEM under varying humidity conditions at 33.2 keV.

For detailed structural investigations the AEMs were subjected to Anomalous SAXS experiments. SAXS is a unique technique for probing nanometer scale structures in polymeric materials. Figure 135 shows the ASAXS pattern for the PE-b-PVBTMA[I^-] membrane at 33.2 keV. It can be seen that the SAXS pattern is not affected by changing humidity which is a result of negligible swelling of the polymer under humidified conditions. This lower swelling is advantageous from fuel cell operations point of view. We also changed the energy of the X ray beam gradually from 33.2 keV to 33.00 keV, but we were not able to see any change in the SAXS pattern showing that the membrane doesn't show any anomalous behavior for Iodide ions. The noise towards the higher q is from X-rays scattered from different electron shells present of the iodine atoms.

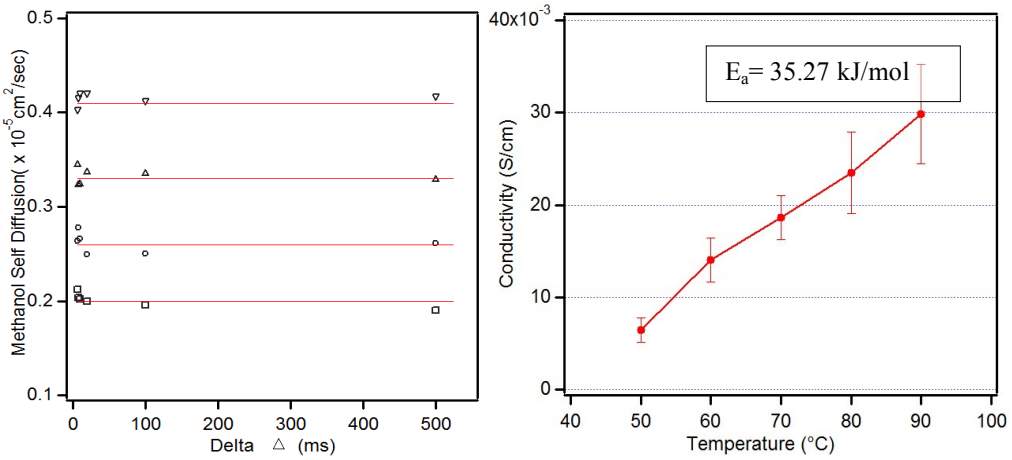

Figure 136. 2M Methanol Self Diffusion in PE-b-PVBTMA[Br^-] at 30°C, 40 °C, 50°C & 55°C from bottom to top as a function of Diffusion time delta, red lines show an average value for a temperature, on the right bromide form of conductivity at 95% Relative humidity

Figure 136 (a) shows self diffusion of 2M methanol using the PGSTE NMR. It can be seen that as temperature increases, the diffusion goes on increasing. Varying the diffusion time Delta gives us the idea about tortuous path present in the membrane. We see that with increasing diffusion time, the self diffusion of methanol does not go down significantly, proving that the path of methanol transport is least tortuous in the time scale of milliseconds to seconds. The methanol diffusion values are lower than those reported in literature for Nafion™-117.[74] This lower methanol diffusion is advantageous for applications in Barrier layers for clothing. Bromide conductivity shown in Figure 136 (b) is very promising (14 mS/cm @ 60°C) with Arrhenius activation energy of 35.27kJ/mol for fuel cell applications. We expect the hydroxide conductivity to be 2-3 fold higher than the bromide conductivity from the results obtained in our lab on some other AEMs.

5.7 Quaternary Phosphonium

Another cation structure we investigate is the tris (2,4,6-trimethoxyphenyl) phosphonium (Figure 45). The calculated theoretical IEC is 1.18 mmol/g. Based on the above study on 1,4,5-trimethyl-2-(2,4,6-trimethoxyphenyl) imidazolium functionalzed polyphenylene oxide, the modification of imidazolium cation by attaching 2,4,6-trimethoxyphenyl group helps to increase the chemical stability of the cation because of both electron donating as well as improved steric effect. Hence, adding three 2,4,6-trimethoxyphenyl groups on the high basicity phosphine expects to display a promising durability under the alkaline condition. Besides, since the volume of tris(2,4,6-trimethoxyphenyl) phosphonium is pretty large, the size of the hydrophilic domain as well as the pattern of aggregations when absorbing water probably are different with small volume cations and display its unique property, thus, directly affect the morphology of the membrane so that further influence the transport property and conductivity performance. This sensitivity on morphology bringing from big volume cation will further study by using of various solvents which have different interactions with cationic groups during the solution cast of the membrane.

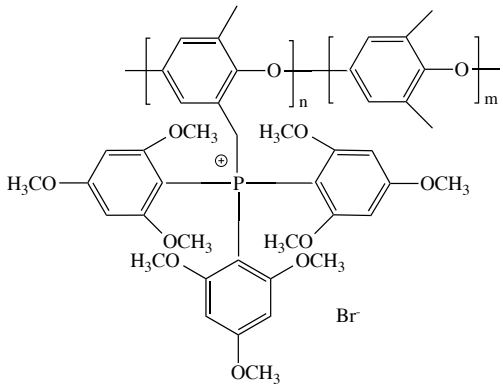

Figure 137 Structure of tris (2,4,6-trimethoxyphenyl) phosphonium functionalized PPO

Based on the Hansen Solubility Parameter calculation, δd, δp and δh of the polymer are 17.5, 10.7 and 11.6 respectively. Interaction radius (R_0) is about 6.2 $Mpa^{0.5}$. So we select DMSO and DMSO/ethyl lactate (41:59 vol%) mixture, which Hansen distance are 6.2 and 1.2 $Mpa^{0.5}$ respectively, as bad and good solvent to drop cast the membrane. In Figure 46 are the images of the formed membranes and both of them are intact and transparent.

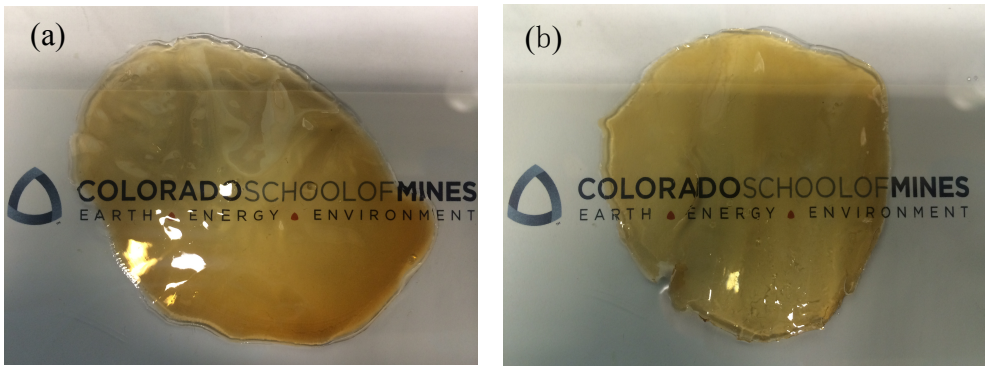

Figure 138 Images of the membranes casted from DMSO (a) and DMSO/ethyl lactate mixture (b)

Arrenhius plots under both 95% RH and 80% RH are shown in Figure 47. We noticed that DMSO cast membrane do not exhibit a linear relation. From 30 ℃ to 50 ℃, conductivities increase faster than in the temperature range between 50 ℃ to 90 ℃. The inflection point at around 50 ℃ indicates either a super Arrhenius transport behavior or two Arrhenius transport combinations. The highest conductivity of the Br^- form membrane is 3.0 mS/cm. However the one casted from mix solvents display a linear Arrhenius behavior with similar conductivity value. Our future work will learn more about the big cation influence on the transport property and future reflect on the conductivity behavior through different solvents cast systems.

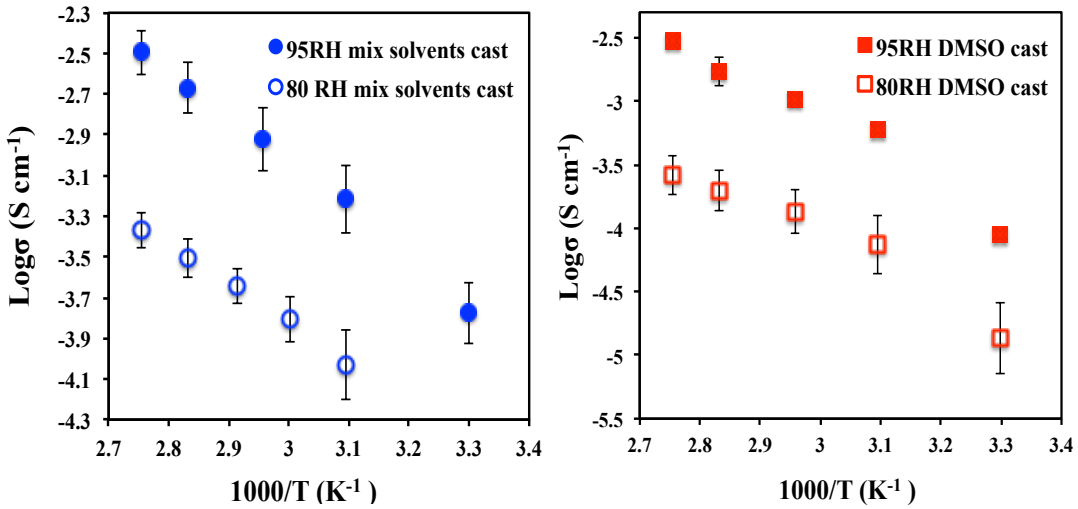

Figure 139. Br form conductivities of tris(2,4,6-trimethoxyphenyl) phosphonium functionalized PPO under 95% RH and 80% RH. (■ DMSO cast, • mix solvents cast).

6. Mechanical Studies and Film Forming

6.1 Simultaneous extensional rheology and SAXS of AEMs

In the desire to understand how the structure of a polymer film changes with extensional forces, several films were brought to the Advanced Photon Source (APS) for testing. Dr. Wesley Burghardt's group at Northwestern University provided an SER fixture mounted inside of an oven that allowed for in situ x-ray analysis (Figure 140).

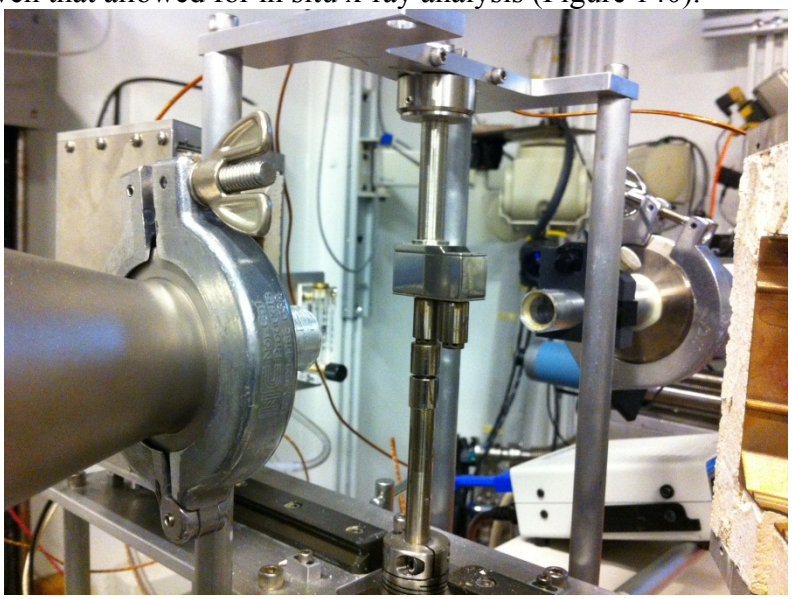

Figure 140 - SER Oven for in situ SAXS analysis. Built by the Burghardt group at Northwestern University.

Several films were tried with this experimental system, but the most interesting film was the Tokuyama A-006. This film easily attaches to the steel drums at a temperature around 150°C, and the film remains adhered as the temperature is lowered. This allows for investigation at varying temperatures. The rheological stress-strain data was collected at CSM with the ARES instrument prior to the scattering experiments performed at the APS.

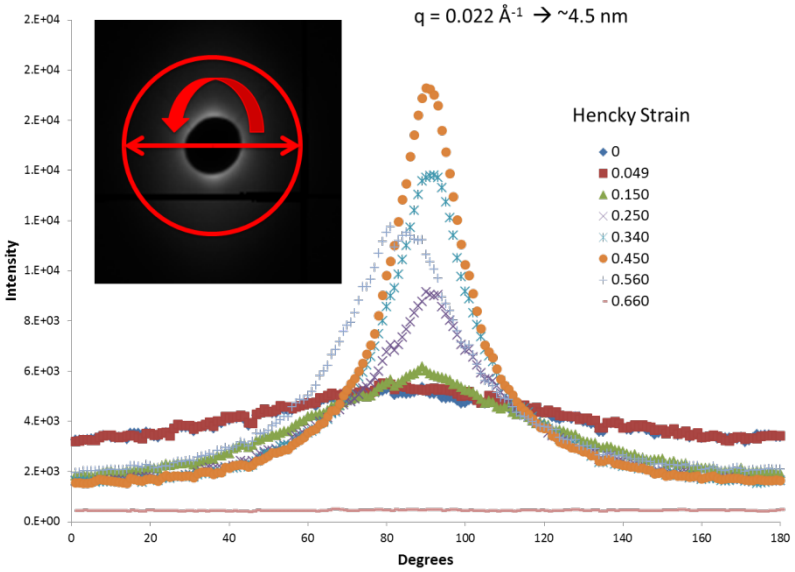

Figure 141- Intensity versus Phi at q = 0.0222 $Å^{-1}$ (~4.5 nm) and 60 °C

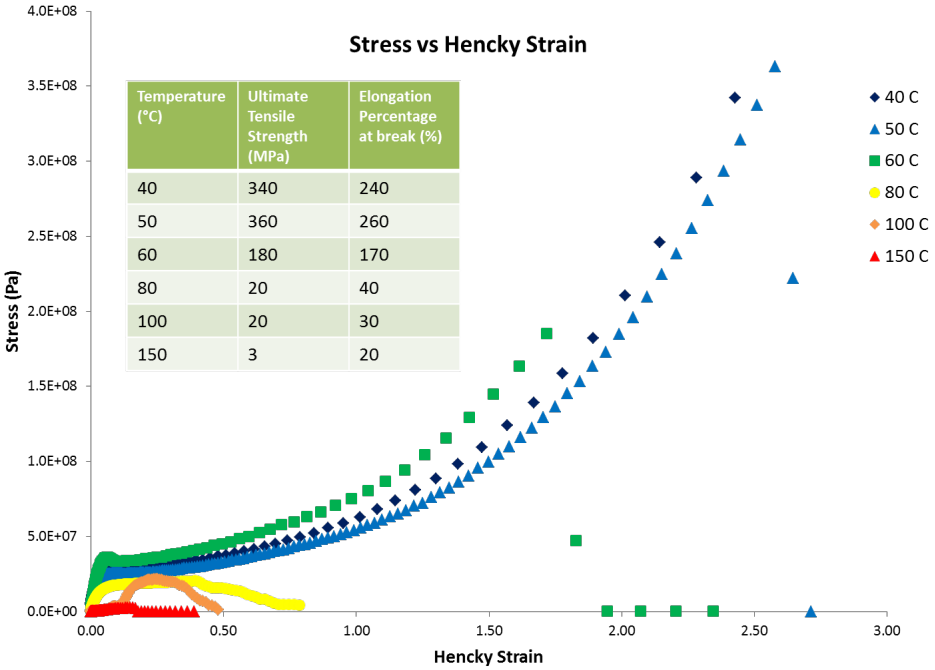

Figure 142 - Rheological data for Tokuyama A-006 at increasing temperature

The scattering and rheological data suggests the alignment of the chains allows the polymer to withstand more stress (Figure 142).

The physical composition of the Tokuyama A-006 membrane is unknown to us so we cannot draw further conclusions from this data. Other membranes made by group members were tested, but the results did not show any conclusive information. It is hopeful in the future to test ordered, known polymers in the same manner as the Tokuyama A-006 film.

6.2 Film Casting and characterization of PS-*b*-PVBC block copolymer and corresponding blends

An automatic film applicator with an adjustable micrometer blade was used to cast consistent films of various thickness from the polystyrene-*b*-poly(vinylbenzyl chloride) (PS-*b*-PVBC) block copolymer synthesized by the Knauss group. Blends of polystyrene (PS) and poly(vinylbenzyl chloroide) (PVBC) homopolymers were also cast into membrane as a comparison to the diblock films. Treatment of the films with trimethylamine converted vinylbenzyl chloride sites to vinylbenzyl trimethylammonium to produce conductive films. These films were characterized by EIS, SAXS, and extensional rheology. The diblock films had a 98% conversion of reactive sites while the homopolymer blend films had only a 45% conversion, even when the quaternization reaction was extended in a pressurized cell at elevated temperature.

Conductivities were an order of magnitude higher for the diblock copolymer compared to the blend (**Figure 143**). At 50°C the conductivities of the diblock films were 24-33 mS/cm, while the conductivities of the blend films were only 1-6 mS/cm. The

activation energy for ion conduction was similar, between 15 and 21 kJ/mol, for both the diblock and blend systems across all thicknesses tested.

Ordering of the diblock copolymer was investigating using SAXS (**Figure 144**). Under dry conditions the diblock film displayed no characteristic peaks to indicated order in the film. After the film was humidified for four hours peaks are distinguishable. The position of the first and second order peaks with respect to the scattering vector, q, correlates to a lamellar ordering with spacing of 140 nm. The lamellar ordering of the diblock polymer when humidified promotes the enhanced conductivity compared to the homopolymer blend films.

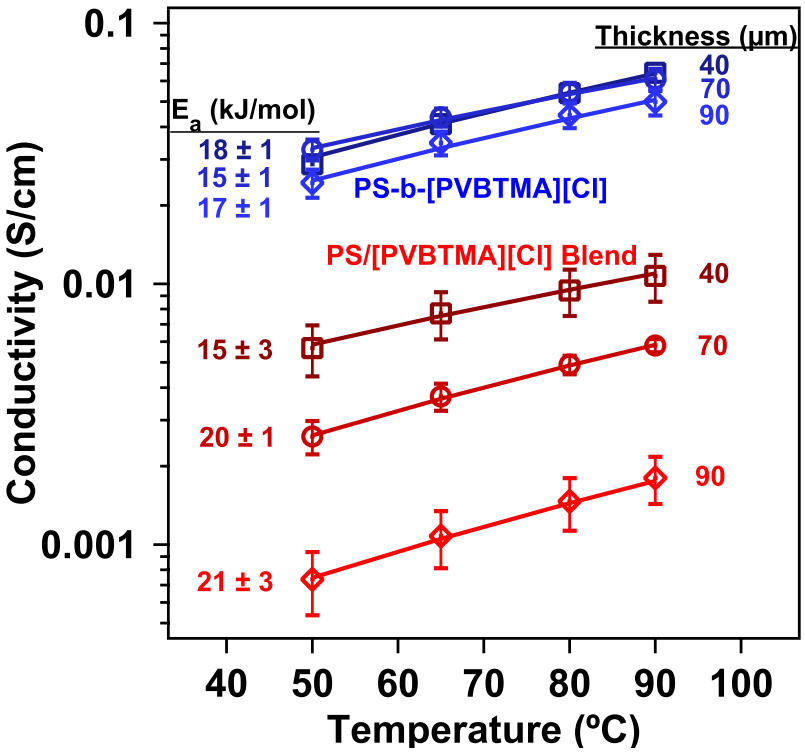

Figure 143: Chloride conductivity of the diblock, PS-b-PVBTMA[Cl], shown in blue and the homopolymer blend, PS/PVBTMA[Cl], shown in red. The darkest of each color corresponds with the thinnest, 40 µm, films transitioning to the lightest colors corresponding to the thickest, 90 µm, films. The activation energies for each data set are listed on the left side of the graph.

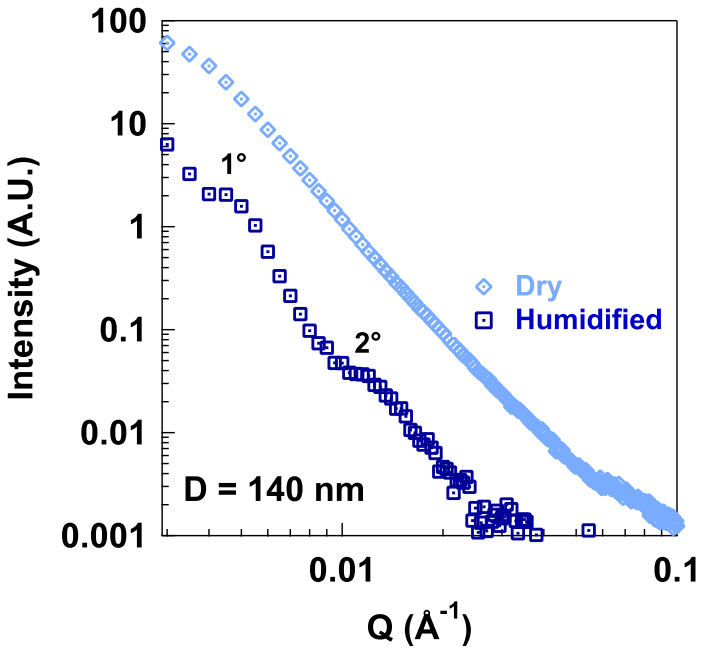

Figure 144: Small angle x-ray scattering patterns for the diblock copolymer membrane under dry (light blue) and humidified (dark blue) conditions.

Mechanical testing of the films was performed by uniaxial stretching the films on an ARES G2 rheomter that was modified to control humidity during testing. The diblock and blend cationic films were tested at 60°C under dry and humidified conditions to determine the effect of water sorption on mechanical properties (Figure 145). Water taken up by the polymer acts as a plasticizer, i.e., increasing fluidity, decreasing the modulus and stress, and an increasing elongation. The Young's modulus for both the diblock and blend films decreased significantly, from between 515 - 675 MPa to between 200 – 275 MPa, when the films were humidified indicating the plasticizing nature of the water increases film elasticity. Elongation increased significantly for the diblock film, from 2% at dry conditions to 43% at 95%RH. Elongation of the blend films did not change significantly with water uptake; this could be a result of the low water uptake of the blend film or the difference in phase separation in the blend. The stress at break for the diblock decreased only slightly from the dry state (8 MPa compared to 9 MPa dry). The blend membrane showed little difference in stress at break from dry to humidified conditions similar to its elongation behavior, likely due to its low water uptake.

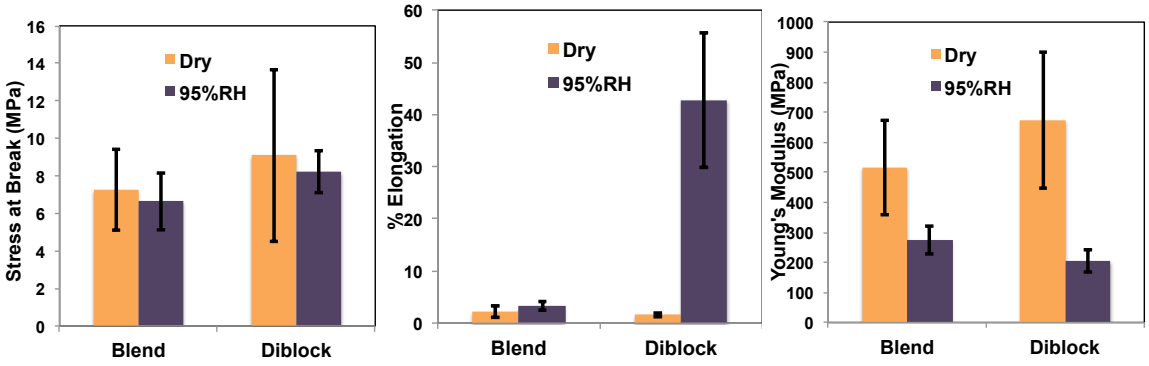

Figure 145: Stress at break, % Elongation, and Young's Modulus for the blend and diblock cationic films at 60°C under dry and humidified conditions.

6.3 Effect of crosslinking method on mechanical properties of poly(isoprene)-ran-poly(vinylbenzyl trimethylammonium) films.

Poly(isoprene)-ran-poly(vinylbenzyl trimethylammonium) (PI-ran-PVBTMA) synthesized by the Coughlin group was cast into thin films and crosslinked by thermal or UV exposure. Mechanical properties were investigated to understand the effect of crosslinking method on film integrity and humidity response. Films were cast at a 0.228 g/mL concentration in ethanol using an automatic films applicator with a draw speed of 20mm/s and a blade height of 500 microns. Films were allowed to dry overnight at room temperature before crosslinking. Thermally crosslinked films were placed in a 140°C oven for 3 or 24 hours. UV crosslinked films had a photoinitiator and dithiol crosslinker added to the casting solution. Films were passed through a F300 Series Fusion UV curing system four times at 15 ft/min under a P300MT power supply corresponding to a power of 300 W/in.

Films were tested at 30°C under dry and humidified conditions by uniaxially stretching films on an ARES G2 rheometer. Engineering stress at failure was similar for all crosslinking conditions; between 5 – 6 MPa for dry films and 1 – 2.3 MPa when humidified. Elongation at dry conditions was greatest for the UV crosslinked film (43%), followed by the 3 hour, thermal crosslinked (15%), and the 24 hour, thermal (2%). Elongation increased with increased humidity for both the thermally crosslinked films. Elongation increased significantly for the 3 hour crosslinked film (127%) and slightly for the 24 hour crosslinked film (7%). Elongation decreased for the UV crosslinked film, down to 19%, when humidified. This result was not expected and will need to be studied in more detail. The Young's modulus at dry conditions was highest for the 24 hour, thermally crosslinked film (360 MPa) followed by the 3 hour, thermally crosslinked film (175 MPa), and the UV crosslinked film (40 MPa). As expected, the modulus decreased for all films when humidified. The 3 hour, thermally crosslinked film has the most drastic reduction in modulus (3 MPa). The 24 hour, thermally crosslinked membrane had a moderate modulus reduction (88 MPa) as did the UV crosslinked membrane (10 MPa). Based on the mechanical data the time of thermally crosslinking significantly impacts elasticity and elongation in the film. Crosslinking via UV exposure produces moderate elasticity and elongation and the change in properties with humidity was less, compared to the thermally crosslinked films. Additional dynamic mechanical testing and comparison of conductive and transport properties of these films will further elucidate the effect of crosslinking method on membrane durability and performance.

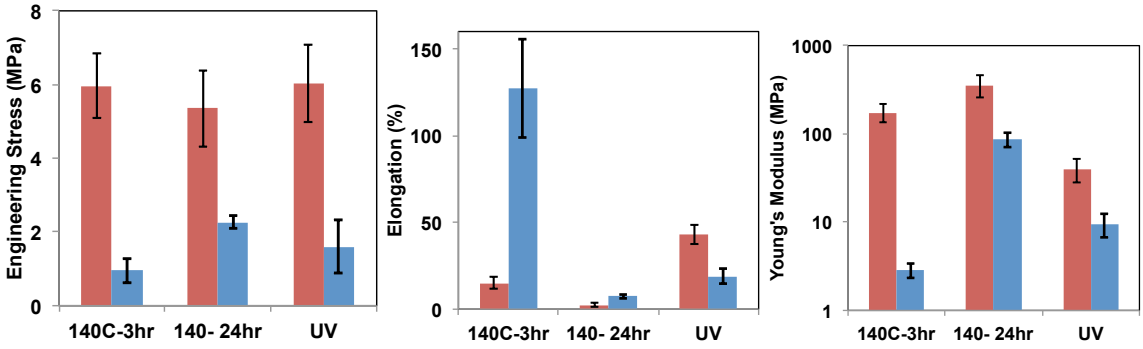

Figure 146: Stress at break, % Elongation, and Young's Modulus for the PI-ran-PVBTMA films crosslinked thermally for 3 and 24 hours and by UV exposure. All films were tested at 30°C under dry (red) and humidified (blue) conditions.

6.4 Build out of humidity controlled rheometry tool

In order to perform rheological testing in an environment with relative humidity and temperature control, the following system was built. The building air supply was used as the medium to carry the humidified gas. The gas supply is nominally at 80-100 psig and dry, but unfiltered. A filter/regulator (5 micron) combination was installed to deliver the air to the system at 40 psig. The airline was split to two separate mass flow controllers (10,000 SCCM, MKS 1179A), for a wet and dry gas supply. A bypass line was put on the dry gas side with a manual ball valve to allow for purging of the line if needed. The exit of the wet gas mass flow controller was piped to a humidity bottle (FCT, Inc.) with 10 m of Nafion™ tubing to allow for gas saturation. The piping leaving the humidity bottle was connected with the dry gas line at a tee junction. All piping downstream of the bottle and just upstream of the tee connection on the dry side has been heated and insulated to prevent condensation. After the tee junction combining the wet and dry gas streams, a static mixer was installed (Koflow, 12 elements). The piping was then run to the ARES instrument and attached to the non-FCO side by using pipe supports attached via the existing holes that secure the plastic housing over the top of the instrument. The hard piping was extended to the edge of the instrument and connected to a 2' flexible heated line (FCT, Inc.). The flexible line was needed to accommodate opening and closing the oven to load the sample. The plugs for the light scattering holes were removed to provide an inlet and exit for the humidified stream. A piece of 1/8" SS Swagelok pipe was bent to 90 degrees and cut to provide delivery of the gas from the flexible heated line to the light scattering holes. The oven can now be closed and the delivery piping makes no contact with the top geometry part connected to the transducer.

The temperature control was split into four zones: the humidity bottle, the piping out of the humidity bottle before the tee junction (encompassing some of the incoming dry gas line as well), the piping from the tee junction up to the flexible heated line, and the heated line. Thermocouples were placed in the humidity bottle and in the piping before the tee and along the ARES instrument. The embedded thermocouple in the flexible heated line was also used. The humidity bottle and flexible heated line came with their own heaters. The piping was heated with flexible heaters (Omega). The thermocouples and heaters were brought into controllers (Watlow EZ-ZONE PM6) with a limit function. The controllers were daisy chained for easy control in the LabView interface.

In situ humidity measurement is essential to accurate control. A relative humidity probe (Vaisala HMT 337) was installed through the camera port on the FCO. TA Instruments provided a camera mount housing in which NPT threads were drilled to allow for a ½" Swagelok fitting to be inserted. The humidity probe was then inserted into the ½" fitting to allow for the polymer sensor to be in the FCO environment. The data from the probe was brought into the LabView interface for feedback control.

In order to have a direct temperature measurement available in LabView, a thermocouple (UTC-USB, Omega) was placed inside the oven through the lower light scattering port. Combined with the dewpoint from the Vaisala probe, a real-time humidity level is shown in LabView.

Figure 147: Humidity delivery system attached to ARES G-2 rheometer.

Modification of SER2 fixture

The standard SER2 drums were modified to handle the thin, solid samples needing characterization (**Figure 148**). The SER2 fixture was designed to primarily test the extensional viscosity of polymers at or near their melting temperature; however, our goals are to test thin polymer films at fuel cell operating conditions. The standard L-shaped pins did not hold our thinner samples to perform the desired tensile test at temperatures well below the polymer melting temperature. Several attachment mechanisms were attempted to enable testing of our materials. Double stick tape, glue, and magnets were not able to hold the films in place on a consistent enough basis to move forward. Since common tensile testers use screw down clamps to hold the samples in place, new drums were machined with screw down clamps. A silicone rubber pad was added to the underside of the clamps to soften the grip on the sample.

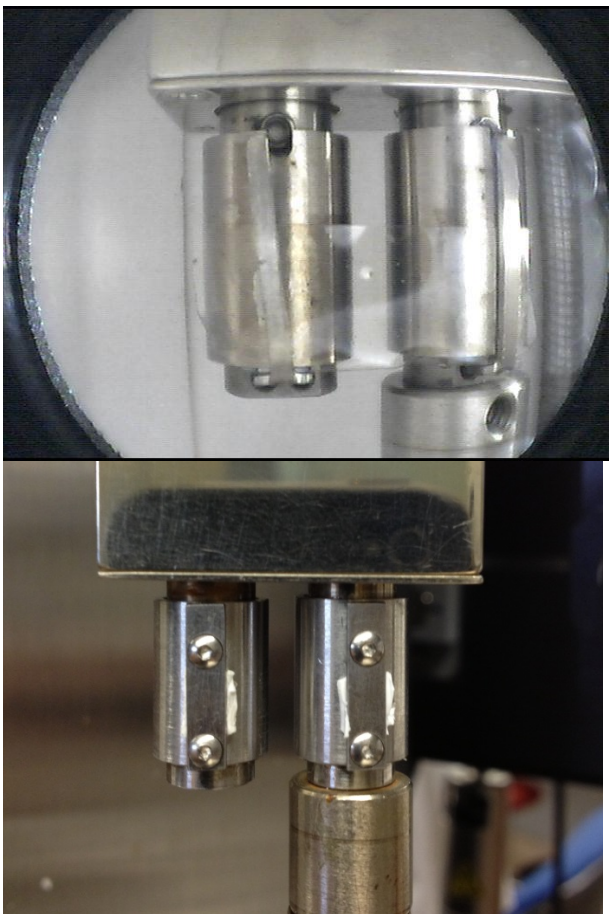

Figure 148: Original drums with pins and modified SER2 drums featuring screw down clamps with silicone rubber pads.

SER Tool as Tensile Tester

The mechanical testing is performed using a Sentmanat Extensional Rheometer (SER2) attached to an ARES-G2 Rheometer from TA Instruments. The standard test method for the establishment of mechanical properties of polymer films less than 1.0 mm in thickness is ASTM D882, Tensile Properties of Thin Plastic Sheeting. According to the standard, the speed of the testing is dependent on the percent elongation at break. The grip separation is also dependent on the percent elongation at break. The speed of the testing is calculated from the initial strain rate specified by the percent elongation at break multiplied by the initial grip separation. With the SER drums, the speed of the drum rotation can be altered, but the separation distance between the drums is fixed. Using the same formula as the ASTM standard, but fixing the grip separation at 12.7 mm (distance between the center point of the two SER drums), a rate of grip separation can be calculated for differing percent elongation at break. This grip separation rate is then converted to a Hencky strain rate using the geometry of the drums, ultimately yielding a rate of 0.33 s^{-1} for films with greater than 100% elongation. The test resulted in a Hencky strain versus stress plot and three properties are taken from the data. In order to compare the data with ASTM D882 data, an Engineering Stress is calculated using the fixed starting area of the sample instead of the typical Extensional Stress which factors in the exponential decrease in area. The stress at break and Young's modulus are calculated

from the Engineering Stress data set. At least five tests are run for each data point. The samples were 15-25 mm long and 3-5 mm wide. The thickness varied from 20-150 microns.

Baseline Data
In order to determine the validity of using the SER2 tool as a tensile tester, polyethylene sheeting and Nafion™ were tested and compared with available third-party data.

Polyethylene
Sheets of a LDPE/LLDPE film were donated by Mountain States Plastics (Johnstown, CO) and tested on the ARES-G2 with the modified SER2 tool at a Hencky strain rate of 0.33 s^{-1} at 23°C and 50%RH. The ExxonMobil data is general for the grade of polyethylene used to make the film, but it is not specific to this film.

Table 22: Mechanical data for a low density polyethylene (LDPE) sheet.

Sample	Tensile Strength (MPa)	Young's Modulus (MPa)	Elongation (%)	Thickness (microns)
Mountain States Plastics LDPE/LLDPE (SER2)	33 ±5	167 ±28	263 ±34	37
Mountain States Plastics LDPE/LLDPE (UMass tensile tester)				
ExxonMobil Exceed® 1018 Series Data Sheet	55	186	500	25.4

There are key differences between a typical tensile tester and the SER2 tool which help explain the data. The gage length on the SER2 tool is fixed at 12.7 mm and is much less than the gage length needed for a tensile tester (100-250 mm) which means that the elongation will be lower on the SER2. The SER2 tool is also a biaxial tester, opposed to a uniaxial tensile tester. This can lead to lower tensile strength and elongation numbers.

Nafion™
Before moving on the team's novel films, it is helpful to gather data on a more common material such as Nafion™. Nafion™ N117 was donated by Proton OnSite as they are interested in mechanical data of this film as well for use in their hydrolysis units. We show a decrease in the modulus in a saturated vapor environment, which is consistent with the theory of water plasticizing the film.

Table 23: Mechanical data for Nafion® N117 at dry and saturated conditions.

Sample Name	Tensile Strength (MPa)	Young's Modulus (MPa)	Elongation (%)	Thickness (microns)

Nafion® N117 30 C, dry	31 ±4	291 ±10	196 ±9	183
Nafion® N117, 30 C, saturated	27 ±4	137 ±17	151 ±7	183

The benchmarking data set will be complete soon and will be published in a Review of Scientific Instruments paper in 3Q 2013.

6.5 Mechanical properties of Anion Exchange Membranes

While there is not an AEM standard, like Nafion™ is for PEMs, there are several membranes that have been heavily published in literature and often act as baseline comparison for new AEM development. The extensional properties of three such standard AEMs were investigated under different temperature and humidity conditions. The AEMs of study are an industrial produced Fumasep™ FAA-PK membrane produced by Fumatech, a radiation grafted poly(ethylene-co-tetrafluoroethylene)-based quaternary ammonium AEM developed by John Varcoe's team at the University of Surrey, and an aminated tetramethyl polyphenylene (ATMPP) membrane developed by Michael Hibbs at Sandia National Laboratory (Figure 149).

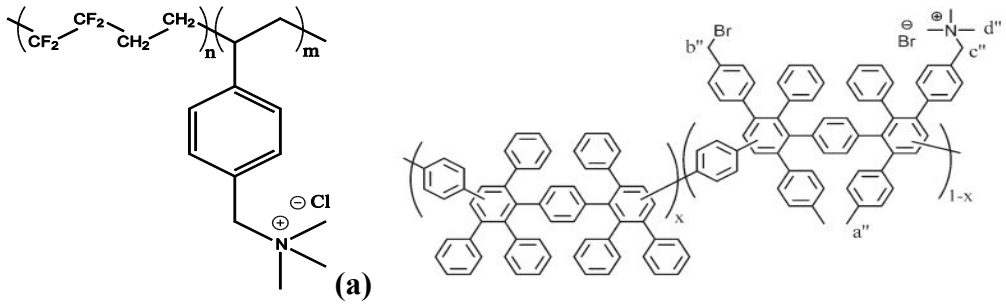

(a) **(b)** Figure 149: Structures of the Surrey membrane (a), and the ATMPP membrane (b).

The Fumasep™ FAA-PK membrane is a PEEK reinforced anion exchange membrane with a dry thickness of 110 μm and an IEC of 1.5 mmol/g. The Fumasep™ membrane was received in a dry state in the Cl^- form and did not undergo further treatment before testing. The ETFE-g-PVBTMA had a dry thickness of 80 μm and an IEC of 1.8 mmol/g. The membrane was received in a dry state in the Cl^- form and tested without further treatment. The ATMPP membrane had a dry thickness of 80 μm and an IEC of 2.5 mmol/g. The ATMPP membrane was received in the Br^- form and stored in liquid water. The ATMPP membrane was dried at ambient conditions prior to dry mechanical testing.

Polymer films were cut into strips of 30mm(L) x 2mm(W) for testing. The SER drums were wrapped in double-sided tape to prevent slipping of the films. Silicon coated screw-down pins secured the film to the drum surface; additionally tape was place over the outer edges of the film, outside the sample area. The films were stretched at a Hencky

strain rate of 0.33 s^{-1} (2.12 mm/s). Samples were tested under dry airflow at 30°C and 60°C. Dry test conditions were achieved using the forced convection oven (FCO) built into the ARES rheometer. Samples were allowed to equilibrate at temperature for 5 min at 30°C and 10 min at 60°C before the tensile tests were started. Samples were also tested under saturated gas conditions at 30°C. Humidified samples were allowed to equilibrate and take up water for 40 min, except the ATMPP membrane that equilibrated for 1 h. These equilibration times were determined by separate dynamic vapor sorption experiments, during which the gravimetric change in mass of polymer is measured with respect to humidity.

At low temperatures under dry conditions all membranes tested were brittle, with a Young's modulus of at least 300 MPa. The rotational nature of the SER tool requires a minimum film elasticity, so that the film wraps around the drum without breaking, to represent a true tensile test. At dry conditions, all AEM films were too brittle leading to failure at the attachment pins, preventing measurement of true tensile properties. While the extensions of these AEMs on the SER are not true tensile tests, the modulus, elongation, and strength measured still serve as a relative comparison between membranes.

The FAA-PK and ETFE-g-PVBTMA membranes are more brittle than the ATMPP membrane as given by the steeper initial slope to the stress-strain curve. The transition from elastic deformation to plastic deformation is similar for all three membranes, around a hencky strain of 0.1. The FAA-PK and ATMPP membranes have similar elongation to break ~20%, but the FAA-PK membrane withstands a higher stress to break, around 50 MPa, compared to only 20 MPa for the ATMPP membrane. The ETFE-g-PVBTMA membrane has the longest elongation to break, over 30%, and withstands stress similar to the FAA-PK membrane, around 55 MPa.

Increasing the testing temperature from 30°C to 60°C is expected to reduce the elastic modulus and stress at break, and increase the elongation of the polymer. Increasing temperature to 60°C reduced the modulus of the samples by 50 to 100 MPa. Elongation increased for two of the three samples but was reduced for the ETFE-g-PVBTMA membrane. The stress at break increases for the two membranes that had increased elongation, and was only reduced for the ETFE-g-PVBTMA. These results may be due in part to the nature of the SER tool. The increase in elasticity allowed the film to better wrap around the SER drums, increasing both elongation and stress to break, as opposed to breaking at the attachment pin due to bending. This effect may not be seen in a true tensile measurement.

Under humidified conditions, such as those in a working fuel cell, water taken up by the polymer has a plasticizing effect on the polymer. The water plasticizer generally reduces the elastic modulus, increases elongation, and decreases the stress to break. Humidifying the membranes reduced the elastic modulus and increased elongation for all samples tested. The stress at break increased upon humidification for FAA-PK and ETFE-g-PVBTMA membrane and remained the unchanged for the ATMPP membrane.

This increase in stress is again likely due to the rotational nature of the extensional test with the SER drums.

Table 24 summarizes the mechanical properties measured for each membrane at the different sample conditions and compares available literature data at similar conditions. The Fumasep™ FAA-PK membrane had a decrease in modulus when temperature or humidity was increased. Strength and elongation both increased for the FAA-PK when temperature increased. The ETFE-g-PVBTMA membrane had a slight decrease in modulus with increased temperature, but a drastic reduction upon hydration. Increasing temperature reduced elongation and strength for the ETFE-g-PVBTMA membrane. Hydrating the ETFE-g-PVBTMA membrane decreased the strength slightly and increased elongation by almost four times. Literature for a hydrated ETFE-g-PVBTMA at room temperature reports lower strength and elongation than current measurements. The ATMPP membrane had a small reduction in modulus when temperature or hydration was increase. Elongation increased for the ATMPP polymer with increased temperature or humidity. Strength was slightly reduced with increased hydration, but increased with increased temperature. Literature on the ATMPP polymer reports similar elongation and strength at dry conditions, and slightly higher elongation and with the same strength at hydrated conditions.

Table 24: Mechanical Properties of AEMs from current tests and literature

	Young's Modulus (MPa)	Ultimate Strength (MPa)	Elongation (%)	Reference
Fumasep® FAA-PK				
30°C, Dry	560 ± 100	40 ± 4	16 ± 6	
60°C, Dry	420 ± 90	50 ± 5	34 ± 7	
30°C, 90%RH	360 ± 30	40 ± 5	40 ± 8	
ETFE-g-PVBTMA				
30°C, Dry	500 ± 50	37 ± 3	28 ± 8	
60°C, Dry	380 ± 30	29 ± 2	10 ± 1	
30°C, 90%RH	140 ± 40	29 ± 7	110 ± 30	
RT, hydrated		14 -19	45 - 75	Varcoe
ATMPP				
30°C, Dry	300 ± 80	25 ± 4	25 ± 9	
50°C, 10%RH		50	27	Hibbs
60°C, Dry	260 ± 60	34 ± 5	40 ± 12	
30°C, 90%RH	190 ± 40	18 ± 2	40 ± 14	
50°C, 90%RH		20	80	Hibbs
Nafion® N115				
23°C, 50%RH	249	43	225	DuPont data
23°C, water soaked	114	34	200	sheet

The rotational nature of the SER fixture resulted in increased strength for some of the AEMs with increased temperature or hydration. For brittle films, extension on the SER is limited due to the bending required by the film at the attachment points. This must be considering when analyzing the mechanical performance of brittle films, such as the AEMs tested. While the SER tool may not be completely representative of a tensile test, the measurements still provide insight and a relative comparison of the mechanical

properties of AEMs. The Fumasep™ FAA-PK membrane had a moderate response to humidity and would be considered the strongest membrane tested. This strength is likely due the PEEK reinforcement that maintains membrane integrity even with water in the polymer. The ETFE-g-PVBTMA had the largest response to humidity with a drastic reduction in modulus and increase in elongation at saturated conditions. While the ETFE-g-PVBTMA performed the best at saturated conditions, the drastic mechanical difference between the dry and hydrated states may be detrimental to membrane performance in a working fuel cell. The ATMPP had the least response to temperature and humidity, and it was the least brittle but also the weakest of the films. Compared to Nafion™, all AEMs tested were brittle having significantly higher moduli under dry and saturated conditions. The AEMs withstood as much if not more stress than Nafion™, but elongations of the AEMs were significantly lower. The ability of Nafion™ to elongate may allow the membrane to withstand the stresses associated with dimensional swelling and contraction during humidity cycling. Further dynamic mechanical testing will help elucidate the mechanical performance of these AEMs during humidity cycling. The data taken on these non-partner AEMs will be used for comparison in subsequent papers with our team's AEMs.

We are working with the Coughlin group on supplying supplemental mechanical data for a paper on a triblock polymer named X-Am-WX-20130127C (Figure 150). Preliminary results indicate a tensile strength of 3.2 MPa (±0.4) and an elongation of 40% (±7) at 30°C and 90% humidity. Further testing at elevated temperatures will be done and added to the synthesis paper by WenXu Zhang.

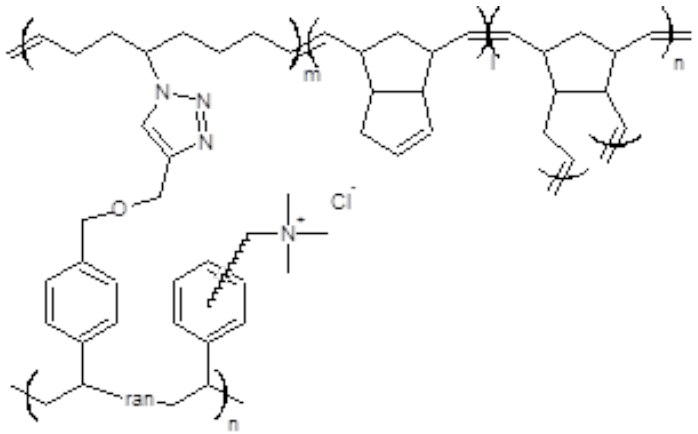

Figure 150: Structure of X-Am-WX-20130127C. IEC value of 3.2 mmol/g.

Using a single gas stream to control temperature and relative humidity limited the upper temperature of the system to 60°C and did not allow for adequate control of intermediate relative humidity conditions. Separate control of temperature and relative humidity has been proven in other systems currently in use in our group so it was decided to build an oven that allowed for the temperature to be controlled via electrical heaters while relative humidity was controlled with the wet gas / dry gas mixture. The clam-shell design features four cartridge heaters (Omega 500W, 128 W/in^2) wired in parallel to act as a single heater placed in the outer shell of the oven. Ports were placed on the oven to allow for a camera, gas inlet, dewpoint sensor, thermocouple and light. Insulation was wrapped around the oven to minimize heat loss and to protect the user. The oven is

mounted to the TA ARES rheometer with a swinging arm mechanism to allow for sample loading.

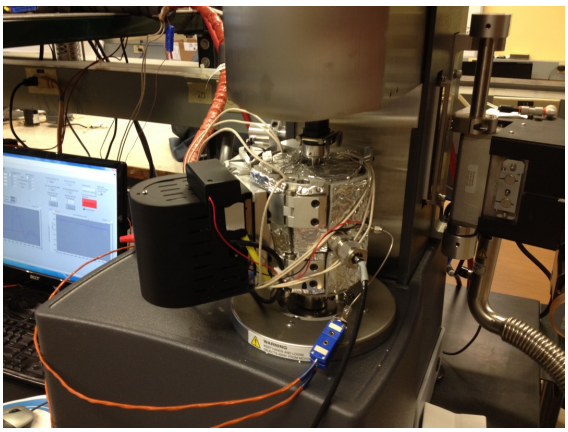

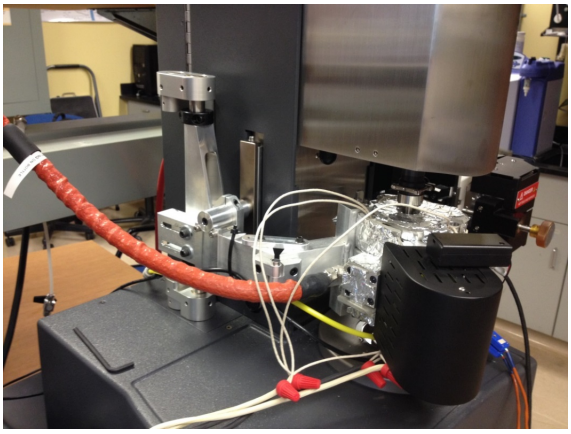

This new oven is capable of generating the full range of temperature and relative humidity conditions needed for mechanical characterization of anion exchange membranes (Figure 151). Although not shown, temperatures up to 150°C are possible in the new oven. There are some spikes in humidity at lower humidity conditions that are probably due to some cold spots in the line (Figure 152). These issues are being addressed and will be corrected in short order. The oven is capable of not only steady-state temperature and relative humidity conditions, but also ramps of both relative humidity (Figure 153) and temperature (Figure 154), while keeping the other variable constant. Ramps like these can be combined with the DMA capability of the upgraded

ARES rheometer to determine things like the glass transition temperature (T_g) of polymers as function of relative humidity.

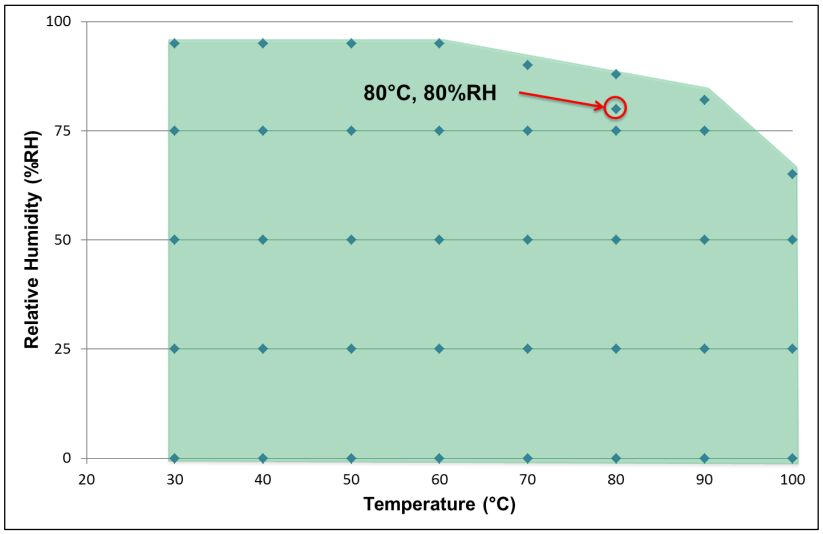

Figure 151 - Range of temperature and relative humidity conditions available

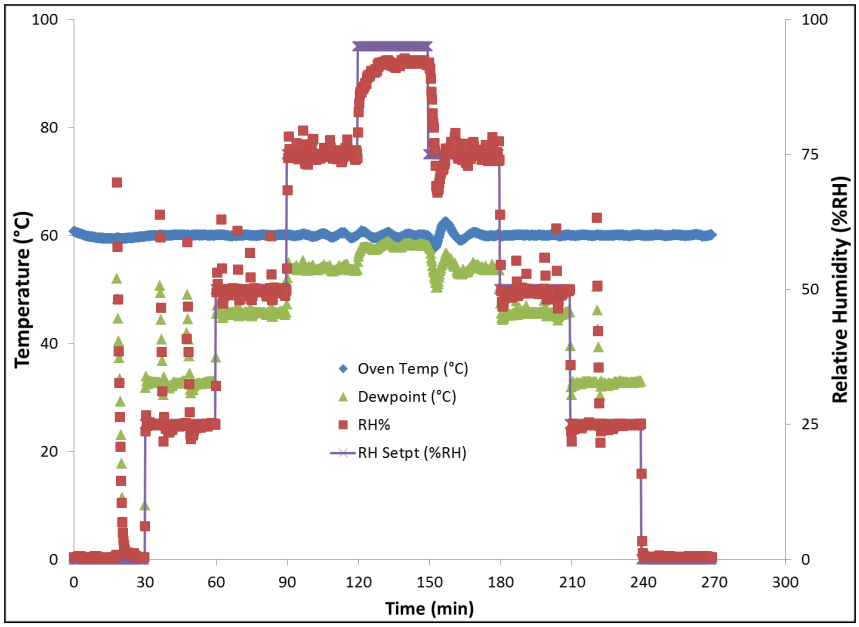

Figure 152 - Maintaining various relative humidity conditions at constant temperature

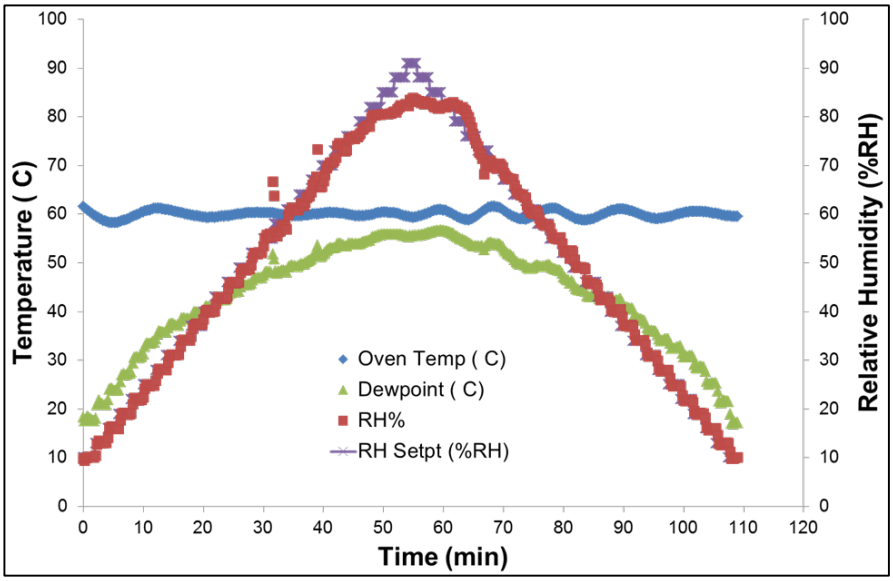

Figure 153 - The relative humidity can be ramped at constant temperature, in this case, 60°C

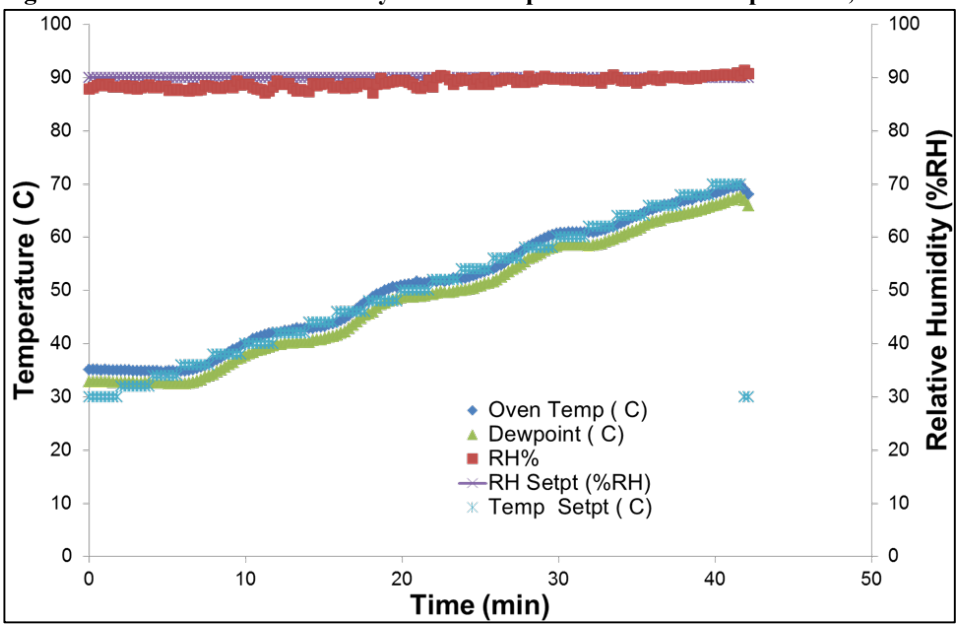

Figure 154 - The temperature can be ramped while maintain constant humidity, in this case, 90%RH

The new oven and modified SER tool (described in 2013 Annual Report) were benchmarked with a low density/linear low density polyethylene and Nafion® 115. In order to control for effects of the relative humidity system on the SER tool, LDPE/LLDPE was tested at dry, 50%RH, and 90%RH conditions. Polyethylene should not have any response to water as it is a hydrophobic polymer. The relative humidity did not have significant effects on any of the mechanical properties at 30°C or 60°C (Figure 155).

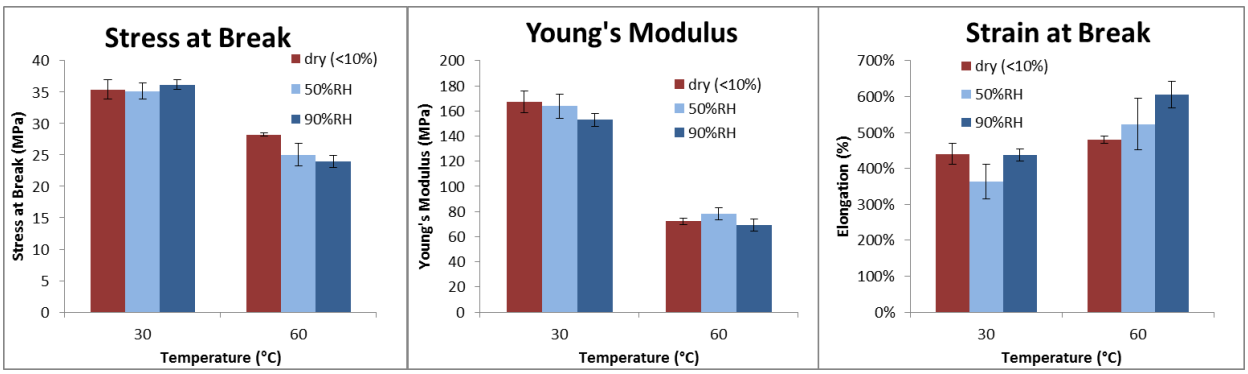

Figure 155 - LDPE/LLDPE mechanical properties at elevated humidity compared to dry

Nafion® 115 was prepared via the standard method of boiling in 0.5M sulfuric acid for an hour, deionized water for an hour, 3wt% hydrogen peroxide for an hour, and finally deionized water again for an hour. The membrane was then placed in an oven at 80°C for over 12 hours.

Samples of Nafion® 115 were then tested on the SER tool. The specimens were about 3 mm wide and 125 microns thick. Mechanical data at room temperature conditions were similar to information on the DuPont™ data sheet (Figure 156).

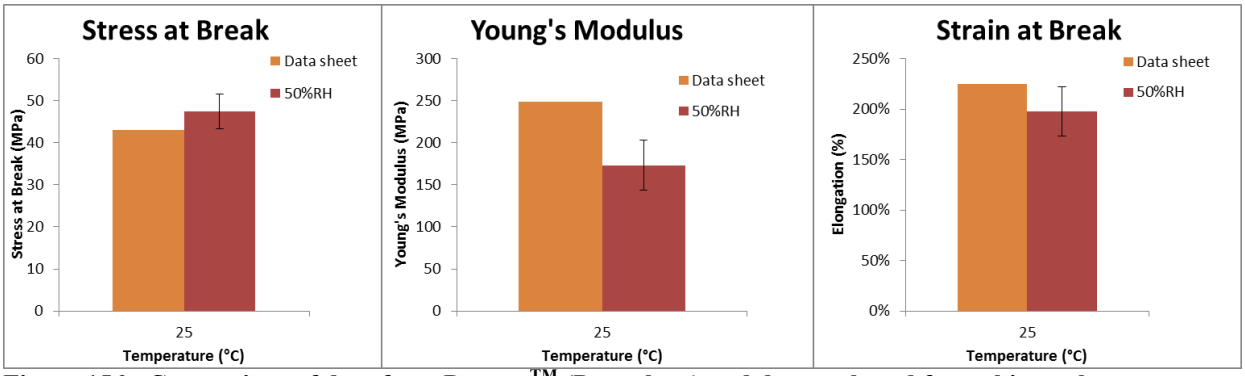

Figure 156 - Comparison of data from Dupont™ (Data sheet) and data gathered from this work

Moving beyond room temperature testing, Nafion® 115 was tested at a low (30°C), medium (60°C), and high (90°C) temperature in dry (<10%RH) and wet (>85%RH) conditions. It is well known that water plasticizes Nafion® and this work shows the typical pattern of the Young's modulus decreasing with increased humidity, as well as a slight decrease in the tensile strength with increased humidity (Figure 158). More granular humidity data is shown at 60°C (Figure 159). The plasticization transition can be seen.

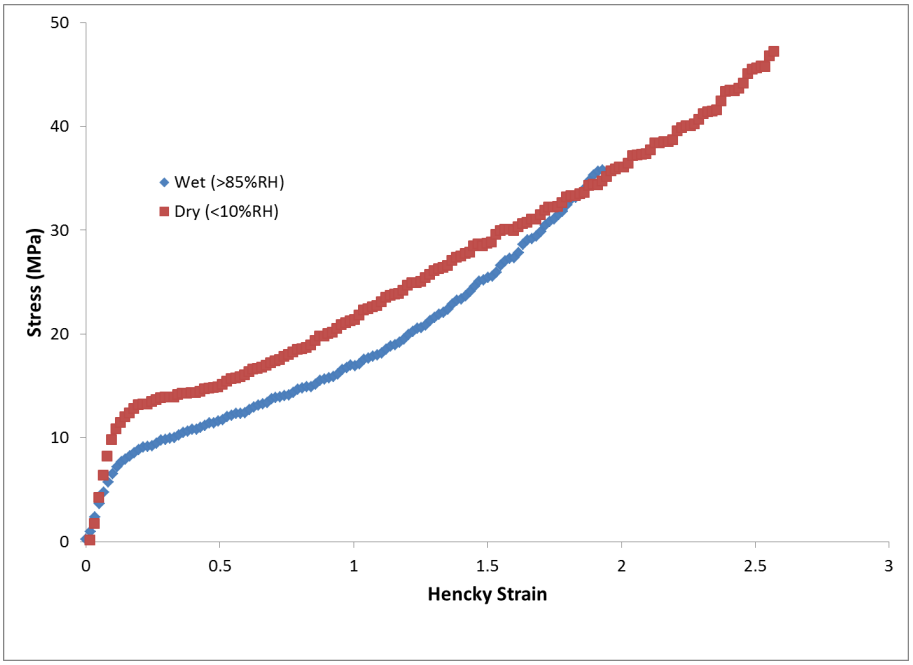

Figure 157 - Stress-strain curve at 60°C of Nafion® 115 in both dry and wet conditions

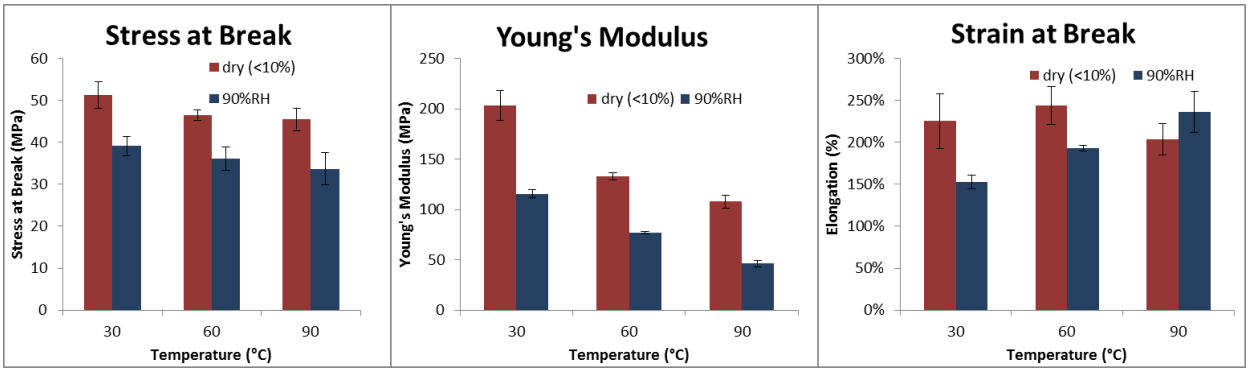

Figure 158 - Nafion 115® at dry and wet conditions across multiple temperatures

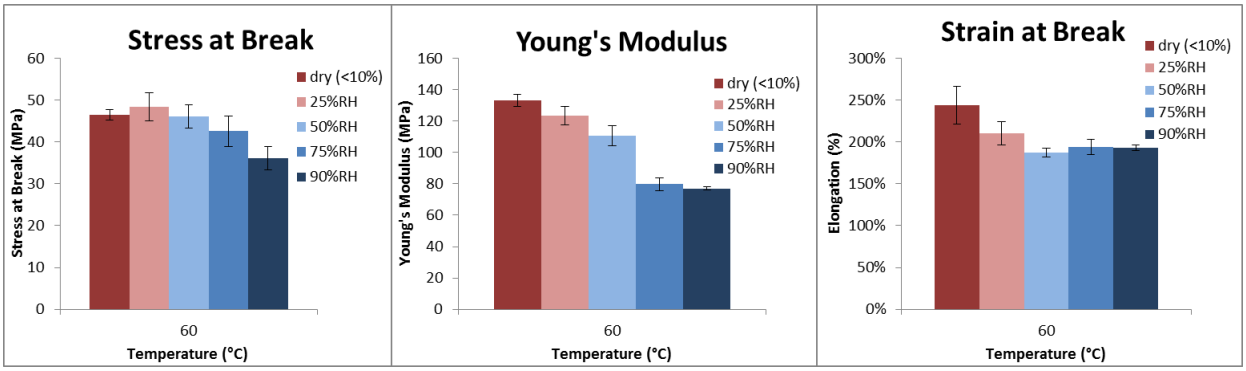

Figure 159 - Nafion 115® at 60°C across a range of humidity conditions

The new tools presented here will aid in the mechanical characterization of the MURI team's novel anion exchange membranes.

Extensional properties of three well-studied AEMs were investigated under different temperature and humidity conditions. The AEMs used in this study are the industrially produced polyetheretherketone (PEEK) reinforced Fumasep® FAA-PEEK membrane from Fumatech, an aminated tetramethyl polyphenylene (ATMPP) developed at Sandia National Laboratory, and a radiation grafted poly(ethylene-co-tetrafluoroethylene)-based quaternary ammonium AEM developed at the University of Surrey. The three membranes were chosen as they have all been produced consistently in multi-gram quantities, the first under industrial quality control standards, the second in large research batches over multiple years, and the third from an industrially produced precursor film. This study compares the mechanical properties of these AEMs at a range of temperature and humidity conditions using a modified extensional rheometer system to simulate traditional tensile tests, and relates these properties to water uptake and swelling of the membranes.

Three AEM membranes were tested: Fumasep® FAA-PEEK (Fumatech), an aminated tetramethyl polyphenylene (ATMPP) with benzyltrimethylammonium functionalities, and a poly(ethylene-co-tetrafluoroethylene) membrane radiation grafted with poly(vinylbenzyl trimethylammonium) groups (ETFE-g-PVBTMA) The Fumasep® FAA-PEEK membrane is a PEEK reinforced anion exchange membrane with a dry thickness of 110 μm and an IEC of 1.5 mmol/g. The chemistry of Fumasep FAA-PEEK was not disclosed, but literature has suggested a polysulfone or perfluorinated backbone with quaternary ammonium functionalities. The Fumasep® membrane was in a dry state in the Cl^- form and was tested as received. The ATMPP membrane was fabricated as previously reported by Hibbs. The ATMPP membrane had a dry thickness of 80 μm and an IEC of 2.5 mmol/g. The ATMPP membrane was received in the Br^- form and stored in liquid water. The ATMPP membrane was dried at ambient conditions prior to mechanical testing. Membranes were tested in their as-received counter-ion form to be comparable to literature, however additional mechanical testing of the ATMPP in the Cl^- form was performed for consistency and to guarantee counter-ion association did not significantly change mechanical properties. The ETFE-g-PVBTMA membrane was fabricated as previous described by the University of Surrey group. The ETFE-g-PVBTMA had a dry thickness of 80 μm and an IEC of 1.8 mmol/g. The membrane was received in a dry state in the Cl^- form and tested without further treatment.

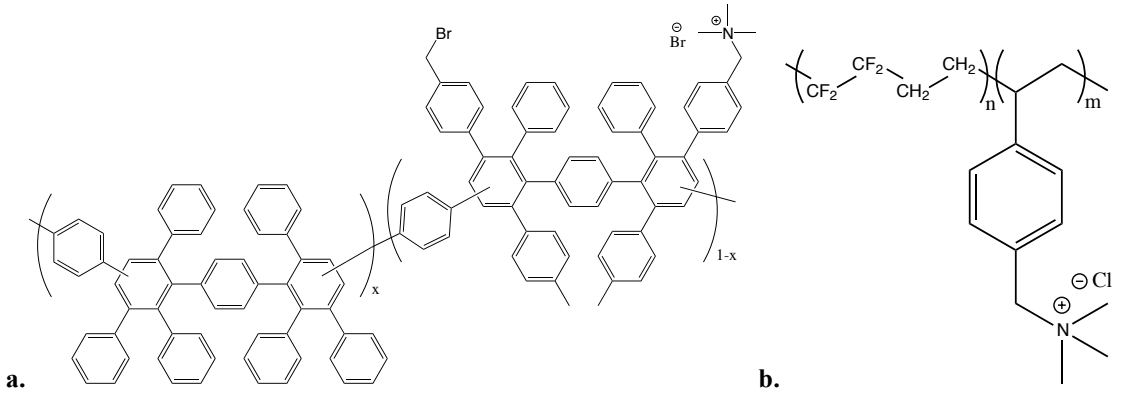

Figure 160. Chemical structures of the a) ATMPP and b) ETFE-g-PVBTMA polymers.

Water uptake, dimensional swelling, conductivity, and mechanical performance were evaluated for these membranes to determine the effect of hydration on membrane performance and durability. Mechanical tests were performed using a Sentmanat Extensional Rheometer (SER) fixture (Xpansion Instruments) on an ARES G2 rheometer platform (TA Instruments). The SER fixture suspends the membrane across two counter rotating drums. The rheometer controls the rotation of the drums, which stretch the sample to failure. The stress on the membrane sample is measured by the rheometer during film extension. The SER fixture is generally used to measure the elongation viscosity of polymers in their melt state, but has been shown to accurately measure tensile properties in the solid state. The stress vs. strain data is used to determine the elastic modulus, ultimate strength, and elongation of the film. The modulus is defined as the slope of the stress vs. strain curve in the initial liner region that corresponds to elastic deformation. The engineering stress at break is defined as the stress measured immediately prior to break, based on the initial film dimensions. The elongation of the membrane is the percent increase in film length as determined by the strain at break.

Polymer films were cut into strips of 25 mm(L) x 3 mm(W), about 5 – 10 mg, for testing. The SER drums were wrapped in double-sided high temperature tape to prevent slipping of the films. Silicon coated screw-down pins secured the film to the drum surface; additionally tape was place over the outer edges of the film, outside the sample area. The Hencky strain rate at which the films were stretched was based on the ultimate elongation: $0.0033s^{-1}$ (0.021mm/s) for elongations less than 20%, $0.0167\ s^{-1}$ (0.106 mm/s) for elongations between 20 and 100%, and $0.33\ s^{-1}$ (2.12 mm/s) for elongations greater than 100%. These strain rates were calculated based on ASTM D882-12 for tensile testing of thin plastic sheeting, but modified to account for the predefined sample distance between the drums. Samples were tested under dry airflow at 30°C and 60°C. Dry test conditions were achieved using the forced convection oven (FCO) built into the ARES rheometer. Samples were allowed to equilibrate at temperature for 10 min before the tensile tests. Samples were also tested under saturated gas conditions at 30°C and 60°C. Humidified gas was supplied by a combination of dry and wet gas flows controlled by to two mass flow controllers (10,000 cm^3/min capacity, MKS 1179A). The wet gas was passed through a humidity bottle (FCT, Inc.) with 10 m of Nafion® tubing to saturate the air with water. The wet and dry gas flows were combined and delivered to the ARES sample chamber through heated lines, to prevent condensation in the tubing. A humidity probe (Vaisala HMT 337) measures the dew point in the sample chamber and provides real time humidity conditions. Humidified samples were allowed to equilibrate (and take up water) for 40 min, except the ATMPP membrane that equilibrated for 1 h. These equilibration times were determined by separate dynamic vapor sorption experiments, during which the gravimetric change in mass of polymer is measured with respect to humidity.

Water uptake was measured for each AEM at 30°C and 60°C to determine the time required to reach full saturation in the film and relate changes in mechanical properties to relative humidity, Figure 161. The FAA-PEEK membrane has the lowest water uptake of the AEMs, 4.8% and 7.2% at 30°C and 60°C respectively, corresponding to lambda equal to 1.8 and 2.7 respectively. The low water uptake of the FAA-PEEK membrane is a result of its low IEC and PEEK reinforcement that restricts dimensionally swelling. Due to its high IEC, the ATMPP membrane had the highest water uptake of

14% (lambda of 3.1) at both temperatures tested. This water uptake is lower than literature values for liquid water uptake (64 - 72%) and gas phase water uptake with 1 hr humidity steps (27%), but similar to the gas phase water uptake with 20 min humidity steps (17%). The ETFE-g-PVBTMA had moderate water uptake of 6.2% at 30°C and 10.4% at 60°C, corresponding to lambda equal to 1.9 and 3.2 respectively. These water uptakes are lower than literature values for uptake from liquid water (40%). The level of water uptake and hydration number will be related to the mechanical behavior of hydrated films described below.

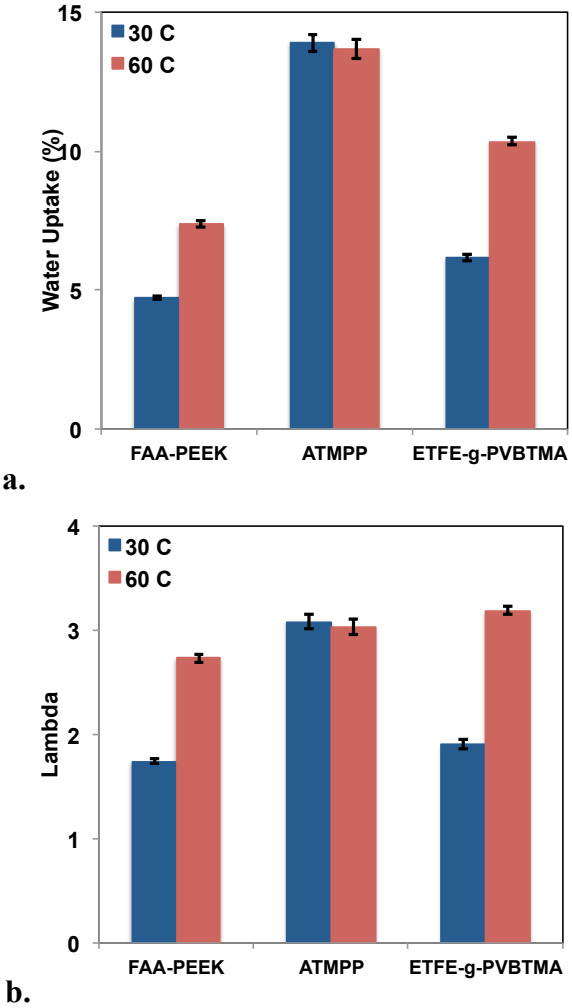

Figure 161: Comparison of water uptake and lambda for the membranes at 30°C and 60°C under saturated gas conditions.

Dimensional swelling was measured with respect to the in-plane area and through-plane thickness of the film (Figure 162). As expected, the FAA-PEEK membrane showed the lowest swelling due to its low water uptake and PEEK reinforcement. The FAA-PEEK membrane is the only AEM to have a larger through-plane swelling, 9%, compared to in-plane swelling, 3%, due to the PEEK reinforcement preventing swelling in the in-plane direction. The ATMPP and ETFE-g-PVBTMA films show a similar amount of swelling, with in-plane swelling being higher, 26 – 27%, compared to 14 – 19% in the through-plane direction. Dimensional swelling can be problematic in AEM based devices because the membrane is constrained by bipolar

plates, and excessive dimensional changes could lead to delamination of the catalyst layers as well as mechanical failure of the membrane. Membrane elasticity must be adequate to allow swelling and deswelling without developing cracks or holes in the membrane. Maintaining adequate hydration and ion conduction while limiting dimensional swelling will improve the lifetime of an AEM based devices.

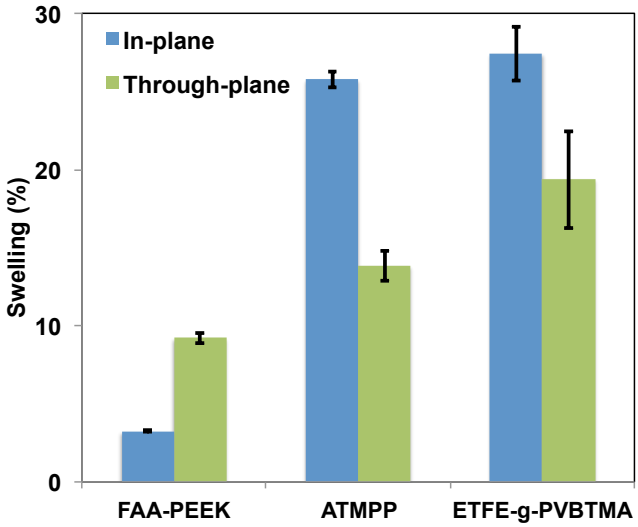

Figure 162. Dimensional swelling of AEM films soaked in liquid water compared to dry films at ambient conditions.

The ionic conductivity of the AEMs was measured to establish the relationship between ion conduction with IEC and water uptake. Conductivity in the halide form, chloride for FAA-PEEK and ETFE-g-PVBTMA and bromide for ATMPP, was measured for all membranes at saturated relative humidity and 60°C. The FAA-PEEK film had the lowest conductivity of 11.6 ± 0.8 mS/cm as a result of its low IEC and relatively low water uptake compared to the other films. The ATMPP film, which had the highest IEC and water uptake of all films tested, had a conductivity of 20 ± 2 mS/cm. This value is similar to ATMPP bromide conductivities reported in literature, 10 - 38 mS/cm . The ETFE-g-PVBTMA had the highest conductivity of 47 ± 3 mS/cm, which is higher than through-plane carbonate or bicarbonate conductivities reported in literature (17 - 25 mS/cm). Ion transport is significantly influenced by IEC and water sorption in the membrane and these factors will also have a large impact on mechanical performance.

At the lower temperature (30°C) and dry conditions all AEMs tested were stiff, having a Young's modulus of at least 425 MPa. While sample elongation on the SER is in one dimension, the strain is not truly uniaxial, because the sample is forced to bend around the SER drum. This makes comparison of SER measurements with traditional tensile tests difficult, particularly for stiff samples where bending may contribute to failure. The stiff nature of the AEM films caused some samples to fail at the attachment pins, however the measured properties (stress, elongation, and modulus) were statistically the same as samples that failed in the middle so all tests were included when calculating average properties and the associated error. All reported properties are the averages of at least five replicate experiments at each temperature and humidity condition, error bars represent one standard deviation.

The mechanical behavior of all three membranes at 30°C and dry conditions are compared in Figure 163. The ATMPP membrane is the stiffest film, represented by the steepest initial slope in the stress strain curve, due to the rigid nature of the branched polyphenylene backbone. The ATMPP film also has a higher yield point, with the yield strain around 15% and yield stress around 65 MPa. The FAA-PEEK and ETFE-g-PVBTMA films both have a lower yield point, around 10% strain and 35 MPa. Due to its stiffer nature and higher yield point, the ATMPP film withstands the highest stress at failure (75 MPa). The FAA-PEEK and ETFE-g-PVBTMA withstood lower stresses, 60 MPa and 47 MPa respectively. Film elongation at dry conditions was low, between 22 and 29%. The modulus and strength of the AEMs at 30°C and dry are reasonable, however film elongation is a concern as the membranes need to withstand swelling and contraction with humidity cycling in a fuel cell.

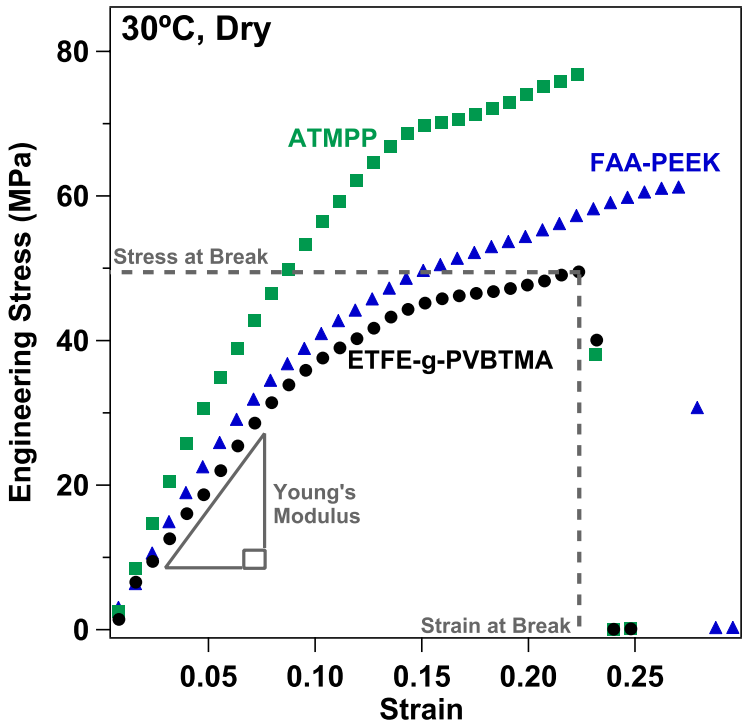

Figure 163. Representative stress vs. strain curves of the AEMs at 30°C under dry conditions. The linear region used to determine Young's Modulus and the defined stress and strain at break are labeled for the ETFE-g-PVBTMA film.

Increasing the testing temperature from 30°C to 60°C is expected to reduce the elastic modulus and stress at break, and increase the elongation of the polymer. However, the thermal responses of the benchmark AEMs tested resulted in a range of responses. Exposing the AEMS to humidity allows the polymer to uptake water, which has a plasticizing effect. The water plasticizer generally reduces the elastic modulus, increases elongation, and decreases the stress to break. The change in mechanical properties due to humidity is dependent on the amount of water taken up by the polymer.

The FAA-PEEK film has a narrow range of mechanical changes over the range of conditions tested (Figure 164). The PEEK reinforcement increases membrane strength and durability because PEEK has a very high modulus (~4500 MPa) and tensile strength

(~100 MPa). The Young's moduli, represented by the initial slope of the stress vs. strain curves, are similar at 30°C (dry and hydrated) and 60°C/dry, being between 400 and 440 MPa. The decrease in slope at 60°C and saturated conditions corresponds to a lower modulus, 250 MPa, indicating a softening of the film due to the plasticizing effect of water. Elongation increases with temperature and humidity as expected, but has a relatively narrow range, from 29% to 44%. Similarly, increases in temperature and humidity correspond to decreases in stress at break, from 60 MPa at 30°C and dry to 42 MPa at 60°C and 95%RH. The relatively narrow range of mechanical properties with respect to temperature and humidity is due to the PEEK reinforcement of the FAA-PEEK film that resists swelling and has no thermal transitions in this range.

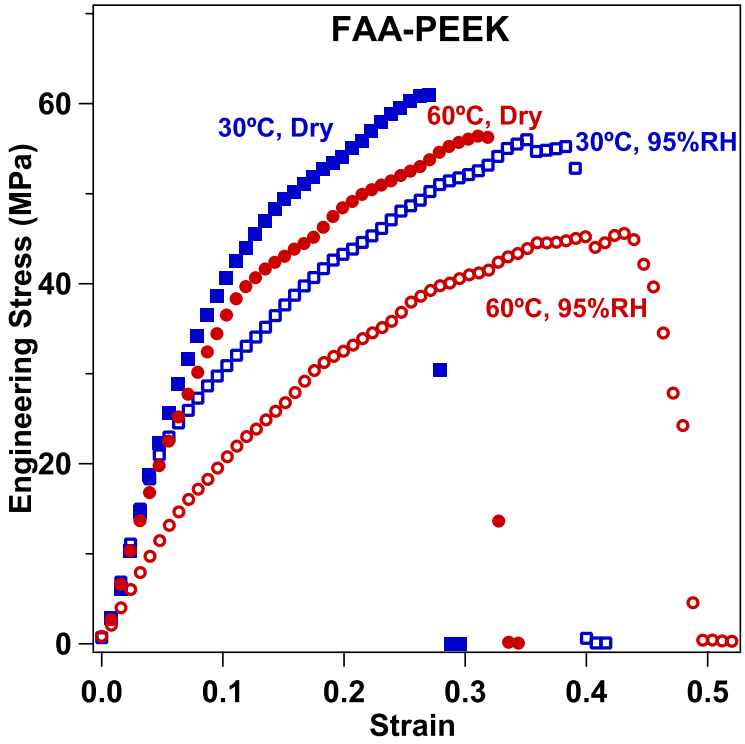

Figure 164. FAA-PEEK representative stress vs. strain curves at range of temperature and humidity conditions.

The ATMPP film has a small response to temperature between 30°C and 60°C, but a large response to humidity (Figure 165). Compared to the ATMPP, a non-ionic, branched polyphenylene film was reported to have a much higher modulus (1900 MPa), similar strength (70 MPa) and lower elongation (6%), however these differences could be due in part to variations in molecular weight and slightly differing chemistries. At dry conditions, increasing temperature from 30°C to 60°C results in a 19% decrease in modulus, from 580 MPa to 470 MPa, and negligible changes in stress at break (73-75 MPa) and elongation (23-26%). The relatively large water uptake, 14%, by the ATMPP film results in dramatically different behavior at saturated conditions. At saturated conditions the material is softened, reducing the modulus to 250 MPa at 30°C and 230 MPa at 60°C. At saturated conditions film strength is reduced to approximately 33% of that at dry conditions, 22-25 MPa, and elongation approximately doubled, 46-56%. At saturated conditions the yield strain is relatively low, around 10%, compared to the final

elongation while the yield stress, around 20 MPa, is similar to the stress at break. The ATMPP was also tested at 60°C in the Cl^- form with negligible changes in the measured properties. The dramatic reduction in modulus and strength at high hydration demonstrates the importance of testing AEM mechanical properties under operating conditions encountered in fuel cells and electrolyzers.

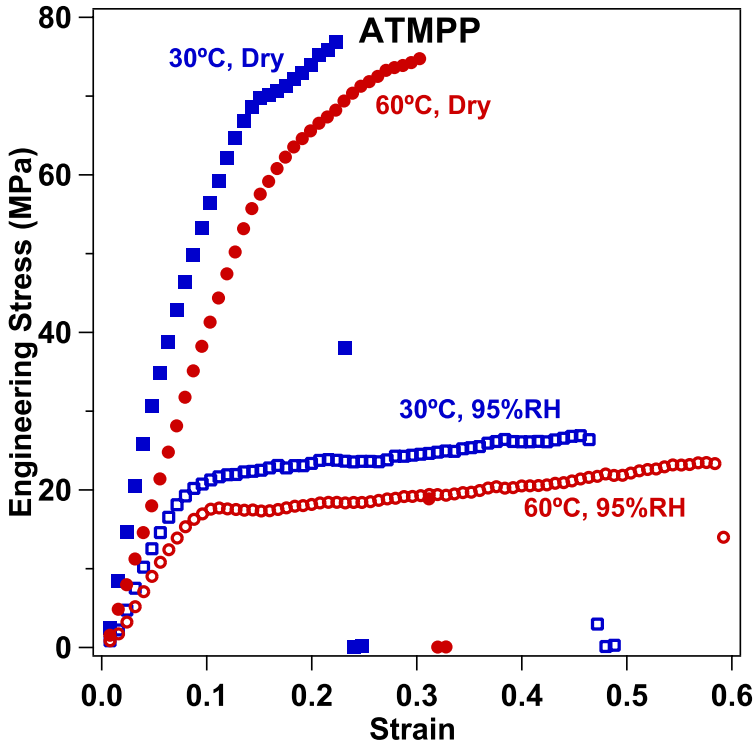

Figure 165: ATMPP representative stress vs. strain curves at range of temperature and humidity conditions.

The ETFE-g-PVBTMA film responds dramatically to both temperature and humidity changes, Figure 166. Radiation grafting cations results in a reduction of all mechanical properties compared to the ETFE precursor film that has high modulus (520 - 570 MPa), strength (150 - 200 MPa), and elongation (350 - 550%). Increasing the temperature from 30°C to 60°C softened the film and resulted in lower stress at break and elongation. The modulus was reduced from 370 MPa at 30°C to 310 MPa at 60°C. Increasing temperature also lowered stress at break to 27 MPa compared to 47 MPa at 30°C, and the final elongation decreased to 10% from 22% at 30°C. The reduction in strength with increased temperature is expected, but the reduction in elongation is counterintuitive, and may be due to a disproportionate decrease in strength compared to modulus, resulting in earlier film failure. Adding water to the polymer under saturated conditions further softens the ETFE-g-PVBTMA film. At saturated conditions the modulus was reduced between 62% to 74%, to 140 MPa at 30°C and 80 MPa at 60°C. Humidified conditions also reduced the stress at break to 32 MPa and 22 MPa at 30°C and 60°C respectively. Elongation is increased significantly when the ETFE-g-PVBTMA film is humidified. Elongation increases to 130% at 30°C and 210% at 60°C. Due to its low elongation at dry conditions, the ETFE-g-PVBTMA film may not be able to withstand the stresses associated with dimensional shrinking when the film undergoes drying. The drastic changes in the

mechanical properties of the ETFE-g-PVBTMA under different temperature and humidity conditions could contribute to membrane failure.

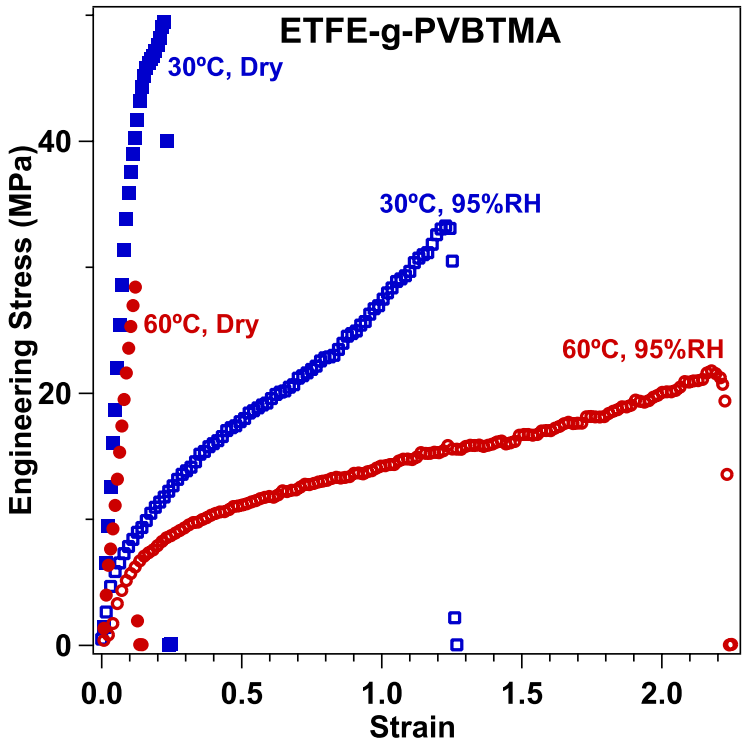

Figure 166. ETFE-g-PVBTMA representative stress vs. strain curves at range of temperature and humidity conditions.

The mechanical properties of the three AEMs are compared in Figure 167. All films are relatively stiff at dry conditions, i.e., having moduli between 310 and 580 MPa. The ATMPP film is the stiffest at dry conditions but undergoes softening under hydrated conditions. The FAA-PEEK is only softened at high temperature and humidity due to low water uptake at lower temperatures. The ETFE-g-PVBTMA membrane is softened by increases in temperature and humidity, and is consistently the most elastic film at all conditions tested. The highest stress at break is seen in the ATMPP film at dry conditions, however the ATMPP film significantly decreases in strength when humidified. The FAA-PEEK has the most consistent strength at all conditions tested, most likely due to PEEK reinforcement that is not effected by changes in humidity. All films had an increase in elongation under saturated conditions. The increase in elongation was least for the FAA-PEEK due to its lower water uptake and the reinforcing mesh. The highest elongations, 130% to 210%, were seen in the ETFE-g-PVBTMA film at saturated conditions, but the low elongations of the film at dry conditions could be problematic during humidity cycling. Ideally, a membrane would have high strength under both dry and humidified conditions and sufficient elongation to account for dimensional changes with hydration level. Membrane reinforcement helps resist membrane changes with temperature and humidity, as shown with the FAA-PEEK film, however adding nonconductive reinforcement also lowers polymer IEC and limits water uptake that may be critical for efficient ion transport. The interplay between ionic conductivity, water uptake, and mechanical integrity makes designing an optimal anion exchange membrane extremely

challenging, but considering all of these criteria in the early stages of development will lead to a robust, well performing anion exchange membrane.

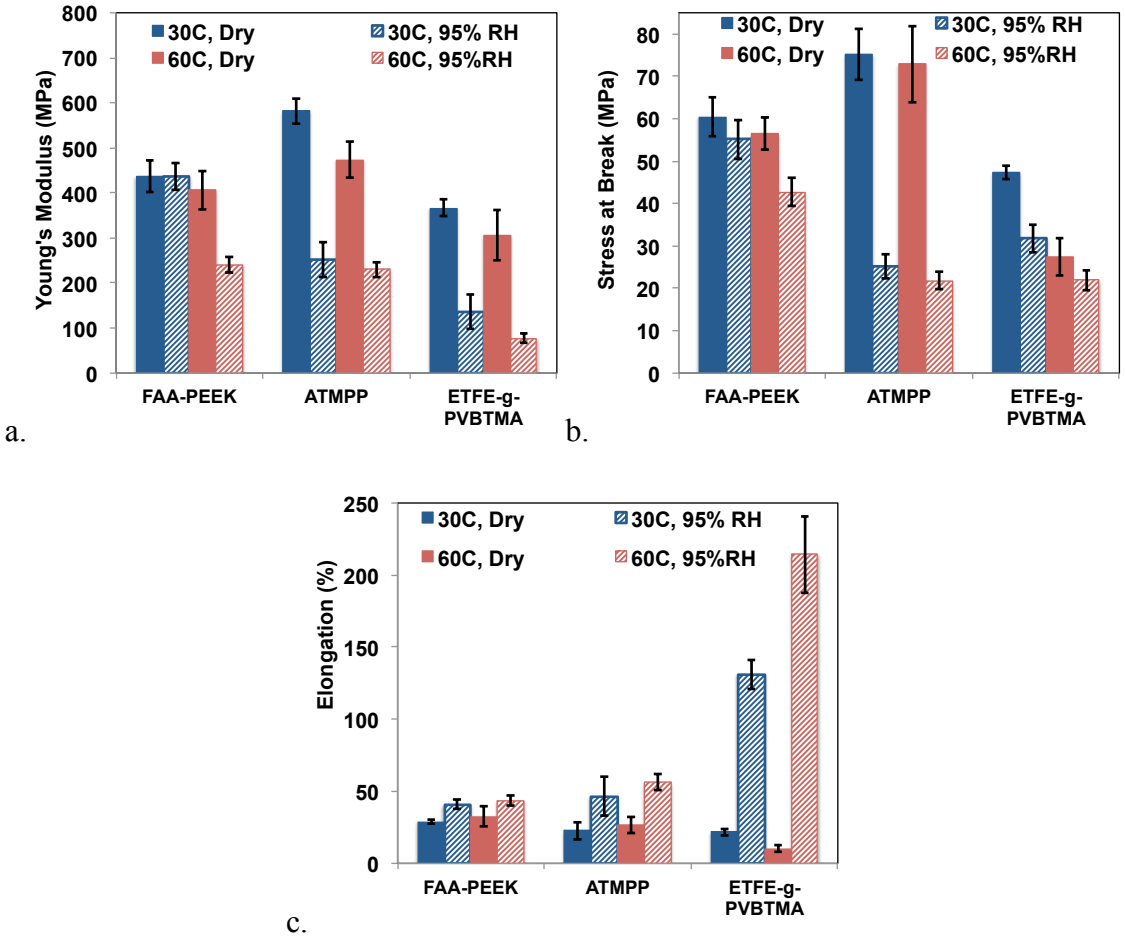

Figure 167. a) Young's modulus, b) Stress at Break, and c) Elongation of the three AEMs at 30°C and 60°C under dry and saturated conditions.

Testing the mechanical performance of common AEMs provided baseline properties for membrane development for electrochemical energy conversion devices and highlights what properties need improvement. The mechanical properties of three common AEMs were investigated at a range of relevant temperature and humidity conditions. The three membranes tested had different chemical and physical properties, so mechanical responses to temperature and humidity varied greatly. The Fumasep FAA-PEEK film is reinforced by a PEEK mesh that restricts water uptake, which means that hydration has a negligible affect on Young's modulus at 30°C and produces only a 40% reduction at 60°C. Similarly, the hydrated strength decreases by only 9% and 24% at 30°C and 60°C respectively. The ATMPP film had the highest IEC, resulting in large water uptake and significant softening, a 51 - 55% reduction in modulus, and a 70% weakening of the film at saturated conditions. The ETFE-g-PVBTMA film responded to both temperature and humidity, having the largest increase in elongation at saturated conditions, over 200% when hydrated at 60°C. The ETFE-g-PVBTMA film may have difficulty maintaining membrane integrity during humidity cycling because the

dimensional swelling exceeds the elongation at dry conditions. Ionic groups of the AEM facilitate water uptake, which is critical to ion transport through the membrane, however water sorption leads to dimensional swelling and variation of mechanical properties. An AEM must be mechanically stable at a range of hydration levels to operate in a fuel cell, electrolyzer, or other electrochemical energy conversion device. Thus, mechanical durability, along with ionic conductivity and chemical stability, should be a fundamental design criterion for new AEM development to achieve robust device membranes.

6.6 Mechanical performance of crosslinked polyiosoprene copolymers

In this study two polyiosoprene copolymers were crosslinked either thermally or with a UV sensitive crosslinking agent and were evaluated in terms conductivity and mechanical performance at a range of hydrations. A random copolymer of polyiosoprene and poly(vinylbenyzl trimethylammonium) (PI-ran-PVBTMA) and terpolymer of polyiosoprene, poly(vinylbenzyl trimethylammonium), and polystyrene (PI-ran-PVBTMA-ran-PS) were solution cast from ethanol. The membranes were rendered insoluble by crosslinking either thermally at 145°C or by addition of a dithiol crosslinker followed by exposure to UV light. The addition of polystyrene allowed the terpolymer to have a higher ion concentration but still be rendered insoluble after crosslinking. Conductivity of the two polymers were measured and correlated to extent of crosslinking and mechanical properties. Extensional properties of the membranes were measured with an extensional rheometer platform to simulate a tensile tester with small membrane samples. Temperature and humidity were controlled during mechanical testing to determine the affect of hydration on membrane performance.

The Coughlin group at UMass, Amherst synthesized the polyiosoprene-based polymers. The copolymer had an IEC of 1.5 mmol/g, while the terpolymer had IEC of 2.3 mmol/g. For thermally crosslinked films, the polymers were dissolved in ethanol at 22wt%. The polymers were mixed at room temperature for 4 hours, sonicated at 30°C for 1.5 hrs, and then stirred again at room temperature for 1 hr. The solution then was poured on a Teflon substrate and a doctor blade at a 500 micron gap height was moved over the solution at 20 mm/s using an automatic film applicator. The films were allowed to dry overnight at a room temperature in a fume hood. To induce crosslinking the films were placed in an oven at 145°C for a duration of 3 or 24 hours. After removal from the oven the films were allowed to cool, removed from the Teflon substrate, and placed in water at room temperature to allow for dimensional swelling. The films were removed from the water after 1 hr and allowed to dry at room temperature. Films were stored under dry conditions for further testing. The extent of crosslinking impacted dimensional swelling, the films crosslinked for a short duration (3-hrs) had larger dimensional swelling and did not fully contract back when drying. This resulted in the 3-hr crosslinked films being significantly thinner (20-30 microns) compared to the 24-hr crosslinked films (60-70 microns).

The photocrosslinked films had a photoinitiator and crosslinking agent added to the casting solution. The photoinitiator, 2-Hydroxy-4′-(2-hydroxyethoxy)-2-methylpropiophenone (Sigma Aldrich), was added to ethanol at 1.5wt%. The polymer was dissolved in the ethanol/initiator solution at the same concentration as the thermally crosslinked films (22wt%). The solution was mixed in the dark, at room temperature for 4 hours and sonicated at 30°C for 1.5 hrs. After sonication the crosslinking agent, 1,10 decanedithiol (Alfa Aesar), was added to the polymer solution and mixed for 1 hr at room

temperature, avoiding light exposure. Dithiol addition was added in a 3:1 ratio compared to the number of 1,2 and 3,4 addition double bonds of the polyiosoprene, as determined by ^{1}H NMR. The 1,2 and 3,4 addition double bonds are susceptible to chemical crosslinking with the dithiol. Addition of the photoinitiator and dithiol crosslinker lowers the polymer IEC because inert mass is added to the film, the copolymer IEC was reduced to 0.9 mmol/g and the terpolymer was reduced to 1.5 mmol/g. The polymer solution was casted using the automatic film applicator using the same method described for the thermally crosslinked films. After casting, the films were covered to prevent light exposure and allowed to dry at room temperature in a fume hood. The dry film was crosslinked by exposure to UV light using a F300 Series Fusion UV curing system with a P300MT power supply. The film was passed through the curing system four times at a speed of 15 ft/min with a power of 300 W/in. After UV crosslinking the films were removed from the Teflon substrate, submerged in water for 1 hr, and allowed to dry before subsequent testing.

In-plane conductivity of the copolymer and terpolymer films was measured as a function of temperature (50 - 90°C) at a constant relative humidity of 95% (Figure 168). Conductivity data is the average of at least three separate membrane samples and multiple impedance spectra at each temperature. Overall the terpolymer had higher conductivity, ranging from 20 - 76 mS/cm at 50°C, compared to the copolymer, 4 - 17 mS/cm, as a result of the terpolymer's higher IEC. Degree and method of crosslinking had a significantly influence membrane conductivity. The UV crosslinked films have IECs reduced from the parent polymer due to the addition of the inert crosslinking agent and photoinitiator. Lowering the IEC results in lower conductivity of the UV crosslinked films, particularly for the copolymer, which is approximately 35% of the thermally crosslinked films. The UV crosslinked terpolymer has lower conductivity than the 3-hr thermally crosslinked film, but slightly higher conductivity compared to the 24-hr thermally crosslinked film. The short duration, 3-hr, thermally crosslinked films had the highest conductivity in both the copolymer and terpolymer systems due to the lower degree of crosslinking and higher swelling that allows better ion mobility. The 3-hr thermally crosslinked films could only be measured at lower temperatures because at higher temperatures the polymer became fluid-like and flowed out of the conductivity cell during testing. This indicates that 3 hrs of thermal crosslinking was not enough to render the film insoluble at higher temperature conditions; this hydration effect will be further investigated with respect to membrane mechanical properties. The 3-hr thermally crosslinked terpolymer film had measurable conductivity up to 80°C, while the copolymer was immeasurable after 65°C, this suggest the terpolymer has better film integrity at higher temperatures under hydrated conditions, despite the fact that the terpolymer has a higher IEC. The addition of glassy polystyrene to the polymer matrix improves film integrity and swelling allowing the higher IEC terpolymer to remain a solid membrane at higher temperatures when hydrated.

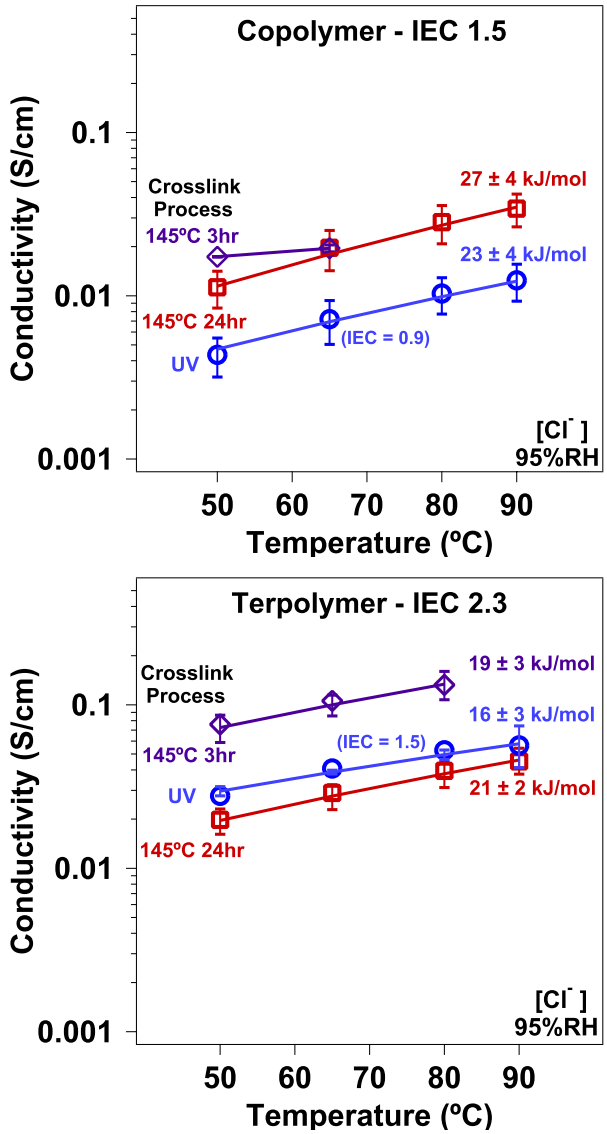

Figure 168: Conductivity of the copolymer and terpolymer films crosslinked either thermally at 145°C for 3 or 24 hrs, or UV crosslinked

Membrane Swelling

Dimensional swelling of the polymer membrane was measured to determine changes of the polymer film between dry and hydrated states that could affect mechanical integrity of the membrane and assembly during operation. Both polymer chemistry and crosslinking method had a significant affect on dimensional swelling (Figure 169). The 3-hr thermally crosslinked copolymer film had the highest degree of swelling at 118% in the in-plane direction, through-plane swelling was much lower at 16%. The other copolymer films (24-hr thermally and UV crosslinked) had significantly lower dimensional swelling, 12-15% in-plane and 5-6% through-plane. Compared to the copolymer the terpolymer had a higher degree of swelling, excluding the high in-plane swelling of the 3-hr thermally crosslinked copolymer. The terpolymer had similar in-plane swelling for all films, 44% and 54% for the 3-hr and 24-hr thermally crosslinked respectively, and slightly less for the UV crosslinked at 34%. Through-plane swelling

was highest for the 3-hr thermally crosslinked film at 58%; this was the only film to have a higher through-plane swelling than in-plane swelling. Through-plane swelling was 30% lower compared to in-plane for the 24-hr thermally crosslinked terpolymer and 76% lower for the UV crosslinked terpolymer. The copolymer has a higher percent of isoprene (87 mol%) compared to the terpolymer (71%), so there are more crosslinkable units in the copolymer. The large number of crosslinkable units, along with a high degree of crosslinking in the 24-hr thermally and UV crosslinked copolymer films prevents significant swelling. The lower number of crosslinkable units in the terpolymer causes swelling to be higher, even when degree of crosslinking is high (24-hr thermal and UV crosslinked). Limiting dimensional swelling is important to prevent membrane degradation and assembly damage when a fuel cell undergoes humidity changes, and crosslinking is one technique to successfully reduce dimensional swelling.

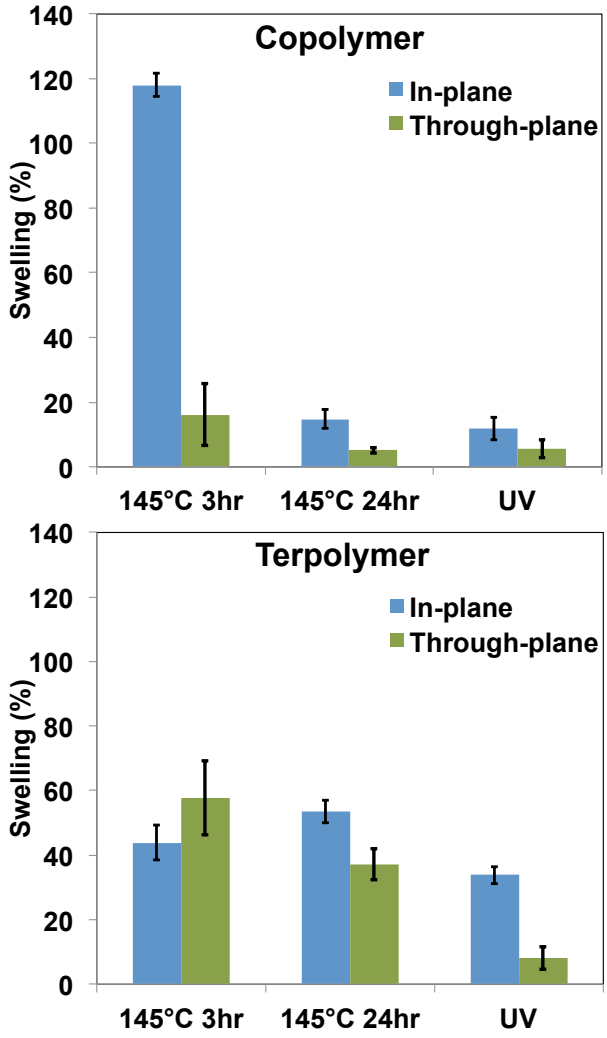

Figure 169: Dimensional swelling of the copolymer and terpolymer measured after soaking in water for 24 hrs compared to films vacuum dried at 50°C overnight.

Extensional Tests

Extensional tests were performed at 30°C and 60°C under dry and hydrated conditions. Films were extremely stiff at dry conditions and underwent severe softening when hydrated (Figure 170) causing films to become extremely weak. Under dry conditions all films are stiff having moduli between 100 and 740 MPa. The terpolymer was generally slightly stiffer than the copolymer due to the addition of glassy polystyrene to the polymer matrix. A lower degree of crosslinking (3-hr thermal) resulted in softer films than those with a higher degree of crosslinking (24-hr thermal/UV). All films were severely softened at hydrated conditions due to the plasticizing effect of water in the film. At 30°C the 24-hr thermally crosslinked films had the least decrease in moduli from dry to hydrated states, however reduction was still 76% and 90% for the copolymer and terpolymer respectively. The 3-hr thermally and UV crosslinked films all had at least a 95% reduction in modulus from dry to hydrated states. Humidifying the films at higher temperature, 60°C, cause several of the films to soften to the point that measured stress on the film was below the noise level of the instrument. Extensional properties were not measurable for either of the 3-hr thermally crosslinked films or the 24-hr thermally crosslinked copolymer at 60°C and saturated. The 24-hr thermally crosslinked terpolymer was measurable, suggesting that adding polystyrene to the polymer matrix improves mechanical durability when hydrated, despite the terpolymer's higher IEC. Both UV crosslinked films were measurable at the 60°C and saturated conditions, however measured moduli were extremely low, being 11 MPa for the copolymer and 5 MPa for the terpolymer.

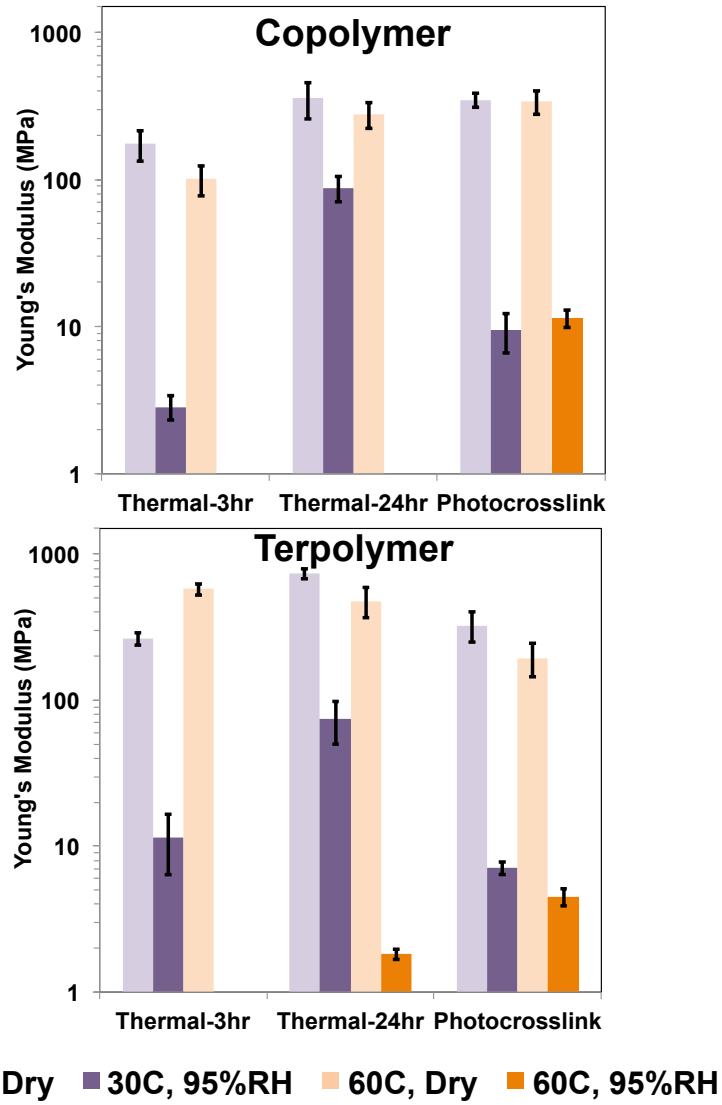

Figure 170. Young's Moduli of the copolymer and terpolymer based on crosslinking technique.

While the moduli values of the films were fairly high at dry conditions, the stress to failure was low to moderate compared to other AEMs and PEMs (Figure 171). At dry conditions the thermally crosslinked copolymer films had relatively low stress to break, between 3 to 6 MPa, while the thermally crosslinked terpolymer films had slightly higher stress to break, 7 to 15 MPa. The UV crosslinked films had consistently higher stress to break, 13 to 30 MPa for the copolymer and 19 to 20 MPa for the terpolymer. At dry conditions the copolymer had a slight decrease in strength from 30°C to 60°C, while the terpolymer had little to know change with temperature, likely due to the added polystyrene that is thermally stable within this temperature range. Hydrating the films causes significant reduction in strength due to the severe softening discussed above. At 30°C film strength was reduced to between 1 MPa to 2.7 MPa, and at 60°C the maximum stress to break measured for any of the films was only 1.4 MPa. The strength of these

films at hydrated conditions is insufficient and the extreme differences in mechanical properties between dry and hydrated states could cause membrane degradation and assembly failure.

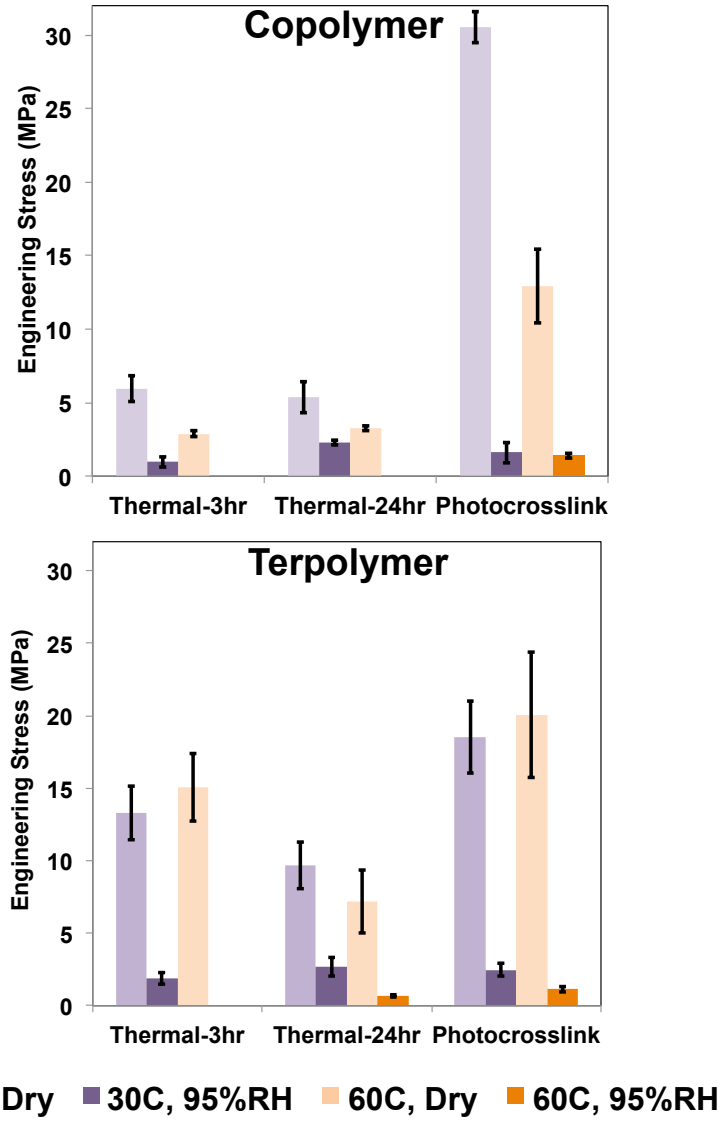

Figure 171. Engineering stress of the copolymer and terpolymer based on crosslinking technique.

Adequate film elongation is important to accommodate dimensional changes with swelling (Figure 172). At dry conditions the films have low elongation, and elongation decreases with crosslinking duration. The 3-hr thermally crosslinked films have dry elongations about 15%, except for the terpolymer at 60°C, while the 24-hr thermally crosslinked films have lower elongations between 2% to 3%. The UV crosslinked films have slightly higher dry elongations between 10% to 23%. The low degree of crosslinking in the 3-hr thermally crosslinked films causes elongation to increase dramatically when hydrated, up to 130% and 100% for the copolymer and terpolymer respectively at 30°C. Alternatively, the higher degree of crosslinking for the 24-hr thermally crosslinked films results in relatively low increase in elongation, up to only 7%

for both the copolymer and terpolymer at 30°C. Elongation of the UV crosslinked films is much more consistent across different temperature and hydration conditions, the copolymer film ranges from 10% to 19% while the terpolymer ranges from 21% to 31%. The narrow range of elongations of the UV crosslinked films suggests that UV crosslinking provides greater mechanical stability compared to the thermal crosslinking.

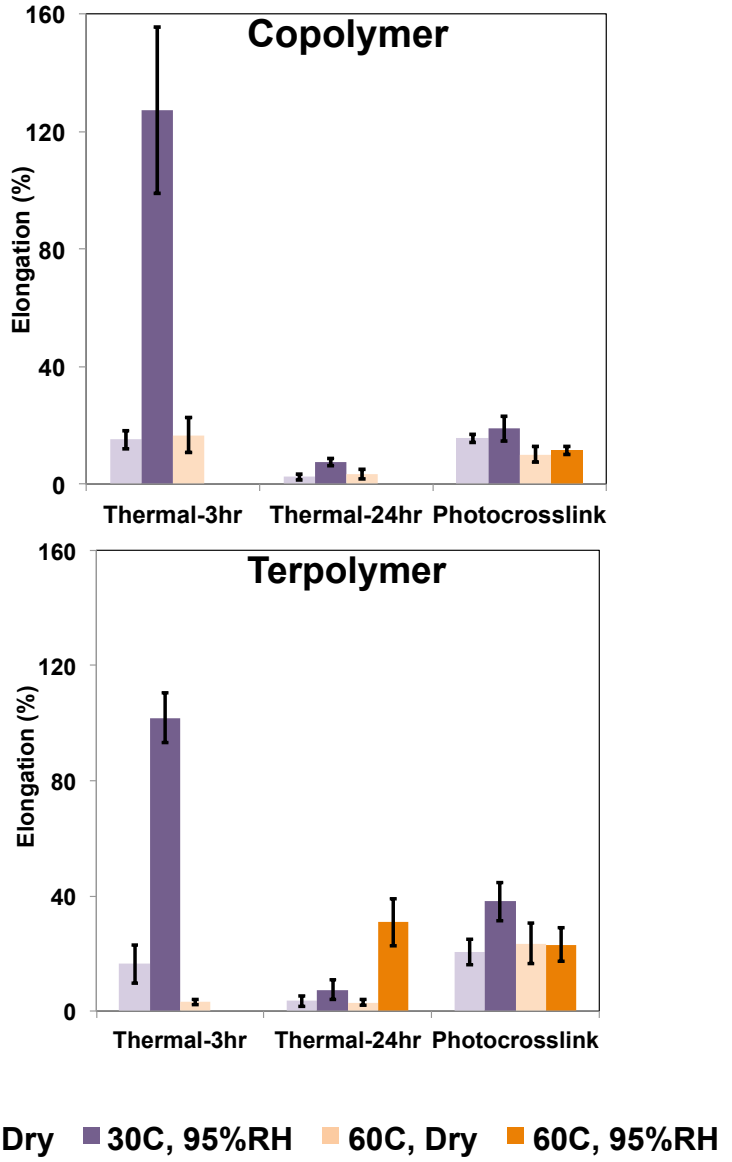

Figure 172: Elongation of the copolymer and terpolymer based on crosslinking technique. Extensional tests revealed dramatic differences in the mechanical properties of the crosslinked polymer films from dry to hydrated states. The films were relatively stiff at dry conditions, particularly as the degree of crosslinking was increase by increasing crosslinking duration. While stiff, the films had relatively low strength and elongation at dry conditions. Hydrating the films caused severely softening and weakening of the films, to the point that at higher temperature some films were immeasurable and deemed to have lost film integrity. Overall, the UV crosslinked films had better, more consistent, mechanical properties over the range of temperatures and hydrations tested. Ultimately,

while crosslinking increased film stiffness, these films are too weak when hydrated for use in an electrochemical device. The extreme disparity between dry and hydrated mechanical properties, and the fact that some films were immeasurable by extensional testing at high hydrations, warranted further study by dynamic measurements of mechanical behavior.

The ARES G2 rheometer was used to perform DMA testing using a film/fiber rectangular tension geometry. The rectangular tension geometry has two screw-down clamps that hold the sample in tension while a small-amplitude oscillatory strain is applied to the film. DMA tests were performed under dry or saturated conditions while ramping temperature from 30°C to 70°C at 0.5°C/min. Samples were about 6 mm (W) by 25 mm (L), but were loaded at a consistent starting gap height of 10 mm. A oscillatory strain of 0.1% was applied at a frequency of 1 Hz. Samples were maintained at minimum axial tension force of 0.008 N and the axial force was set to be at least 20% greater than the oscillatory force applied to strain the film. Under hydrated conditions the films were extremely soft and maintaining tension on the sample resulted in significant sample elongation as temperature was ramped. Films were loaded at ambient conditions, for saturated humidity tests the samples were allowed to equilibrate at 30°C and 90% relative humidity for 1 hr prior to the start of the test to take up water. For dry tests the samples were allowed to equilibrate at 30°C and <10%RH for 10 min prior to the start of the test. Dynamic mechanical analysis was used to observe moduli changes while ramping temperature from 30°C to 70°C at dry and saturated relative humidity conditions (Figure 173). DMA tests were repeated at least twice at each condition to confirm a consistent moduli response; tests were limited due to sample availability. DMA was used to distinguish mechanical changes due to temperature compared to those due to hydration level. At dry conditions there is little change in storage modulus between 30°C and 70°C. The copolymer films have slightly different moduli based on crosslinking technique. The 24-hr thermally crosslinked copolymer has the highest modulus starting at 1.5×10^9 Pa and reducing very little with temperature. The UV crosslinked copolymer also has consistent dry moduli over the temperature range around 6×10^8 Pa. The 3-hr thermally crosslinked copolymer has a slight decrease in modulus from 7.5×10^8 Pa at 30°C down to 3.2×10^8 Pa at 70°C. Alternatively, the terpolymer modulus does not change with crosslinking method and is consistent over the 30°C to 70°C temperature range, having a modulus around 1×10^9 Pa for all films tested.

Compared to the narrow change in moduli with temperature at dry conditions, the responses of the films at saturated conditions were significant, spanning orders of magnitude. When saturated, the 24-hr thermally crosslinked films had starting moduli closer to the dry films while the 3-hr thermally and UV crosslinked films had moduli at least two orders of magnitude lower than the dry films at 30°C. The 24-hr thermally crosslinked films were measurable over the entire temperature range when hydrated, while the softer 3-hr thermally and UV crosslinked films became so soft as temperature increased that modulus was immeasurable by the instrument. Before the films became immeasurable there was a sharp decrease in modulus indicating severe softening. While general moduli values and behavior were consistent between tests, the temperature for the onset of modulus decrease varied slightly between runs, so rather than define film integrity loss by the onset of the modulus decrease a modulus of minimum integrity was defined at 1×10^9 Pa (1 MPa). This minimum modulus is shown in Figure 173 by the

dashed line. The temperature for this minimum modulus was consistent by crosslinking technique; both of 3-hr thermally crosslinked films reached this minimum modulus at 40°C while the minimum moduli for UV crosslinked films were at 46°C for the copolymer and 47°C for the terpolymer. As mentioned earlier, the 24-hr thermally crosslinked films were measurable over the entire temperature range when hydrated and did not reach the minimum modulus. The 24-hr thermally crosslinked copolymer had the highest starting modulus at 4×10^8 Pa that steadily declined with temperature reaching 1×10^7 Pa by 70°C. The 24-hr thermally crosslinked terpolymer had a lower starting modulus at 6×10^7 Pa and decreased to 2×10^6 Pa by 70°C; however, unlike the copolymer that steadily declined, the terpolymer had a steady decline in modulus between 30°C to 42°C, a sharp decrease at 42°C, and a shallow decline from 42°C to 70°C. This film was tested three times to confirm that this transition was real and all test had a sharp decline in modulus, however the exact transition temperature varied slightly between tests. The extreme decrease in moduli, even to the point of being immeasurable, as temperature is increased at saturated conditions compared to near constant moduli at dry conditions proves how significant membrane hydration is to mechanical performance and membrane integrity. Anion exchange membranes must be mechanically stable over a large range of temperature and humidity conditions, the change in moduli by orders of magnitude from dry to saturated conditions makes these crosslinked films inadequate for a working fuel cell or electrochemical device.

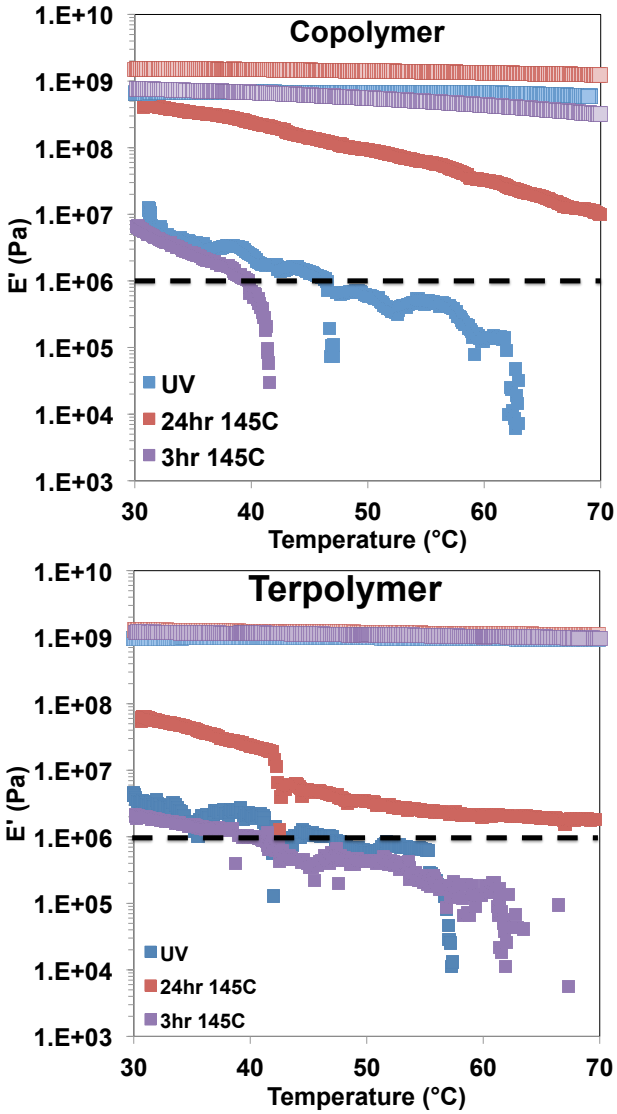

Figure 173: Storage modulus vs. temperature for the copolymer and terpolymer, solid points are at saturated relative humidity and the light filled data point are dry conditions. Dashed line shown is defined as minimum modulus for film integrity.

6.7 Polyethylene-b-poly(vinylbenzyl trimethylammonium) anion exchange membrane

Casting the PE-b-PVBBr from xylene using the automatic film applicator resulted in large, ~300 cm^2, flexible films with a consistent thickness of 10-15 μm (Figure 174). Functionalization of the polymer with vinylbenzyl trimethylammonium cations was confirmed by titration. The theoretical IEC of the brominated polymer was 1.63 mmol/g based on the ^{1}H NMR spectra. The titrated IEC of the PE-b-PVBTMA was 1.21 ± 0.08 mmol/g corresponding to a 74% conversion of brominated sites. The incomplete conversion of brominated sites to cations may be a result of low dimensional swelling (discussed later) of these films that would restrict transport of the trimethylamine into the polymer.

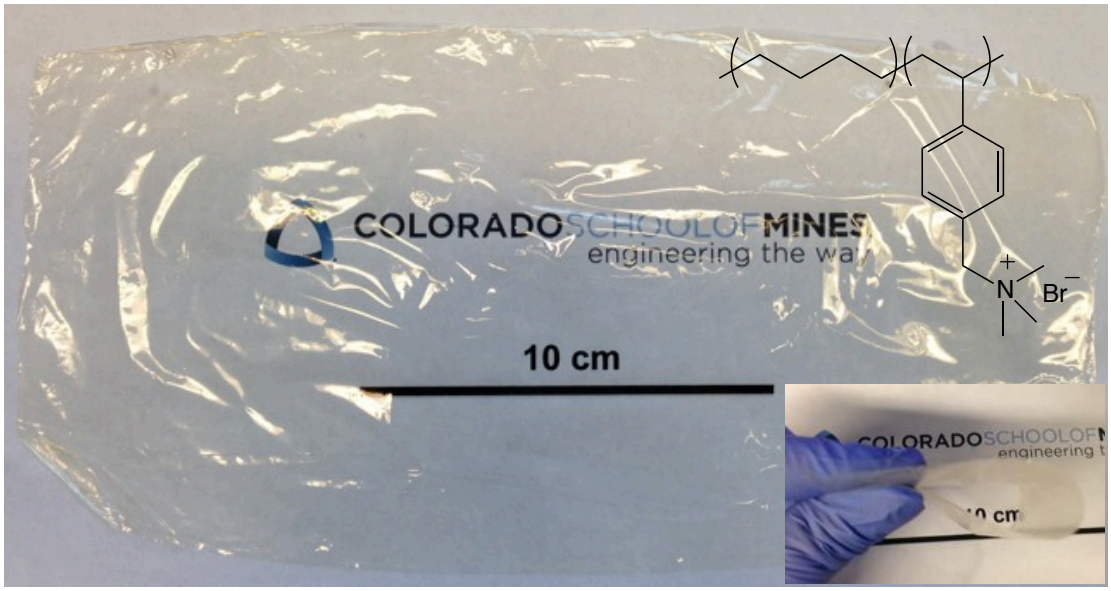

Figure 174: Photograph of PE-b-PVBTMA[Br] film after casting and functionalization. Film was pliable as shown by the folded film in the right lower inset.

Ionic conductivity of the PE-b-PVBTMA polymer in the bromide counter ion form was measured as a function of temperature at saturated conditions (95%RH). Conductivity ranged from 5 mS/cm at 50°C to 15 mS/cm at 90°C and had an E_a of 27 kJ/mol based on an Arrhenius fit (Figure 175). These conductivities are similar to other AEMs with similar IECs. The activation energy of the PE-b-PVBTMA membrane is higher than standard PEMs and similar to slightly higher than AEMs.

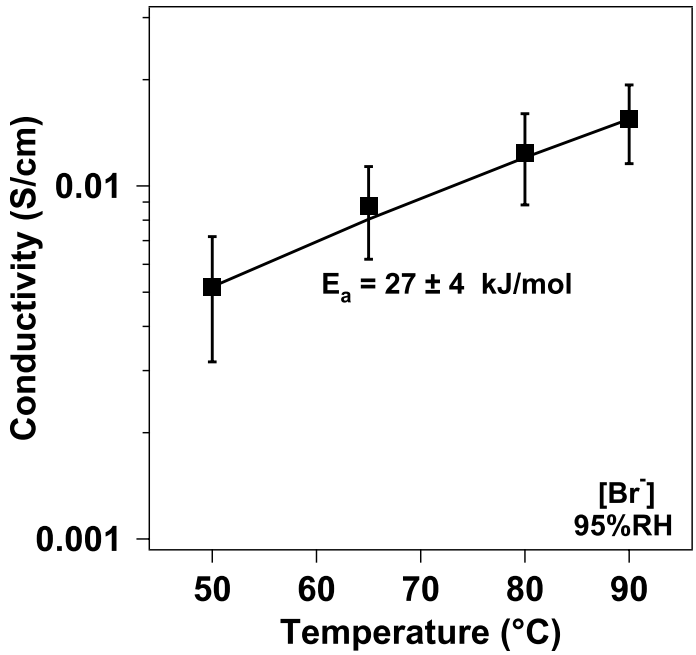

Figure 175: Ionic conductivity of the PE-b-PVBTMA[Br] polymer at 95%RH.

Liquid water uptake and swelling were measured to determine dimensional stability. Water uptake was relatively low for the PE-b-PVBTMA at 17 ± 5%, corresponding to a lambda value of 8 ± 2. This water uptake is smaller than most other AEMs, due in part to

its relatively low IEC. The low water uptake results in low dimensional swelling of the film. Dimensional swelling was 8 ± 3% in the in-plane direction, and 5 ± 2% in the through-plane direction. A low level of dimensional swelling is beneficial to prevent significant hygrothermal stresses due to elongation and contraction of the membrane during humidity changes and reducing the chance of delamination or cracking of catalyst layers in the stack.

Small angle x-ray scattering was performed to identify nanometer scale phase separation and organization in the membrane (Figure 176). The scattering of the PE-b-PVBTMA[Br] at dry and 90%RH conditions exhibited a first order peak at q* = 0.146 nm^{-1}, that corresponds to a d-spacing of 43 nm, and secondary shoulder at q ~ 0.43 nm^{-1}, approximately three times q*. No distinguishable changes in scattering pattern were observed from dry to saturated gas conditions, other than a slight increase in intensity in the low q range. However, the first order peak shifted to lower q when the sample was soaked in liquid water. A first order peak in the liquid equilibrated sample at q* = 0.112 nm^{-1} corresponded to a d-spacing of 56 nm, and a secondary shoulder at q ~ 0.33 maintained the 3q* ratio seen in the humidified sample. While the scattering pattern of the PE-b-PVBTMA[Br] suggested nanometer scale phase separation, the broad nature of the scattering features prevented specific characterization of copolymer morphology. The SAXS patterns suggested that the membrane is dimensionally stable on the nanometer scale across all humidity conditions, however liquid water uptake causes some domain swelling.

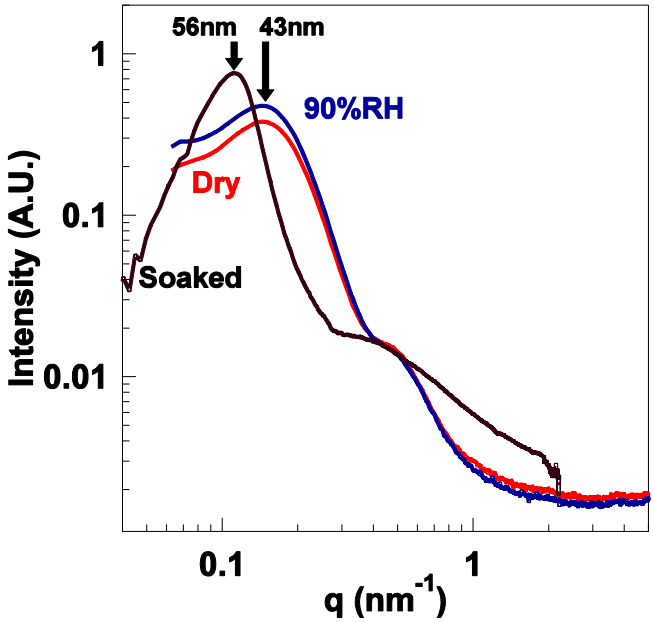

Figure 176: SAXS scattering patterns of the PE-b-PVBTMA[Br] membrane at dry (<5%RH), 90%RH, and liquid soaked conditions. There is a first order scattering peak corresponding to a d-spacing of 43 nm for the dry and 90%RH conditions that shifts to 56 nm in the liquid soaked condition

Extensional tests were performed to measure tensile properties of the PE-b-PVBTMA[Br] films under dry and saturated gas conditions at 60°C (Figure 177). When hydrated, water taken up by the polymer acts as a plasticizer, increasing elasticity and elongation and reducing strength. Water plasticization can be detrimental to the

mechanical durability and performance of ion exchange membranes. Maintaining sufficient mechanical performance over a range of hydration levels is critical for long-term stability of AEMs. The PE-b-PVBTMA[Br] membrane had good strength at dry conditions, 28 ± 4 MPa, and strength was only reduced by 29% to 20 ± 4 MPa when fully saturated. The strength of the PE-b-PVBTMA is lower than Nafion®, but better than many AEMs, and the narrow change between dry to hydrated conditions is promising for stable performance in an electrochemical device. Elongation of the PE-b-PVBTMA[Br] film was 150 ± 20% at dry conditions and 220 ± 20% at saturated conditions. Elongation must be sufficient to accommodate dimensional swelling due to water uptake, and the elongation of the PE-b-PVBTMA is significantly larger than the dimensional swelling from liquid water, discussed previously. At dry conditions the PE-b-PVBTMA polymer has a Young's modulus of 210 ± 30 MPa, similar to Nafion®, meaning the membrane is stiff enough to be dimensionally stable, but not brittle. However, when hydrated the membrane is severely softened, with the Young's modulus being reduced by 95% to 11 ± 2 MPa. This reduction in modulus is significant and may be a concern for stable mechanical performance. The severe reduction of modulus between dry and hydrated states warranted further study by dynamic mechanical analysis.

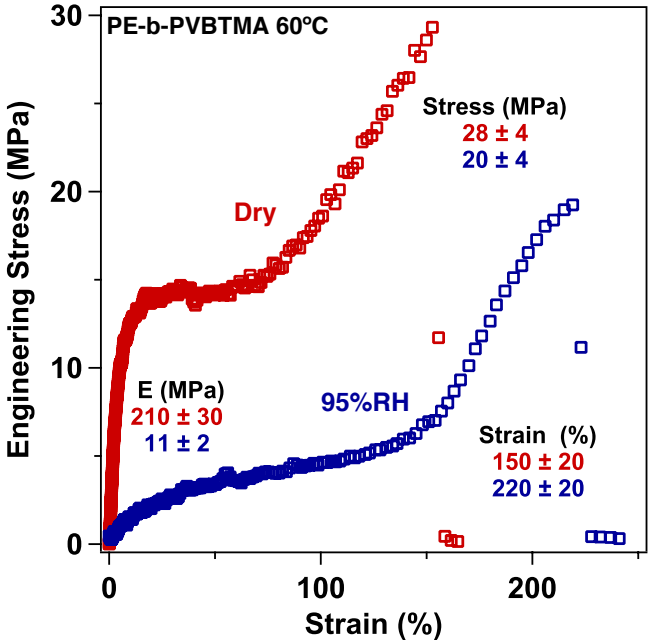

Figure 177: Representative stress vs. strain curves of the PE-b-PVBTMA[Br] films at dry (red) and 95%RH (blue) conditions. Average tensile properties of Young's modulus (E), stress, and elongation are shown inside the figure.

Dynamic mechanical analysis was performed while ramping temperature under dry or saturated relative humidity conditions to identify thermomechanical transitions within the fuel cell operating range (Figure 178). At dry conditions, the storage modulus has a fairly narrow range varying from 420 ± 120 MPa at 30°C to 210 ± 10 MPa at 90°C and shows no hysteresis between the heating and cooling. While the dry storage modulus changed by about 50% between 30 - 90°C, under hydrated conditions the change in modulus was more significant ranging from 43 ± 13 MPa at 30°C to 6 ± 1 MPa at 90°C.

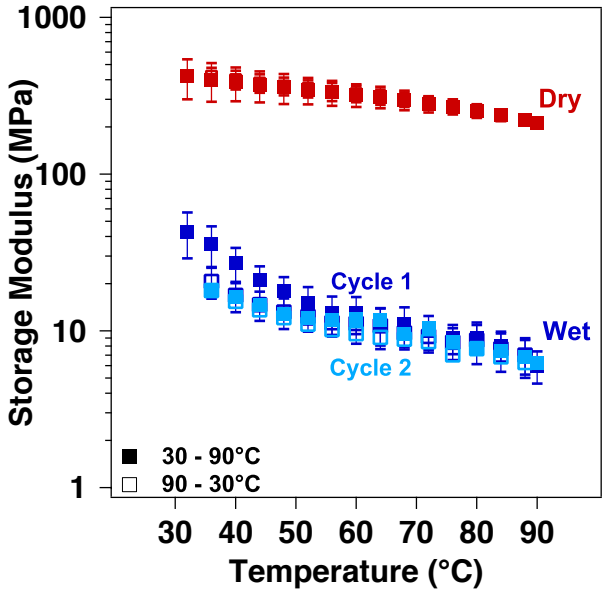

Figure 178: Storage modulus, measured by DMA, of the PE-b-PVBTMA[Br] membranes as a function of temperature under dry and saturated relative humidity conditions. Solid markers are during heating from 30 - 90°C and open markers are during cooling from 90 - 30°C. The light blue data is the second cycle of heating and cooling for one sample at saturated conditions.

At hydrated conditions hysteresis in the storage modulus is observed. Upon cooling from 90°C to 30°C, the storage modulus measured only 21 ± 5 MPa, compared to 43 ± 13 MPa at the start of the test. This hysteresis could be due to different sorption kinetics during heating compared to cooling, incomplete saturation at the start of the test even after 1 h of equilibration, or higher sample elongation during the initial heating ramp to maintain sample tension. During the initial heating ramp, the sample elongates between 15 - 25% in order to maintain tension on the sample, and upon cooling the sample contracts but not fully, remaining 5 - 15% elongated. This hysteresis was further investigated by allowing the sample to undergo a second cycle of heating and cooling. The second cycle showed no hysteresis between heating and cooling steps, so it is likely that incomplete hydration at the start of the test resulted in higher moduli at low temperatures for the initial heating compared to cooling and subsequent cycle. While the storage moduli decreased with increasing temperature at both dry and hydrated conditions, no major mechanical transitions were observed over this range of temperatures, suggesting the large difference in moduli between dry and hydrated states is result of hydration alone.

Mechanical transitions related to hydration (humidity), hygromechanical, were analyzed by performing DMA while ramping humidity from 10 to 90%RH and back to 10%RH, at a constant temperature (Figure 179). Humidity testing was initially performed at 60°C to match extensional testing. During humidification, the storage and loss moduli remained relatively steady until a sharp decrease in moduli between 55 - 75%RH, when both moduli are reduced by an order of magnitude. Upon dehumidification, the moduli transitioned back to its stiffened state, but the location for the transition was shifted down to 35 - 50%RH. Returning to 10%RH the storage modulus was slightly larger, 350 ± 4 MPa, than the initial value, 200 ± 17 MPa, and the loss modulus decreased slightly, 16.5 ± 0.7 MPa, compared to the initial value of 24.5 ± 0.7 MPa. This hysteresis of the moduli at dry conditions is most likely due to initial stretching of the film during the first humidification, because hysteresis was not seen in subsequent cycles. The samples were

humidified and dehumidified a second time to determine further hysteresis of the membranes. The second cycle displayed the same softening transition during humidification and stiffening transition during dehumidification as the first cycle. At low humidities, the moduli values of the second cycle align with dehumidification values of the first cycle, further confirming that the low humidity hysteresis is due to initial sample elongation rather than differences of the kinetics of sorption and desorption.

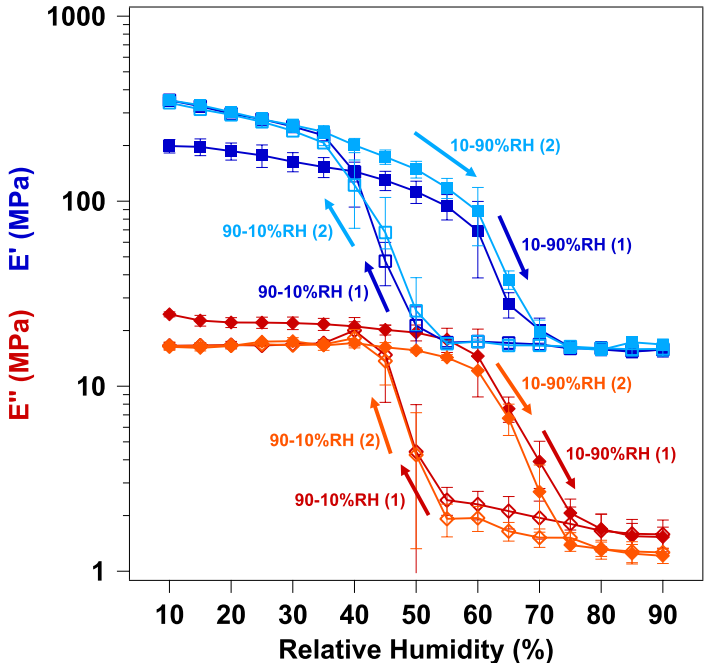

Figure 179: Storage (E') and loss (E'') moduli of PE-b-PVBTMA[Br] as function of humidity. Solid markers are during humidification from 10 - 90%RH, open markers are during dehumidification from 90 - 10 %RH. Cycle 1 is shown in dark blue (E') and red (E''), cycle 2 is shown in light blue (E') and orange (E'').

The hysteresis of the hygromechanical transition from humidification to dehumidification could be a result of different kinetics of water sorption compared to desorption. Polymer sorption and desorption kinetics were investigated by measuring gravimetric water uptake, using DVS, at the same conditions (ramp rate and cycle conditions) as the DMA testing. A small hysteresis in water uptake is measured during humidification compared to dehumidification (Figure 180), resulting in slightly differences in lambda values, up to 1.5 differences, between humidification and dehumidification for the same relative humidity value.

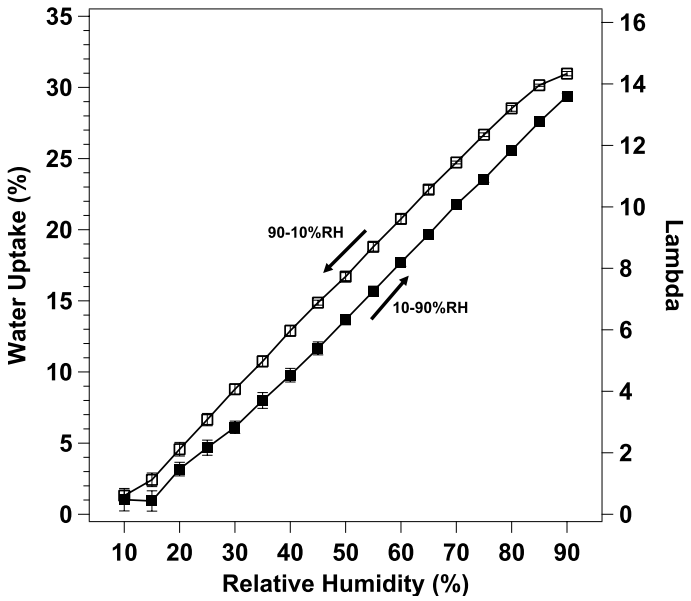

Figure 180: Water uptake and lambda vs. relative humidity. Solid markers are during humidification from 10 - 90 %RH and open markers are during dehumidification from 90 - 10%RH. There was no significant difference from cycle 1 to cycle 2 so data from the two cycles was averaged together.

Hysteresis in the moduli remained even after normalization by lambda, proving that the hysteresis was not due to sorption kinetics alone, rather the interaction of water with the polymer differs between sorption and desorption affecting the mechanical properties. Infrared spectroscopy is helpful in examining water-polymer interactions through shifts in the infrared spectrum.[14] The shift in peak position of –C-H stretch (Figure 181) as a function of RH indicated the increase in –C-H molecular vibrational frequency. At 60%RH, the –C-H stretching peak position was 3015 cm^{-1} and 3017 cm^{-1} for humidification and dehumidification, respectively. The presence of hysteresis in frequency peak position of –C-H stretching that corresponds to $[-N(CH_3)_3^+]$ provides evidence that the water-polymer interaction is different at same RH during humidification vs. dehumidification and contributes to the hysteresis in mechanical properties discussed previously.

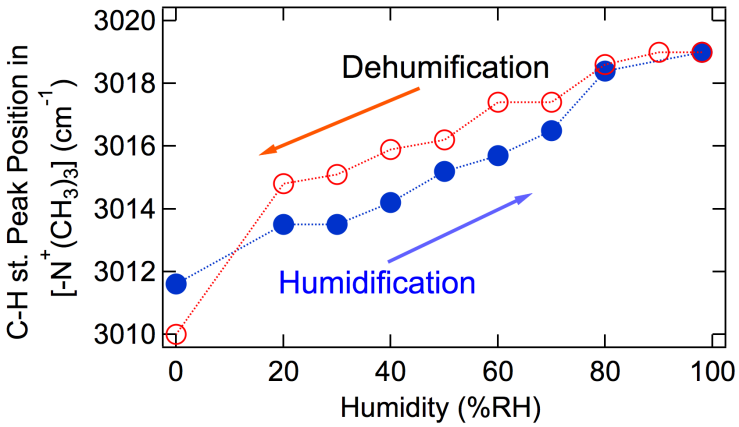

Figure 181: The shift in –C-H peak that corresponds to [-N(CH$_3$)$_3^+$] showing different –C-H bond strength for the humidification and dehumidification cycles.

An increase in conductivity was measured following mechanical softening of the material at higher water contents (Figure 182). Conductivity is already highly dependent on water content,[1,15,16] but increased chain flexibility due to mechanical softening with hydration may also contribute to enhanced ion transport. The relationship between ion conduction and mechanical softening is important to understanding AEM performance, and could help identify operating conditions for maintaining membrane and device performance. It may be beneficial to fully saturate the membrane at the start of operation, to ensure mechanical softening, and then maintain humidity above the stiffening transition for sustained ion transport.

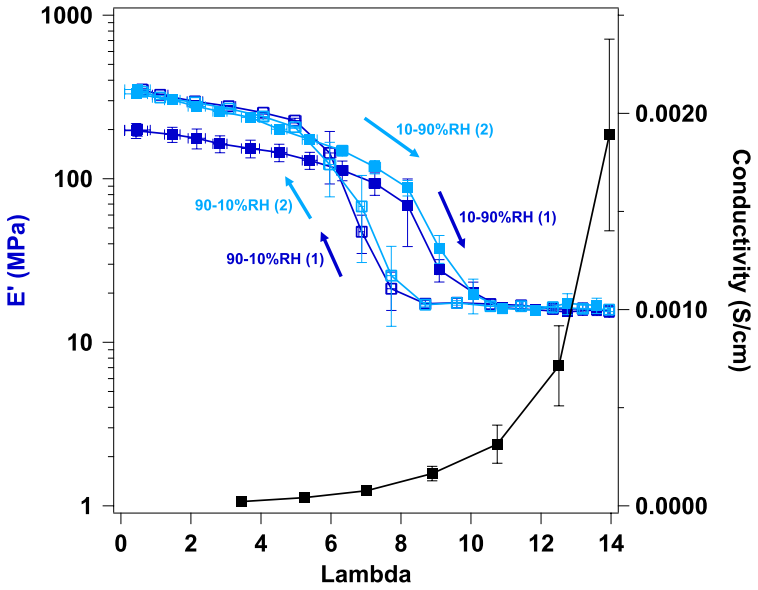

Figure 182: Storage modulus and ionic conductivity as a function of lambda.

References

[i] D. Marx, A. Chandra, and M. E. Tuckerman, "Aqueous Basic Solutions: Hydroxide Solvation, Structural Diffusion, and Comparison to the Hydrated Proton," *Chemical Reviews,* vol. 110, pp. 2174-2216, 2010.

[ii] I. S. Ufimtsev, A. G. Kalinichev, T. J. Martinez, and R. J. Kirkpatrick, "A multistate empirical valence bond model for solvation and transport simulations of OH- in aqeous solutions," *Phys. Chem. Chem. Phys.,* vol. 11, pp. 9420-9430, 2009.

[iii] I. S. Ufimtsev, A. G. Kalinichev, T. J. Martinez, and R. J. Kirkpatrick, "A charged ring model for classical OH-(aq) simulations," *Chemical Physics Letters,* vol. 442, pp. 128-133, 2007.

[iv] I. S. Ufimtsev, A. G. Kalinichev, T. J. Martinez, and J. R. Kirkpatrick, "A multistate empirical valence bond model for solvation and transport simulations of OH- in aqueous solutions," *Physical Chemistry Chemical Physics,* vol. 11, pp. 9420-9430, 2009.

[v] C. Knight and G. A. Voth, "Coarse-graining away electronic structure: a rigorous route to accurate condensed phase interaction potentials," *Molecular Physics,* vol. 110, pp. 935-944, 2012.
[vi] C. D. Wick and L. X. Dang, "Investigating Hydroxide Anion Interfacial Activity by Classical and Multistate Empirical Valence Bond Molecular Dynamics Simulations," *The Journal of Physical Chemistry A,* vol. 113, pp. 6356-6364, 2009.
[vii] C. D. Wick, "Hydronium Behavior at the Air,ÄìWater Interface with a Polarizable Multistate Empirical Valence Bond Model," *The Journal of Physical Chemistry C,* vol. 116, pp. 4026-4038, 2012.
[viii] Y. Wu, H. Chen, F. Wang, F. Paesani, and G. A. Voth, "An Improved Multistate Empirical Valence Bond Model for Aqueous Proton Solvation and Transport," *The Journal of Physical Chemistry B,* vol. 112, pp. 467-482, 2007.
[ix] E. Guardia, I. Skarmoutsos, and M. Masia, "On Ion and Molecular Polarization of Halides in Water," *Journal of Chemical Theory and Computation,* vol. 5, pp. 1449-1453, 2009.
[x] C. Knight, G. E. Lindberg, and G. A. Voth, "Multistate Reactive Molecular Dynamics," *The Journal of Chemical Physics,* vol. 137 (Nonadiabatic Dynamics special issue), 2012.
[xi] F. H. Stillinger and T. A. Weber, "Computer simulation of local order in condensed phases of silicon," *Physical Review B,* vol. 31, pp. 5262-5271, 1985.
[xii] S. Chempath, J. M. Boncella, L. R. Pratt, N. Henson, and B. S. Pivovar, "Density Functional Theory Study of Degradation of Tetraalkylammonium Hydroxides," *Journal of Physical Chemistry C,* vol. 114, pp. 11977-11983, 2010.
[xiii] H. Long, K. Kim, and B. S. Pivovar, "Hydroxide Degradation Pathways for Substituted Trimethylammonium Cations: A DFT Study," *The Journal of Physical Chemistry C,* vol. 116, pp. 9419-9426, 2012.
[xiv] Sata, T.; Tsujimoto, M.; Yamaguchi, T.; Matsusaki, K. *Journal of Membrane Science* **1996**, 112, 161-170.
[xv] A) Danks, T. N.; Slade, R. C. T.; Varcoe, J. R. *Journal of Materials Chemistry* **2003**, 13, 712-721. B) Herman, H.; Slade, R. C. T.; Varcoe, J. R. *Journal of Membrane Science* **2003**, 218, 147-163. C) Varcoe, J. R.; Slade, R. C. T. *Electrochemistry Communications* **2006**, 8, 839-843.
[xvi] A) Hibbs, M. R.; Hickner, M. A.; Alam, T. M.; McIntyre, S. K.; Fujimoto, C. H.; Cornelius, C. J. *Chemistry of Materials* **2008**, 20, 2566-2573. B)Wang, G.; Weng, Y.; Chu, D.; Chen, R.; Xie, D. *Journal of Membrane Science* **2009**, 332, 63-68. C) Wang, J.; Zhao, Z.; Gong, F.; Li, S.; Zhang, S. *Macromolecules* **2009**, 42, 8711-8717.
[xvii] Yan, J.; Hickner, M. A. *Macromolecules* **2010**, 43, 2349-2356.
[xviii] Robertson, N. J.; Kostalik, H. A.; Clark, T. J.; Mutolo, P. F.; Abruña, H. c. D.; Coates, G. W. *Journal of the American Chemical Society* **2010**, 132, 3400-3404.
[xix] A) Lin, B.; Qiu, L.; Lu, J.; Yan, F. *Chemistry of Materials* **2010**, 22, 6718-6725. B) Qiu, B.; Lin, B.; Si, Z.; Qiu, L.; Chu, F.; Zhao, J.; Yan, F. *Journal of Power Sources* **2012**, 217, 329-335.
[xx] Gu, S.; Cai, R.; Luo, T.; Chen, Z.; Sun, M.; Liu, Y.; He, G.; Yan, Y. *Angewandte Chemie International Edition* **2009**, 48, 6499-6502.
[xxi] Wang, J.; Li, S.; Zhang, S. *Macromolecules* **2010**, 43, 3890-3896.

[xxii] Thomas, O. D.; Soo, K. J. W. Y.; Peckham, T. J.; Kulkarni, M. P.; Holdcroft, S. *Journal of the American Chemical Society* **2012**, 10753-10756.
[xxiii] Lin, B.; Qiu, L.; Qiu, B.; Peng, Y.; Yan, F. *Macromolecules* **2011**, 44, 9642-9649.
[xxiv] Luo, Y.; Guo, J.; Wang, C.; Chu, D. *Journal of Power Sources* **2010**, 195, 3765-3771.
[xxv] Xu, H.; Fang, J.; Guo, M.; Lu, X.; Wei, X.; Tu, S. *Journal of Membrane Science* **2010**, 354, 206-211.
[xxvi] A) Khandpur, A. K.; Foerster, S.; Bates, F. S.; Hamley, I. W.; Ryan, A. J.; Bras, W.; Almdal, K.; Mortensen, K. *Macromolecules* **1995**, 28, 8796-8806. B) Bates, F. S. *Science* **1991**, 251, 898-905.
[xxvii] A) Elabd, Y. A.; Napadensky, E.; Walker, C. W.; Winey, K. I. *Macromolecules* **2006**, 39, 399-407. B)Elabd, Y. A.; Napadensky, E.; Sloan, J. M.; Crawford, D. M.; Walker, C. W. *Journal of Membrane Science* **2003**, 217, 227-242. C) Peckham, T. J.; Holdcroft, S. *Advanced Materials (Weinheim, Germany)* **2010**, 22, 4667-4690. D) Park, M. J.; Balsara, N. P. *Macromolecules* **2009**, 43, 292-298. E) Park, M. J.; Downing, K. H.; Jackson, A.; Gomez, E. D.; Minor, A. M.; Cookson, D.; Weber, A. Z.; Balsara, N. P. *Nano Letters* **2007**, 7, 3547-3552. F) Park, M. J.; Balsara, N. P. *Macromolecules* **2008**, 41, 3678-3687. G) Elabd, Y. A.; Hickner, M. A. *Macromolecules* **2010**, 44, 1-11.
[xxviii] Tanaka, M.; Fukasawa, K.; Nishino, E.; Yamaguchi, S.; Yamada, K.; Tanaka, H.; Bae, B.; Miyatake, K.; Watanabe, M. *Journal of the American Chemical Society* **2011**, 133, 10646-10654.
[xxix] S. T. Milner. Polymer Brushes. *Science*, **1991**, 251, 905.
[xxx] J. M. H. M. Scheutjens and G. J. Fleer, *Journal of Physical Chemistry*, **1979**, 83, 1619.
[xxxi] Shull, K. R.; Winey, K. I. *Macromolecules* **1992**, *25*, 2637.
[xxxii] Milner, S. T. *J. Chem. Soc., Faraday Trans.* **1990**, *86*, 1349.
[xxxiii] Sarode, H.; Vandiver, M.; Caire, B.; Liu, Y.; Horan, J. L.; Yang, Y.; Li, Y.; Herbst, D.; Lindberg, G. E.; Tse, Y.-L. S. *ECS Transactions* **2013**, *58*, 393.
[xxxiv] Thomas, et al., *Polym. Chem.* **2011**, 2, 1641.
[xxxv]. R. Z. Greenley, In *Polymer Handbook*; J. Brandrup, E. H. Immergut, E. A. Grulke, Eds.; John Wiley & Sons, Inc., 1999.
[xxxvi]. S. Harrisson, P. Couvreur, and J. Nicolas, *Macromolecules*, **44**(23), 9230 (2011).
[xxxvii] Dizman, C.; Tasdelen, M. A.; Yagci, Y.: Recent advances in the preparation of functionalized polysulfones. *Polymer International* 2013,
[xxxviii] Ehud Shchori, McGrath, J.E.: Spectrophotometric analysis of phenolic end groups in polymers. *Journal of Applied Polymer Science: Applied Polymer Symposium* 1978, *34*.
[xxxix] Marino, M. G.; Melchior, J. P.; Wohlfarth, A.; Kreuer, K. D.: Hydroxide, halide and water transport in a model anion exchange membrane. *Journal of Membrane Science* 2014, *464*, 61-71.
[xl] Hickner, M. A.; Herring, A. M.; Coughlin, E. B.: Anion exchange membranes: Current status and moving forward. *Journal of Polymer Science Part B: Polymer Physics* 2013, *51*, 1727-1735.
[xli] Robertson, N. J.; Kostalik, H. A.; Clark, T. J.; Mutolo, P. F.; Abruña, H. D.; Coates, G. W.: Tunable high performance cross-linked alkaline anion exchange membranes for fuel cell applications. *Journal of the American Chemical Society* 2010, *132*, 3400-4.
[xlii] Koshikawa, H.; Yoshimura, K.; Sinnananchi, W.; Yamaki, T.; Asano, M.; Yamamoto, K.; Yamaguchi, S.; Tanaka, H.; Maekawa, Y.: Counter-Anion Effect on the Properties of

Anion-Conducting Polymer Electrolyte Membranes Prepared by Radiation-Induced Graft Polymerization. *Macromolecular Chemistry and Physics* 2013, *214*, 1756-1762.

[xliii] (a) H. Matsumoto, T. Matsuda and Y. Miyazaki, *Chem. Lett.*, 2000, 1430-1431; (b) O. O. Okoturo and T. J. VanderNoot, *J. Electroanal. Chem.*, 2004, **568**, 167-181.

[xliv] (a) G. Couture, A. Alaaeddine, F. Boschet and B. Ameduri, *Prog. Polym. Sci.*, 2011, **36**, 1521-1557; (b) G. Merle, M. Wessling and K. Nijmeijer, *J Membrane Sci*, 2011, **377**, 1-35; (c) E. B. Trostyanskaya and S. B. Makarova, *Zh. Fiz. Khim.*, 1966, **39**.

[xlv] (a) K. Gyoryova and B. Mohai, *Thermochim. Acta*, 1985, **92**, 771-774; (b) J. F. Cameron, T. G. Adams, A. J. Orellana, R. M. M. and R. F. Sinta, *J. Proc. SPIE*, 1997, **3049**, 473-484.

[xlvi] J. V. Crivello, *Adv. Polym. Sci.*, 1984, **62**, 1-48.

[xlvii] S. Lindenbaum, G. E. Boyd and G. E. Myers, *J. Phys. Chem.*, 1958, **62**, 995-999.

[xlviii] (a) H. Herman, R. C. T. Slade and J. R. Varcoe, *J Membrane Sci*, 2003, **218**, 147-163; (b) J. Fang and P. K. Shen, *J Membrane Sci*, 2006, **285**, 317-322; (c) G. G. Wang, Y. M. Weng, D. Chu, D. Xie and R. R. Chen, *J Membrane Sci*, 2009, **326**, 4-8; (d) J. H. Wang, Z. Zhao, F. X. Gong, S. H. Li and S. B. Zhang, *Macromolecules*, 2009, **42**, 8711-8717; (e) Y. Xiong, Q. L. Liu and Q. H. Zeng, *J. Power Sources*, 2009, **193**, 541-546.

[xlix] S. Gu, R. Cai and Y. S. Yan, *Chem. Commun.*, 2011, **47**, 2856-2858.

[l] J. H. Wang, S. H. Li and S. B. Zhang, *Macromolecules*, 2010, **43**, 3890-3896.

[li] B. C. Lin, L. H. Qiu, B. Qiu, Y. Peng and F. Yan, Macromolecules, 2011, 44, 9642-9649.

[lii] J. Pan, Chen C., L. Zhuang and J. T. Lu, Acc. Chem. Res., 2012, 45, 473-481.

[liii] J. Pan, S. F. Lu, Y. Li, A. B. Huang, L. Zhuang and J. T. Lu, Adv. Funct. Mater., 2010, 20, 312-319.

[liv] F. X. Zhang, H. M. Zhang and C. Qu, J. Mater. Chem., 2011, 21, 12744-12752.

[lv] S. Gu, R. Cai, T. Luo, K. Jensen, C. Contreras and Y. S. Yan, Chemsuschem, 2010, 3, 555-558.

[lvi] Balkus, K. J.; Synthesis of nonasil molecular sieves in the presence of cobalticinium hydroxide; Microporous Materials 1993, 1, 383-391.

[lvii] Balkus, K. J.; Gabrielov, A. G.; Shepelev, S.; Synthesis of Aluminum Phosphate Molecular-Sieves Using Cobalticinium Hydroxide; Microporous Materials 1995, 3, 489-495.

[lviii] F. Zhang, H. Zhang, and C. Qu, J. Mater. Chem., 2011, 21, 12744.

[59] Hibbs, M. R.; Hickner, M. A.; Alam, T. M.; McIntyre, S. K.; Fujimoto, C. H.; Cornelius, C. J. *Chem. Mater.* **2008**, *20*, 2566-2573.

[60] Wende, C.; Schonhoff, M. *Langmuir* **2010**, *26*, 8352-8357.

[61] Rollet, A. L.; Simonin, J. P.; Turq, P.; Gebel, G.; Kahn, R.; Vandais, A.; Noel, J. P.; Malveau, C.; Canet, D. *J. Phys. Chem. B* **2001**, *105*, 4503-4509.

[62] Liu, Y.; Sambasivarao, S. V.; Horan, L. J.; Yang, Y.; Maupin, M. C.; Herring, A. M. *J. Phys. Chem. C* **2014**, *118*, 854-863.

[63] Latour, L. L.; Mitra, P. P.; Kleinberg, R. L.; Sotak, C. H. *J. Magn. Reson., Ser A* **1993**, *101*, 342-346.

[64] Hou, J. B.; Li, J.; Mountz, D.; Hull, M.; Madsen, L. A. *J. Membr. Sci.* **2013**, *448*, 292-299.

[65] Arges, C. G.; Parrondo, J.; Johnson, G.; Nadhan, A.; Ramani, V. *J. Mater. Chem.* **2012**, *22*, 3733-3744.

[66] Wang, J. H.; Gu, S.; Kaspar, R. B.; Zhang, B. Z.; Yan, Y. S. *Chemsuschem* **2013**, *6*, 2079-2082.

[67] McIntosh, L. D.; Kubo, T.; Lodge, T. P. *Macromolecules* **2014**.

[68] Ye, Y.; Elabd, Y. A. *Polymer* **2011**, *52*, 1309-1317.

[69] Karger, N.; Vardag, T.; Ludemann, H. D. *J. Chem. Phys.* **1990**, *93*, 3437-3444.

[70] Pendzig, P.; Dieterich, W.; Nitzan, A. *J. Non-Cryst. Solids* **1998**, *235*, 748-752.

[71] Ratner, M. A. *Polymer electrolyte reviews* **1987**, *1*, 173-236.

[72] Cowie, J. M. G.; Martin, A.; Firth, A. M. *Brit. Polym. J.* **1988**, *20*, 247-252.

[73] Ohkubo, T.; Kidena, K.; Ohira, A. *Macromolecules* **2008,** *41* (22), 8688-8693.

[74] Jayakody, J. R. P.; Khalfan, A.; Mananga, E. S.; Greenbaum, S. G.; Dang, T. D.; Mantz, R. *Journal of Power Sources* **2006,** *156* (2), 195-199.